



HAL
open science

Micromechanical modeling of microtubules

Melis Arslan

► **To cite this version:**

Melis Arslan. Micromechanical modeling of microtubules. Mechanics [physics.med-ph]. École Nationale Supérieure des Mines de Paris, 2010. English. NNT : 2010ENMP1684 . tel-00472078

HAL Id: tel-00472078

<https://pastel.hal.science/tel-00472078>

Submitted on 9 Apr 2010

HAL is a multi-disciplinary open access archive for the deposit and dissemination of scientific research documents, whether they are published or not. The documents may come from teaching and research institutions in France or abroad, or from public or private research centers.

L'archive ouverte pluridisciplinaire **HAL**, est destinée au dépôt et à la diffusion de documents scientifiques de niveau recherche, publiés ou non, émanant des établissements d'enseignement et de recherche français ou étrangers, des laboratoires publics ou privés.

École doctorale n°432 : Sciences des Métiers de l'Ingénieur

Doctorat ParisTech

THÈSE

pour obtenir le grade de docteur délivré par

l'École nationale supérieure des mines de Paris

Spécialité Mécanique

présentée et soutenue publiquement par

Mélis ARSLAN

le 26 janvier 2010

MICROMECHANICAL MODELING OF MICROTUBULES

Directeurs de thèse : *Mary C. Boyce, Sabine Cantournet*

Jury

Prof. Martine Ben Amar Président
Prof. Mathias Brieu Rapporteur
Prof. Erwan Verron Rapporteur
Dr. Julie Diani Examineur

T
H
È
S
E

ABSTRACT

Microtubules serve as one of the structural components of the cell and govern some of the important cellular functions such as mitosis and vesicular transport. Microtubules are comprised of tubulin subunits formed by α and β tubulin dimers arranged in a cylindrical hollow tube structure with a diameter of 20nm. They are typically comprised of 13 or 14 protofilaments arranged in spiral configurations. The longitudinal bonds between the tubulin dimers are much stiffer and stronger than the lateral bonds. This implies a highly anisotropic structure and mechanical properties of the microtubule. In this work, the aim is to define a complete set of elastic properties that capture the atomistic behaviour and track the deformation of the microtubules under different loading conditions. A seamless microtubule wall is represented as a two dimensional triangulated lattice of dimers from which a representative volume element is defined. A harmonic potential is adapted for the dimer–dimer interactions. Estimating the lattice elastic constants and following the methodology from the analysis of the mechanical behaviour of triangulated spectrin network of the red blood cell membrane (Arslan and Boyce, 2006); a general continuum level constitutive model of the mechanical behaviour of the microtubule lattice wall is developed. The model together with the experimental data given in the literature provides an insight to defining the mechanical properties required for the discrete numerical model of an entire microtubule created in finite element analysis medium. The three point bending simulations for a microtubule modeled using shell elements, give tube bending stiffness values that are in accordance with the experimental bending stiffness values and also reveal the mechanisms of local wall bending and shearing govern the deformation of short tubes transitioning to tube shearing and bending governing moderate length tubes and, finally, very long tubes displace by bending during the three point loading. These results uncover the importance of the anisotropic response of the tube in different loading conditions and also explain the length dependent bending stiffness reported in the literature. Furthermore, micrographs also show that shrinking ends of microtubules (due to microtubule instabilities) curl out. This implies the existence of prestress. A “connector model” is proposed to include the effect of the prestress and to capture the dynamic instabilities of microtubules during polymerization/depolymerization.

RESUME

Les microtubules sont des composants structuraux de cellules et gouvernent des fonctions cellulaires essentielles telles que les mitoses et le transport des vésicules. Ils sont composés de deux sous-unités non identiques (tubulines α et β), formant un dimère, et sont arrangés de sorte à former une structure tubulaire de 20nm de diamètre. Généralement, ils sont constitués de 13 ou 14 protofilaments arrangés en spirale. Les liaisons longitudinales entre dimères sont plus rigides et fortes que les liaisons latérales. Aussi, les microtubules sont des structures fortement anisotropes.

Dans ces travaux de thèse, nous avons pour but de définir l'ensemble des coefficients élastique qui permet de reproduire leur comportement atomistique ainsi que de rendre compte de leur réponse mécanique selon des chemins de chargement variés. En négligeant la discontinuité hélicoïdale souvent observée, un microtubule est représenté par une structure triangulaire de dimères à partir desquels un volume élémentaire représentatif est défini. Un potentiel harmonique est utilisé pour décrire les interactions entre dimères voisins. A partir de l'estimation des constantes élastiques et de l'utilisation de la méthode proposée par Arslan et Boyce (2006) -alors pour analyser le comportement mécanique d'un réseau triangulaire de spectrines composant les membranes des globules rouges-, un modèle continu de comportement mécanique est présenté pour reproduire le comportement des parois des microtubules. Un modèle numérique éléments finis est ensuite créé pour modéliser le comportement d'un microtubule dans sa globalité. Des éléments coques sont utilisés pour reproduire les fines parois des microtubules. Les propriétés du modèle éléments finis sont ajustées à partir des résultats du modèle présenté ainsi qu'aux données expérimentales provenant de la littérature. La rigidité de flexion calculée au cours de simulation des tests de flexion 3 points est en accord avec les valeurs de la littérature. Ces tests révèlent les mécanismes de déformation en fonction de la longueur utile du tube utilisé: Flexion et cisaillement locaux de la paroi gouvernent la déformation pour de "petits" tubes. Pour des longueurs "moyennes" le cisaillement et la flexion du tube prédominent. Enfin, dans le cas de tubes "longs", la déformation est uniquement associée aux effets de flexion. Ces résultats témoignent de l'influence de l'anisotropie du tube sur la réponse observée selon différents mode de sollicitation. Ils permettent également d'expliquer l'évolution de la rigidité de flexion avec la longueur utile du tube, comme reportée dans la littérature. Enfin, des micrographes montrent la propension des extrémités des microtubules à diverger radialement -"à boucler"-. Une telle géométrie est causée par des instabilités propres aux microtubules et implique un état précontraint. Un «modèle d'interactions» est alors proposé de manière à considérer un état précontraint et ainsi reproduire la cinétique des instabilités des microtubules au cours de la polymérisation/dépolymérisation.

TABLE OF CONTENTS

ABSTRACT.....	III
TABLE OF CONTENTS.....	V
LIST OF TABLES.....	VII
LIST OF FIGURES AND ILLUSTRATIONS.....	VIII
1. CHAPTER 1: INTRODUCTION.....	1
1.1. Cytoskeleton.....	1
1.1.1. Cytoskeletal Filaments.....	1
1.1.2. Basic Characteristics of the Constituents of the Cytoskeleton.....	3
1.1.2.1. Actin Filaments.....	4
1.1.2.2. Intermediate Filaments.....	4
1.1.2.3. Microtubules.....	5
1.2. Microtubules Inside the Cell.....	6
1.2.1. Microtubule Functions.....	6
1.2.2. Microtubule Structure.....	7
1.2.2.1. Lattice Structure.....	9
1.2.2.2. Tubulin-Tubulin Interactions.....	11
1.2.3. Microtubule Mechanics.....	14
1.2.3.1. Review of Experimental Techniques.....	16
1.2.3.2. Review of Modeling Methods.....	26
1.2.4. Microtubule Dynamics.....	27
1.2.4.1. Importance of Microtubule Dynamics in Mitosis.....	29
1.2.4.2. Dynamic Behaviour of Microtubules.....	30
1.3. Summary and Outline.....	31
2. CHAPTER 2: MICROMECHANICAL MODEL.....	33
2.1. Introduction.....	33
2.2. Estimation of Tubulin-Tubulin Interactions.....	33
2.2.1. Intra-Protofilament Interactions.....	33
2.2.2. Inter-Protofilament Interactions.....	35
2.3. Continuum Modeling Method for Seamless Microtubules.....	38
2.3.1. Deformation of the Lattice RVE.....	39
2.3.2. Constituent Bond Interactions.....	41
2.3.3. Strain Energy Density of the RVE.....	41
2.3.4. Energy Method and the Spring Constants for the A Lattice and the B Lattice.....	42
2.3.5. Stress- Stretch Relationships.....	45
2.3.6. The Stiffness Matrix.....	46
2.3.7. Results for the Seamless Microtubules.....	48
2.3.7.1. TEST 1: Pure Shear.....	49
2.3.7.2. TEST 2: Uniaxial Tensile Strain in the 1-Direction.....	52

2.3.7.3.	TEST 3: Uniaxial Tensile Strain in the 2-Direction	55
2.3.7.4.	Uniaxial Tension in the 1-Direction	58
2.3.8.	B Lattice	64
2.4.	Discussion and Concluding Remarks	71
3.	CHAPTER 3: EQUIVALENT CONTINUUM MODEL	78
3.1.	Introduction	78
3.2.	The mechanical thickness	79
3.3.	Finite Element Methods	82
3.3.1.	Three Point Bending	82
3.3.1.1.	FEM: Loading and Boundary Conditions	87
3.3.1.2.	Results	88
3.3.2.	Radial Indentation	117
3.3.2.1.	FEM: Loading and Boundary Conditions	120
3.3.2.2.	Results	121
3.4.	Discussion and Concluding Remarks	129
4.	CHAPTER 4: MICROTUBULE DYNAMICS	142
4.1.	Introduction	142
4.2.	Intrinsic Curvature and Energy Exchange	143
4.3.	Previous Models	145
4.4.	Prestress	151
4.5.	Finite Element Methods for Analyzing Microtubule Dynamics	152
4.5.1.	Whole Tube Stress Relief Analysis	152
4.5.2.	Single Strand Analysis	157
4.5.3.	Connector Analysis	159
4.6.	Discussion and Concluding Remarks	169
	APPENDICES	172
	REFERENCES	192

LIST OF TABLES

Table 1-1 The main constituents of the cytoskeleton and their mechanical properties

Table 1-2 Summary of the experimental findings on microtubule elastic properties (ϕ_{int} and ϕ_{ext} depicting the internal and external diameter of the microtubule (MT) respectively).

Table 2-1 Spring Constants

Table 2-2 Microtubule Mechanical Properties for a unit thickness (A Lattice)

Table 2-3 Microtubule Mechanical Properties for a unit thickness (B Lattice)

Table 3-1 The bending modulus and flexural rigidity values for different boundary conditions for the thin-shell discrete formulation of an individual microtubule of length $1\mu\text{m}$ for an effective modulus and thickness pair of $E_{11}^ = 2.4\text{GPa}$ and $t^* = 1\text{nm}$.*

Table 3-2 The bending modulus and flexural rigidity values for different boundary conditions for the thin-shell discrete formulation of an individual microtubule of length $1\mu\text{m}$ for an effective modulus and thickness pair of $E_{11}^ = 2.4\text{GPa}$ and $t^* = 1\text{nm}$.*

Table 3-3 The effective microtubule properties for different mechanical thicknesses

Table 3-4 The bending modulus and flexural rigidity values obtained by Kis et al. (2002; 2003) using AFM three-point bending experiments.

Table 3-5 The bending modulus and flexural rigidity values obtained by Kis et al. (2002; 2003) compared to the simulations carried out for different microtubule thickness values.

Table 3-6 The bending modulus and flexural rigidity values of Kis et al. (2002; 2003) modified by a factor of “1/2” to mimic the effect of a pure microtubule.

Table 3-7 The effective microtubule properties for different effective “E, t” pairs.

LIST OF FIGURES AND ILLUSTRATIONS

<i>Figure 1-1 A schematic of cytoskeleton (Raven et al., Biology, 2004).</i>	1
<i>Figure 1-2 Micrographic comparison of the cytoskeleton network with other fibrous materials' networked structure ((A): Hartwig, 1992; (B)-(E): Gibson and Ashby, 1999).</i>	2
<i>Figure 1-3 Fluorescent micrographs showing actin microfilaments (left), microtubules (center) and intermediate filaments (right) (Ingber, 1998).</i>	3
<i>Figure 1-4 Stress/strain behavior of actin, tubulin, vimentin and fibrin polymers (Janmey et al., 1991).</i>	5
<i>Figure 1-5 Fragment of a microtubule bundle from a flagellum (Lodish et al., 2007).</i>	7
<i>Figure 1-6 Microtubules doublet structure cross-section (Lodish et al., 2007).</i>	8
<i>Figure 1-7 Dimeric tubulin subunit showing α-tubulin and β-tubulin monomers and their bound non-exchangeable GTP and exchangeable GDP nucleotides (Lodish et al., 2007).</i>	9
<i>Figure 1-8 Models of singlet (left and middle) and doublet (right) microtubules with different surface lattices of tubulin dimers. In each microtubule, α-tubulin is shaded darkly and β-tubulin is shaded more lightly (Song and Mandelkow, 1993).</i>	10
<i>Figure 1-9 A schematic view of the geometrical configurations of the A and B lattices (Tuszynski et al., 2005).</i>	11
<i>Figure 1-10 A lattice and B lattice configuration showing the RVE associated with it and highlighting the helix angles (This will be further discussed in Chapter 2).</i>	12
<i>Figure 1-11 Force-extension behaviour calculated using a harmonic potential between the dimers are represented here with springs (picture adopted from the molecular dynamics model of Deriu et al., 2007).</i>	12
<i>Figure 1-12 (A) Geometrical model of a microtubule (Portet et al., 2005), (B) In Sept et al. (2003) studies four dimers are used to calculate the binding energies. Further details of this study will be discussed in Chapter 2. M loops are shown in the figure.</i>	13
<i>Figure 1-13 Pampaloni and Florin (2008) showed the protofilament to protofilament interactions on a schematic figure using the information for 1TUB from PDB.</i>	15
<i>Figure 1-14 Dark-field microscopy reveals that the high rigidity of the microtubule leads to very small fluctuations in curvature (Gittes et al., 1993).</i>	19

<i>Figure 1-15 Microtubule thermal fluctuation data points include the first three modes of microtubules. The red, horizontal line is a mean of the measurements giving a mean value of a persistence length of ~ 5.1 μm (Gittes et al., 1993).</i>	19
<i>Figure 1-16 A simple representation of optical tweezers apparatus: (A) A generic optical tweezers diagram with only the most basic components, (B) A schematic diagram showing the force on a dielectric sphere.</i>	21
<i>Figure 1-17 (A) As a result of trapping forces up to 2.2 pN, microtubule buckling is observed (Kurachi et al. 1995), (B) Flexural rigidity results for different microtubule lengths.</i>	22
<i>Figure 1-18 Schematics of the two different methods of Felgner et al. (1996).</i>	22
<i>Figure 1-19 (A) Microtubule lying on a substrate with a hole (Kis et al., 2002), (B) Image of the microtubule before (a) and after (b) indentation (de Pablo et al., 2003).</i>	24
<i>Figure 1-20 Deriu et al. (2007) calculated the interaction energies monomer-monomer and dimer-dimer in the microtubule structure.</i>	26
<i>Figure 1-21 Chretien is one of the pioneers of the microtubule dynamics research (figure by: Chretien et al., 1995). This electron microscope image shows the ends of microtubules after 3 minutes of growth in a 13 μM tubulin solution.</i>	28
<i>Figure 1-22 (a) At prometaphase, the nuclear envelope has broken down, microtubules probe the cytoplasm until they contact a chromosome, (b) In early metaphase, most chromosomes have lined up in the equator, (c) In anaphase, the duplicated chromosomes have separated and are moving towards the spindle poles to form two daughter cells, (d) In telophase, the cell is dividing to become 2 daughter cells (Jordan and Wilson, 2004). Here blue dye marks the chromosomes, green dye the kinetochores and the red dye marks the microtubules.</i>	29
<i>Figure 1-23 Dynamic instabilities of the microtubules; schematic adapted from (Kirschner and Mitchison, 2004).</i>	30
<i>Figure 2-1 Schematic of the model proposed by Deriu et al. (2007). The choice of the nodal points in this thesis work is the center of masses of the dimers as marked in the figure (modified from Deriu et al., 2007).</i>	35
<i>Figure 2-2 Binding free energy between two protofilaments as a function of subunit rise between adjacent dimers (modified from Sept et al., 2003).</i>	36
<i>Figure 2-3 Binding free energy for the A and B lattice structures recreated using the data from Sept et al., 2003).</i>	37

Figure 2-4 A schematic of the two-dimensional sheet model is presented here depicting the subunit rise and the helix angle for the A-lattice. The RVE is shown to be a triangle.	39
Figure 2-5 A schematic of the B-lattice sheet model is presented here depicting the subunit rise, helix angle and the RVE.	40
Figure 2-6 Here a plot of the strains are given (A) for a pure shear stress. The related stress-shear behaviour is shown in (B) depicting the shear stiffness for the microtubule lattice. Here, K_s represents the shear stiffness ($G_{12}^* t^*$). This will be further explained in the next chapter.	51
Figure 2-7 A plot of the stress (T_{11}) vs. strain (e_{11}) is shown here depicting the deformed and undeformed configurations of the RVE (A). The resulting lateral stress and the shear stress are also shown in (B).	54
Figure 2-8 A plot of the stress (T_{22}) vs. strain (e_{22}) is shown here depicting the deformed and undeformed configurations of the RVE (A). The resulting longitudinal stress and the shear stress are also shown in (B).	56
Figure 2-9 The area change in the RVE under uniaxial tension in the 1-direction (A) and the resulting strains in lateral direction and the shear deformation (B) are given here.	59
Figure 2-10 Uniaxial Stress, T_{11} vs. e_{11} is shown in this figure.	60
Figure 2-11 The longitudinal stiffness in the transformed axis system for different transformation angles.	62
Figure 2-12 The shear stiffness in the transformed axis system for different transformation angles.	63
Figure 2-13 The tension-shear coupling components in the transformed axis system for different transformation angles.	63
Figure 2-14 Schematic of different lattice structures for the microtubule lattice, marking the seamless microtubules (modified from Mandelkew et al., 1986) (A). The B lattice structure together with the “skew angle” and the geometric parameters are given in (B).	64
Figure 2-15 Uniaxial Stress, T_{11} vs. e_{11} and shear stress T_{12} vs. γ_{12} is shown here depicting the longitudinal stiffness ($K_A = E_{11}^* t^*$) (A) and the shear stiffness ($K_s = G_{12}^* t^*$) (B) for the seamless B lattice.	66
Figure 2-16 The longitudinal stiffness in the transformed axis system for different transformation angles.	68

<i>Figure 2-17 The shear stiffness in the transformed axis system for different transformation angles.</i>	<i>69</i>
<i>Figure 2-18 The tension-shear coupling components in the transformed axis system for different transformation angles.</i>	<i>70</i>
<i>Figure 3-1 Range of length scales of the simulation methods (Gates et al., 2005).....</i>	<i>78</i>
<i>Figure 3-2 (A) The average radius of curvature is 19 nm (Muller et al., 1998), (B) Schematic representation of the bending of a dimer (VanBuren et al., 2005), (C) Schematic representation of a dimer unit cell.</i>	<i>80</i>
<i>Figure 3-3 Schematics of the AFM basic modes of operation.....</i>	<i>83</i>
<i>Figure 3-4 (A) A schematic of three-point bending by an AFM tip, (B) Microtubule deposited on a substrate under a loading force (Kis et al., 2002).....</i>	<i>83</i>
<i>Figure 3-5 Kis et al. experimental set up (2002).....</i>	<i>84</i>
<i>Figure 3-6 Kis et al. (2002) experimental results:(A)Bending modulus is given in terms as a function of the external diameter (25 nm), internal diameter (15 nm) and the suspended length, (B) Bending modulus measured for different temperature values for a microtubule suspension length of 200 nm.</i>	<i>85</i>
<i>Figure 3-7 Force vs. displacement curve for the three-point bending simulation comparing an anisotropic and an isotropic response for an effective modulus and thickness pair of $E_{11}^* = 2.4\text{GPa}$ and $t^* = 1\text{nm}$. The inset shows the deformed configuration of the microtubule. The suspension length (L) of the microtubule is 80 nm.....</i>	<i>89</i>
<i>Figure 3-8 Contour plots showing the longitudinal stress distribution (S_{11}) for the three-point bending of (A)Anisotropic tube and (B) Isotropic tube with a suspension length of $L = 80\text{ nm}$. On the right is the top view of the experiments depicting the shear stress distribution (S_{12}) profiles for each case. A “bottom node” on the opposite side to the indenter contact node is depicted in the figure and is to be analyzed in this section.....</i>	<i>91</i>
<i>Figure 3-9 Contour plots showing the shear strain distribution (LE_{12}) for the three-point bending of (A)Anisotropic tube and (B) Isotropic tube with a suspension length of $L = 80\text{ nm}$.....</i>	<i>92</i>
<i>Figure 3-10 The plot shows the vertical displacement of the bottom node opposite to the top surface of the tube which is in contact with the indenter for a suspension length of (A) 80 nm and (B) 200 nm.</i>	<i>94</i>
<i>Figure 3-11 Contour plots showing the longitudinal stress distribution (S_{11}) for the three-point bending of (A)Anisotropic tube and (B) Isotropic tube with a</i>	

<i>suspension length of $L = 200$ nm. On the right is the top view of the experiments depicting the shear stress distribution (S_{12}) profiles for each case.</i>	95
<i>Figure 3-12 Force vs. displacement curves for the three-point bending simulation comparing the anisotropic responses (A) and the isotropic responses (B) for an effective modulus and thickness pair of $E_{11}^* = 2.4\text{GPa}$ and $t^* = 1\text{nm}$ with suspension lengths; $L = 80$ and $L = 200$ nm.</i>	96
<i>Figure 3-13 The plot shows the vertical displacement of the bottom node opposite to the top surface of the tube which is in contact with the indenter for an effective modulus and thickness pair of $E_{11}^* = 2.4\text{GPa}$ and $t^* = 1\text{nm}$ for an isotropic and an anisotropic tube. The suspension length (L) of the microtubule is $L = 500$ nm and $L = 1000$ nm.</i>	98
<i>Figure 3-14 Contour plots showing the longitudinal stress distribution (S_{11}) and the shear stress distribution (S_{12}) for (A,E)Isotropic Tube with a suspension length of 500 nm, (B, F) Isotropic Tube with a suspension length of 1000 nm, (C, G)Anisotropic Tube with a suspension length of 500 nm and (D, H) Anisotropic Tube with a suspension length of 1000 nm.</i>	100
<i>Figure 3-15 Force vs. displacement curves for the three-point bending simulation comparing the anisotropic responses and the isotropic responses for an effective modulus and thickness pair of $E_{11}^* = 2.4\text{GPa}$ and $t^* = 1\text{nm}$ with suspension lengths; $L = 500$ nm and $L = 1000$ nm.</i>	101
<i>Figure 3-16 The sketch of the principal 1- and 2- direction of the microtubule and the transferred coordinate system as shown in Chapter 2.</i>	104
<i>Figure 3-17 Force vs. displacement curve for the three-point bending results comparing an anisotropic and an orthotropic response for a microtubule suspension length of 200nm and an effective modulus and thickness pair of $E_{11}^* = 2.4\text{GPa}$ and $t^* = 1\text{nm}$.</i>	105
<i>Figure 3-18 Force vs. displacement curve for an effective modulus and thickness pair of $E_{11}^* = 2.4\text{GPa}$ and $t^* = 1$ nm, an effective modulus and thickness pair of $E_{11}^* = 1.2\text{GPa}$ and $t^* = 2\text{nm}$ also an effective modulus and thickness pair of $E_{11}^* = 0.96\text{GPa}$ and $t^* = 2.5$ nm. The simulations given are for suspension lengths of 80 nm and 200 nm.</i>	107
<i>Figure 3-19 Force vs. displacement curves for an effective modulus and thickness pair of $E_{11}^* = 2.4\text{GPa}$ and $t^* = 1$ nm, an effective modulus and thickness pair of $E_{11}^* = 1.2\text{GPa}$ and $t^* = 2\text{nm}$ also an effective modulus and thickness pair</i>	

of $E_{11}^* = 0.96\text{GPa}$ and $t^* = 2.5\text{ nm}$. The simulations given are for a suspension length of 80 nm.....	108
Figure 3-20 Force vs. displacement curves for the three-point simulations for an effective modulus and thickness pair of $E_{11}^* = 2.4\text{GPa}$ and $t^* = 1\text{ nm}$, an effective modulus and thickness pair of $E_{11}^* = 1.2\text{GPa}$ and $t^* = 2\text{ nm}$ also an effective modulus and thickness pair of $E_{11}^* = 0.96\text{GPa}$ and $t^* = 2.5\text{ nm}$. The simulations given are for a suspension length of 200 nm.	108
Figure 3-21 Force vs. displacement curve for the three point simulations for an effective modulus and thickness pair of and $t^* = 1\text{ nm}$, an effective modulus and thickness pair of and $t^* = 2\text{ nm}$ also an effective modulus and thickness pair of and $t^* = 2.5\text{ nm}$. The simulations given are for a suspension length of 80 nm.	112
Figure 3-22 Force vs. displacement curve for the three point simulations for an effective modulus and thickness pair of $E_{11}^* = 2.4\text{GPa}$ and $t^* = 1\text{ nm}$, an effective modulus and thickness pair of $E_{11}^* = 1.2\text{GPa}$ and $t^* = 2\text{ nm}$ also an effective modulus and thickness pair of $E_{11}^* = 0.96\text{GPa}$ and $t^* = 2.5\text{ nm}$. The simulations given are for a suspension length of 200 nm.	113
Figure 3-23 Force vs. displacement curves reduced from the results of the three-point bending experiments of Kis et al. (2002; 2003) for suspension lengths of 83 nm and 200 nm including the results modified by a factor of “1/2”.	115
Figure 3-24 (A) Side view of a dimer and a (B) top view of a 13 protofilament created using cryo electron microscope images (courtesy of Dr. Denis Chretien) showing the thickness and the external diameter of the microtubule.....	116
Figure 3-25 Experimental force versus vertical displacement (indentation depth) curves obtained by Vinckier et al. (1996), nonlinear curves depicting Hertz approximations.	117
Figure 3-26 (A) de Pablo et al. (2003) experiments show that microtubule indentation is linear and reversible for forces up to 300 pN. (B) Schaap et al. (2006) show that for 2 different types of cantilever stiffnesses the microtubule stiffness averages to give a mean of 0.074 N/m.	119
Figure 3-27 The indentation experiment is simulated in the finite element medium. The example shown is the indentation of a 11.14 nm radius tube with anisotropic properties and for effective modulus and thickness pair of $E_{11}^* = 2.4\text{GPa}$ and $t^* = 1.0\text{ nm}$	121
Figure 3-28 Force versus displacement for the radial indentation for an isotropic and an anisotropic tube for two different effective pairs: for an effective modulus and	

thickness pair of $E_{11}^* = 2.4\text{GPa}$ and $t^* = 1.0\text{ nm}$, also an effective modulus and thickness pair of $E_{11}^* = 1.6\text{GPa}$ and $t^* = 1.5\text{ nm}$	122
Figure 3-29 Force versus displacement plots for the radial indentation of anisotropic tubes with different set of effective properties. Here E^* is the effective longitudinal modulus and t^* is the effective mechanical thickness.	124
Figure 3-30 The stress contours indicating the longitudinal stress (S_{11}) distribution[A-D] and the shear stress (S_{12}) distribution [E-F] at the indenter contact area for different E^* , t^* pairs and comparing isotropic and anisotropic tubes.	127
Figure 3-31 Force versus displacement for the radial indentation simulation giving a comparison with the experimental results.	128
Figure 3-32 The relative contributions of the tube bending deformation on the total displacement of the indenter in three-point bending for an isotropic and anisotropic tube.	133
Figure 3-33 The relative contributions of the shearing deformation on the total displacement of the indenter in three-point bending for an isotropic and anisotropic tube.	134
Figure 3-34 The relative contributions of tube wall bending/ ovalization deformation on the total displacement of the indenter in three-point bending for an isotropic and anisotropic tube for different E^* , t^* pairs.	135
Figure 4-1 Ribbon diagram of the tubulin dimer showing α -tubulin with bound GTP (top), and β -tubulin containing GDP (bottom). The arrow indicates the direction of the protofilament and microtubule axis(Nogales, 1998).	143
Figure 4-2 Structural model showing the microtubule instability. (a) Microtubules grow as 2D-sheets, (b)GTP hydrolyzed resulting in “blunt-ended” microtubules, (c)Microtubules lateral bonds are in a strained state about to break, (d) The unstable blunt-ended microtubule results in the loss of the GTP region (Arnal et al., 2000). During assembly, microtubules are observed to have “blunt ends”, while during disassembly they are observed to have “tapered” or “coiled” ends.	144
Figure 4-3 The micrographs show that growing ends of microtubules often taper to long, narrow.....	145
Figure 4-4 (A) A fit of the derived $r(z)$ is shown here. (B) Energy is in the units of $\frac{ac_o^2 z_o}{\sqrt{2}}$ (a is a material parameter) on the left axis and $k_B\theta$ on the right axis. The end deflection is in the units of r_o in the bottom axis and nanometers in the top axis. The dotted limit shows a hypothetical value beyond which the lateral	

<i>bonds break (Janosi et al., 2002). Note that the parameters are not given in the article.</i>	<i>147</i>
<i>Figure 4-5 Estimation of $\Delta G_{longitudinal}$ versus $\Delta G_{lateral}$ is shown. The researchers (VanBuren et al., 2002) predicted the energy of “curling out” as $2.5k_B\theta$ from the lateral energy change for a disassembly of $-30\mu\text{m}/\text{min}$.</i>	<i>148</i>
<i>Figure 4-6 (A) Initial microtubule configuration, (B) Side view of the protofilaments in the initial state, (C)The equilibrium configuration of the microtubule forming “ram’s horns” (Molodtsov et al., 2005).</i>	<i>150</i>
<i>Figure 4-7 The plot shows the relief of the prestress at the tip of the tube, two different shell elements are marked (2701 and 2703) for future reference.</i>	<i>153</i>
<i>Figure 4-8 (A) The tensile stress relief in the 1-direction (tube axis direction, S_{11}) is shown (B) which results in the accumulation of lateral tensile stress (S_{22}) and shear stress (S_{12}).</i>	<i>155</i>
<i>Figure 4-9 The plot shows the built-up of the lateral stress at the tip of the tube, two different shell elements are marked (2701 and 2703) for reference.</i>	<i>156</i>
<i>Figure 4-10 The plots shows the strain energy relief of the whole tube shell model; θ is chosen as 280 K.</i>	<i>156</i>
<i>Figure 4-11 (A) Depolymerization at the tip of the microtubules in the presence of calcium Muller-Reichert et al. (1998), (B)The single strand finite element analysis showing the strain energy release from a single strand with the inset depicting the evolution of the conformation change in the strand with the stress release.</i>	<i>158</i>
<i>Figure 4-12 The potential function used for the lateral connectors depicting the corresponding force versus extension (dimer separation) and the related stiffness in the inset are created using equation (72) and taking the necessary derivatives with respect to the dimer separation.</i>	<i>160</i>
<i>Figure 4-13 The undeformed configuration of the cylindrical tube with an axial prestress of 0.06 GPa at the most outer radial position.</i>	<i>162</i>
<i>Figure 4-14 The energy of one of the tip connectors is monitored during the finite element analysis with respect to the tip radius change of the tube giving a profile showing the energy profile suggested by equation (72). The inset shows the tip of the tube with the related connector element.</i>	<i>162</i>
<i>Figure 4-15 (A) The pictures shows the deformed contours of the cylindrical tube after the prestress is allowed to release, the tip elements are stress-free, (B) Similar conformations have been observed in the literature by researchers (Mandelkow et al., 1991).</i>	<i>163</i>

Figure 4-16 The plot shows the “energy change” associated with the prestress release for the model. A comparison of the contour plot and cryo-electron microscope images (Mandelkow et al., 1991) are shown. 165

Figure 4-17 (A) The contours for the cylindrical tube showing the accumulated lateral stress and the shear stress causing an unfavourable condition for the tube, (B) This unfavourable condition was discussed earlier with this sketch by Hunyadi et al. (2005). 165

Figure 4-18 (A) The simulation result having changed the connector stiffness down to about 0.001 N/m resulting in breaking of them under the induced prestress showing the “catastrophe” form. (B) The cryo-electron microscopic image shows the depolymerization and “coiling out” of microtubules in the presence of calcium (Muller-Reichert et al., 1998). 166

Figure 4-19 A few molecules of Vinblastine bound to the microtubule end to suppress microtubule dynamics (Jordan and Wilson, 2004). 168

1. CHAPTER 1: INTRODUCTION

1.1.Cytoskeleton

The cytoskeleton (Figure 1-1), the system of protein filaments that permeate the cytoplasmic space of all eukaryotic cells, is primarily responsible for the structural integrity exhibited by a cell and governs its deformation in response to a given stress.

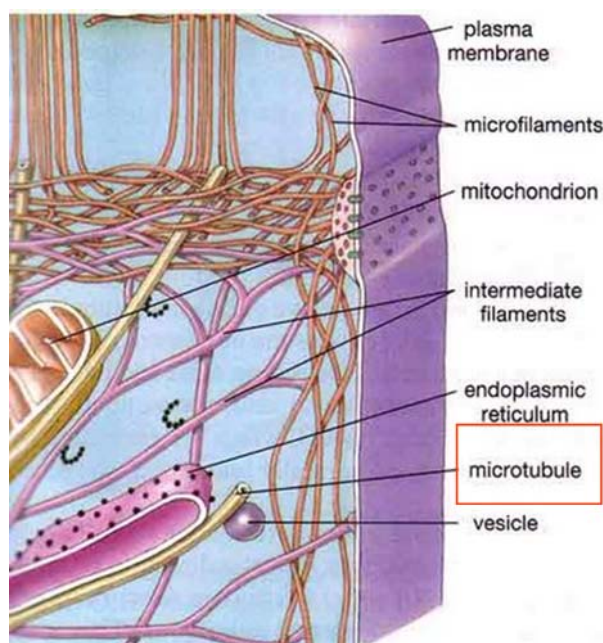


Figure 1-1 A schematic of cytoskeleton (Raven et al., Biology, 2004).

1.1.1. Cytoskeletal Filaments

The protein network of the cytoskeleton is comprised of several types of intertwined filaments with a variety of interconnections (Figure 1-2, A). The stiffness of the network depends upon the elastic properties of the constituent fibres and their geometric assembly. This chapter will examine the biological composition and the properties of the primary biopolymers that constitute the cytoskeletal network.

The cytoskeletal matrix is primarily composed of three constituents, actin microfilaments, microtubules, and intermediate filaments (Figure 1-3). These members form a complex interconnected network with varying degrees of interconnection existing in a state of dynamic equilibrium.

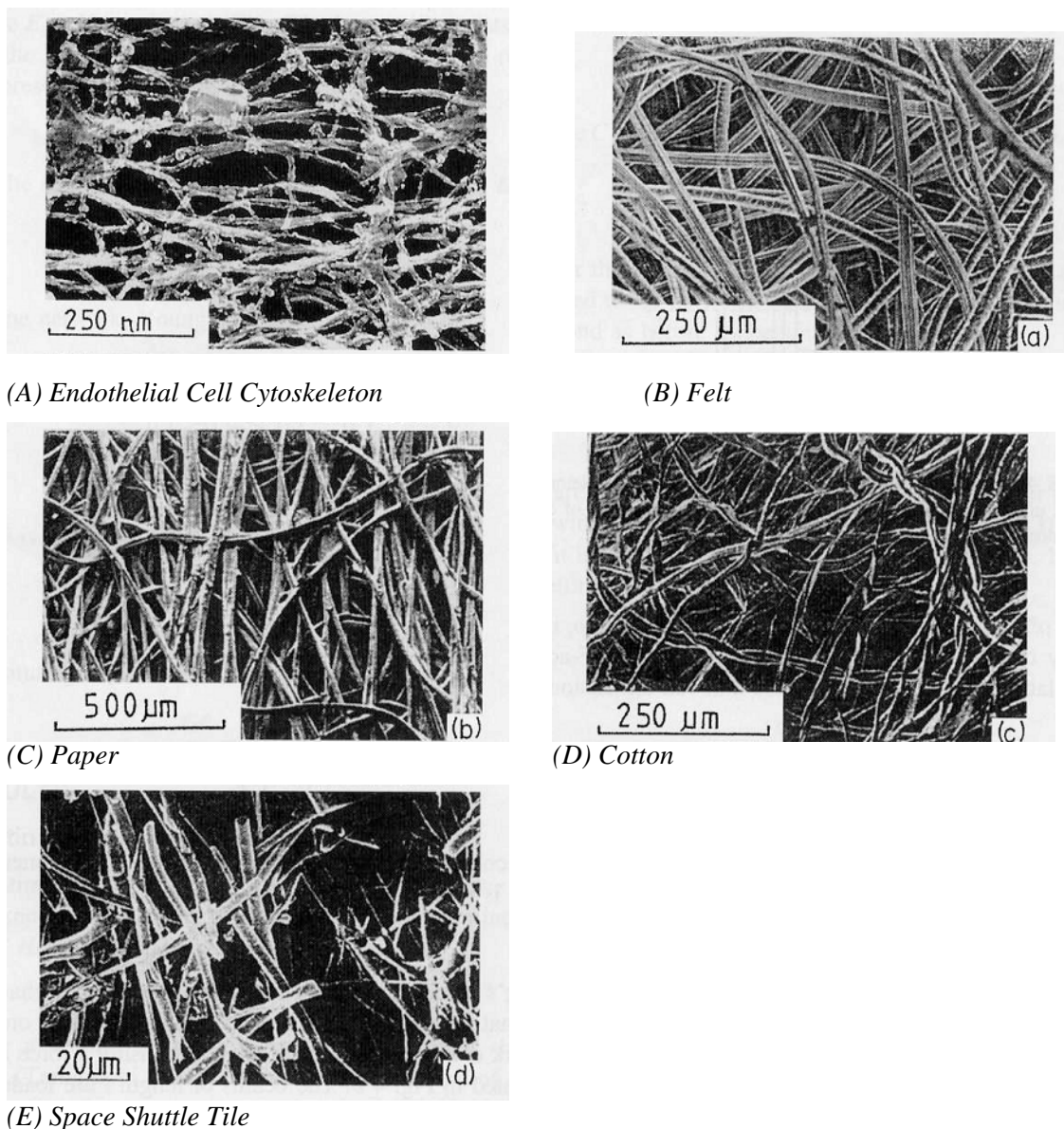


Figure 1-2 Micrographic comparison of the cytoskeleton network with other fibrous materials' networked structure ((A): Hartwig, 1992; (B)-(E): Gibson and Ashby, 1999).

Table 1-1 gives a summary of the basic characteristics of the constituents of the cytoskeleton.

Table 1-1 The main constituents of the cytoskeleton and their mechanical properties

	Diameter [nm]	Persistence Length [μm]	Flexural Rigidity [Nm ²]	Young's Modulus, E [GPa]
Actin Filament	6-8	15	7×10^{-26}	1.3-2.5
Microtubule (Length > $1 \mu\text{m}$)	25	6000	2.6×10^{-23}	1.2
Intermediate Filaments	10	1-3	$4-12 \times 10^{-27}$	1.3

1.1.2. Basic Characteristics of the Constituents of the Cytoskeleton

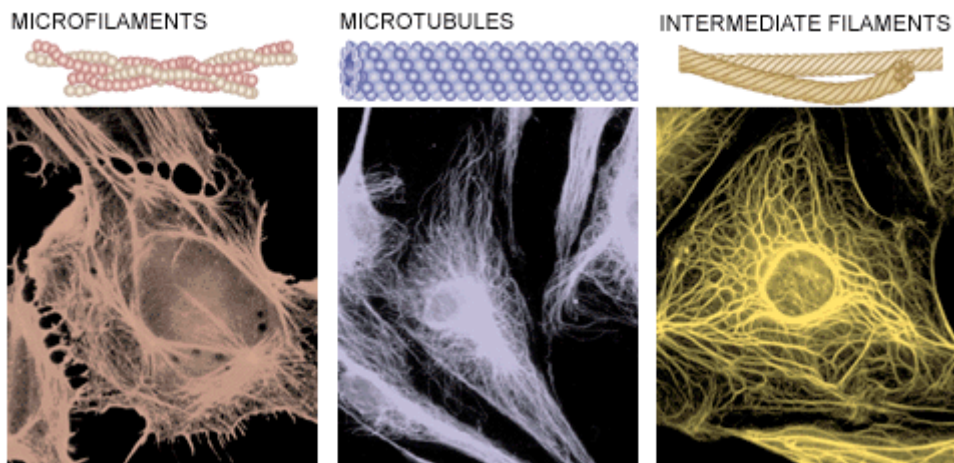


Figure 1-3 Fluorescent micrographs showing actin microfilaments (left), microtubules (center) and intermediate filaments (right) (Ingber, 1998).

1.1.2.1. Actin Filaments

Actin constitutes a main part of proteins in the cell, about 1-10 wt. % of total cell proteins in non-muscle cells and up to 20% in muscle cells. Molecular actin is comprised of 375 residues (molecular weight 43 kDa). Actin exists either in globular form (G-actin monomers) or filamentous form (F-actin polymer).

Actin filaments participate in many important cellular functions, including muscle contraction, cell motility, cell division and cytokinesis, vesicle and organelle movement, cell signalling, and the establishment and maintenance of cell junctions and cell shape. They play an essential role in all types of motility. In muscle cells, actin filaments are the scaffold on which myosin proteins generate force to support muscle contraction. In non-muscle cells, they serve as a track for cargo transport myosin.

F-actin filaments can further organize into tertiary structures such as bundles or a lattice network with the help of actin binding proteins.

1.1.2.2. Intermediate Filaments

The intermediate filaments appear to play a primary structural role in the cytoskeleton. They constitute roughly 1% of total protein in most cells, but can count for up to 85 % in cells such as epidermal keratinocytes and neurons (Fuchs and Cleveland, 1998).

The intermediate filaments are a family of related proteins that share common structural and sequence features. Intermediate filaments have an average diameter of 10 nanometers, which is between that of actin filaments and microtubules.

Although intermediate filaments are more stable than microfilaments, they can be modified by phosphorylation. This occurs on a time scale typically longer than for changes in the F-actin structures, however.

1.1.2.3. Microtubules

A microtubule, found in almost every living system, is a polymer of tubulin protein subunits, which are arranged in a cylindrical tube structure with an outside diameter of about 25nm and an inside diameter of about 15nm.

Varying in length from a fraction of a micrometer to hundreds of micrometers, microtubules are much stiffer than either actin filaments or intermediate filaments.

The constitutive behaviour of the cytoskeletal filaments can be integrated into structure-based micromechanical models of the entire cell to predict the mechanical response of the combined network in the cytoplasm.

Actin filaments, intermediate filaments and microtubules each have their specific physical properties and structure suitable for their specific role in the cytoskeleton. For example, the two dimensional arrangement of actin filaments in stress fibres, appears to form cable-like structures involved in the maintenance of the cell shape and the transduction pathways. F-actin filaments can support large stresses without high deformation and it ruptures at approximately 3.5 N/m^2 (Janmey et al., 1991). It provides the highest resistance to deformation until a certain critical value of local strain. Actin networks are believed to “fluidize” under high stresses to facilitate cell locomotion (Janmey et al., 1991).

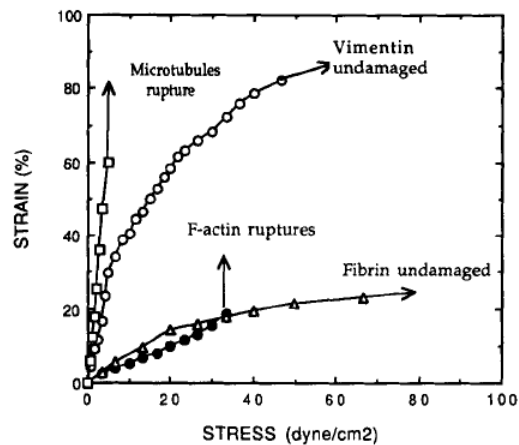


Figure 1-4 Stress/strain behavior of actin, tubulin, vimentin and fibrin polymers (Janmey et al., 1991).

Intermediate filaments are mainly involved in the maintenance of the cell shape and integrity. It is shown that (Ma et al., 1999) the intermediate filaments resist high applied pressures by increasing their stiffness. These filaments can stand higher stresses than the other two components without damage (Figure 1-5).

Microtubules undergo relatively larger strains (~60%, see: Figure 1-5) when compared to the other filaments. The rupture stress is about $0.4 - 0.5 \text{ N/m}^2$ (Janmey et al., 1991). Long microtubules ($Length > 1\mu\text{m}$) have the highest flexural rigidity when compared to the other filaments. They also resist high compression with the support from the microtubule associated proteins (Brangwynne et al., 2006). Because they are the most rigid elements of the cytoskeleton, they are largely responsible for the shape and mechanical rigidity of cells. They are also the thickest filaments in the cytoskeleton.

Microtubules have been a topic of interest for numerous experimental and theoretical researches, including those on elastic buckling (Kurachi et al., 1995; Brangwynne et al., 2006), force-related dynamic instability analysis (Molodtsov et al., 2005; Liedewij et al., 2008; Grishchuk et al., 2005), and bending experiments (Kis et al., 2002 and Pampaloni et al, 2008)

1.2. Microtubules Inside the Cell

1.2.1. Microtubule Functions

Microtubules in eukaryotic cells can be classified into two general groups; axonemal groups and cytoplasmic microtubules. The first group, *axonemal microtubules*, includes the highly organized, stable microtubules found in specific structures associated with cell movement; cilia, flagella (Figure 1-5) and the basal bodies to which these appendages are attached. The central shaft or axoneme of a cilium or flagellum consists of a highly ordered bundle of axonemal microtubules. The second group is the more loosely

organized, dynamic network of *cytoplasmic microtubules*. The second group of microtubules has not been recognized until the early 1960s.

Cytoplasmic microtubules are responsible for a variety of functions. They maintain the axons, nerve cell extensions in mammalian cells. Some migrating mammalian cells require cytoplasmic microtubules to maintain their polarized shape. Cytoplasmic microtubules form the mitotic and meiotic spindles that are essential for the movement of chromosomes during mitosis and meiosis. Cytoplasmic microtubules also contribute to the spatial disposition and directional movement of vesicles and other organelles by providing an organized system of fibres to guide the movement.

1.2.2. Microtubule Structure

The basic subunit of a microtubule protofilament is a heterodimer of the protein *tubulin*. The heterodimers are composed of one molecule of α -*tubulin* and one molecule of β -*tubulin*, each with a molecular mass of about 50 000 Da. Pairs of α -tubulin and β -tubulin form a unit 8 nm length (Figure 1-7). As soon as individual α - and β -*tubulin* molecules are synthesized, they bind tightly to each other to produce an $\alpha\beta$ -*heterodimer* that does not dissociate under normal conditions.

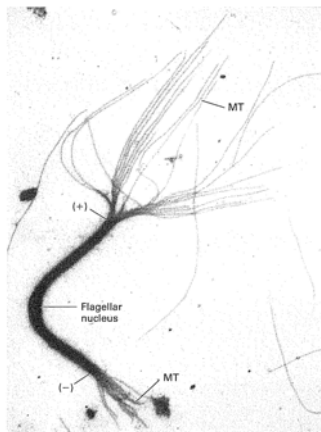


Figure 1-5 Fragment of a microtubule bundle from a flagellum (Lodish et al., 2007).

Individual α - and β -tubulin molecules have diameters of about 4-5 nm. α - and β -tubulin molecules have nearly identical three-dimensional structures (Nogales et al., 1998).

Each tubulin subunit binds two molecules of GTP (Guanosine-5'-triphosphate). One GTP-binding site, located in α -tubulin, binds GTP irreversibly and does not hydrolyze it, whereas on the second site, located on β -tubulin, binds GTP reversibly and hydrolyzes it to GDP (Guanosine-5'-diphosphate).

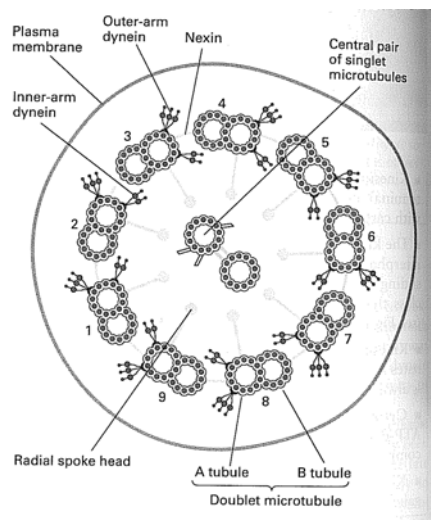


Figure 1-6 Microtubules doublet structure cross-section (Lodish et al., 2007).

The microtubule wall consists of longitudinal arrays of linear polymers called *protofilaments*. There are usually 13 protofilaments arranged side by side around the hollow center, lumen. In a microtubule, lateral and longitudinal interactions between tubulin subunits are responsible for maintaining the tubular shape. In rare cases, singlet microtubules contain more or fewer number of protofilaments (e.g. 11, 15). In addition to the simple singlet structure, doublet (in cilia and flagella) or triplet microtubules exist (centrioles, basal bodies), (Figure 1-6).

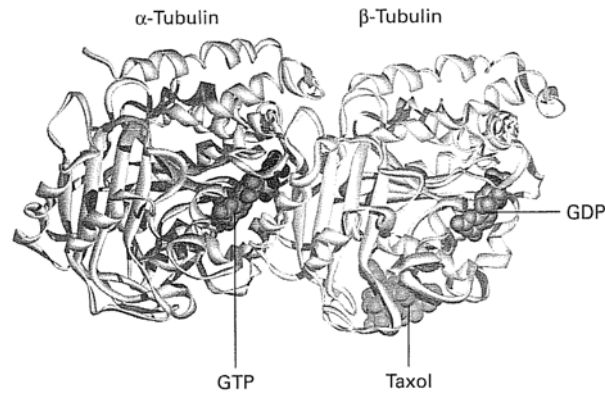


Figure 1-7 Dimeric tubulin subunit showing α -tubulin and β -tubulin monomers and their bound non-exchangeable GTP and exchangeable GDP nucleotides (Lodish et al., 2007).

A microtubule is a polar structure, its polarity arising from the head-to-tail arrangement of the exposed α - and β -tubulin dimers in a protofilament. Microtubules have a (+) and a (-) end (Lodish et al., 2007).

Because microtubules assemble from microtubule organizing centers (MTOC), microtubule polarity becomes fixed in a characteristic orientation. In most mammalian cells, the (-) ends of microtubules are closest to the MTOC.

The (+) end is the fast growing end and the (-) end is the slow growing end. This information is important in determining the direction of motion of the microtubules.

Microtubules assemble by polymerization of α - and β -tubulin dimers. Once they are assembled, their stability is temperature dependent.

1.2.2.1. Lattice Structure

Ledbetter and Porter (1963) were the first to describe the tubules found in the cytoplasm.

The experimental data in the literature covers microtubules of protofilament number ranging from 12 to 17. Chretien et al. (1992) showed that in vitro assembled microtubules mostly have 14 protofilaments whereas the cell extracts contain 13 protofilament microtubules. The predominant 13 protofilament structure in vivo has a helical pitch of 3 monomers per turn of the helix (Mandelkow et al., 1986). These microtubules are usually

referred to as “13₃ microtubules”; where 13 denoted the number of protofilaments and 3 denotes the helical pitch.

The small difference between the α - and β -monomers allows the existence of different lattice structures; A and B lattices (Figure 1-8). For the commonly accepted 13₃ model, moving around the microtubule, in a left-handed sense, protofilaments of the A lattice have a vertical shift of 4.9 nm upwards relative to their neighbours (Song and Mandelkow, 1993). In the B lattice, this offset is only 0.9 nm. This change results in a “seam” a structural discontinuity in the B lattice. The seam implies a neighbouring interaction (α - β) that differs from the majority of the lateral interactions (α - α and β - β) (Figure 1-9).

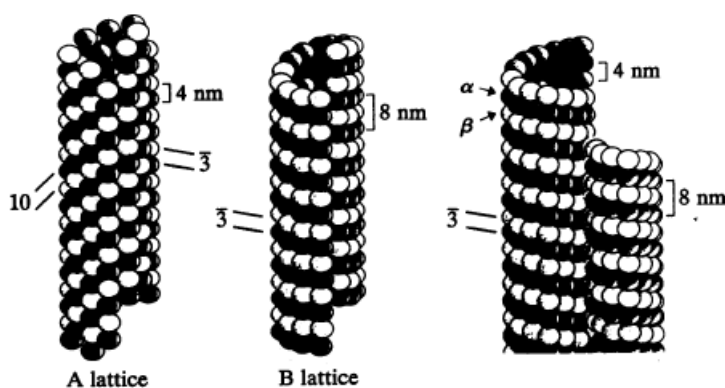


Figure 1-8 Models of singlet (left and middle) and doublet (right) microtubules with different surface lattices of tubulin dimers. In each microtubule, α -tubulin is shaded darkly and β -tubulin is shaded more lightly (Song and Mandelkow, 1993).

These two models have initially been proposed by Amos and Klug (1974). The researchers noted that A and B “sub-fibres” have the same lattice structure; however, B lattice structure shows an oblique line up of the dimers whereas in the A lattice structure, the dimers are in a staggered arrangement.

A careful look at the Figure 1-8 and the Figure 1-9, it is observed that the A lattice has a “checkered” appearance, while the B lattice gives a rather “banded” appearance. However the 8 nm dimer to dimer length is observed to be the same in both configurations.

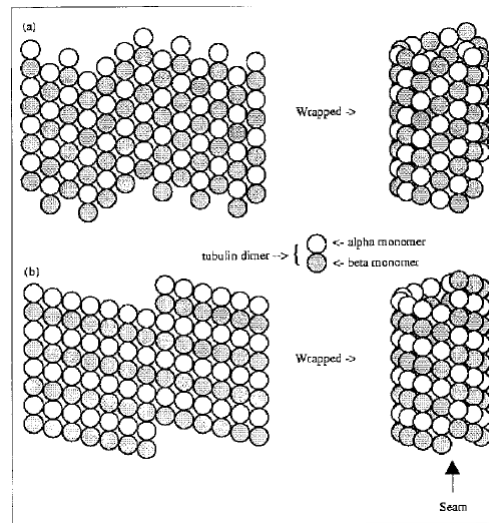


Figure 1-9 A schematic view of the geometrical configurations of the A and B lattices (Tuszynski et al., 2005).

Because of the existence of the “seam” the discontinuity in the B lattice, A lattice stacking is usually the favoured lattice for modeling. In an A lattice, the α and β subunits alternate along the helix, while in a B lattice the subunits are the same along the helix (Figure 1-9).

1.2.2.2. Tubulin-Tubulin Interactions

Once the individual monomers are synthesized, they bind tightly to each other and do not separate; a dimer could be graphically represented by a node that lies at the center of mass of the α and β monomers (Figure 1-10).

Note that in this work, it will be assumed that the monomer to monomer bonds are inextensible and that they do not break during disassembly of microtubules. Therefore the dimer can be taken as a rigid unit.

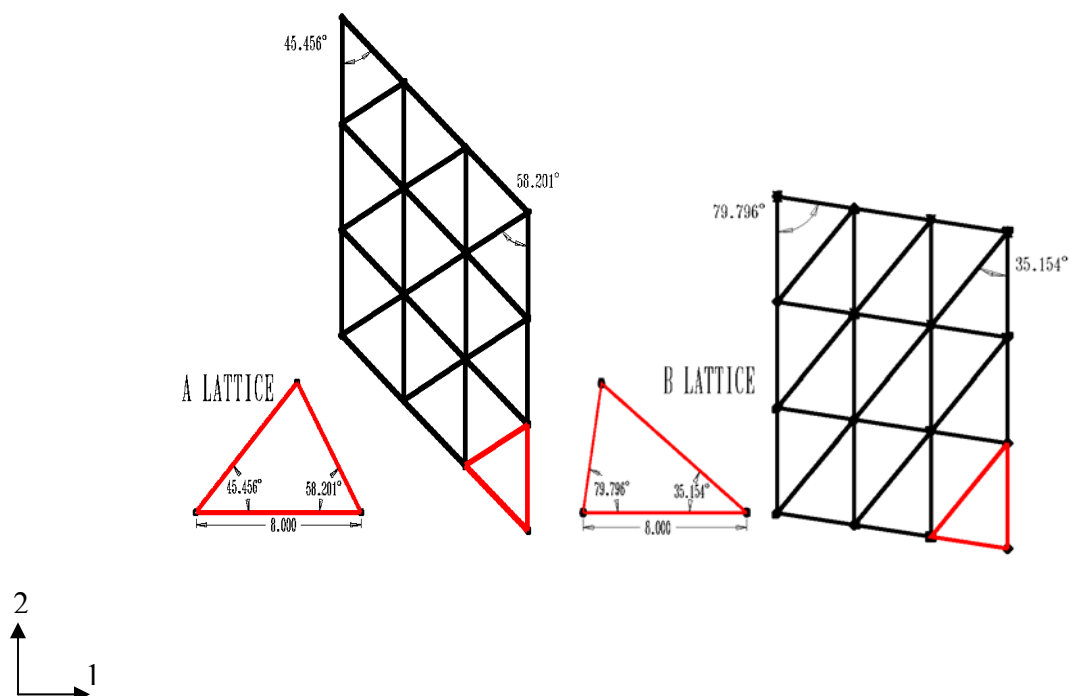


Figure 1-10 A lattice and B lattice configuration showing the RVE associated with it and highlighting the helix angles (This will be further discussed in Chapter 2).

Figure 1-10 shows that the helical angle of 45.6° corresponds to the A lattice and 79.8° corresponds to the B lattice. Further details of the lattice structure will be discussed in Chapter 2.

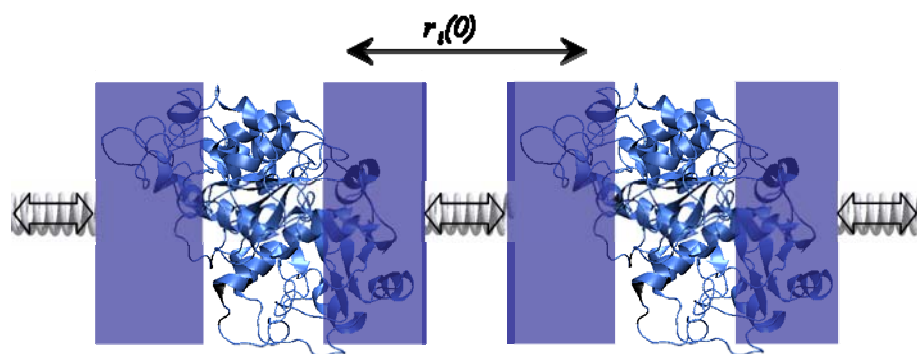


Figure 1-11 Force-extension behaviour calculated using a harmonic potential between the dimers are represented here with springs (picture adopted from the molecular dynamics model of Deriu et al., 2007).

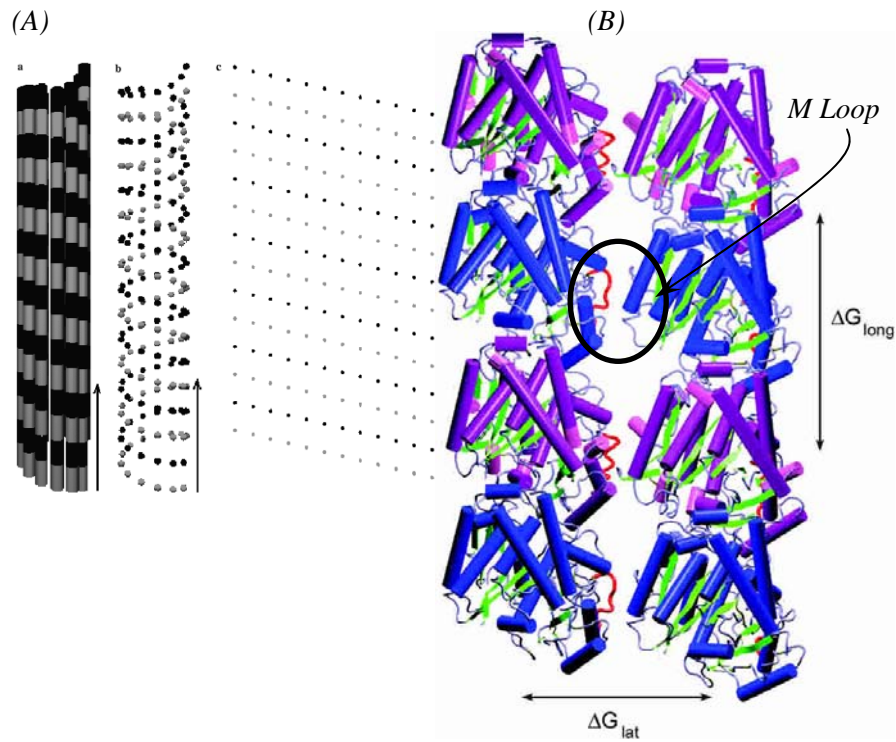


Figure 1-12 (A) Geometrical model of a microtubule (Portet et al., 2005), (B) In Sept et al. (2003) studies four dimers are used to calculate the binding energies. Further details of this study will be discussed in Chapter 2. M loops are shown in the figure.

Metoz and Wade (1997) noted that a seamless microtubule can be modeled as a three dimensional helical lattice of dimers (Figure 1-12, A). The microtubule lattice is demonstrated with a two-dimensional sheet where the small bond stretches are approximated by a harmonic energy potential (Figure 1-11) and is represented as the parabolic equation given as:

$$\mathcal{U}_{harmonic}(r_i) = \frac{1}{2} k_i |r_i(t) - r_i(0)|^2 \quad (1)$$

The exact potential functions for the intra- and inter-protofilament bonds are unknown. In the literature, different researchers (Molodtsov et al., 2005 and Deriu et al., 2007) considered different interaction potentials for the longitudinal and lateral bonds. For the former, within the protofilament, the interaction force is chosen such that it either brings

the dimers closer or separates them apart without rupture of the bonds (except from the extreme cases), but for the latter, the dimer pair tends to be in attraction until a disturbance is applied which results in separation of the pair and even breakage of the bond. This lateral interaction is captured by:

$$\mathcal{V}^* = A\xi^2 \exp(-\xi / r_o) \quad (2)$$

Here, r_o is the distance in which the bond exerts the maximum attractive force, ξ characterizes the dimers' deviation from the equilibrium configuration and A is the stiffness parameter. This kind of an energy potential captures the bending and breaking of the protofilaments during disassembly of a microtubule. This will later be discussed in Chapter 4.

1.2.3. Microtubule Mechanics

Structural investigations (Nogales et al., 1998 and Li et al., 2002) and theoretical calculations (Sept et al., 2003; VanBuren et al., 2002; Molodtsov et al., 2005 and Deriu et al., 2007) show that lateral and longitudinal tubulin interactions have different properties. While the lateral inter-protofilament contacts (α - α , β - β) are mostly electrostatic, the longitudinal intra-protofilament contacts (α - β , β - α) are hydrophobic, Van der Waals (Nogales et al., 1998). The different strengths of the inter- and intra-protofilaments bonds suggest that the longitudinal and lateral moduli are different for a microtubule, i.e. the existence of anisotropy in the microtubule structure. It's shown by Sept et al. (2003) using five dimers and an electrostatic calculations package (Baker et al., 2001) that the longitudinal bonds along the protofilaments are found to be $\sim 7 \text{ kcal/mol}$ stronger than the lateral bonds (Figure 1-12, *B*). The findings of Sept et al. (2003) have enlightened the study presented in this thesis work and the details of it will be discussed in Chapter 2.

Thus, the longitudinal and lateral interactions should be treated differently in modeling. The X-ray crystallography and cryo-electron microscopy have shown that the main

structural motif involved in inter-protofilament interactions is the ‘M-loop’ (Figure 1-12, *B* and Figure 1-13). The terminal parts of the M-loops are considerably flexible and appear to work like a hinge, allowing relative motion between the protofilaments such as shearing. They provide resilience to the microtubules to allow shear deformation in loading conditions such as bending.

Despite the various attempts in the literature to determine the lateral bonding strengths of the protofilaments (Sept et al., 2003; VanBuren et al., 2002; Molodtsov et al., 2005 and Deriu et al., 2007), there hasn’t been a mathematical method found to determine the bonding coefficients. To be able to make that possible, various approaches will be compared in this section.

A stochastic model of microtubule assembly dynamics that estimates the tubulin-tubulin bond energies-and mechanical energy stored in the lattice dimers has been developed by VanBuren et al. in 2002. From Monte Carlo simulations the researchers determined the lateral bonding energy which they found to be between $3.2k_B\theta < \Delta G_{lat} < 5.7 k_B\theta$ where k_B is the Boltzmann’s constant ($1.38 \times 10^{-23} \text{ N.m/K}$) and θ is the absolute temperature. The longitudinal bonding energy is found to be $6.8k_B\theta < \Delta G_{long} < 9.4 k_B\theta$. From here one can estimate that the longitudinal bonds are around 2-3 times stronger than the lateral bonds. This is also agreed up on in the research of Molodtsov (2005).

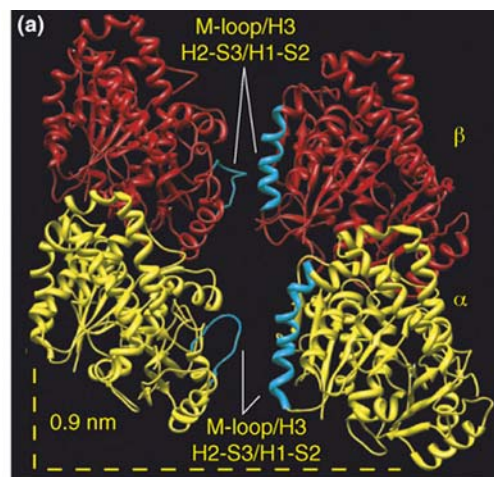


Figure 1-13 Pampaloni and Florin (2008) showed the protofilament to protofilament interactions on a schematic figure using the information for 1TUB from PDB.

If one observes the indentation experiments carried out by de Pablo et al. (2003), which will be investigated in Chapter 3, it's seen that force versus AFM tip displacement has been found to be $k \sim 0.1 \text{ N/m}$. Portet et al. (2005) have taken this to be the lateral stiffness coefficient. However it's important here to note that the indentation response is a combination of the shear stiffness and lateral stiffness; so the assumption of this last reference requires further study.

There is no direct technique to measure the elastic properties of microtubules and as a result, most experimentalists estimate the effective elastic properties of the microtubules by comparing the experimental data with static solid beam models. Theorists estimate the microtubule properties by applying atomistic dynamic models. However, in the literature we cannot find a complete description of the mechanical behaviour of the microtubules that capture the atomistic behaviour and tracking the deformation under different loading conditions and giving a complete set of mechanical properties.

Measurement results related to the mechanical properties of microtubules differ greatly. The largest discrepancies concern estimations of Young's modulus. Depending on the authors, reported values range between 1 MPa (Vinckier et al., 1996) and 7 GPa (Kurachi et al., 1995).

1.2.3.1. Review of Experimental Techniques

Experimental attempts for determining the elastic properties of microtubules date back to 1980s. In spite of the increasing level of sophistication in the analyses, there still is some conflict in the results.

We will briefly review the latest experimental techniques and the latest results from the literature. The experimental methods reviewed will include thermal fluctuation and hydrodynamic flow measurements (Gittes et al., 1993; Venier et al., 1994; Mickey and

Howard, 1995), optical tweezers (Felgner et al., 1996 and Kurachi et al, 1995) and atomic force microscopy (Kis et al., 2002; de Pablo et al., 2003 and Schaap et al. 2006).

The application of Hooke's Law to various mechanical tests of micro- and nano-scale objects enables approximation of the elastic properties. Recent advances in microscale experiments provide techniques that permit the application of forces in the pico- to micro-Newton (pN- μ N) range. Since deformations of biomacromolecules lie within this range, they can be tested using available instruments. In principle, one could directly measure the flexural rigidity of the microtubules by directly applying a known axial force at the free end and measuring its deflection. However, due to the small size and the high stiffness of the microtubules, such a measurement has not been possible. Instead, the researchers chose to apply thermal forces to the microtubule and measure the bending of constrained microtubules. Such measurements have been carried out earlier for actin filaments but it has been more challenging for microtubules because of the higher rigidity resulting in small deflections. The next section discusses thermal fluctuation measurement methods.

Analysis of Fluctuations

Gittes et al. (1993) reported the first accurate measurements of the flexural rigidity of the microtubules. By analyzing the thermally driven fluctuations in their shape, the flexural rigidity of 25-26 μ m long microtubules was reported.

Microtubules vibrate when subjected to thermal excitation. The frequencies of the natural vibrations and the shape changes are referred to as modes. Modes depend on the material mass, stiffness and damping properties of the material, as well as on the boundary conditions. As the filament shape fluctuates over time due to thermal motions, the amplitude of each mode fluctuates and this provides an estimate for the flexural rigidity of the filament. By analyzing the fluctuations associated with shape changes in the microtubules recording using dark-field and video-enhanced microscopy, the flexural rigidity of the microtubule can be estimated using the mean square vibration amplitude.

In thermal fluctuation analyses, the shape of the filament (in terms of the local tangential angle, $\theta(s)$) is represented as a sum of cosine modes (Landau and Lifshitz, 1980):

$$\theta(s) = \sum_{n=0}^{\infty} \theta_n(s) = \sqrt{\frac{2}{L}} \sum_{n=0}^{\infty} a_n \cos\left(\frac{n\pi s}{L}\right), \quad (3)$$

where L is the length of the microtubule and a_n is the amplitude of the n^{th} mode. The related bending energy is the sum of these coefficients:

$$U = \frac{1}{2} EI \sum_{n=1}^{\infty} \left(\frac{n\pi}{L}\right)^2 (a_n - a_n^0)^2. \quad (4)$$

Here a_n^0 denotes the amplitude in the absence of thermal forces and EI is the flexural rigidity.

The equipartition theorem (Reif, 1965) states that each harmonic mode has a mean energy of: $\frac{1}{k_B \theta}$. This implies that the mean square amplitude of the n^{th} mode will be:

$$\text{var}(a_n) = \left\langle (a_n - a_n^0)^2 \right\rangle = \frac{k_B \theta}{EI} \left(\frac{L}{n\pi}\right)^2. \quad (5)$$

Here k_B is the Boltzmann's constant, θ is the temperature. From here, the persistence length, l_p , is derived as:

$$l_p = \frac{EI}{k_B \theta} = \frac{L^2}{n^2 \pi^2 \left\langle (a_n - a_n^0)^2 \right\rangle}. \quad (6)$$

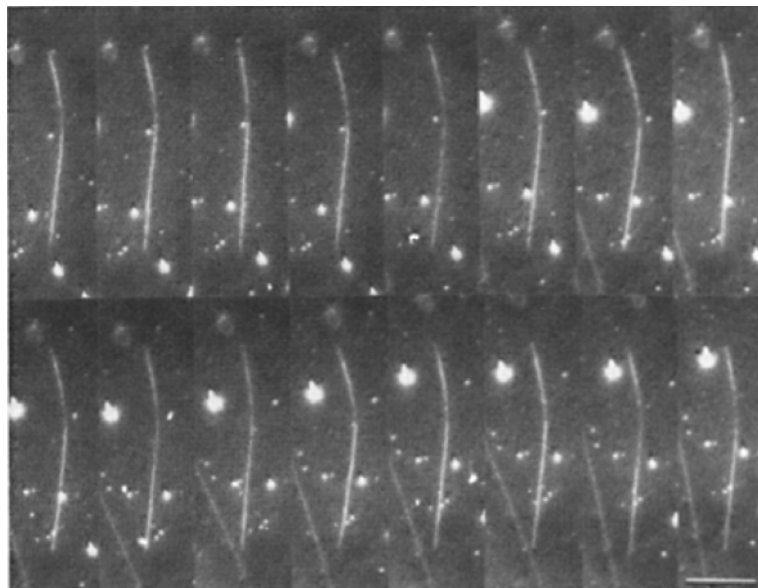


Figure 1-14 Dark-field microscopy reveals that the high rigidity of the microtubule leads to very small fluctuations in curvature (Gittes et al., 1993).

Figure 1-14 shows that the high rigidity of the microtubule leads to very small fluctuations in curvature.

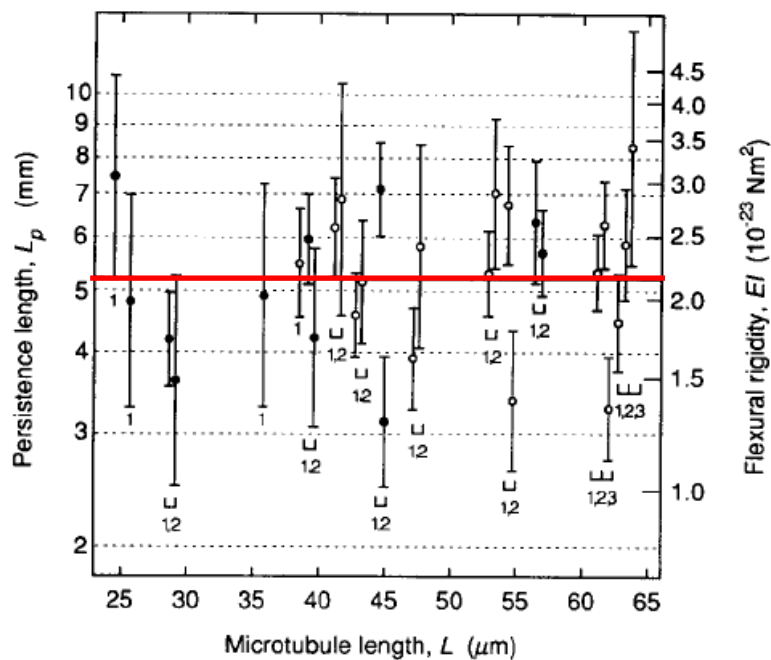


Figure 1-15 Microtubule thermal fluctuation data points include the first three modes of microtubules. The red, horizontal line is a mean of the measurements giving a mean value of a persistence length of ~ 5.1 mm (Gittes et al., 1993).

The flexural rigidity of taxol stabilized microtubules were calculated to be $2.15 \times 10^{-23} \text{ Nm}^2$. The persistence length was then derived to be $\sim 5.1 \text{ nm}$ (Figure 1-15).

The researchers (Gittes et al., 1993), using the experimental result of flexural rigidity, calculated the Young's modulus (isotropic) of the microtubules to be $E \sim 1.2 \text{ GPa}$ assuming microtubules to be hollow cylinders with an external diameter of 28 nm and an internal diameter of 23 nm . This modulus is similar to rigid plastics such as Plexiglas or polypropylene.

However, it's important to discuss a bending modulus which is different than the longitudinal modulus when shear effects are considered. Shear effects decrease the resistance to bending in a manner which depends on how bending is applied, thus the bending modulus can be much lower than the longitudinal modulus as will be shown later in this Chapter 3.

Venier et al. (1994) used a similar method to measure microtubule stiffness. They estimated flexural rigidity of $5\text{-}7 \text{ }\mu\text{m}$ long microtubules by analyzing the thermal fluctuations of axoneme-bound microtubules whose axonemal end was fixed to a glass cover-slip. The principle is based on the fact that when microtubules are attached at one end and subjected to thermal forces in solution, the free end undergoes fluctuations around an average position. The researchers used two different methods: *dynamic* and *static*. In the first method, a hydrodynamic flow was applied to microtubules and the flexural rigidity was derived from the analysis of the bending shape of the microtubules (dynamic method). In the second method, the flexural rigidity was derived from thermal fluctuation of the free end of axoneme-bound microtubules (static method). As a result, a good agreement between the values of flexural rigidity of microtubules derived from the dynamic and the static methods ($0.85 \times 10^{-23} \text{ Nm}^2$ and $0.92 \times 10^{-23} \text{ Nm}^2$, respectively).

The effect of the stabilizing agents on the microtubule rigidity has been studied by Mickey and Howard (1995) using the same techniques as Gittes et al. (1993). The researchers measured the flexural rigidity of pure microtubules to be $\sim 2.60 \times 10^{-23} \text{ Nm}^2$.

The flexural rigidity of taxol stabilized microtubules was measured to be $\sim 3.20 \times 10^{-23} \text{ Nm}^2$.

Optical Tweezers Technique

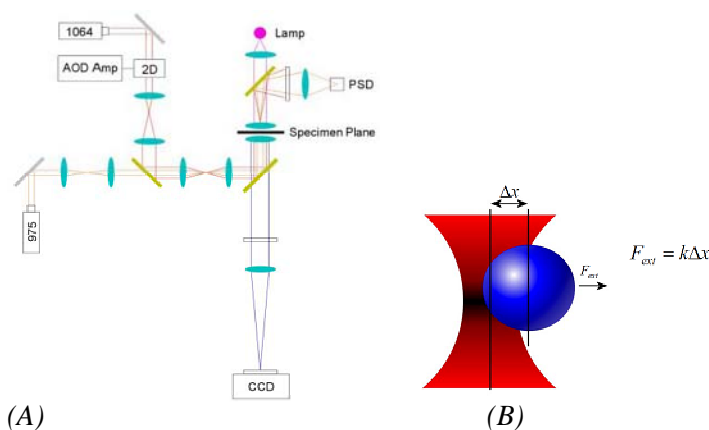
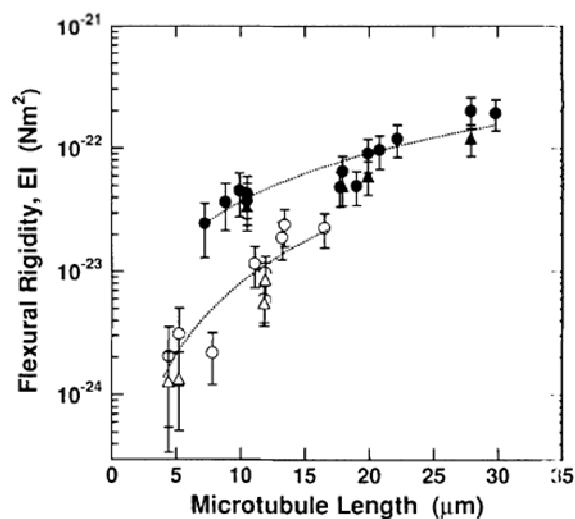
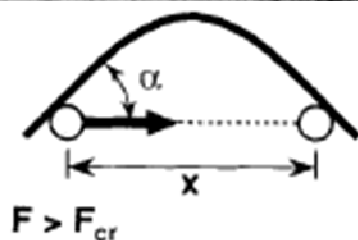
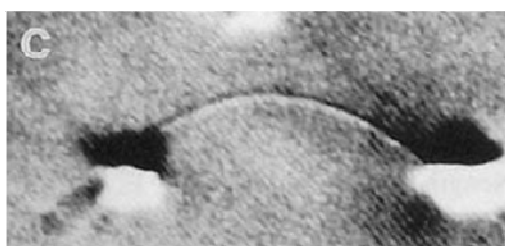


Figure 1-16 A simple representation of optical tweezers apparatus: (A) A generic optical tweezers diagram with only the most basic components, (B) A schematic diagram showing the force on a dielectric sphere.

An optical tweezer (Figure 1-16) is a scientific instrument that uses a focused laser beam to provide an attractive or repulsive force (typically on the order of piconewtons, pN), depending on the refractive index mismatch to physically hold and move microscopic dielectric objects.

Optical tweezers offer a further option for measuring the mechanical properties of cytoskeletal proteins. This technique was first used to measure the stiffness of microtubules by Kurachi et al. (1995). Buckling of microtubules was induced by the attachment of polystyrene microspheres (Figure 1-17). The stiffness of these structures was then deduced by estimating the critical buckling load (using *Euler buckling theory* and assuming an effective EI), as well as from the analysis of the deflected lengths and the bending angles. The measurements were made on taxol-stabilized and MAP-decorated microtubules. The persistence lengths, which were dependent on the deflected lengths, varied between 8 mm and 47 mm.



(A)

(B)

Figure 1-17 (A) As a result of trapping forces up to 2.2 pN, microtubule buckling is observed (Kurachi et al. 1995), (B) Flexural rigidity results for different microtubule lengths.

Felgner et al. (1996) used optical tweezers in the absence of the polystyrene microspheres. They used two different methods (Figure 1-18). The microtubules were attached at one end to axonemes glued to the cover-slip. In the first method (RELAX), the microtubule is bent perpendicularly to its long axis with the optical tweezers only once. After switching off the laser power, the microtubule relaxes and quantitative analysis of the relaxation movement yields its flexibility. In the second method (WIGGLE), the optical tweezers are used to move the microtubule back and forth against the surrounding buffer. The flexural rigidity is calculated from the bending shape of the microtubule at the moment of maximum deflection.

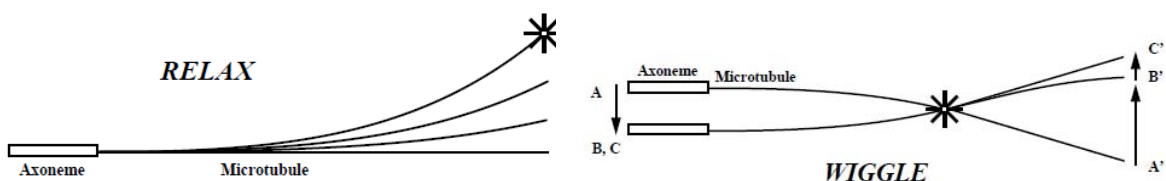


Figure 1-18 Schematics of the two different methods of Felgner et al. (1996).

The two methods yielded consistent measurements of flexural rigidity: $4.5 \times 10^{-24} \text{ Nm}^2$ for pure microtubules, about $2 \times 10^{-24} \text{ Nm}^2$ for taxol treated microtubules.

Atomic Force Microscopy (AFM)

AFM relies on probing the interaction between a sharp tip located at the end of a cantilever and the sample. The first measurements of microtubule stiffness using atomic force microscopy were made by Vinckier et al. (1996). These involved radial indentation of the microtubules and recording force versus vertical tip displacement curves in the presence of different concentrations of glutaraldehyde. The measurements revealed Young's moduli to range from 1 MPa to 12 MPa using a Hertz approximation (Sneddon, 1965).

In Kis et al. (2002) work, the microtubules were deposited on APTES-functionalized alumina membranes containing holes (Figure 1-19, A) and were subjected to three point bending using AFM. The maximum deflection of the suspended part of the microtubule was measured. The analysis considered this deflection to be the sum of the deflection due to bending and that due to shearing. The researchers derived the shear modulus to be 2 orders of magnitude lower than the Young's modulus using *Timoshenko beam bending theory* (Timoshenko, 1970).

De Pablo et al. (2003) have also used atomic force microscopy to measure the deformation of microtubules (Figure 1-19, B). The researchers applied radial indentation to microtubules. However, unlike Vinckier et al. (1996), they used taxol instead of glutaraldehyde to stabilize the microtubules. The microtubules were deposited on a glass surface that was coated with aminopropyltriethoxysilane to promote their adhesion. The force versus tip distance curves data were recorded in the linear or elastic mode. In the elastic regime, the microtubule behaved like a spring, with a spring constant of about 0.1 N/m . The authors reported the microtubules to behave linearly up to an indentation of 4 nm .

In Chapter 3, AFM methods and the findings of Kis et al. (2002) and de Pablo et al. (2003) will be discussed in more detail and will be compared with the finite element simulations based on the proposed discrete model.



(A)

(B)

Figure 1-19(A) Microtubule lying on a substrate with a hole (Kis et al., 2002), (B) Image of the microtubule before (a) and after (b) indentation (de Pablo et al., 2003).

Table 1-2 gives a summary of the experimental method findings. Note that some of the values are missing due to the fact that they were not specified in the publication.

Table 1-2 Summary of the experimental findings on microtubule elastic properties (ϕ_{int} and ϕ_{ext} depicting the internal and external diameter of the microtubule (MT) respectively).

Author	Method	MT type	Length (μm)	EI ($\text{Nm}^2 \times 10^{24}$)	Geometry	E (GPa)
Gittes <i>et al.</i> , 1993	Thermal Fluctuations	Taxol	25-65	22	Isotropic-cylinder $\phi_{int} \cong 23\text{nm}$ $\phi_{ext} \cong 28\text{nm}$	1.2
Venier <i>et al.</i> , 1994	Hydrodynamic Flow	Taxol	5-7	4.7	Isotropic-cylinder $\phi_{int} \cong 23\text{nm}$ $\phi_{ext} \cong 28\text{nm}$	0.27
Mickey And Howard, 1995	Thermal Fluctuations	Pure Tubulin	24-68	26	Isotropic-cylinder $\phi_{int} \cong 23\text{nm}$ $\phi_{ext} \cong 28\text{nm}$	1.4
		Taxol		32		1.7
Kurachi <i>et al.</i> , 1995	Optical Tweezers	Taxol	10	10	Isotropic-cylinder $\phi_{int} \cong 12.5\text{nm}$ $\phi_{ext} \cong 25\text{nm}$	0.6
Felgner <i>et al.</i> , 1996	Optical Tweezers	Pure Tubulin	6.1-14	3.7-4.7	-	-
		Taxol		1-1.9		
Vinckier <i>et al.</i> , 1996	AFM (contact mode)	Taxol, Glutaraldehyde	4	-	-	0.003
Kis <i>et al.</i> , 2003	AFM (contact mode)	Taxol, Glutaraldehyde	-	> 0.17	Isotropic-cylinder $\phi_{int} \cong 15\text{nm}$ $\phi_{ext} \cong 25\text{nm}$	> 0.1
de Pablo <i>et al.</i> , 2003	AFM (jumping mode)	Taxol	-	3.2	Isotropic-cylinder $\phi_{int} \cong 16.8\text{nm}$ $\phi_{ext} \cong 20\text{nm}$	0.8

1.2.3.2. Review of Modeling Methods

In addition to experimental investigations, there also have been many attempts to construct theoretical and numerical models of microtubules in order to better understand the physics of the deformation of the microtubules and also to interpret and to validate the experimental results.

Molecular Dynamics

Applying molecular dynamics, the mechanical characteristics of different types of interactions present in the microtubules (both between the dimers and the monomers) can be simulated.

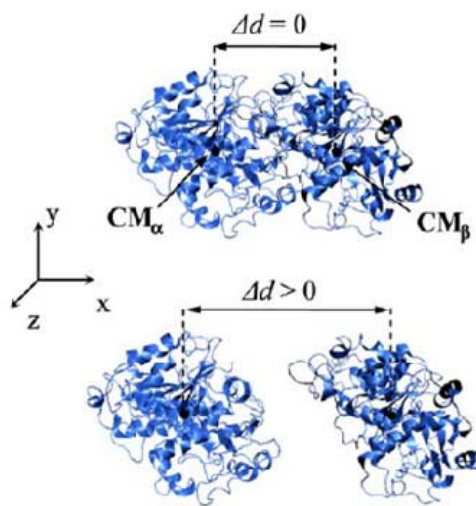


Figure 1-20 Deriu et al. (2007) calculated the interaction energies monomer-monomer and dimer-dimer in the microtubule structure.

Molecular dynamics simulations were carried out by Deriu et al. (2007) to obtain the mechanical characteristics of the different types of interactions present in the microtubules. For each molecular system, several configurations were generated with different distances ($\Delta d = d - d_o$, Figure 1-20). Minimum interactions energies together with the distance between centers of masses of the monomers were recorded and helped derive the stiffness of the constituent bonds of the microtubule. This analysis is explained in

more detail in Chapter 2 where the interaction stiffnesses derived in this work will be used and compared to the proposed work.

Finite Element Analysis

In contrast to the molecular dynamics simulations, finite element analysis requires less computation power and can be used to model larger portions or the entire length of microtubule. Therefore finite element analysis is a useful tool to approximate and estimate the mechanical properties of the microtubules.

1.2.4. Microtubule Dynamics

One of the unique properties of the microtubules is that they exhibit the “time-dependent” mechanical behaviour of “dissipative systems”; i.e. under conditions far from thermal equilibrium, they can add or remove dimers to their structure through polymerizing and depolymerizing. Microtubules enable this by changing chemical energy into “free tubulin”, to accomplish decomposition of their strongly bound structure. This is done by a self-organizational process.

Microtubules can oscillate between growing (Figure 1-21) and shortening phases. In order to achieve this behaviour, they should be able to quickly assemble or disassemble.

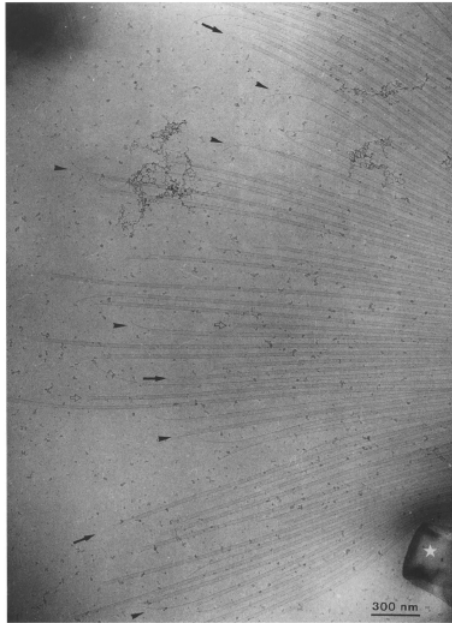


Figure 1-21 Chretien is one of the pioneers of the microtubule dynamics research (figure by: Chretien et al., 1995). This electron microscope image shows the ends of microtubules after 3 minutes of growth in a 13 μ M tubulin solution.

At low β -tubulin concentrations above the critical concentration level, the dimers polymerize into microtubules, while at concentrations below the critical level they depolymerise. During polymerization, dimers add to both ends of a growing microtubule, but the addition of tubulin subunits occurs preferably at one end. This end is usually designated by (+) and the other end by (-). In the electron microscope, growing microtubules appear to have relatively smooth ends, although some protofilaments elongate faster, creating an uneven appearance. The disassembly process appears to be different than the assembly process. Under shortening conditions, the microtubule ends are splayed, the lateral bonds between the dimers are broken. Once frayed apart and freed from lateral stabilizing interactions, protofilaments might depolymerise by endwise disassociation of tubulin subunits. The splayed appearance of a shortening microtubule shows the dynamic instability of a microtubule.

1.2.4.1. Importance of Microtubule Dynamics in Mitosis

Microtubules are extremely important in the process of mitosis as they are highly dynamic cytoskeletal fibres. During mitosis, microtubules are visible by a dramatic rise in the rate of growth and shrinkage, as they seek out the attachment point (kinetochore) on a chromosome. “Kinetochore microtubule” is the name of the microtubule that has successfully reached its target. Some microtubules during the growth process catch another microtubule coming from the opposite centriole. Meeting plus end (+) to plus end (+), these microtubules may be linked by other proteins to form a dynamic bond and are referred to as “polar microtubules”, running between the spindle poles. Microtubules can support compressive forces when they are several microns long (Gittes et al. (1996) showed that microtubules can support up to 6 pN forces). Microtubules in the cell are longer than the ones assembled in vitro; they polymerize up to several microns long during mitosis. Thus, they are rigid enough to support the polymerization forces in the cell.

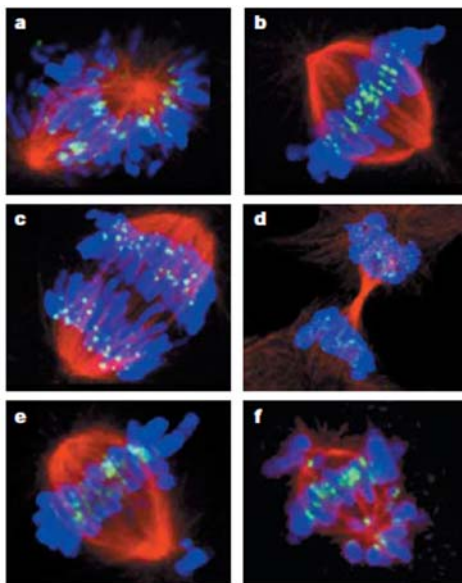


Figure 1-22 (a) At prometaphase, the nuclear envelope has broken down, microtubules probe the cytoplasm until they contact a chromosome, (b) In early metaphase, most chromosomes have lined up in the equator, (c) In anaphase, the duplicated chromosomes have separated and are moving towards the spindle poles to form two daughter cells, (d) In telophase, the cell is dividing to become 2 daughter cells (Jordan and Wilson, 2004). Here blue dye marks the chromosomes, green dye the kinetochores and the red dye marks the microtubules.

1.2.4.2. Dynamic Behaviour of Microtubules

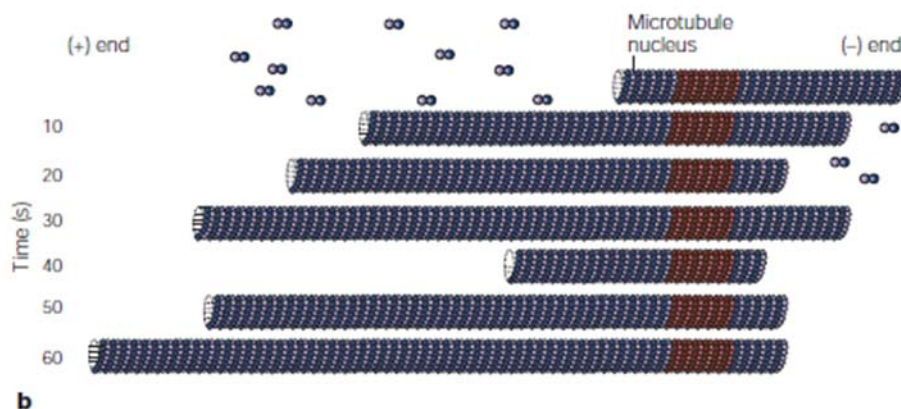


Figure 1-23 Dynamic instabilities of the microtubules; schematic adapted from (Kirschner and Mitchison, 2004).

Microtubules are highly dynamic structures, switching stochastically between growing (rate: $\sim 1\mu\text{m/s}$) and shrinking (rate: $\sim 10\mu\text{m/s}$) which occurs by addition of subunits at the ends of the polymer both in vivo and in vitro. Dynamic instabilities are the long periods of slow lengthening, brief periods of rapid shortening and periods of pause. The difference from tread milling (a treadmilling polymer gains subunits at one end and loses them at the other; i.e. the subunits move through the filament) is that the net length of the microtubule is changed and only the “+” end is active. In vivo, the “-” end which is the inactive end is connected to the centriole.

Nearby microtubules can grow and shrink independent of one another. As there can be both shrinking and growing microtubules in a given solution in vitro or in a cell in vivo, the ensemble will appear to be in a steady state.

Tim Mitchinson and Marc Kirschner proposed the Dynamic Instability (DI) model (Mitchison and Kirschner, 1984; Kirschner Mitchison, 1986). The basic theory states that growing microtubules have GTP attached to them and the shrinking microtubules have GDP bound to them. In the growing microtubules a GTP cap forms which promotes further growth. However, when the concentration of GTP-tubulin falls, the rate of polymerization falls and if the hydrolysis rate of GTP exceeds the rate of polymerization then shrinkage happens.

The factors that cause the instability of microtubules are:

- Concentration of the Mg^{2+} , Ca^{2+} ions
- Concentration of the monomers
- Temperature
- The presence of microtubule-associated-proteins (MAP)

The effects and consequences of dynamic instabilities in microtubules and the proposed models (Janosi et al., 2002; VanBuren et al., 2002 and Molodtsov et al., 2005) will be studied in Chapter 4.

1.3.Summary and Outline

The aim of this work is to develop a constitutive model to explain the deformation of the microtubule in different loading conditions. The constitutive model, together with the experimental data given in the literature provides an insight to defining the parameters required for the discrete numerical model created in finite element analysis medium. Using the published information regarding dimer-dimer interactions and the molecular geometry of the microtubules, estimates of the elastic stiffness matrix will be developed.

Chapter 2 of this work will be devoted to developing the constitutive model. The microtubule lattice (dimers defined as the crosslinking sites) is composed of a triangular lattice of dimers from which a representative volume element (RVE) can be defined. Following the methodology from the analysis of the mechanical behaviour of spectrin (Arslan and Boyce, 2005), a general continuum level constitutive model of the mechanical behaviour of the microtubules will be developed.

Chapter 3 will develop a discrete model of a tube taking into account the constitutive relationships derived in Chapter 2. Experimental techniques that are applicable to the microtubules will be presented and their applicability to the current model will be discussed.

Chapter 4 will present the biophysical facts about the microtubules and their instabilities. The energy related instability analyses that are applicable to the current model will be

discussed and presented, showing the capabilities of the model developed being able to capture the microtubule dynamics.

Résumé

Ce chapitre a pour but le développement d'une loi de comportement permettant d'expliquer le mode de déformation des microtubules selon des chemins de chargement variés. Associée aux résultats expérimentaux de la littérature, cette loi permet d'identifier les paramètres nécessaires à la conduite de simulation par éléments finis. Ayant recours à des informations publiées concernant les interactions dimère-dimère et la géométrie moléculaire des microtubules, une estimation de la matrice rigidité élastique sera proposée.

Le second chapitre de ce travail de thèse est consacré au développement d'une loi de comportement. L'organisation microtubulaire (les dimères étant définis comme les nœuds d'enchevêtrement du réseau) est composée de l'arrangement en triangle de ces dimères, à partir duquel un volume élémentaire représentatif est défini. En suivant la procédure d'analyse du comportement mécanique de spectrines (Arslan et Boyce 2006), une formulation continue de la loi de comportement des microtubules est développée.

Au cours du 3eme chapitre, un tube est représenté par un modèle discret en prenant soin d'associer au présent modèle les relations constitutives présentées au cours du chapitre précédent. Les techniques expérimentales applicables aux microtubules sont présentées et leur applicabilité au modèle développé discutée.

Le 4eme chapitre présente les faits biophysiques relatifs aux microtubules et leurs instabilités. L'énergie associée aux instabilités et applicable au modèle seront exposées et discutées, le but avoué étant de montrer la capacité du modèle développé à reproduire la dynamique des microtubules.

2. CHAPTER 2: MICROMECHANICAL MODEL

2.1. Introduction

The unique elastic properties of microtubules depend on the properties of the tubulin dimers that form the cylindrical microtubule configuration and the dimer-dimer interactions. The geometry of the microtubules was revealed fully by the detailed work of Nagoles et al. (1998). To have a complete understanding of the mechanical behaviour of microtubules, the dimer-dimer interactions and the change in these interactions with macroscopic deformations need to be investigated further. This analysis requires knowledge of the interaction energies of the dimers as well as the lattice configurations.

We describe the macroscopic deformation behavior of microtubules using a molecular statics based continuum model based on an appropriate lattice of dimers. Adopting a harmonic approximation for the dimer–dimer interactions and estimating the lattice elastic constants, we make predictions of the mechanical behavior of the microtubules under generic deformation conditions.

The basis of this chapter follows the methodology of Arslan and Boyce (2005). The microtubule lattice is a triangular lattice structure from which a representative volume element (RVE) can be defined. A general continuum level constitutive model of the mechanical behaviour of the microtubules is then developed.

2.2. Estimation of Tubulin-Tubulin Interactions

2.2.1. Intra-Protofilament Interactions

To obtain approximate intra-molecular chain stiffnesses Deriu et al. (2007) used an analogy with the mechanical springs obeying Hooke's Law ($k = F/\delta l$). For springs in series, the force across each spring is common, while the overall elongation is the

summation of individual spring elongations. For springs in parallel, however, the overall load is summed from the force across each individual spring, while the elongation is common for all springs.

Deriu et al. (2007) carried out Monte Carlo experiments to determine the bond strengths mimicked by a network of springs (Figure 2-1). The researchers built a 1 μm long microtubule constituted of 10 protofilaments with 2 start-helices (10_2). A vertical shift of 0.8 nm was considered. This vertical shift corresponds closer to a B lattice. The correct vertical shift for the 10_2 type microtubules has actually been measured by cryo-electron microscopy to be 0.94 nm (Hunyadi et al., 2005).

The longitudinal stiffness of the bonds (α - β intra-prot filament bonds) is considered to be the same for different types of seamless microtubule lattices (i.e. different number of protofilaments). Hence, the longitudinal modulus for a 13_3 microtubule that will be constructed in this work will be derived from the information provided by the molecular dynamics methods of Deriu et al. (2007).

For the spring model given in Figure 2-1 (modified from Deriu et al., 2007), where the nodal points have been chosen to be the centre of masses of the monomers unlike in the proposed model where the nodal points are taken to be the centre of masses of the dimers. This difference is marked in Figure 2-1. The equivalent longitudinal (intra-prot filament) bond equation is given as:

$$k_{11} = \left[2 \left(\frac{1}{2k_{\alpha}} \right) + 2 \left(\frac{1}{2k_{\beta}} \right) + \frac{1}{k_{\alpha\beta}} + \frac{1}{k_{\beta\alpha}} \right]^{-1} \quad (7)$$

The elastic constants were evaluated using molecular dynamics simulations.

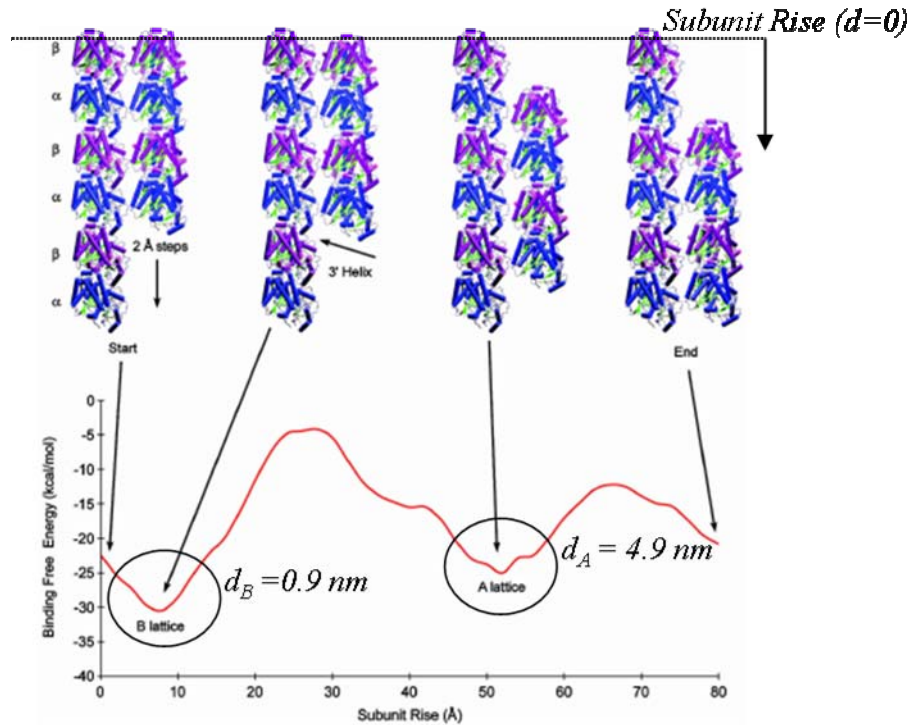


Figure 2-2 Binding free energy between two protofilaments as a function of subunit rise between adjacent dimers (modified from Sept et al., 2003).

The electrostatic calculations were performed using the molecular simulation package APBS (Baker et al., 2001). Poisson-Boltzmann equations were used to capture both Coulombic and polar inter-protofilament energies. After unit conversions, the binding free energy for the sample set of dimers is recreated in Figure 2-3.

The Sept data will be used to determine the overall lateral stiffnesses for the A and B lattices. Figure 2-3 shows that the binding free energies for both lattice configurations can be approximated using parabolic functions.

The energy functions are derived as follows;

For the B lattice:

$$\mathcal{V}(d) = 0.11d^2 - 0.16d - 0.15 \quad (8)$$

And for the A lattice:

$$\mathcal{U}(d) = 0.075d^2 - 0.77d + 1.80 \quad (9)$$

where d is the subunit rise.

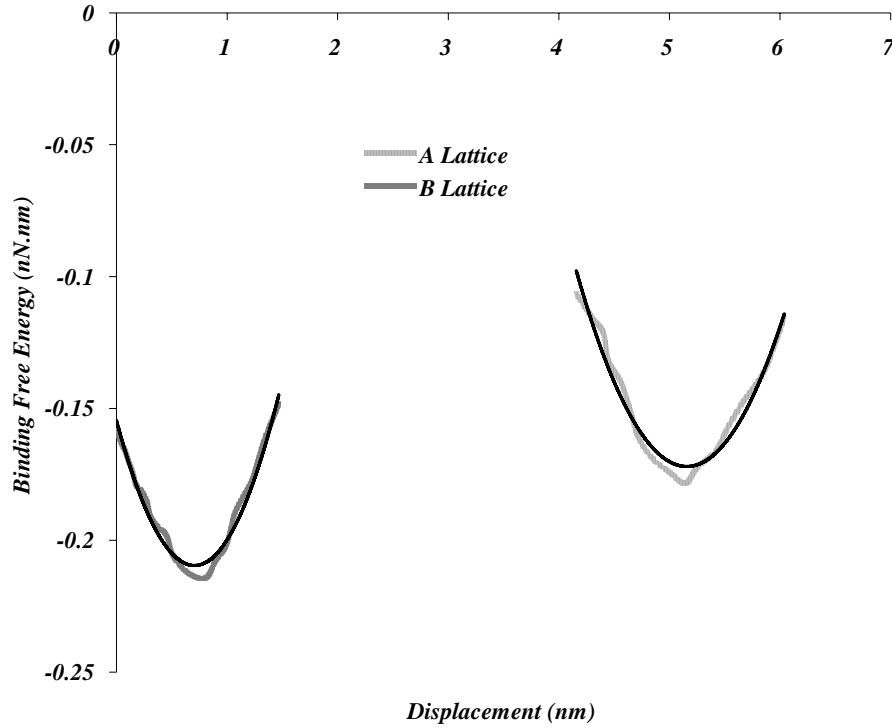


Figure 2-3 Binding free energy for the A and B lattice structures recreated using the data from Sept et al., 2003).

The longitudinal shift response shows the response of the lateral stiffness of the bonds of the microtubule lattice. With this in mind, the lateral stiffness of each lattice is derived as;

$$k_{22,B} = \frac{\partial^2 \mathcal{U}(d)}{\partial d^2} = 0.22 \frac{N}{m}, \text{ and}$$

$$k_{22,A} = \frac{\partial^2 \mathcal{U}(d)}{\partial d^2} = 0.15 \frac{N}{m}$$

In the next section, a detailed analysis of the lattice geometry and bond strength derivations of the A and B lattices are given within the context of the experimental observations from the literature (Grimstone and Klug, 1966; Amos, 1999; Chretien et al., 1992; Chretien et al., 1995; Chretien et al., 1998 and Chretien and Fuller, 2000).

2.3. Continuum Modeling Method for Seamless Microtubules

In this section, following the methodology of Arslan and Boyce, 2005 (Arslan and Boyce, (2005)) a general continuum level constitutive model for the mechanical behaviour of the microtubules is developed. The continuum level approach is used to derive the Cauchy Stress-Stretch relationships for the lattice defined.

The objective is to define a microstructurally-informed continuum level constitutive model which accounts for the triangulated lattice structure developed and which tracks individual bond deformation behaviour as well as the overall macroscopic lattice stress-strain behaviour.

A strain energy density function is constructed using the representative volume element (RVE) defined in the previous section (and elaborated on further later) together with the underlying molecular bond force-extension behaviour where the bond extensions are kinematically determined by the macroscopic deformation gradient.

Expressions for the nonlinear finite deformation stress-strain behaviour of the lattice are obtained by proper differentiation of the strain energy function. The corresponding stress-strain behaviour of the lattice when subjected to tensile and simple shear loading in different directions are obtained, demonstrating the capabilities of the proposed microstructurally-detailed constitutive modeling approach in capturing the small to large strain nonlinear, anisotropic mechanical behaviour.

2.3.1. Deformation of the Lattice RVE

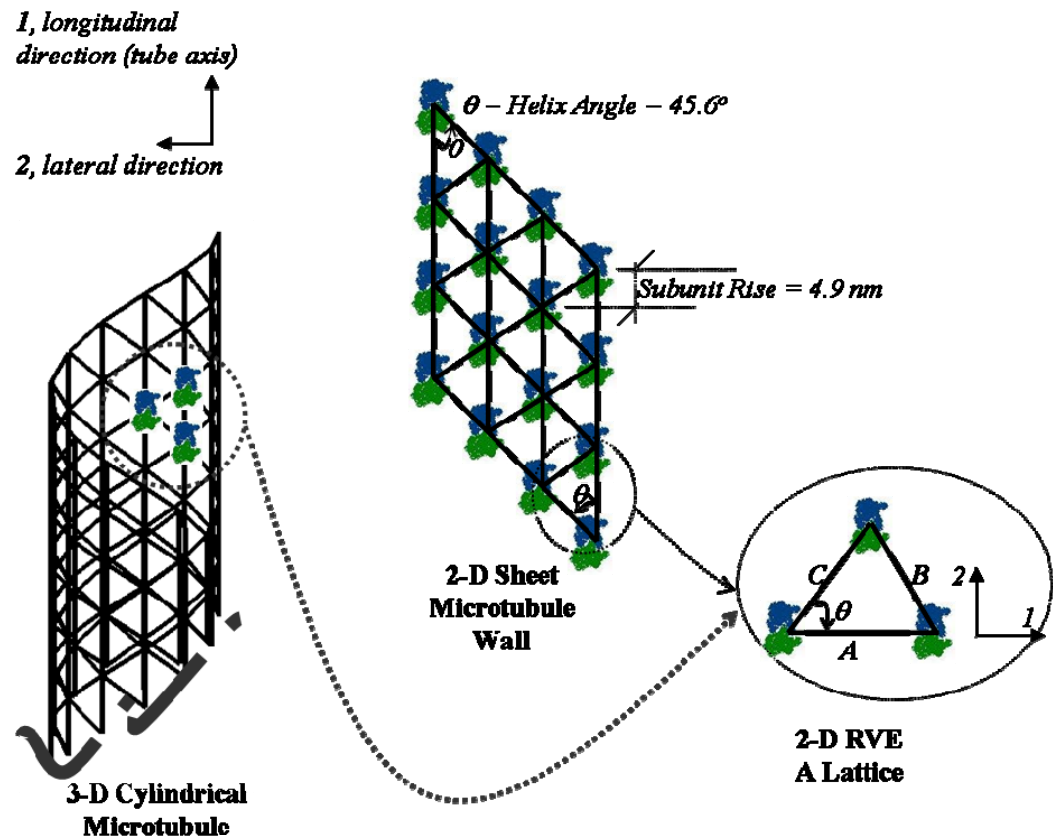


Figure 2-4 A schematic of the two-dimensional sheet model is presented here depicting the subunit rise and the helix angle for the A-lattice. The RVE is shown to be a triangle.

A seamless microtubule can be modeled as a three-dimensional helical lattice of dimers (Chapter 1). We consider dimers as points at their centers of mass as explained in Chapter 1. We open the three-dimensional lattice along the length of a protofilament, parallel to the microtubule axis as we consider a 13- or 14- protofilament microtubule, and unroll it to obtain a two-dimensional planar lattice of dimers (Figure 2-4).

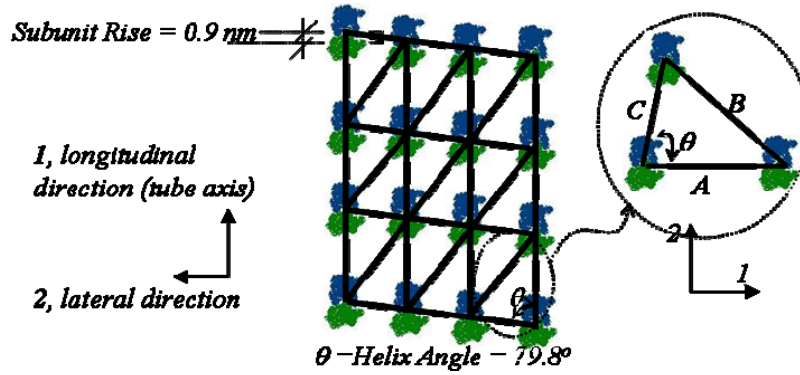


Figure 2-5 A schematic of the B-lattice sheet model is presented here depicting the subunit rise, helix angle and the RVE.

The representative unit cell is chosen to be a triangle. (Figure 2-4 and Figure 2-5).

An arbitrary deformation is applied to the unit cell triangle (Figure 2-4 and Figure 2-5) where the lattice deformation gradient \mathbf{F}_{2D} is defined in the 1-2 frame as:

$$\mathbf{F}_{2D} = \frac{\partial \mathbf{x}}{\partial \mathbf{X}} = \begin{bmatrix} F_{11} & F_{12} \\ F_{21} & F_{22} \end{bmatrix} \quad (10)$$

Here \mathbf{x} is the deformed position of a material point and \mathbf{X} is the reference position. The RVE is subjected to an arbitrary deformation gradient, giving the stretch of constituent lattice bonds A, B, C in terms of the macroscopic deformation gradient. The simplicity of the unit cell triangle RVE provides a unique, kinematically-determined mapping of the macroscopic deformation gradient to the microscopic lattice deformation. Denoting the current end-to-end distance of each spring as r_i ($i = A, B, C$), the axial stretch of each bond in the lattice is, $\lambda_i = \frac{r_i}{r_o}$ ($i = A, B, C$) and can be expressed in terms of an arbitrary deformation gradient (Appendix 2-1 gives a summary of the derivation of bond stretch functions in terms of the applied deformation gradient).

2.3.2. Constituent Bond Interactions

The stress vs. stretch relationship of the lattice system will depend on the axial force-extension behaviour of the constituent bonds. This modeling approach can incorporate any chain force-extension behaviour. The strain energy for a bond will be taken as the quadratic expression given in equation. It would therefore be written as:

$$\mathcal{U}(r_i) = \frac{1}{2} k_i r_{oi}^2 (\lambda_i - 1)^2 \quad (11)$$

Here k_i (k_A , k_B or k_C) is the bond axial stiffness in units of force/length and r_{oi} is the initial bond length.

The related linear force-extension behaviour of a bond is given by:

$$\mathcal{P}(r_i) = k_i r_{oi} (\lambda_i - 1) \quad (12)$$

The force-displacement relationship displayed here is a linear one. However, in this analysis the function could also be defined as a nonlinear one. The same methodology then would be used to derive the macroscopic stress-strain relationships.

2.3.3. Strain Energy Density of the RVE

The strain energy of the RVE \mathcal{U} is the summation of the strain energy in each chain:

$$\mathcal{U} = \mathcal{U}_A + \mathcal{U}_B + \mathcal{U}_C \quad (13)$$

Strain energy density is typically defined as the strain energy divided by the initial volume of the material. The microtubule wall is a lattice of essentially single molecule

thickness spanning a surface¹ Therefore the strain energy density, \mathcal{U}^* , is taken here to be strain energy per unit initial surface area. The initial surface area of the RVE is twice the area of the unit cell triangle following Voronoi tessellation (as given in Arslan and Boyce, 2006):

$$\mathcal{U}^* = \frac{1}{2A_{\text{triangle}}} (\mathcal{U}_A + \mathcal{U}_B + \mathcal{U}_C) \quad (14)$$

Using the strain energy expressions for each element found earlier together with the kinematics describing the deformation for each element, the following expression for the strain energy density function for the lattice, \mathcal{U}^* is obtained:

$$\mathcal{U}^* = \frac{1}{2A_{\text{triangle}}} \sum_{i=A,B,C} \frac{1}{2} k_i r_{oi}^2 (\lambda_i - 1)^2 \quad (15)$$

2.3.4. Energy Method and the Spring Constants for the A Lattice and the B Lattice

In order to employ the modeling procedure and derive the strain energy contributions from the constituent members of the RVE, one needs to define k_A , k_B and k_C for both of the lattice configurations.

Note that, here, the “seam” that results in a discontinuity of the lattice structure is not taken into account.

Two cases will be considered in order to derive the individual spring constants with the information of the overall longitudinal and the lateral stiffness; $k_{11} = 1.6 \text{ N/m}$ and $k_{22} = 0.22 \text{ N/m}$ for the B lattice and 0.15 N/m for the A lattice.

¹ The thickness of the microtubule wall could be intuitively thought of as being $(25 - 15)/2 = 5\text{nm}$, which is the dimer thickness. However in the mathematical model, this is not the thickness that is going to be used. This will later be explained in the next chapter.

One of the cases is uniaxial strain in the lateral direction, $\mathbf{F} = \begin{bmatrix} 1 & 0 \\ 0 & F_{22} \end{bmatrix}$. The overall external work done on the lattice is given by:

$$\mathcal{U}^* = \frac{1}{2} k_{22} y_c^2 (F_{22} - 1)^2 \quad (16)$$

here, y_c is the 2-direction component of node “c” as given in detail in the appendix (Appendix 2-1).

This external work is then equated to the internal strain energy; i.e. the strain energy in the stretched springs:

$$\frac{1}{2} k_{22} y_c^2 (F_{22} - 1)^2 = \frac{1}{2} k_A r_{oA}^2 (\lambda_A - 1)^2 + \frac{1}{2} k_B r_{oB}^2 (\lambda_B - 1)^2 + \frac{1}{2} k_C r_{oC}^2 (\lambda_C - 1)^2 \quad (17)$$

Similarly, for the second case; uniaxial tensile strain in the longitudinal direction, $\mathbf{F} = \begin{bmatrix} F_{11} & 0 \\ 0 & 1 \end{bmatrix}$ we have:

$$\frac{1}{2} k_{11} x_B^2 (F_{11} - 1)^2 = \frac{1}{2} k_A r_{oA}^2 (\lambda_A - 1)^2 + \frac{1}{2} k_B r_{oB}^2 (\lambda_B - 1)^2 + \frac{1}{2} k_C r_{oC}^2 (\lambda_C - 1)^2 \quad (18)$$

Using the information from the experimental data (k_{11} , k_{22}), there are two equations (17) and (18) and 3 unknowns; k_A , k_B , k_C for each of the cases (A and B lattice). Here $k_B = 0.1 k_C$ has been chosen judiciously.

Solving for the unknowns in the equations (17) and (18) reveals the approximated spring constants as listed in Table 1. Note that the results are consistent with the arguments in the beginning of this section ($k_A \gg k_B, k_C$).

Table 2-1 Spring Constants

	k_A (N/m)	k_B (N/m)	k_C (N/m)
13_3 Lattice A Lattice	1.51	0.025	0.25
14_4 Lattice B Lattice	1.55	0.022	0.22

In the present work, we ignored any torsional potential at the junction points (the center of mass of the dimers) due to the lack of information on the bond energies. The details of the torsional potential energies are explained in Appendix 2-2.

Longitudinal interactions between dimers have polar, hydrophobic and electrostatic components (Nogales, 1998). The contact interface is highly complementary in shape; hence Van der Waals interactions are important. Lateral interactions have an electrostatic nature (Nogales, 1999). The lateral contacts have a decisive role in microtubule dynamics, stability and rigidity (Nogales, 1999). Tubulin dimers are relatively strongly bound in the longitudinal direction, while the lateral interaction between the protofilaments is much weaker (Nogales et al., 1999; Kis et al., 2002; Sept et al., 2003). Li et al. (2002) also noted that while all the longitudinal intra-protofilament interactions are assumed to be the same, the lateral inter-protofilament interactions are known to be different depending on the direction. Tuszynski et al. (2004), using the three point bending test result estimated k_C to be 0.1 N/m and assumed k_B to be 0.01 N/m from intuition. The researchers also assumed the longitudinal interaction constants for the seamless A lattice to be $k_A = 4$ N/m noting that it was calculated from the potential maps of Sept et al. (2003). The flaw in this argument is, as mentioned earlier, that the potential maps of Sept et al. provide the lateral interactions between the dimers, and not the longitudinal. When one protofilament is moved longitudinally whilst keeping the neighbouring protofilament fixed, the motion is dominated by shearing forces and the result would give an approximation for the lateral bonds in the lattice.

The model used in the current study assumes that the dimers are positioned in a helix with zero pitch (a 13₃ helix; see Chapter 1); therefore, all the protofilaments are identical.

The following section will investigate the deformation characteristics of the A lattice using continuum mechanics analysis methods.

2.3.5. Stress- Stretch Relationships

The stress-stretch behaviour is determined by proper differentiation of the strain energy density function. Given a strain energy density which is a function of the deformation gradient, the 1st Piola Kirchoff Stress is derived as:

$$\mathbf{T}_o = \frac{\partial(\psi^*)}{\partial(\mathbf{F})} \quad (19)$$

The Cauchy Stress tensor is then obtained from:

$$\mathbf{T} = \frac{1}{J} \mathbf{T}_o \mathbf{F}^T \quad (20)$$

where $J = \det(\mathbf{F})$ is the surface area ratio (ratio of current area to original area).

Noting that the ψ_i ($i = A, B, C$) are functions of λ_i ($i = A, B, C$) and are functions of the deformation gradient, gives:

$$\mathbf{T} = \frac{1}{J} \left[\frac{\partial(\psi_A^*)}{\partial(\lambda_A)} \frac{\partial(\lambda_A)}{\partial(\mathbf{F})} + \frac{\partial(\psi_B^*)}{\partial(\lambda_B)} \frac{\partial(\lambda_B)}{\partial(\mathbf{F})} + \frac{\partial(\psi_C^*)}{\partial(\lambda_C)} \frac{\partial(\lambda_C)}{\partial(\mathbf{F})} \right] \mathbf{F}^T \quad (21)$$

The $\left(\frac{\partial \lambda_i}{\partial \mathbf{F}}\right)$ terms are independent of bond constitutive behaviour and obtained by direct differentiation as shown in Appendix 2-1.

The presented formulation follows a formal continuum mechanics methodology for hyperelasticity: the macroscopic deformation gradient is mapped to microscopic constituent elements; the strain energy of the system is formulated; and the strain energy density is then differentiated with respect to an appropriate and general large deformation measure (here, the deformation gradient) to obtain the stress. This approach is general and can account for any constituent member behaviour.

Using a continuum micromechanical analysis, an estimate of the stiffness matrix for seamless microtubules will be derived and the required number of tests in order to derive the stiffness matrix will be determined in the next section.

2.3.6. The Stiffness Matrix

For a linear elastic material, the stress-strain relationship can be expressed as:

$$T_{ij} = \sum_{k=1}^3 \sum_{l=1}^3 C_{ijkl} e_{kl} \quad (22)$$

Here, e is the strain and T is the Cauchy stress. e could also be written in terms of the deformation gradient as;

$$e = \frac{1}{2}(\mathbf{F}^T \mathbf{F} - \mathbf{1}) = \begin{bmatrix} \frac{1}{2}(F_{11}^2 + F_{21}^2 - 1) & (F_{11}F_{12} + F_{21}F_{22}) \\ (F_{11}F_{12} + F_{21}F_{22}) & \frac{1}{2}(F_{12}^2 + F_{22}^2 - 1) \end{bmatrix} \quad (23)$$

This implies 81 constants. However, these constants are not independent. Firstly, the symmetry of the stress tensor $T_{ij} = T_{ji}$ gives $C_{ijkl} = C_{jikl}$, which reduces the number of independent constants to 54.

Secondly, the symmetry of the strain tensor $e_{kl} = e_{lk}$, gives $C_{ijkl} = C_{ijlk}$, which further reduces the number of independent constants to 36.

Thirdly, given that the elastic strain relationship is derivable from the strain energy density \mathcal{U}^* of the material, therefore;

$$C_{ijkl} = \frac{\partial^2 \mathcal{U}^*}{\partial e_{ij} \partial e_{kl}} \quad (24)$$

Since the order of differentiation is arbitrary, it gives: $C_{ijkl} = C_{klij}$. This finally reduces the number of independent constants to 21.

Further reductions in the number of independent constants rely on the symmetry of the microtubule.

The details of the stiffness matrix derivations are given in the Appendix 2-3.

The microtubule wall stiffness properties can be examined in a similar fashion to fibre-reinforced composite materials. In composite structures, thin plates are of common applications. Similarly, for the mechanical analysis of the microtubule wall, the three dimensional problem can be simplified to a two-dimensional problem assuming that there's no stress in the thickness direction; $T_{33} = T_{23} = T_{13} = 0$. Therefore the general compliance matrix for a 2D structure can be finally reduced to:

$$\mathbf{S}_{2D} = \begin{bmatrix} S_{11} & S_{12} & S_{16} \\ S_{12} & S_{22} & S_{26} \\ S_{16} & S_{26} & S_{66} \end{bmatrix} = \begin{bmatrix} \frac{1}{E_{11}} & \frac{-\nu_{12}}{E_{11}} & \frac{-\nu_{16}}{E_{11}} \\ -\frac{\nu_{12}}{E_{11}} & \frac{1}{E_{22}} & \frac{-\nu_{26}}{E_{22}} \\ \frac{-\nu_{16}}{E_{11}} & \frac{-\nu_{26}}{E_{22}} & \frac{1}{G_{12}} \end{bmatrix} \quad (25)$$

Using $C_{2D} = S_{2D}^{-1}$ and equation (25), the members of the C_{2D} matrix can be derived as:

$$\begin{aligned}
 C_{11} &= \frac{1}{|\mathbf{S}|} \left(\frac{1}{E_{22}} \frac{1}{G_{12}} - \frac{\nu_{26}^2}{E_{22}^2} \right), & C_{12} &= \frac{1}{|\mathbf{S}|} \left(\frac{\nu_{16}}{E_{11}} \frac{\nu_{26}}{E_{22}} + \frac{\nu_{12}}{E_{11}} \frac{\nu_{12}}{G_{12}} \right), \\
 C_{16} &= \frac{1}{|\mathbf{S}|} \left(\frac{\nu_{12}}{E_{11}} \frac{\nu_{16}}{E_{11}} + \frac{1}{E_{22}} \frac{\nu_{16}}{E_{11}} \right), & C_{22} &= \frac{1}{|\mathbf{S}|} \left(\frac{1}{E_{11}} \frac{1}{G_{12}} + \frac{\nu_{12}}{E_{11}} \frac{1}{G_{12}} \right), \\
 C_{26} &= \frac{1}{|\mathbf{S}|} \left(\frac{\nu_{12}}{E_{11}} \frac{\nu_{16}}{E_{11}} + \frac{1}{E_{11}} \frac{\nu_{26}}{E_{22}} \right), & C_{66} &= \frac{1}{|\mathbf{S}|} \left(\frac{1}{E_{11}} \frac{1}{E_{22}} - \frac{\nu_{12}^2}{E_{11}^2} \right)
 \end{aligned} \tag{26}$$

Here, $|\mathbf{S}|$ is the determinant of the compliance matrix. Note that there is no obvious symmetry in the structure to suggest further reduction to an orthotropic material (i.e. there does not appear to be an axis system whereby the shear-normal coupling 16 and 26 terms would be zero).

In order to solve for the compliance matrix of the anisotropic microtubule lattice matrix, we need to derive S_{11} , S_{12} , S_{16} , S_{22} , S_{26} and S_{66} ; 6 unknowns. This would imply that three tests are required.

In the next section, we will examine three different tests that will help define the mechanical properties of the microtubules; i.e. these 6 constants.

2.3.7. Results for the Seamless Microtubules

For each test, either a strain or a stress will be imposed. The response will be provided in terms of the expression for the general anisotropic material and also for the RVE. The RVE result is then mapped to general anisotropic expression to obtain values for the elastic constants of the general anisotropic model.

2.3.7.1. TEST 1: Pure Shear

The first test to be conducted is a pure shear stress test. For this test, the strain-stress relationship can be written as:

$$\begin{bmatrix} e_{11} \\ e_{22} \\ \gamma_{12} \end{bmatrix} = \begin{bmatrix} \frac{1}{E_{11}} & \frac{-\nu_{12}}{E_{11}} & \frac{-\nu_{16}}{E_{11}} \\ \frac{-\nu_{12}}{E_{11}} & \frac{1}{E_{22}} & \frac{-\nu_{26}}{E_{22}} \\ \frac{-\nu_{16}}{E_{11}} & \frac{-\nu_{26}}{E_{22}} & \frac{1}{G_{12}} \end{bmatrix} \begin{bmatrix} 0 \\ 0 \\ T_{12} \end{bmatrix} \quad (27)$$

In order to obtain pure shear stress for the RVE model, one has to calculate the necessary deformation gradient to be applied as the microtubule lattice is anisotropic and the strains that the pure shear is imposing cannot be predicted but should rather be calculated given the geometry of the lattice.

In order to find the necessary deformation gradient a Newton Raphson method is utilized. This methodology is defined as follows;

- An initial deformation guess for the deformation gradient to be defined;

$$\mathbf{F} = \begin{bmatrix} 1 & \frac{\gamma}{2} \\ \frac{\gamma}{2} & 1 \end{bmatrix}.$$

The aim is to solve for the correct deformation gradient for an applied stress of $\mathbf{T} = \begin{bmatrix} 0 \\ 0 \\ T_{12} \end{bmatrix}$.

- The periodic boundary conditions using the equation:

$$\mathbf{u}_i - \mathbf{u}_j = (\mathbf{F} - \mathbf{1})(\mathbf{X}_i - \mathbf{X}_j)$$

defines the displacements which are specified in terms of the applied arbitrary deformation gradient for the nodal points (cross-links).

- The nodal displacements and thus the extensions, forces, and strain energy in each element are found.
- The macroscopic stress-stretch relationships at time $t+\Delta t$ ($T_{11\ t+\Delta t}$, $T_{22\ t+\Delta t}$ and $T_{12\ t+\Delta t}$ in terms of the applied deformation gradient, \mathbf{F}) are then determined using the energy method.

- The condition of pure shear stress, $\mathbf{T} = \begin{bmatrix} 0 \\ 0 \\ T_{12} \end{bmatrix}$ is verified to be within the tolerance limit (tolerance = $T_{11t} - T_{11t+\Delta t} = 10^{-10}$ N/m).

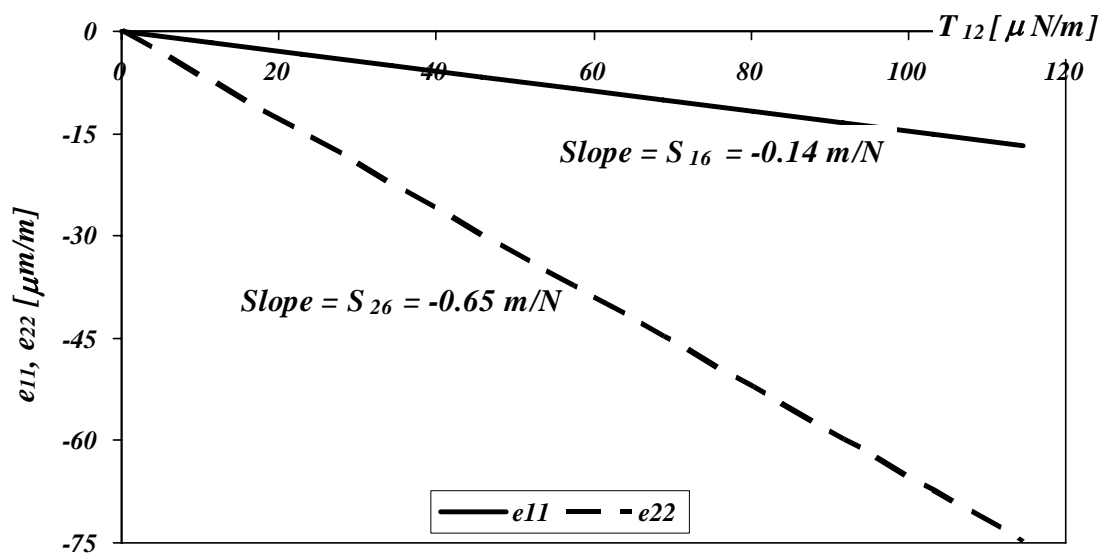
- The new deformation gradient is calculated using the Newton Raphson method;

$\mathbf{F}_{t+\Delta t} = \mathbf{F}_t - \frac{J}{\mathbf{T}}$;where J is the Jacobian of the Cauchy Stress function;

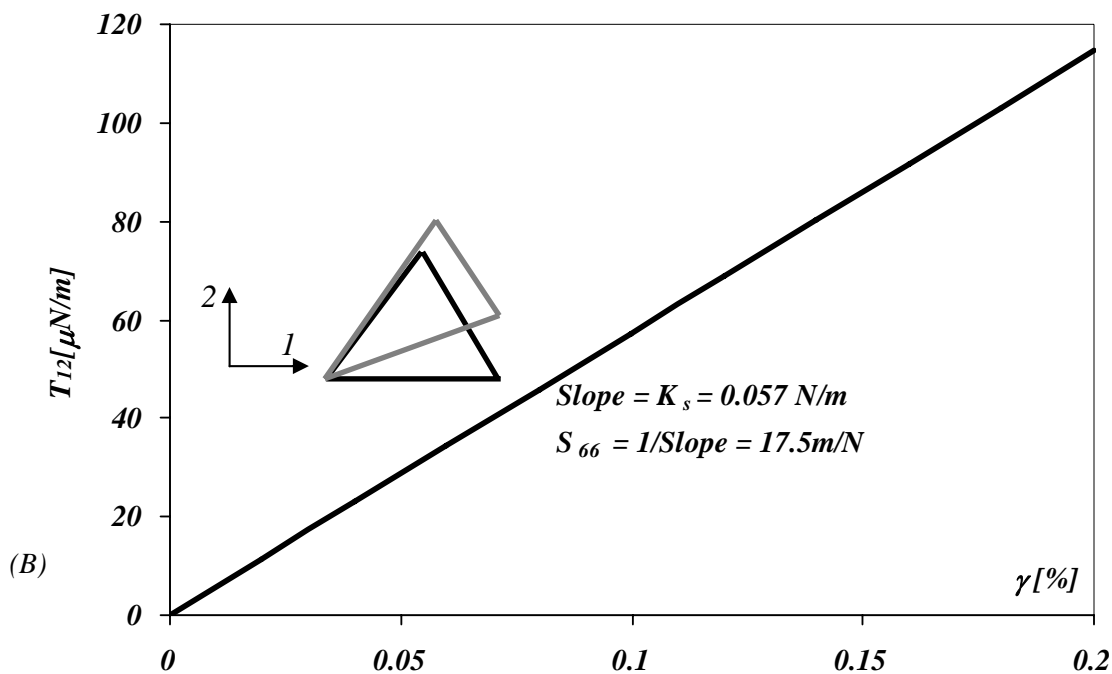
$$J = \begin{bmatrix} \frac{\partial T_{11}}{\partial F_{11}} & \frac{\partial T_{22}}{\partial F_{11}} \\ \frac{\partial T_{11}}{\partial F_{22}} & \frac{\partial T_{22}}{\partial F_{22}} \end{bmatrix}.$$

- The nodal displacements and hence the extensions, forces, and strain energy in each element are recalculated according to the new deformation gradient.
- The procedure is continued until the tolerance limit is reached.

For the shear stress applied; $\mathbf{T} = [0 \ 0 \ T_{12}]^{-1}$, the corresponding strain matrix; $\mathbf{e} = [e_{11} \ e_{22} \ \gamma_{12}]^{-1}$ is derived. Figure 2-6 gives the plot of the strains derived for a very small strain of $\gamma_{12} = 0.002$.



(A)



(B)

Figure 2-6 Here a plot of the strains are given (A) for a pure shear stress. The related stress-shear behaviour is shown in (B) depicting the shear stiffness for the microtubule lattice. Here, K_s represents the shear stiffness ($G_{12}^* t^*$). This will be further explained in the next chapter.

Following Figure 2-6, A the ratios of $\left[\frac{e_{11}}{T_{12}} \right]$ and $\left[\frac{e_{22}}{T_{12}} \right]$ are determined. This gives us the values of S_{16} and S_{26} from the compliance matrix. S_{16} is found to be - 0.14 m/N and S_{26} is found to be -0.65 m/N. These non-zero values imply the typical characteristic of a monoclinic material behaviour which carries the reduced form of an anisotropic material compliance matrix. One observes that in a general anisotropic material, a uniaxial stress causes a shear stress and a pure shear stress causes a uniaxial strain in the material.

Figure 2-6, B shows the shear stress response.

The slope of this figure gives the planar shear stiffness, $G_{12}^* t^*$. It is derived to be 0.057 N/m. The validity of this shear modulus for different effective thickness values will be discussed in the next chapter in parallel with the experimental findings from the literature.

2.3.7.2. TEST 2: Uniaxial Tensile Strain in the 1-Direction

The next two loading sets comprise a more straight forward procedure to solve for the remaining unknowns in the compliance matrix. S_{11} , S_{12} , S_{22} have to be derived and two further tests allow this; here taken as uniaxial tensile strain in the 1-direction and uniaxial tensile strain in the 2-direction.

The following expression explains the stress strain behaviour for uniaxial tensile strain in the 1-direction;

$$\begin{bmatrix} e_{11} \\ 0 \\ 0 \end{bmatrix} = \begin{bmatrix} \frac{1}{E_{11}} & \frac{-\nu_{12}}{E_{11}} & \frac{-\nu_{16}}{E_{11}} \\ \frac{-\nu_{12}}{E_{11}} & \frac{1}{E_{22}} & \frac{-\nu_{26}}{E_{22}} \\ \frac{-\nu_{16}}{E_{11}} & \frac{-\nu_{26}}{E_{22}} & \frac{1}{G_{12}} \end{bmatrix} \begin{bmatrix} T_{11} \\ T_{22} \\ T_{12} \end{bmatrix} \quad (28)$$

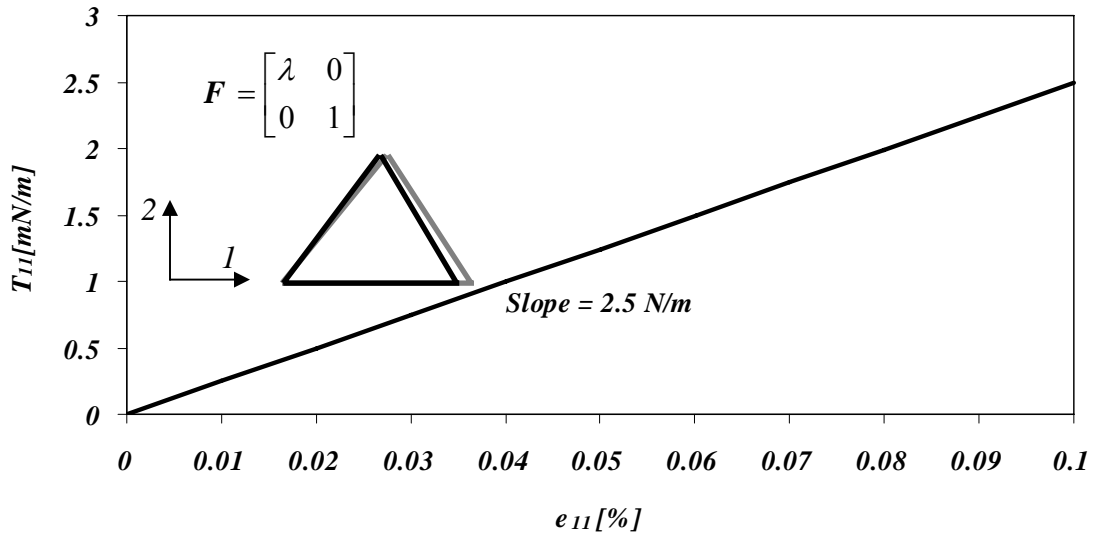
which leads to three linear equations;

$$e_{11} = S_{11}T_{11} + S_{12}T_{22} + S_{16}T_{12} = \frac{1}{E_{11}}T_{11} - \frac{\nu_{12}}{E_{11}}T_{22} - \frac{\nu_{16}}{E_{11}}T_{12} \quad (29)$$

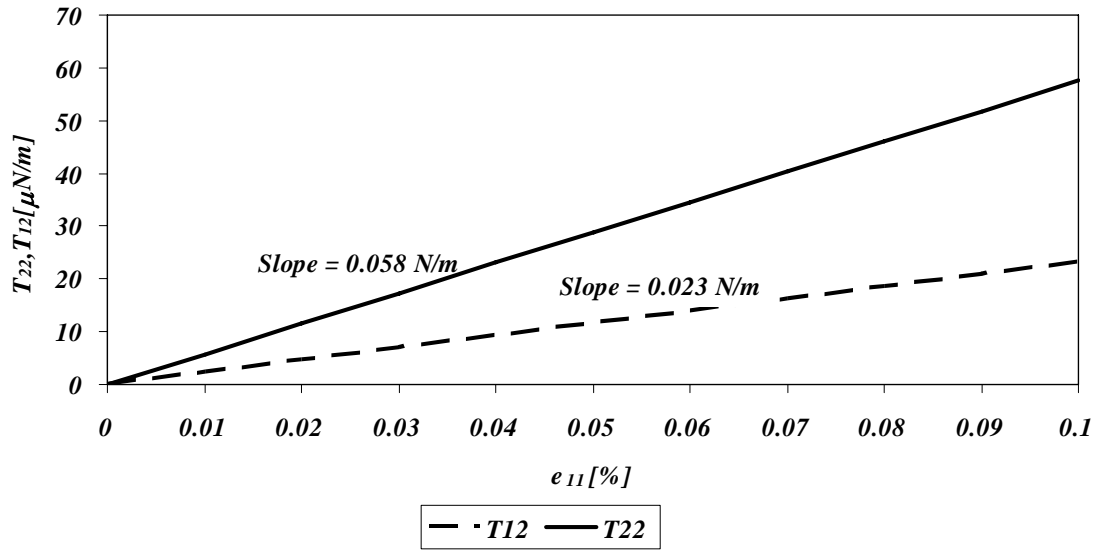
$$0 = S_{12}T_{11} + S_{22}T_{22} + S_{26}T_{12} = \frac{\nu_{12}}{E_{11}}T_{11} + \frac{1}{E_{22}}T_{22} - \frac{\nu_{26}}{E_{22}}T_{12} \quad (30)$$

$$0 = S_{16}T_{11} + S_{26}T_{22} + S_{66}T_{12} = -\frac{\nu_{16}}{E_{11}}T_{11} - \frac{\nu_{26}}{E_{22}}T_{22} + \frac{1}{G_{12}}T_{12} \quad (31)$$

This same strain condition is imposed on the RVE and the resulting stress response is calculated to give the stress coefficients for the equations (29)-(31) which are then used to derive the unknowns.



(A)



(B)

Figure 2-7 A plot of the stress (T_{11}) vs. strain (e_{11}) is shown here depicting the deformed and undeformed configurations of the RVE (A). The resulting lateral stress and the shear stress are also shown in (B).

Equation (31) verifies the finding of TEST 1 and equations (29) and (30) are solved together here. According to the slopes found from the plots given in Figure 2-7 A and B the equations are modified as follows;

$$1 = 2.5S_{11} + 0.058S_{12} + 0.023S_{16} \quad (32)$$

$$0 = 0.4S_{12} + 0.058S_{22} + 0.023S_{26} \quad (33)$$

Since the values of S_{16} and S_{26} are found by TEST 1, in order to solve for S_{11} , S_{12} and S_{22} , we need TEST 3; uniaxial tensile strain in the 2-direction.

2.3.7.3. TEST 3: Uniaxial Tensile Strain in the 2-Direction

The following expression explains the stress strain behaviour for uniaxial tensile strain in the 2-direction;

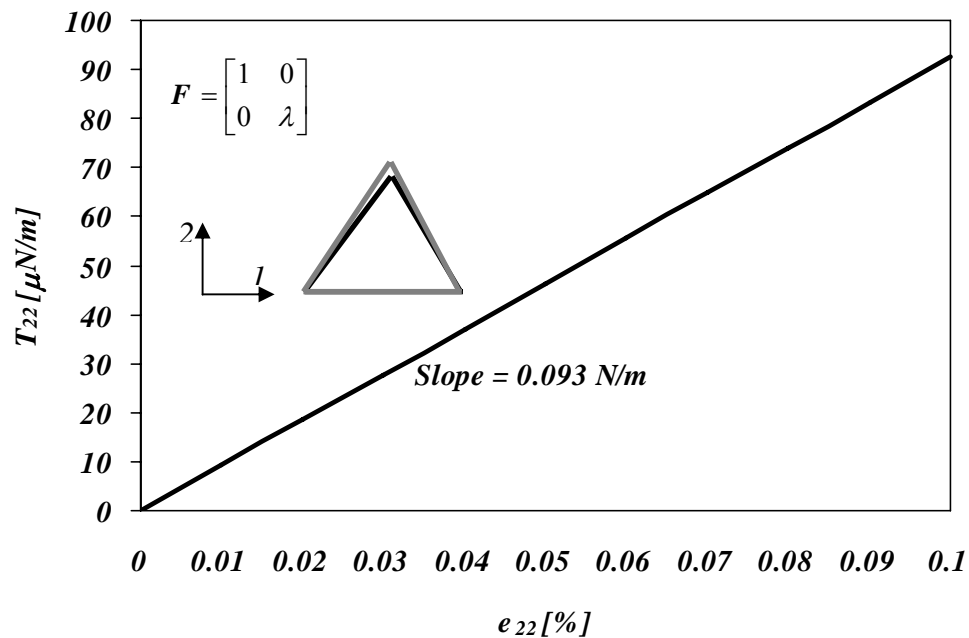
$$\begin{bmatrix} 0 \\ e_{22} \\ 0 \end{bmatrix} = \begin{bmatrix} \frac{1}{E_{11}} & \frac{-\nu_{12}}{E_{11}} & \frac{-\nu_{16}}{E_{11}} \\ \frac{-\nu_{12}}{E_{11}} & \frac{1}{E_{22}} & \frac{-\nu_{26}}{E_{22}} \\ \frac{-\nu_{16}}{E_{11}} & \frac{-\nu_{26}}{E_{22}} & \frac{1}{G_{12}} \end{bmatrix} \begin{bmatrix} T_{11} \\ T_{22} \\ T_{12} \end{bmatrix} \quad (34)$$

which leads to three linear equations;

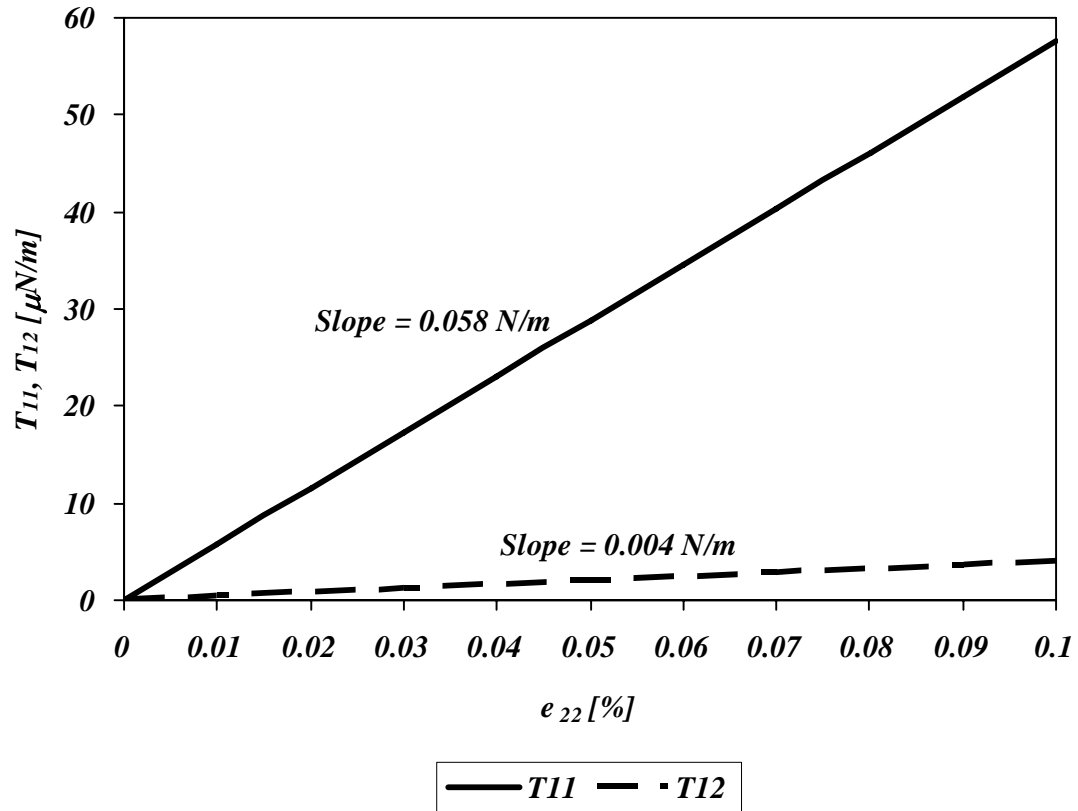
$$0 = S_{11}T_{11} + S_{12}T_{22} + S_{16}T_{12} = \frac{1}{E_{11}}T_{11} - \frac{\nu_{12}}{E_{11}}T_{22} - \frac{\nu_{16}}{E_{11}}T_{12} \quad (35)$$

$$e_{22} = S_{12}T_{11} + S_{22}T_{22} + S_{26}T_{12} = \frac{\nu_{12}}{E_{11}}T_{11} + \frac{1}{E_{22}}T_{22} - \frac{\nu_{26}}{E_{22}}T_{12} \quad (36)$$

$$0 = S_{16}T_{11} + S_{26}T_{22} + S_{66}T_{12} = -\frac{\nu_{16}}{E_{11}}T_{11} - \frac{\nu_{26}}{E_{22}}T_{22} + \frac{1}{G_{12}}T_{12} \quad (37)$$



(A)



(B)

Figure 2-8 A plot of the stress (T_{22}) vs. strain (e_{22}) is shown here depicting the deformed and undeformed configurations of the RVE (A). The resulting longitudinal stress and the shear stress are also shown in (B).

The same strain condition is imposed on the RVE and the stress response is calculated to give the coefficients for the equations (29)-(31) which then help us solve for S_{11} , S_{12} and S_{22} .

Equation (37) verifies the finding of TEST 1 and equations (35) and (36), one of which will be redundant, are utilized here. According to the slopes found from the plots given in Figure 2-8, the equations are modified as follows;

$$0 = 0.058S_{11} + 0.093S_{12} + 0.004S_{16} \quad (38)$$

$$1 = 0.058S_{12} + 0.093S_{22} + 0.004S_{26} \quad (39)$$

Solving the linear equations (32), (33), (38) and (39) leads to the find of:

$$S_{11} = 0.41 \text{ m/N},$$

$$S_{12} = -0.25 \text{ m/N},$$

$$S_{22} = 11 \text{ m/N}.$$

The entire set of constants for the compliance matrix, stiffness matrix and the elastic properties of the A lattice microtubules are summarized in Table 2-2.

Table 2-2 Microtubule Mechanical Properties for a unit thickness (A Lattice)

S [1/GPa]	C [GPa]	E^*, G^*, ν
$S_{11} = 0.41$	$C_{11} = 2.48$	$E_{11}^* = 2.44 \text{ GPa}$
$S_{12} = -0.25$	$C_{12} = 0.058$	$E_{22}^* = 0.09 \text{ GPa}$
$S_{16} = -0.14$	$C_{16} = 0.022$	$G_{12}^* = 0.057 \text{ GPa}$
$S_{22} = 11$	$C_{22} = 0.093$	$\nu_{12} = 0.6$
$S_{26} = -0.65$	$C_{26} = 0.0039$	$\nu_{16} = 0.34$
$S_{66} = 17.45$	$C_{66} = 0.058$	$\nu_{26} = 0.06$

We have shown that the lateral elastic modulus of A lattice type microtubules ($E_{22} = 0.09 \text{ GPa}$) is lower than the longitudinal elastic modulus ($E_{11} = 2.44 \text{ GPa}$) by a few orders of magnitude, clearly showing an aspect of the anisotropy.

In addition to this, the shear modulus of microtubules ($G_{12}^* = 0.057 \text{ GPa}$) is much lower than the longitudinal elastic modulus ($E_{11}^* = 2.44 \text{ GPa}$). This shows the high anisotropy level in the microtubule structure.

In order to demonstrate the level of anisotropy, we could calculate the shear stiffness for the A lattice structure with the isotropic material assumption;

$$C_{66}^{iso \text{ A.lattice}} = 2G_{12}^* = \frac{C_{11} - C_{12}}{2} = \frac{2.48\text{GPa} - 0.058\text{GPa}}{2} \cong 1.21\text{GPa} \quad (40)$$

Here, G_{12}^* is the shear stiffness of the isotropic material which comes out to be $\sim 0.6 \text{ GPa}$.

However for the present case;

$$C_{66 \text{ A.lattice}} = 0.058\text{GPa} \ll \frac{C_{11} - C_{12}}{2} \quad (41)$$

This shows the level of anisotropy in the microtubule lattice structure.

In microtubules, there's also a tension-shear coupling between the normal and shear directions (i.e. $\nu_{16} = 0.34$, $\nu_{26} = 0.06$). Orthotropic material have three mutually orthogonal axes of rotational symmetry and normal-shear coupling effect is not observed for orthotropic materials (i.e. $\nu_{16} = 0$, $\nu_{26} = 0$). In microtubules it is derived that each normal stress depends on the shear strain, e_{12} , and the shear stress, T_{12} , depends on all of the three normal strains. This is a typical characteristic of monoclinic materials.

2.3.7.4. Uniaxial Tension in the 1-Direction

For completeness, uniaxial tension (i.e. uniaxial stress) results will be shown. The same methodology (the Newton Raphson Method) as TEST 1 is used here to determine the deformation gradient which will provide a uniaxial tension stress state (in the 1-direction in this present case). For uniaxial tension in the 1-direction, a stretch of F_{11} will result; additionally, due to the anisotropy of the structure, the resulting deformation gradient components in the 12- and the 22-directions are presented in Figure 2-9. If we ignore the change in the lattice thickness, then the surface area change can be found from:

$$\Delta Area = \frac{F_{11}F_{22} - 1}{1} \tag{42}$$

The percentage of area change is plotted in Figure 2-9.

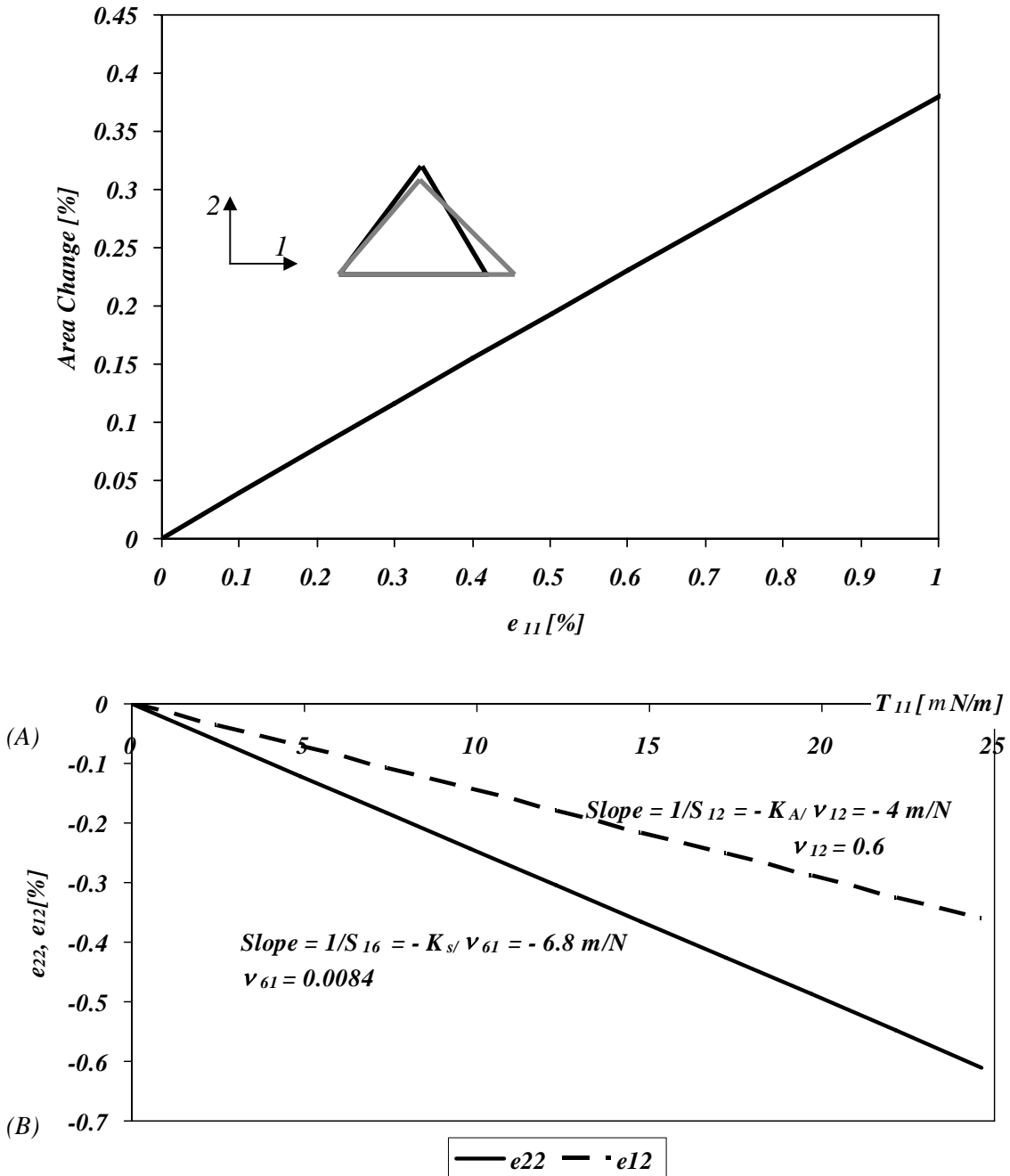


Figure 2-9 The area change in the RVE under uniaxial tension in the 1-direction (A) and the resulting strains in lateral direction and the shear deformation (B) are given here.

In Figure 2-9, K_A represents the axial stiffness ($E_{11}^* t^*$) and K_s represents the shear stiffness ($G_{12}^* t^*$). This will be further explained in the next chapter.

Here, we note that the strain in the stress direction is accompanied by a normal strain in the lateral direction giving a Poisson ratio of $\nu_{12} = 0.6$. It's also important to note that, there is also a shear strain observed in the uniaxial stress condition giving a $\nu_{16} = 0.34$. In bending and uniaxial tension, the existence of the M-loops is expected to provide a shearing motion in the connections and lower the overall stiffness of the microtubules. The coupling between macroscopic tension and microscopic shear will be discussed in greater detail in the next chapter.

The uniaxial stress vs. strain is revealed as shown in Figure 2-10, A. The slope of this T_{11} vs. e_{11} curve multiplied with a unit thickness gives the longitudinal modulus of the microtubules. The “effective thickness” will be calculated when the macroscopic behaviour of the microtubules is compared to the experimental results in the next chapter.

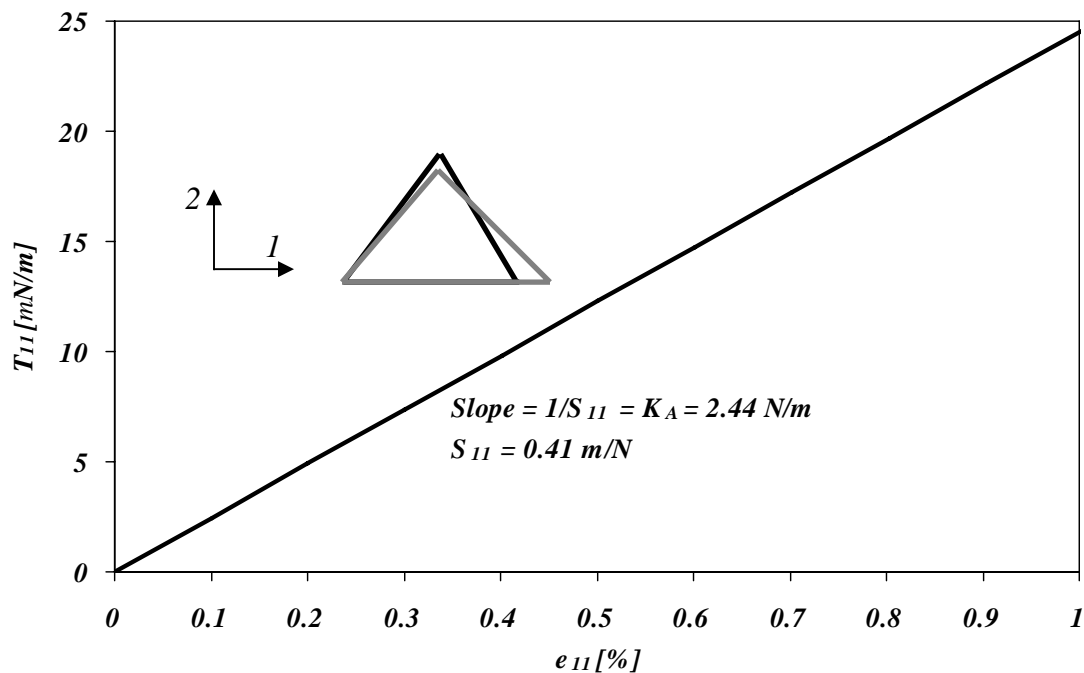


Figure 2-10 Uniaxial Stress, T_{11} vs. e_{11} is shown in this figure.

Here, the longitudinal modulus for the RVE; and thus the microtubule wall is calculated to be $E_{11}^* = 2.44 \text{ GPa}$. The thickness of the lattice is taken to be 1nm. This shall later be adjusted when an “effective thickness” is calculated in the next chapter.

The slope of the curve in Figure 2-10 being 2.5 N/m is very close to the E_{11}^* (2.44 N/m) derived from the uniaxial tension test. Although the uniaxial tensile strain plot slope in the 1-direction does not yield the longitudinal modulus value, it still is a very close value.

As previously mentioned, there is no obvious symmetry in the structure an orthotropic material. However, the principal directions of orthotropy do not always coincide with coordinate directions that are geometrically natural to the structure. Thus, the method of transforming stress-strain relations is used to find if there is an axis system whereby the shear-normal coupling 16 and 26 terms are close to zero.

The transformation will be carried for the compliance matrix, S :

$$S^* = Q^T S Q \quad (43)$$

Here S^* is the transformed compliance matrix and Q is the transformation matrix. Q^T is the transpose of the transformation matrix. The transformation matrix is given as (Cook, 1981):

$$Q = \begin{bmatrix} \cos^2(\theta) & \sin^2(\theta) & 2\sin(\theta)\cos(\theta) \\ \sin^2(\theta) & \cos^2(\theta) & -2\sin(\theta)\cos(\theta) \\ -\sin(\theta)\cos(\theta) & \sin(\theta)\cos(\theta) & \cos^2(\theta) - \sin^2(\theta) \end{bmatrix} \quad (44)$$

θ is the transformation angle.

Using equation (43), the transformed compliance matrix, S^* , is calculated and the corresponding material properties for each of the transformation angle is determined using equation (25).

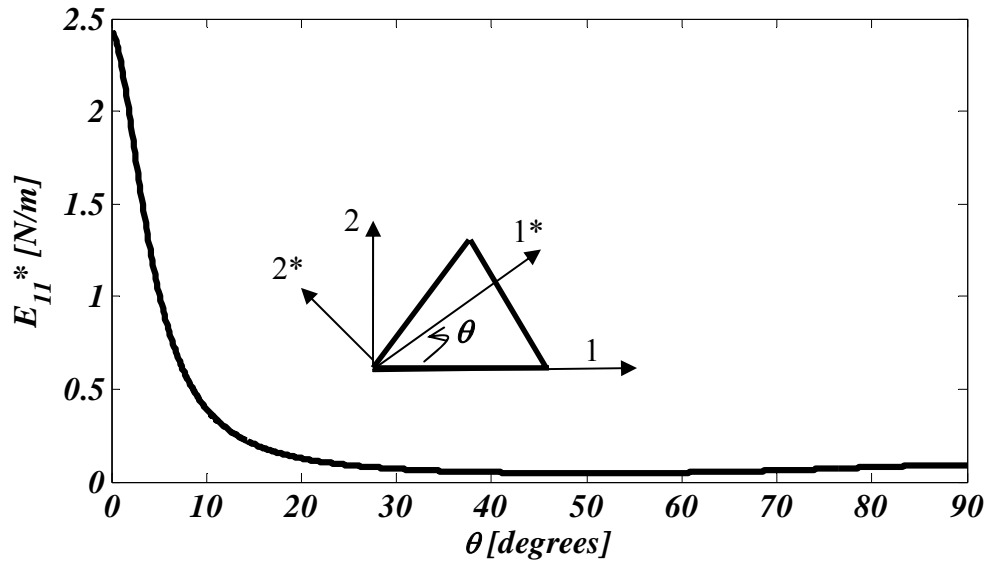


Figure 2-11 The longitudinal stiffness in the transformed axis system for different transformation angles.

Figure 2-11 shows the change in the longitudinal stiffness, E_{11}^* with the transformation angle. We can observe that the highest stiffness value ($E_{11}^* = 2.4 \text{ N/m}$) corresponds to $\theta = 0^\circ$, the material orientation we've used in our model. After about $\theta = 40^\circ$, the longitudinal modulus is $E_{11}^* = 0.09 \text{ N/m}$ for $40^\circ - 90^\circ$; its minimum value.

Figure 2-12 shows the change in the shear modulus, G_{12}^* with the transformation angle.

The highest value of shear stiffness ($G_{12}^* = 0.083 \text{ N/m}$) is at $\theta = 46^\circ$. The smallest values of the shear stiffness correspond to $\theta = 0^\circ$ and $\theta = 90^\circ$ with $G_{12}^* = 0.057 \text{ N/m}$.

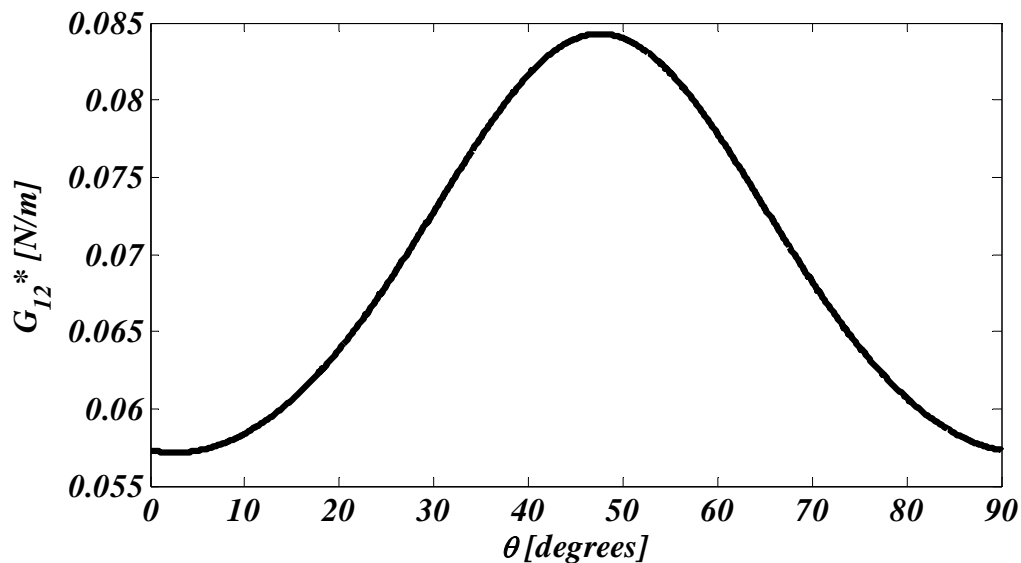


Figure 2-12 The shear stiffness in the transformed axis system for different transformation angles.

Figure 2-13 shows the change in the monoclinic effect (tension-shear coupling) components; ν_{16}^* and ν_{26}^* . The components have the smallest value at $\theta = 46^\circ$ with $\nu_{16}^* = \nu_{26}^* = 0.25$. This is the same axis system where the shear modulus is the highest.

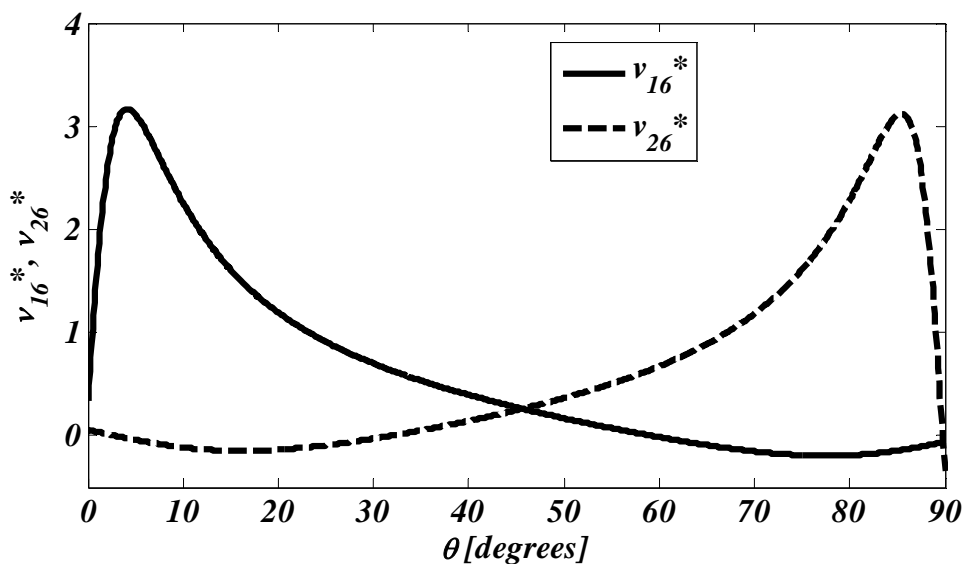


Figure 2-13 The tension-shear coupling components in the transformed axis system for different transformation angles.

The minimum value of ν_{16}^* and ν_{26}^* at $\theta = 46^\circ$ still does not suggest orthotropy in this direction as these values are not negligible.

2.3.8. B Lattice

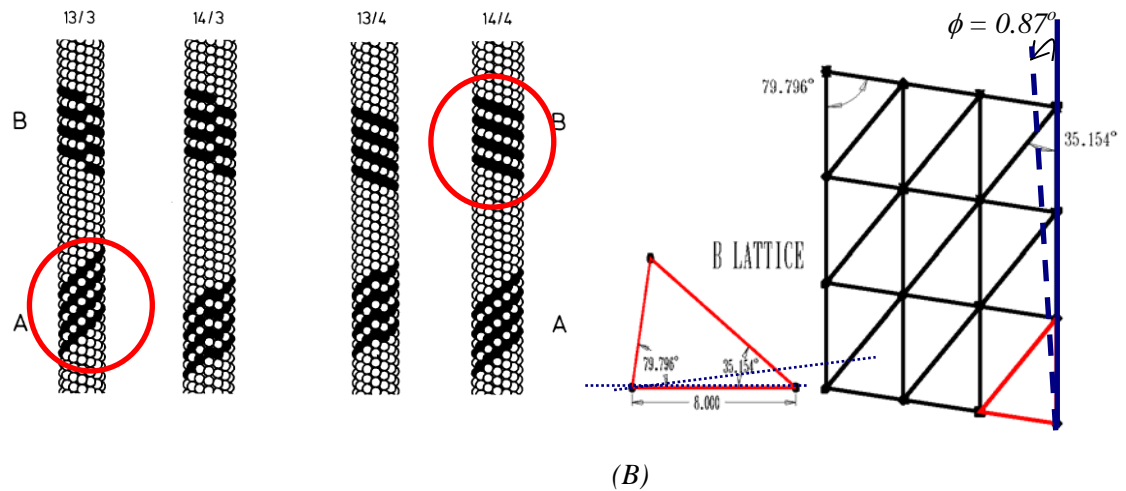


Figure 2-14 Schematic of different lattice structures for the microtubule lattice, marking the seamless microtubules (modified from Mandelkow et al., 1986) (A). The B lattice structure together with the “skew angle” and the geometric parameters are given in (B).

As previously shown, A and B type microtubules have identical monomer arrangements but differing dimer lattices. Both have longitudinal protofilaments with a 8 nm dimer to dimer distance but the helix angle is different for respective cases.

It has been shown that (Chretien and Fuller, 2000) most of the microtubules comprise of a B lattice which is expected to have a higher level of anisotropy. This could be explained by the possible contribution of the protofilament sliding across one another; i.e. shear during high bending loads that the microtubules are subjected to in the cell. That could also be a mechanism for the microtubules to resist high compressive loads in the cell by shearing. This could explain the abundance of B lattice observed in nearly all of the latest experimental work. In order to investigate that, in this section we will show the results for the constants for the compliance matrix for a seamless B lattice.

It is observed in the literature that the B lattice can exist without a seam if the microtubule contains 14 protofilaments and has a four-start monomer helix (Figure 2-14) however it also has to have a skew angle (ϕ). This skew angle is quite low; $\phi=0.87^\circ$ when compared to the helix angle but will be taken into account when modeling the seamless B lattice.

The coordinate system we used to map the deformation gradient to the bond stretches had aligned 1-axis with microtubule longitudinal direction. Hence in order to include the skew angle in the calculations; we transform the deformation gradient and the Cauchy Stress tensor through:

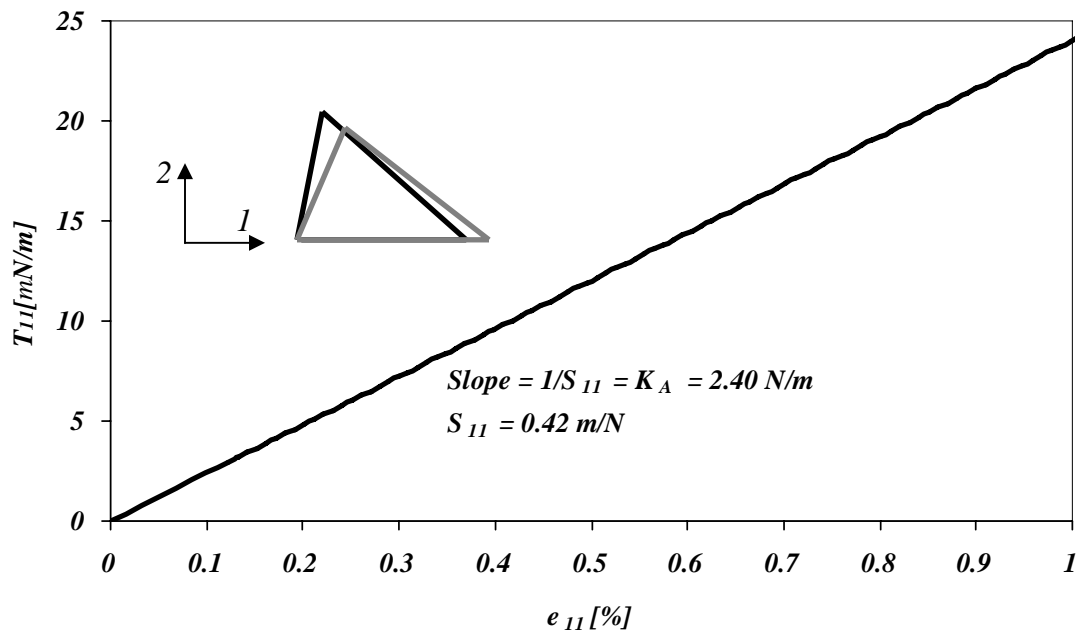
$$\mathbf{F}^* = \mathbf{R}^T \mathbf{F} \mathbf{R} \quad (45)$$

where \mathbf{R} is the rotation matrix:

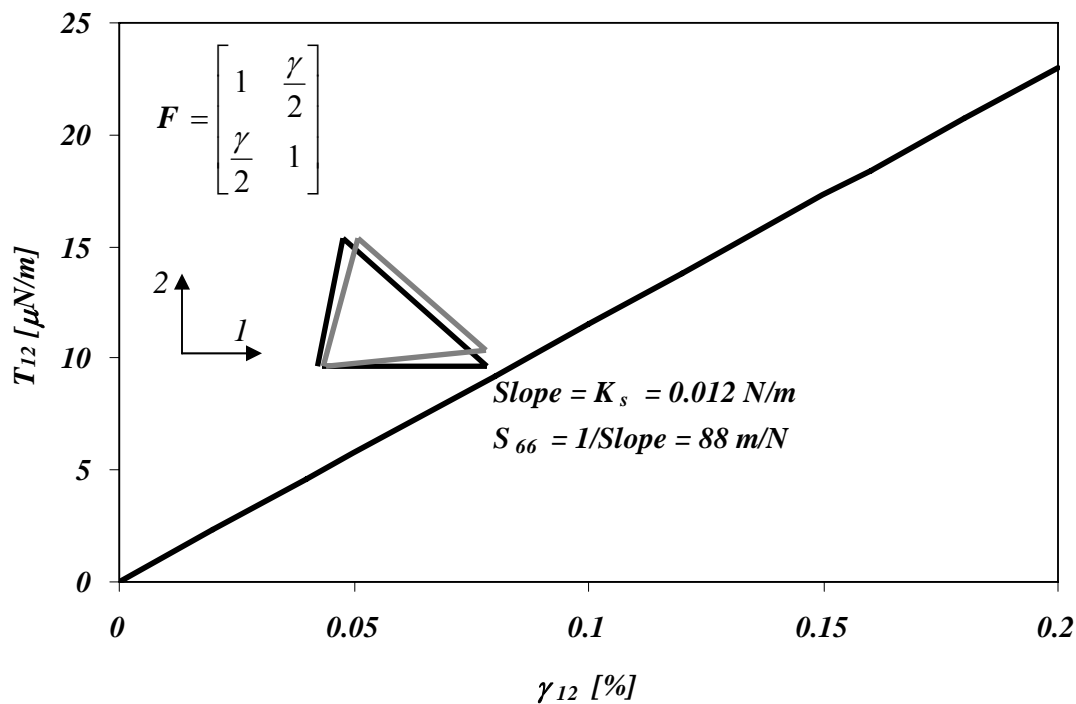
$$\mathbf{R} = \begin{bmatrix} \cos(\phi) & \sin(\phi) \\ -\sin(\phi) & \cos(\phi) \end{bmatrix} \quad (46)$$

And using equation (44), the transformation of the stress tensor is:

$$\mathbf{T}^* = \mathbf{Q}^{-1} \mathbf{T} \quad (47)$$



(A)



(B)

Figure 2-15 Uniaxial Stress, T_{11} vs. e_{11} and shear stress T_{12} vs. γ_{12} is shown here depicting the longitudinal stiffness ($K_A = E_{11}^* t^*$) (A) and the shear stiffness ($K_s = G_{12}^* t^*$) (B) for the seamless B lattice.

Using a similar methodology as conducted for the A lattice microtubules, the material properties of a seamless 14_4 B Lattice microtubule are derived and are given in the Table 2-3.

Table 2-3 Microtubule Mechanical Properties for a unit thickness (B Lattice)

S [1/GPa]	C [GPa]	E^*, G^*, ν
$S_{11} = 0.42$	$C_{11} = 2.4$	$E_{11}^* = 2.40 \text{ GPa}$
$S_{12} = -0.18$	$C_{12} = 0.015$	$E_{22}^* = 0.1 \text{ GPa}$
$S_{16} = -0.92$	$C_{16} = 0.023$	$G_{12}^* = 0.012 \text{ GPa}$
$S_{22} = 10.14$	$C_{22} = 0.12$	$\nu_{12} = 0.3$
$S_{26} = 12.6$	$C_{26} = -0.017$	$\nu_{16} = -1.2$
$S_{66} = 88$	$C_{66} = 0.014$	$\nu_{26} = 1.2$

The seamless B lattice structure has a shear modulus ($G_{12}^* = 0.012 \text{ GPa}$) much lower than the longitudinal elastic modulus ($E_{11}^* = 2.40 \text{ GPa}$) and lateral elastic modulus ($E_{22}^* = 0.1 \text{ GPa}$) is lower than longitudinal elastic modulus by a few orders of magnitude.

The anisotropy is more pronounced for seamless B lattice microtubules in comparison to A lattice type microtubules (i.e. the shear modulus is lower while the longitudinal elastic modulus is the same).

In order to demonstrate the level of anisotropy, we will calculate B lattice structures with the isotropic material assumption;

$$C_{66}^{iso} B.lattice = 2G_{12}^* = \frac{C_{11} - C_{12}}{2} = \frac{2.40GPa - 0.015GPa}{2} \cong 1.19GPa \quad (48)$$

Here, G_{12}^* is the shear stiffness of the isotropic material which comes out to be ~ 0.6 *GPa*.

However for the present case;

$$C_{66} B.lattice = 0.014GPa \ll \frac{C_{11} - C_{12}}{2} \quad (49)$$

The shear stiffness for the A lattice microtubules and the seamless B lattice microtubules come out to be 0.057 *GPa* and 0.012 *GPa* respectively which are far smaller than the isotropic values calculated. This shows the level of anisotropy in microtubules.

Before concluding the analyses of the B Lattice structure, we will investigate if there is an axis system whereby the shear-normal coupling 16 and 26 terms are close to zero. The details of this analysis were shown for the A Lattice in the previous section and it had not been possible to define an axis of orthotropy.

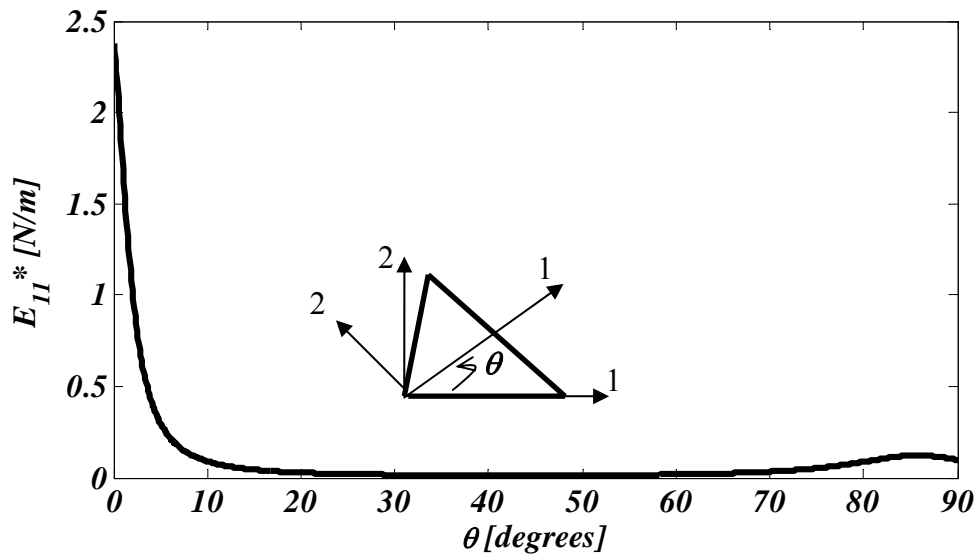


Figure 2-16 The longitudinal stiffness in the transformed axis system for different transformation angles.

Figure 2-16 shows the change in the longitudinal stiffness, E_{11}^* with the transformation angle. We can observe that the highest stiffness value ($E_{11}^* = 2.4 \text{ N/m}$) corresponds to $\theta = 0^\circ$, the material orientation we've used in our model. After about $\theta = 30^\circ$, the longitudinal modulus is $E_{11}^* = 0.01 \text{ N/m}$ for $30^\circ - 60^\circ$; its minimum value. The minimum value of the longitudinal modulus is lower for the B lattice than the A lattice.

Figure 2-17 shows the change in the shear modulus, G_{12}^* with the transformation angle. The highest value of shear stiffness ($G_{12}^* = 0.12 \text{ N/m}$) is at $\theta = 40^\circ$. The smallest values of the shear stiffness correspond to $\theta = 0^\circ$ and $\theta = 90^\circ$ with $G_{12}^* = 0.012 \text{ N/m}$. The difference in the minimum and the maximum shear modulus is much higher in the B lattice structure than in the A Lattice structure.

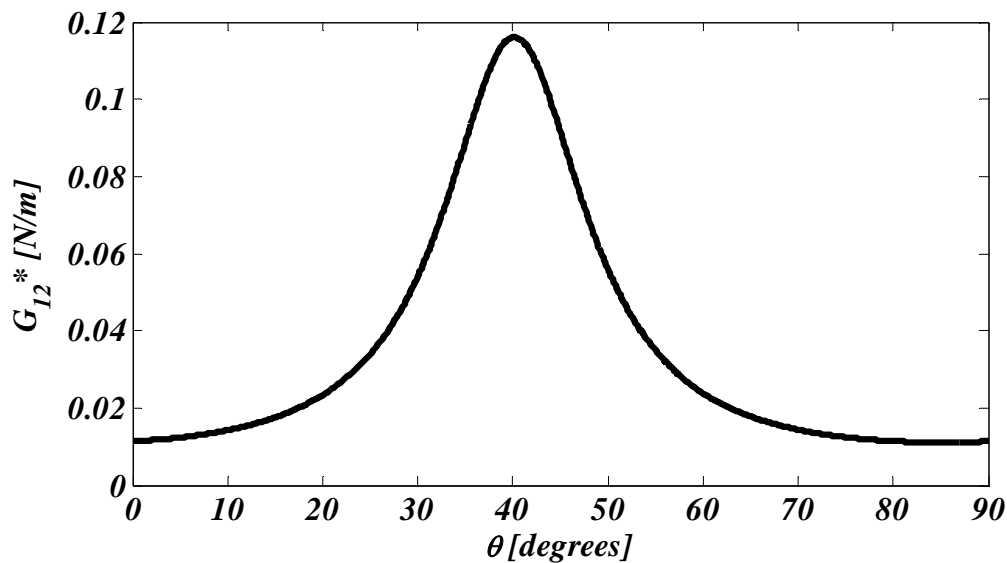


Figure 2-17 The shear stiffness in the transformed axis system for different transformation angles.

Figure 2-18 shows the change in the tension-shear coupling components: ν_{16}^* and ν_{26}^* . The components have the smallest value at $\theta = 40^\circ$ with $\nu_{16}^* = \nu_{26}^* = 0.05$. This is the same axis system where the shear modulus is the highest.

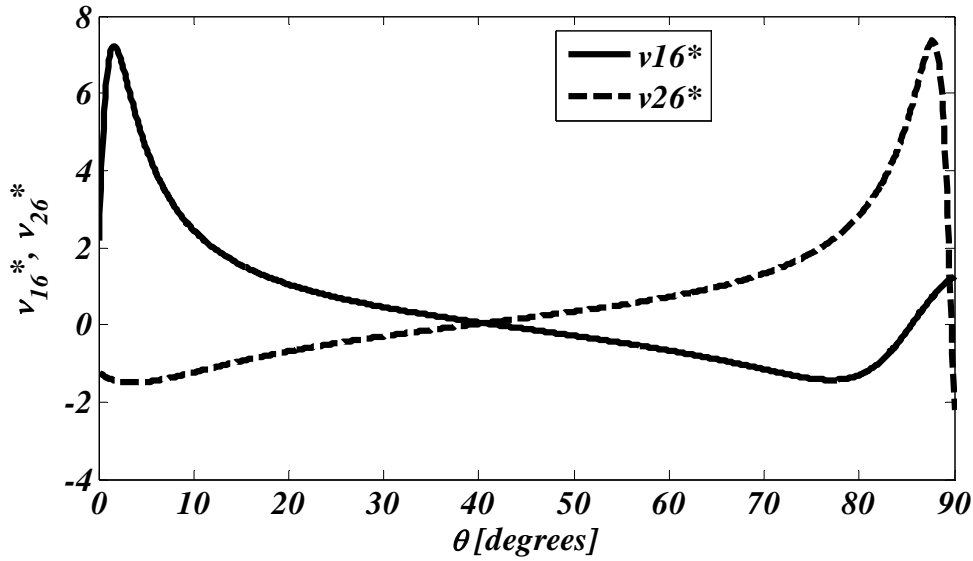


Figure 2-18 The tension-shear coupling components in the transformed axis system for different transformation angles.

The minimum value of v_{16}^* and v_{26}^* at $\theta = 40^\circ$ suggests that the microtubule can be assumed orthotropic in this direction as these values are very small.

In both A and B lattice structures, the coupling between the tension and the shear effect in the axis system that aligns with the tube axis ($\theta = 0^\circ$) might have an effect on critical buckling.

The analysis explained here could also give us a clue of why the microtubule assemble in the configuration they do. It will in the next chapter be shown that in the three point bending experiments, the bending deformation of microtubules occurs not only by stretching of filaments but also by sliding between filaments. This is possible by the low shear modulus of the microtubules (the lowest value being at the $\theta = 0^\circ$ with $G_{12}^* = 0.012 \text{ N/m}$ for the B lattice).

Another effect of the low shear modulus is seen in the microtubule dynamics. The low shear modulus implies a weak link between the protofilaments that constitute the microtubule. In order to facilitate cell division microtubules polymerize and depolymerize by the stretching and even breaking of the lateral bonds between the constituent protofilaments. This is only possible by a low shear modulus.

2.4. Discussion and Concluding Remarks

Microtubules are one of the stiffest elements of the cytoskeleton of eukaryotic cells. They provide cells their shapes and they provide stiffness to cilia and flagella. Rigidity of microtubules has been a topic of interest to many researchers (Amos and Klug 1991; Gittes et al., 1993; Venier et al., 1994; Kurachi et al., 1995; Mickey and Howard 1995...). These researchers treated microtubules with a thin isotropic elastic beam approximation. In 1998, the geometry of the microtubules was revealed by the detailed work of Nogales et al. To have a complete understanding of the mechanical behaviour of microtubules, the dimer-dimer interactions with macroscopic deformations need to be investigated. This analysis requires knowledge of the interaction energies of the dimers as well as the lattice configurations.

Structural investigations (Nogales et al. 1998; Nagoles et al. 1999 and Li et al. 2002) show that lateral and longitudinal tubulin interactions have different properties. α and β monomers are bonded very strongly while the lateral interactions (marked by the contact of the M-loop of one protofilament with the H3 and H1-S2 loop of the adjacent protofilament) are weaker in nature and the interaction surface is smaller. This results in a high anisotropy in the mechanical behaviour of microtubules.

The high longitudinal stiffness is associated with the contribution of the microtubules in the mechanical stability of the cell. The low shear modulus; i.e. the weaker lateral bonds allow the dynamic stabilities which reorganize the cell in the activities such as: cell division.

The aim of the present work is to increase the understanding of the microtubules' mechanical behaviour starting from available knowledge of the constituent dimers' molecular structure and the geometry of the microtubule wall lattice. Following the methodology of Arslan and Boyce (2005) a new bottom-up hierarchical approach was presented in this chapter. The basic building blocks and their interaction interfaces were

identified considering the structure of the microtubule as reported by the electron crystallography analyses (Nogales et al., 1998).

A seamless microtubule can be modeled as a three dimensional helical lattice of dimers. The microtubule lattice in this work is demonstrated with a two-dimensional sheet where the small bond stretches are approximated by a harmonic energy potential. This was carried out using experimental and simulation data coming from several groups who described a number of physical and structural properties of microtubules (Deriu et al., 2007; Nogales et al., 1999 and Sept et al. 2003). The most marked aspect of microtubules observed is the anisotropic character of microtubule elasticity which is reflected in the difference between the longitudinal (aligned with the tube axis) and the lateral (perpendicular to the tube axis) spring constants. Theoretical estimates of the elastic constants required knowledge of the tubulin dimer–dimer interaction potential or relevant experimental data. With the knowledge of particular interaction strengths between two neighbouring dimers, resulting from the protofilament–protofilament shifting along the microtubule axis (Sept et al. 2003) and molecular dynamics simulations (Deriu et al. 2007), as guidance, we obtained estimates of the molecular elastic constants (spring constants) along three different directions on the microtubule wall lattice. These values were used for the modeling of the macromechanical response of the microtubule lattice.

The approach undertaken for the macromolecular modeling started by defining the RVE (Representative Volume Element) for the triangular lattice. This in turn facilitates the tracking of the microscopic deformation in each constituent bond as a function of imposed macroscopic deformation. The strain energy contribution for each bond was then determined. Using continuum mechanics, the macroscopic stress-stretch behaviour of the network was derived from the strain energy density function.

The small difference between the α - and β -monomer geometry allows the existence of different lattice structures; A and B lattices. For the commonly accepted 13₃ (13 protofilaments with a 3 helix start) model, protofilaments of the A lattice have a vertical

shift of 4.9 nm upwards relative to their neighbours whereas in the B lattice, this offset is 0.9 nm. This change results in a “seam” a structural discontinuity in the B lattice. The seam implies a neighbouring interaction (α - β) that differs from the majority of the lateral interactions (α - α and β - β). In this work, the lattice of dimers without mismatch has lateral contacts between α - α and β - β monomers. Microtubules that possess a seam in which lateral contacts exist between α - β monomers laterally require further attention.

In another commonly accepted lattice configuration for the microtubules, the 14₄ model, both of A and B lattice exist in a seamless configuration (helically symmetric), however the B lattice has to have a slightly skewed configuration which is believed to cause an initial unfavoured conformation related excess energy in the lattice which is relieved through depolymerisation and catastrophes. This phenomenon will further be investigated in the Microtubule Dynamics chapter concluding this work.

Debate still continues over whether the A Lattice exists at all (Mandelkow et al., 1991; Amos and Lowe 1999), however we've studied both cases while developing our methodology but will carry out the rest of the work assuming a B lattice type model in the rest of the chapters. The advantage of the proposed model is that given the helix angle and the related geometry, the material behaviour for different lattice configurations could be derived given the periodicity of the dimer staggering.

For both types of lattices (A and B) a monoclinic material behaviour is derived here from the atomistic representation to provide an effective continuum level representation of the mechanical behaviour of the microtubule wall. The model presented here captures the essence of the monoclinic material behaviour, i.e. a uniaxial tension is accompanied with shearing strain in the 1-2 plane and a shearing stress is accompanied with uniaxial strain. It was also shown here that the B lattice could be assumed to have an orthotropic material behaviour in an axis system 40° off the tube axis.

From the continuum model, a shear stiffness of 2 orders of magnitude and a lateral modulus of 1 order of magnitude smaller than the longitudinal modulus was observed for the microtubule wall which shows the highly anisotropic nature of the microtubule structure.

An additional advantage of the proposed model is that the evolution in microstructure (bond stretches, forces, and orientations) is naturally monitored during macroscopic deformation thus capturing the effects of structural evolution on macroscopic mechanical loading behaviours and vice versa. Also, unlike the AFM experiments, one can observe large deformations efficiently and in a computationally feasible manner unlike the molecular dynamics simulations.

Résumé

Les microtubules sont parmi les éléments constitutifs des cellules eucaryotiques du cytosquelette les plus résistants. Ils assurent aux cellules leur forme et sont responsables de la rigidité des ciliés et flagelles. Leur rigidité fut le sujet de nombreuses études (Amos and Klug 1991; Gittes et al., 1993; Venier et al., 1994; Kurachi et al., 1995; Mickey and Howard 1995...). Dans ces différents travaux, les microtubules sont associés à des poutres minces élastiques et isotropes. En 1998, la géométrie des microtubules fut détaillée par Nogales et al. Toutefois, les interactions dimère-dimère et leur incidence sur la déformation macroscopique doivent être étudiées afin de compléter la compréhension du comportement mécanique des microtubules. Cette analyse requiert la connaissance des énergies d'interaction entre dimères autant que de la configuration initiale de la structure. Des analyses microstructurales montrent que les interactions qu'elles soient latérales ou longitudinales ont des propriétés différentes. Les monomères α et β sont connectés par des liaisons fortes tandis que les interactions latérales (marquées par le contact de la M-loop d'un protofilament avec le H3 et H1-S2 du protofilament adjacent) sont de nature plus faibles avec une surface d'interaction inférieure. De fait, le comportement mécanique des microtubules est fortement anisotrope.

L'importante rigidité longitudinale des microtubules est admise comme un facteur important à la stabilité mécanique de la cellule. Le faible module de cisaillement, i.e. les liaisons latérales faibles, quant à lui, permet la stabilité dynamique qui aide à réorganiser la cellule lors d'événements biologiques tels que la division cellulaire.

Le présent travail a pour but d'approfondir la compréhension du comportement mécanique des microtubules à partir des connaissances disponibles concernant l'arrangement moléculaire des dimères et la géométrie de la structure formant les parois des microtubules. Inspirés de la méthode proposée par Arslan et Boyce (2006), une nouvelle approche hiérarchique est présentée dans ce chapitre. Les blocs constitutifs élémentaires et leurs interfaces d'interaction ont été identifiés en considérant la structure des microtubules reportée par microscopie électronique cristallographique (Nogales et al., 1998).

Un microtubule sans discontinuité hélicoïdale ("seam" est le terme anglais décrivant cette particularité géométrique) est modélisé par un réseau tridimensionnel de dimères disposés en spirale. Dans ce travail, la structure microtubulaire est reproduite par un plan bidimensionnel où la déformabilité des liaisons est retranscrite par une énergie potentielle harmonique. Une telle approche s'inspire de nombreuses données simulées et expérimentales de groupes de recherche attachés à décrire différentes propriétés physiques et structurales des microtubules (Deriu et al., 2007; Nogales et al., 1999 and Sept et al. 2003). L'aspect le plus marquant concerne l'anisotropie élastique des microtubules manifestée par la différence notable entre les constants élastiques axiale et latérale. Une estimation théorique des constantes élastiques a nécessité la connaissance des forces d'interaction dimère-dimère ou de données expérimentales pertinentes.

En s'appuyant sur la connaissance des forces d'interaction entre deux dimères voisins conduisant au déplacement relatif entre protofilaments selon l'axe du microtubule (Sept et al. 2003), et sur des résultats de simulations de dynamique moléculaire (Deriu et al. 2007), les propriétés élastiques moléculaires (modules élastiques) ont été évaluées selon

trois directions associées à la structure bi-dimensionnelle des parois des microtubules. Ces valeurs ont été utilisées pour les calculs menés sur un microtubule entier.

La modélisation du microtubule à l'échelle macromoléculaire a été développée comme suit: un volume élémentaire représentatif associé à la structure triangulaire a tout d'abord été défini, permettant la caractérisation de la déformation microscopique dans chacune des liaisons des constituants en fonction de la déformation macroscopique.

L'énergie de déformation des différentes liaisons fut ensuite déterminée.

Enfin, la relation entre contrainte et étirement macroscopique du réseau a été dérivée à partir de la fonction de densité d'énergie de déformation.

La légère différence géométrique entre monomères α et β conduit à deux arrangements du réseau, dénommés A et B. Dans le cas du modèle 13-3 -largement admis- (13 protofilaments et 3 monomères à l'extrémité pour compenser l'arrangement hélicoïdal), les protofilaments de la structure A sont décalés verticalement de 4.9nm par rapport à leurs proches voisins, tandis que selon l'arrangement B, le décalage est limité à 0.9nm. Cette différence implique une discontinuité au niveau de l'attache de la configuration B. L'attache implique une interaction entre voisins (α - β) qui diffère de la majeure partie des interactions latérales (α - α et β - β). Dans ce travail, l'organisation de dimères sans discontinuité possède des liaisons latérales entre monomères α - α et β - β . Les microtubules avec une discontinuité hélicoïdale ("seam") et où, de fait, les liaisons latérales existent entre monomères α - β , requièrent une attention particulière.

Dans une autre organisation microtubulaire largement acceptée, le modèle 14_4, les arrangements A et B coexistent dans une configuration sans discontinuité hélicoïdale (hélice symétrique). Cependant l'arrangement B est légèrement oblique ce qui semble être à l'origine d'une configuration initiale non favorable, reliée à un excès d'énergie dans la structure, qui sera dégagée au cours d'événements tels que la dépolymérisation ou catastrophes. Ce phénomène sera à l'étude dans le chapitre associé à la dynamique des microtubules qui conclura ce travail de thèse.

La littérature reste divisée quant à l'existence de l'arrangement de type-A (Mandelkowitz et al., 1991; Amos and Lowe 1999). Même si nous avons étudié les deux arrangements possibles au cours du développement de notre méthode, la seule configuration B sera considérée par la suite. L'avantage du présent modèle consiste à pouvoir étudier la réponse mécanique en fonction de l'angle de la structure hélicoïdale et de sa géométrie (nombre de tubulines). Aussi, le comportement pour différentes configurations peut être dérivé à partir de la description de l'empilement régulier des dimères.

Pour les deux types d'arrangement (A et B), le comportement monoclinique est déduit de la représentation moléculaire développée précédemment, permettant ainsi de proposer une représentation continue des parois des microtubules. Le modèle ici présenté capture les particularités du comportement monoclinique du matériau : une tension uniaxiale s'accompagne d'un cisaillement selon le plan 1-2 et, de la même manière, une contrainte de cisaillement induit une contribution uniaxiale à la déformation. Ici, Il est montré que la structure B peut être assimilée à un matériau orthotrope selon un axe incliné à 40° par rapport à l'axe du tube.

Aidé du modèle continu, la rigidité de cisaillement et le module latéral sont évalués, à, respectivement, deux et un ordre de grandeur inférieur au module longitudinal des parois du microtubule. Ce résultat confirme l'importante anisotropie de la structure microtubulaire.

Un autre avantage du modèle repose sur le fait que l'évolution de la microstructure (liaisons, elongations, forces et orientations) est évaluée au cours de la déformation macroscopique, reliant de fait l'évolution structurale à l'état de chargement macroscopique et inversement. Aussi, au contraire des mesures AFM, l'étude aux grandes déformations peut-être aisément réalisée, nécessitant, qui plus est, des coûts de calcul nettement inférieurs aux résultats que produiraient des calculs de dynamique moléculaire.

3. CHAPTER 3: EQUIVALENT CONTINUUM MODEL

3.1. Introduction

One of the most interesting fundamental challenges in modeling nano-structured materials is to draw the link between the molecular structure of the material and the macroscopic material. In this work, the aim is to develop a methodology for linking computational chemistry and solid mechanics models. The advantage of the proposed method is its simplicity and the direct connection between the microscopic properties and the macroscopic properties of the material.

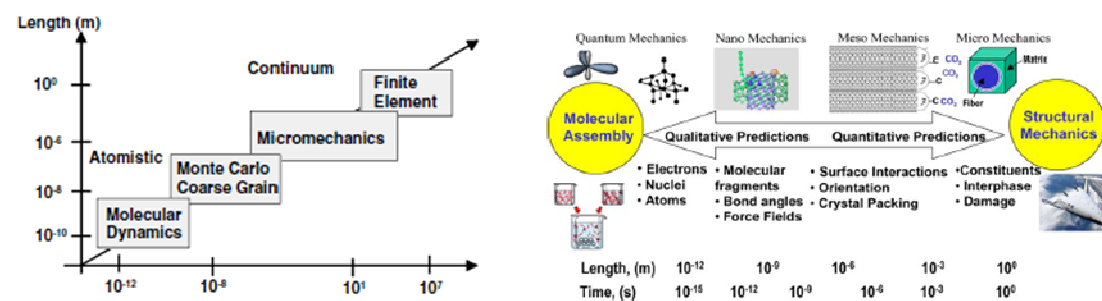


Figure 3-1 Range of length scales of the simulation methods (Gates et al., 2005)

With proper understanding of the molecular structure and the mechanical behaviour of the molecules, the mechanical behaviour can be homogenized (Figure 3-1). At the continuum level, the observed macroscopic behaviour is explained by disregarding the discrete atomistic and molecular structure and homogenizing this behaviour as mechanical properties of a continuum level “material point” where a material point is actually typically many molecules. Finite element methods (FEM) provide a numerical, approximate solution to problems to larger scale structures which are composed of hundreds to millions of material points.

The effective anisotropic model of the elastic behaviour of a material point (Chapter 2) together with the experimental data given in the literature provides an insight to defining

the parameters required for the discrete numerical model created in finite element analysis medium.

In this chapter the finite element modeling approach is used to simulate the mechanical behaviour of microtubules subjected to three-point bending and radial indentation using a thin shell tube approximation where each material point in the wall possesses the anisotropic elastic behaviour determined in the molecular mechanics based modeling of Chapter 2.

3.2. The mechanical thickness

Specific pairing of elastic properties and mechanical thickness of the tube wall must be defined to enable successful modeling of the effective mechanical behaviour of the tube wall with shell theory. The strategy of defining an effective modulus, thickness pair to capture the stretching and bending behaviour of shells of single molecule thickness has been successfully applied to carbon nanotubes in Pantano et al. (2003, 2004-a, 2004-b).

In order to derive the effective “mechanical thickness”, t^* , modulus, E^* pair for a thin-shell model, the stretching and bending of the microtubule wall should first be examined. In Chapter 2, various aspects of stretching behaviour were presented which will be utilized later in this Chapter together with bending to find an appropriate E^* , t^* pair. We now examine bending.

Micrographs in the literature show that the growing or shrinking ends of microtubules often taper to long narrow tips whereby protofilaments separate and curve away from the tube axis. The GTP bound to the β -tubulin end tends to hydrolyze to GDP and inorganic phosphate. Following GTP hydrolysis, the tubulin conformation changes to a curved form with the result that the tubulin-GDP that is connected to the microtubule core is in a strained conformation. The bent form of GDP bound tubulin is constrained by the microtubule lattice. The curvature during the assembly process induces an accumulation of elastic energy in the microtubule wall. Near the end of the microtubule wall, this

accumulated energy is relieved through slight protofilament bending. In essence, the curved geometry of the protofilament is the stress-free state. The radius of curvature of the individual protofilaments has been measured as given in Figure 3-2, A. The average radius of curvature is $\rho = 19\text{nm}$ (Muller et al., 1998).

The work per dimer to bend one individual protofilament into an arc of radius ρ :

$$W = \frac{1}{2} \frac{K_{PF} d}{\rho^2} \quad (50)$$

Here, K_{PF} is the effective flexural stiffness (the effective “ EI ”) of the protofilament, d is the length of a dimer which was measured to be 8 nm (Nogales et al., 1999).

Modeling the protofilament as an effective beam, then we take $K_{PF} = E_{11}^* I_{PF}$, where

$I_{PF} = \frac{bt^{*3}}{12}$ is the second moment of area for a protofilament having a rectangular cross

section of effective thickness t^* and width b . b is the radial separation between protofilaments and has been measured to be ~ 5 nm (Nogales et al., 1999), (Figure 3-2, C).

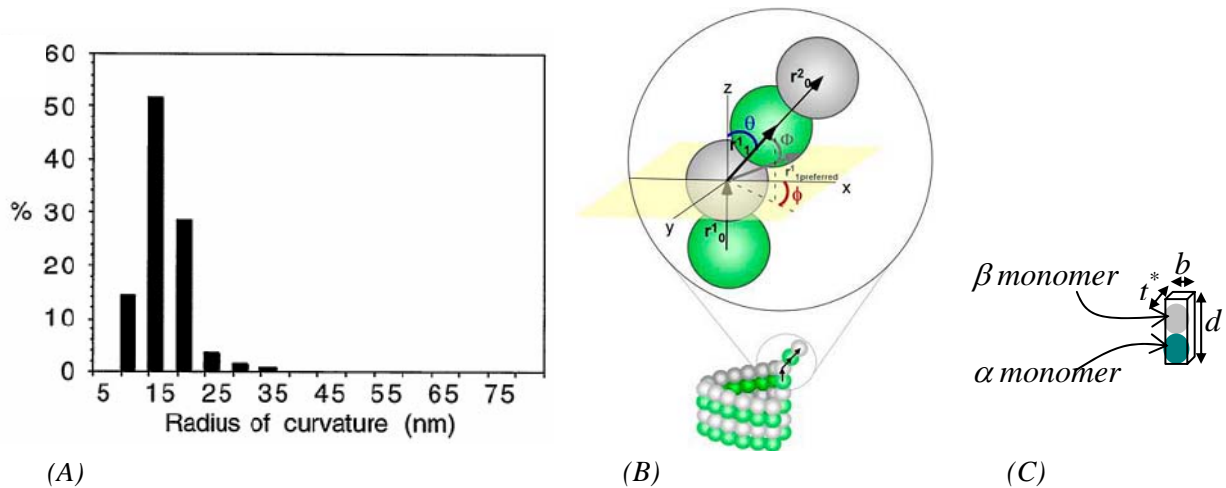


Figure 3-2 (A) The average radius of curvature is 19 nm (Muller et al., 1998), (B) Schematic representation of the bending of a dimer (VanBuren et al., 2005), (C) Schematic representation of a dimer unit cell.

VanBuren et al. (2002) predicted a potential energy of $W \cong 2.5k_B\theta$ to straighten a tubulin-GDP or to curl out a tubulin-GTP dimer to 22° and the microtubules are reported to curl into a radius of $\rho = 19nm$ as measured from the cryo-electron microscope images in the literature (Figure 3-2, A). The depolymerization is cold-induced, the cryo-electron microscope images were obtained typically at temperatures around $\theta = 4-7^\circ C$ (Muller-Reichert et al., 1998).

Utilizing $K_{PF} = E_{11}^* I_{PF}$, equation (50) becomes;

$$2.5k_B\theta = \frac{1}{2} \frac{E_{11}^* \frac{bt^{*3}}{12} d}{\rho^2} \quad (51)$$

From here:

$$E_{11}^* t^{*3} = \frac{60k_B\theta}{bd} \rho^2 \quad (52)$$

Recalling from Chapter 2, the tensile stiffness gives us:

$$E_{11}^* t^* = K_A \quad (53)$$

where: K_A^* was found to be 2.4 N/m.

Together, equation (52) and (53) provide an effective protofilament modulus and an effective thickness pair of: $E_{11}^* = 2.4GPa$ and $t^* = 1nm$.

This pair provides a tensile stiffness of: $K_A = E_{11}^* t^* = 2.4 N/m$ and a protofilament

flexural rigidity of $K_{PF} = E_{11}^* \frac{bt^{*3}}{12} = 1 nNm^2$.

3.3. Finite Element Methods

Two decades of measurements on microtubules employing different techniques (optical tweezers, hydrodynamic flow, AFM...), as explained in Chapter 1, resulted in the values of Young's modulus ranging from 0.01 to 7 GPa (Gittes et al., 1993; Venier et al., 1994; Mickey and Howard, 1995; Vinckier et al., 1996; Felgner et al., 1997...). In all these experiments, what was calculated has been the effective flexural rigidity ($K_B = EI''_{effective}$). Young's modulus, E , was calculated from this data by assuming that the microtubules are homogeneous, isotropic tubes. This assumption is far from being true. The highly helical microstructure of the microtubules indicates that they cannot be modeled as isotropic tubes of a particular cross section and geometry. The shear modulus, which is lower than it would be for an isotropic tube, plays an important role in the deformation of the microtubules in bending and other deformations and shear strain will also accompany axial stretch under loads of uniaxial tension. Some investigators did make attempts to examine some aspects of the shear contributions to the behaviour (Kis et al., 2002; 2003).

In this section, the elastic properties for the microtubule wall obtained in Chapter 2 together with the concept of effective mechanical thickness, modulus pairs will be used to model the behaviour of the tube wall in simulations of the overall deformation behaviour of microtubules. The effectiveness of the model developed in Chapter 2 in accurately interpreting the experimental results is illustrated through the numerical simulation of two experimental procedures in cell mechanics: three-point bending and radial indentation through atomic force microscopy (AFM).

3.3.1. Three Point Bending

The atomic force microscope experiment is widely accepted in the area of cell mechanics due to its high quality of derivable structural and functional information. Atomic force microscope (AFM) was developed in 1986 by Binnig, Quate and Gerber (1986). AFM probes the interactions between a sharp tip and a surface. The tip is located at the free end

of a cantilever, where the beam is typically 100 μm long. Forces between the tip and the sample cause the cantilever to bend. The cantilever is raster-scanned across the sample and a detection system is used to measure the cantilever deflection. Basic modes of operation of AFM are shown in Figure 3-3.

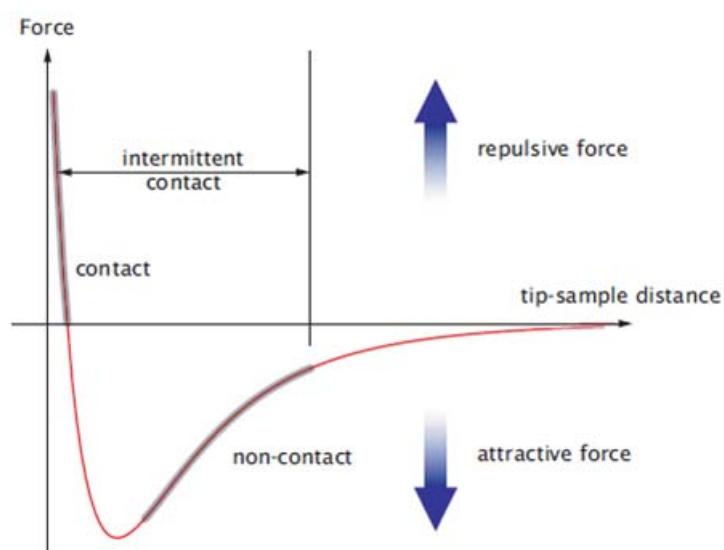


Figure 3-3 Schematics of the AFM basic modes of operation.

Three-point bending provides a measure of the flexural rigidity of a sample (Figure 3-3, A). An example of a three-point bending test on nano-structured materials is the Salvetat et al. (1999) test on carbon nanotubes and the Kis et al. (2002) test on microtubules.

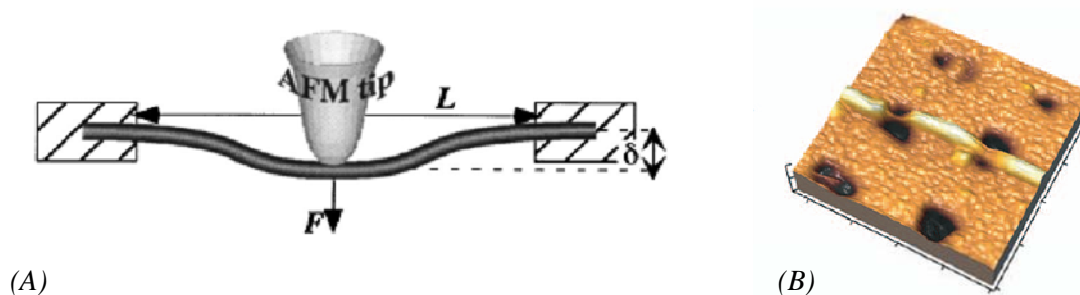


Figure 3-4 (A) A schematic of three-point bending by an AFM tip, (B) Microtubule deposited on a substrate under a loading force (Kis et al., 2002).

In the Kis et al. (2002) work, microtubules were deposited on APTES-functionalized alumina membranes (Figure 3-4, B) and imaged in contact mode. The elastic deformation of microtubules bound to such a surface containing holes ranging from 80 nm to 200 nm diameter (Figure 3-4, B) was determined by atomic force microscopy with the set-up shown in Figure 3-5.

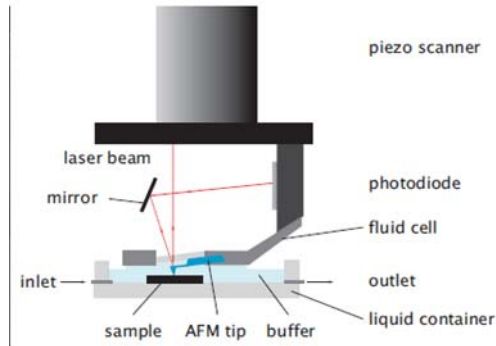


Figure 3-5 Kis et al. experimental set up (2002).

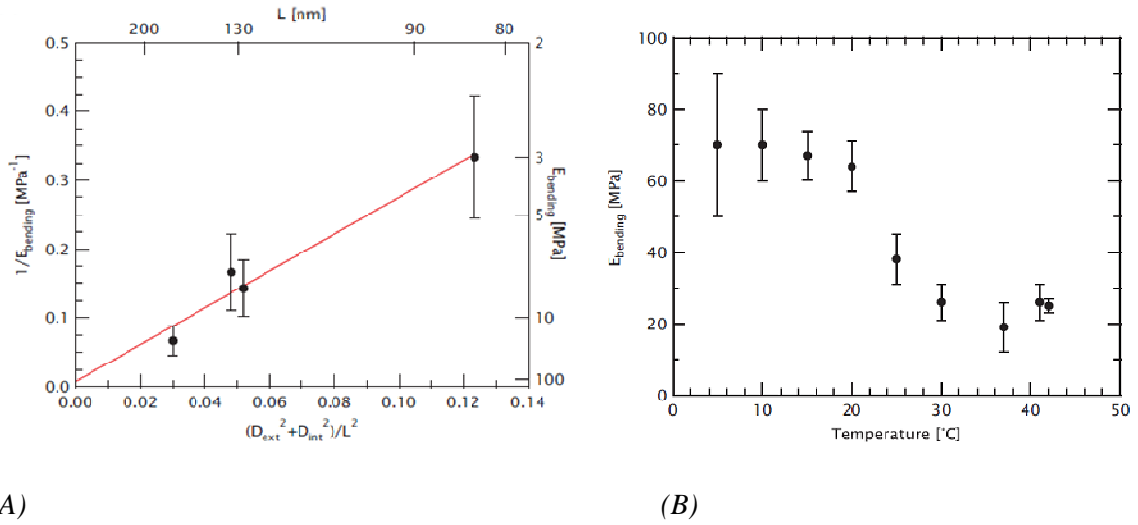
Kis et al. determined the effective bending stiffness, K_B , through these experiments reducing the force-displacement data assuming that the microtubules could be modelled as beams using the formula for three-point bending for a clamped-clamped beam:

$$\delta = \frac{PL^3}{192K_B} \quad (54)$$

Then, approximating $K_B = E_{bending} I$;

$$K_B = E_{bending} I = \frac{P L^3}{\delta 192} \quad (55)$$

Here, P is the vertical force and δ is the vertical displacement and L is sampled length of the microtubule and I is the second moment of area for the geometry in question. The geometry was assumed to be a hollow cylinder with an external diameter of 25 nm and an internal diameter of 15 nm.



(A) (B)
 Figure 3-6 Kis et al. (2002) experimental results:(A) Bending modulus is given in terms as a function of the external diameter (25 nm), internal diameter (15 nm) and the suspended length, (B) Bending modulus measured for different temperature values for a microtubule suspension length of 200 nm.

In order to show the dependence of stiffness, $E_{bending}$, on the suspended length, hole diameters were varied between 80-200 nm and the bending modulus was measured and reduced accordingly (Figure 3-6, A). The effective flexural rigidity, using equation (55), was found to increase with an increase in tube length, then the bending modulus was reduced to be 3 MPa for $L = 83$ nm and 14 MPa for $L = 168$ nm. The microtubule was modeled as a hollow cylinder with an internal diameter, $D_{internal}$, of 15 nm and an external diameter, $D_{external}$, of 25 nm with a second area of moment:

$$I_b = \frac{\pi}{64} (D_{external}^4 - D_{internal}^4).$$

Using the same measurement and data reduction technique, the bending modulus was found for different temperature values (Figure 3-6, B) for a microtubule suspension length of 200 nm.

From their studies, for a microtubule suspension length of 200 nm, Kis et al. reduced a bending modulus, $E_{bending}$ of 40 MPa (using an assumption of a hollow beam as described earlier) at a room temperature of 25° (Figure 3-6, B).

The force versus tip displacement data for the Kis et al. analyses will be extracted from Figure 3-6 in the next section to compare their results to our results.

In order to derive the elastic properties of the microtubules, Kis et al. used the *Timoshenko beam theory* (Timoshenko, 1970) to write the total vertical displacement in terms of the bending and shear components for the total bending of a hollow cylinder:

$$\delta = \delta_{bending} + \delta_{shear} = \frac{PL^3}{192EI_b} + f \frac{PL}{4GA} = \frac{PL^3}{192E_{bending}I_b} \quad (56)$$

where f is a shape factor ($f = 1.38$ corresponding to a hollow cylinder), $\delta_{bending}$ is the bending and δ_{shear} is the shear component of the total tube bending.

In equation (56), A is the cross section area of the microtubule:

$$A = \frac{\pi}{4} (D_{external}^2 - D_{internal}^2), E \text{ is the longitudinal modulus and } G \text{ is the shear modulus.}$$

The researchers rewrote equation (56) as:

$$\frac{1}{E_{bending}} = \frac{1}{E} + \frac{1}{G} \frac{3f(D_{external}^2 + D_{internal}^2)}{L^2}. \quad (57)$$

For the $E_{bending}$ values they obtained from the experiments, for the related suspension

lengths, they plotted $\frac{1}{E_{bending}}$ with respect to $\frac{(D_{external}^2 + D_{internal}^2)}{L^2}$ (Figure 3-6, A).

In Figure 3-6, A, the x-intercept corresponds to $\frac{1}{E}$ following equation (57). From the x-intercept, they derived a Young's modulus of $E = 100MPa$ and, a shear modulus of $G = 1.5MPa$. This implied a shear modulus 2 orders of magnitude lower than the Young's modulus.

The flexural rigidity results of Kis et al. (2002; 2003) will be shown and compared along with the proposed work in the next section where the finite element analysis of the thin shell tube undergoing three-point bending will be presented for different suspension lengths.

3.3.1.1. FEM: Loading and Boundary Conditions

Here, finite element analysis of an AFM three-point bending technique will be presented as described in the previous section. A spherical indenter of $20nm$ radius is used to bend B Lattice type (14_4) microtubules.

The following assumptions are made for the finite element analysis of the microtubule:

- The material is linear elastic.
- The length of the microtubule (to be suspended through different size of holes) is chosen to be $1 \mu m$.
- The material properties for the anisotropic material for "thin shell analysis" were derived in Chapter 2.
- An effective longitudinal modulus and an effective wall thickness pair: $E_{11}^* = 2.4GPa$ and $t^* = 1nm$ are used satisfying an axial wall stretch stiffness of $K_A = E_{11}^* t^* = 2.4 N/m$ and wall bending stiffness of $E_{11}^* t^{*3} = 2.4nNm$. The remaining moduli of the anisotropic tensor are scaled for effective thickness as well.

- The average radius of the microtubule is calculated using the circumferential separation of protofilaments ($b=5nm$; Nogales et al., 1999). For a 14 protofilament microtubule, $R_{avg} = \frac{14b}{2\pi}$. The radius comes out to be $R_{avg} = 11.14nm$.
 - The microtubule is placed on two rigid plates at the ends with a separation length varied between 80 to 1000 nm.
 - The indenter tip is given a vertical displacement of $15 nm$.
- Finite element analysis is performed using the software ABAQUS. The model consists of 6420 nodes and 6400 shell elements (S4R).

3.3.1.2. Results

Figure 3-7 shows the force vs. displacement curve for the three-point bending simulation for a suspended length of $80 nm$. The microtubule is modelled as a thin walled cylindrical tube (as shown in the inset of the figure) with the tube wall modelled with shell elements. For the “anisotropic material” case, the material behaviour is taken as that of a seamless B Lattice type microtubule with the effective material properties of: $E_{11}^* = 2.4GPa$, $E_{22}^* = 0.1GPa$, $G_{12}^* = 0.012GPa$, $\nu_{12} = 0.34$, $\nu_{16} = -1.2$, $\nu_{26} = 1.2$ where the 1-direction is the tube axis direction and the 2-direction is the circumferential direction with a thin shell effective thickness of $t^* = 1nm$. (Note that these properties in fact correspond to a nearly orthotropic behaviour where the near orthotropy axis was found to be 40° from the 1-direction; see Chapter 2. However, the orientation of the tube axis with respect to the orthotropy axis gives a coupling behaviour between axial and shear deformation.)

For the anisotropic tube, a force versus displacement initial slope of $0.0044 N/m$ is observed.

In order to observe the effect of anisotropy, the force versus displacement behaviour for an “isotropic material” with properties: $E_{11}^* = 2.4GPa$, $t^* = 1nm$ and $\nu_{12} = 0.34$ is also

simulated (Isotropic tube has a much higher shear modulus ($G_{12}^{*} = \frac{E_{11}}{2(1+\nu_{12})} \cong 0.9GPa$) than the anisotropic case ($G_{12}^{*} = 0.012GPa$)). Even for the isotropic tube, we would expect a possible shear contribution for the case of short suspended lengths in three-point bending experiments/simulations.

For the “isotropic material” case, the slope of the force vs. displacement curve is calculated as $0.078 N/m$. This result is about 15 times higher than the anisotropic material response.

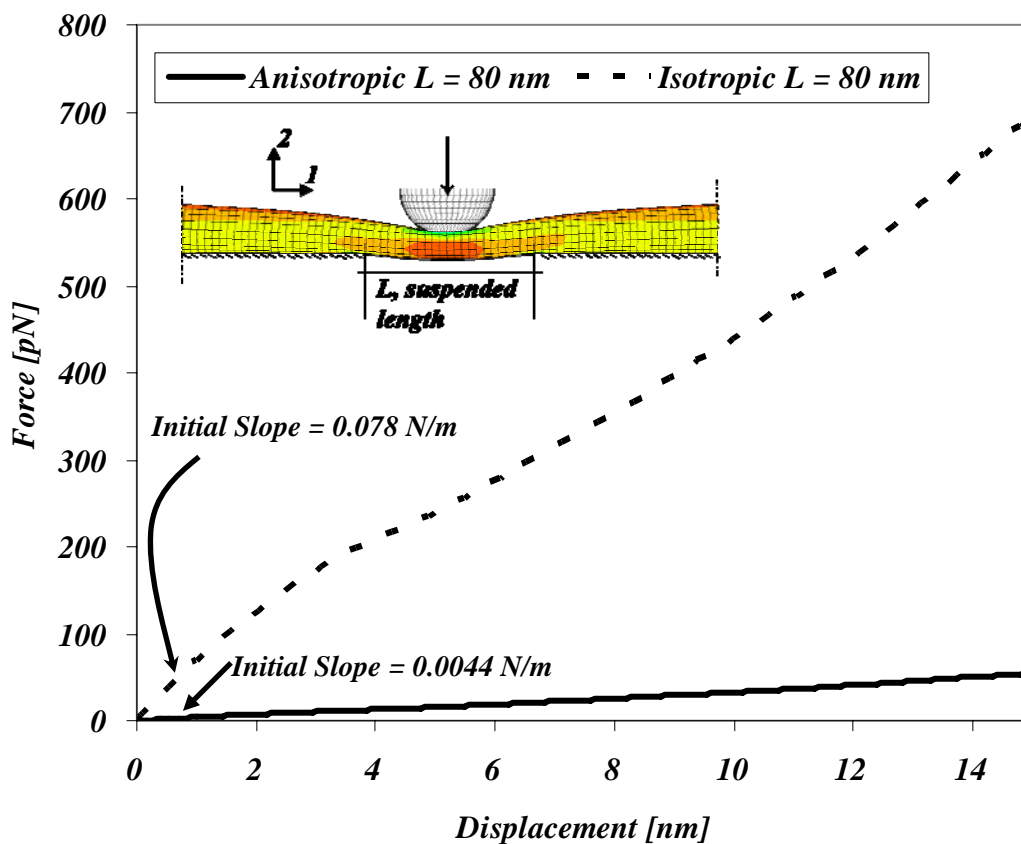


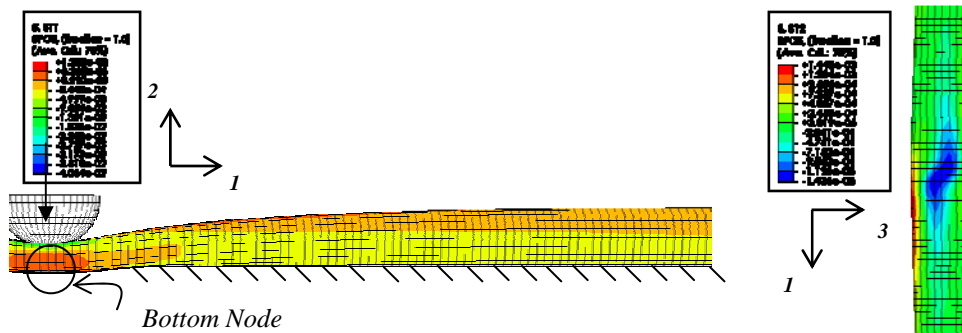
Figure 3-7 Force vs. displacement curve for the three-point bending simulation comparing an anisotropic and an isotropic response for an effective modulus and thickness pair of $E_{11}^{*} = 2.4GPa$ and $t^{*} = 1nm$. The inset shows the deformed configuration of the microtubule. The suspension length (L) of the microtubule is 80 nm.

In order to derive a “bending stiffness”, $E_{bending}$, for microtubules we have to examine the applicability of equation (54): $\frac{P}{\delta} = \frac{192E_{bending}I}{L^3}$ to microtubules under these particular loading conditions, more carefully.

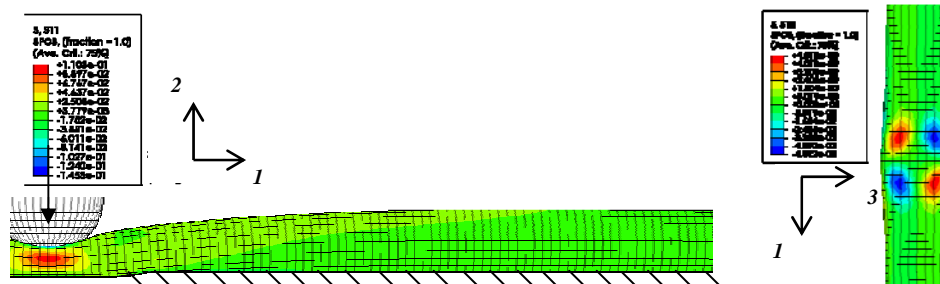
Here, the second moment of area is:

$$I = \frac{\pi}{4} \left[\left(R_{avg} + \frac{1}{2}t^* \right)^4 - \left(R_{avg} - \frac{1}{2}t^* \right)^4 \right]. \quad (58)$$

From equation (54), the initial slope 0.078 N/m (isotropic tube) gives a bending stiffness of $E_{bending} = 48 \text{ MPa}$. If the loading conditions do provide the bending conditions where equation (54) would indeed apply, then the expected initial slope should have given a bending modulus of 2.4 GPa . Therefore we can conclude that equation (54) does not provide an accurate estimate for the thin shell isotropic cylinder response ($E_{bending} = 48 \text{ MPa} \ll E_{11}^* = 2.4 \text{ GPa}$) for a suspension length of 80 nm and that either shear or other deformations provide significant contributions to the displacement during this loading.



(A)



(B)

Figure 3-8 Contour plots showing the longitudinal stress distribution (S_{11}) for the three-point bending of (A) Anisotropic tube and (B) Isotropic tube with a suspension length of $L = 80$ nm. On the right is the top view of the experiments depicting the shear stress distribution (S_{12}) profiles for each case. A “bottom node” on the opposite side to the indenter contact node is depicted in the figure and is to be analyzed in this section.

Therefore, to understand this loading in more detail, we examine the contours of the deformed tubes. Figure 3-8 shows the contour plots of the longitudinal stress distribution (S_{11}) and the shear stress (S_{12}) for the three-point bending of the anisotropic tube and the isotropic tube with a suspension length of 80 nm.

We can observe higher longitudinal stresses associated with the isotropic case. We can also observe that the S_{11} contours do not exhibit a stress distribution consistent with bending and that the deformed images also indicate that this loading condition does not bend the tube in any meaningful way.

Viewing the tube from the indentation axis (right figures) reveals the ovalization of the tube in both the anisotropic and the isotropic cases. This ovalization suggests that it is either the bending or shearing of the tube wall beneath the indenter (as opposed to bending the tube) that accommodates the displacement of the indenter. The shear stress contours shown in this view also reveal significant differences in shearing the anisotropic and isotropic cases (with dramatically lower shear stresses in the anisotropic case due to the lower shear modulus and therefore greater deformation by shearing –noting greater ovalization of the isotropic case due to more wall bending compared to wall shearing). The shear strain contours are given in Figure 3-9 (The shear strain contours for the rest of the analyses can be found in Appendix 3-2). These contours suggest that due to the very low shear modulus of the anisotropic tube, significant shear strain accompanies the

indenter displacement. However in isotropic and anisotropic cases, the flattening/ovalization also occurs because of the bending of the tube wall under the indenter. This shows that in the three-point bending test (with a very short suspension length (80 nm)) instead of tube bending, what is being observed is the tube shearing, the tube wall bending and tube wall shearing. Because of the effect of tube wall shearing and tube wall bending, the slope of the force versus indenter vertical displacement curves (Figure 3-7) does not indicate the exact bending modulus. Thus, although the very low shear modulus of the anisotropic tube results in a much lower slope for the three-point bending force – displacement curves than the isotropic tube, we still could not conclude that the compliant anisotropic tube response is only due to this low shear modulus giving overall shearing but also giving tube wall shearing beneath the indenter as well as tube wall flattening. The influence of this local wall bending and shearing behaviour will be shown to decrease with increasing suspended lengths.

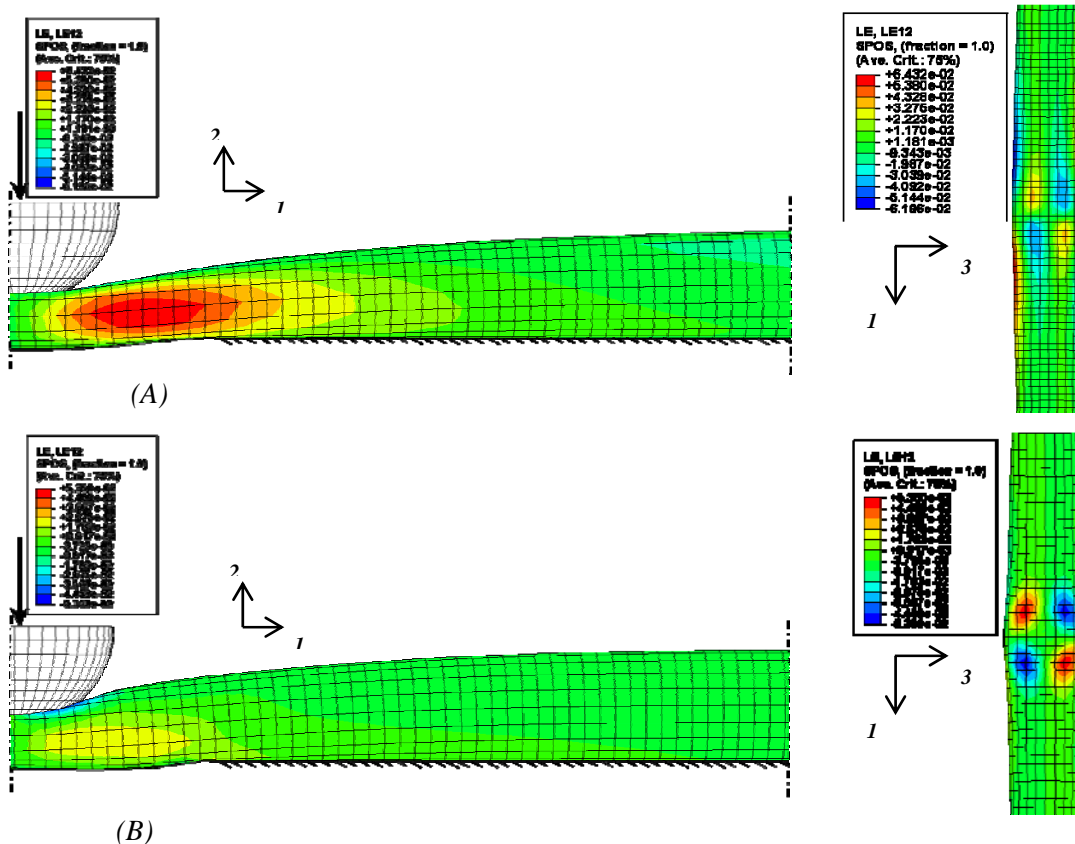
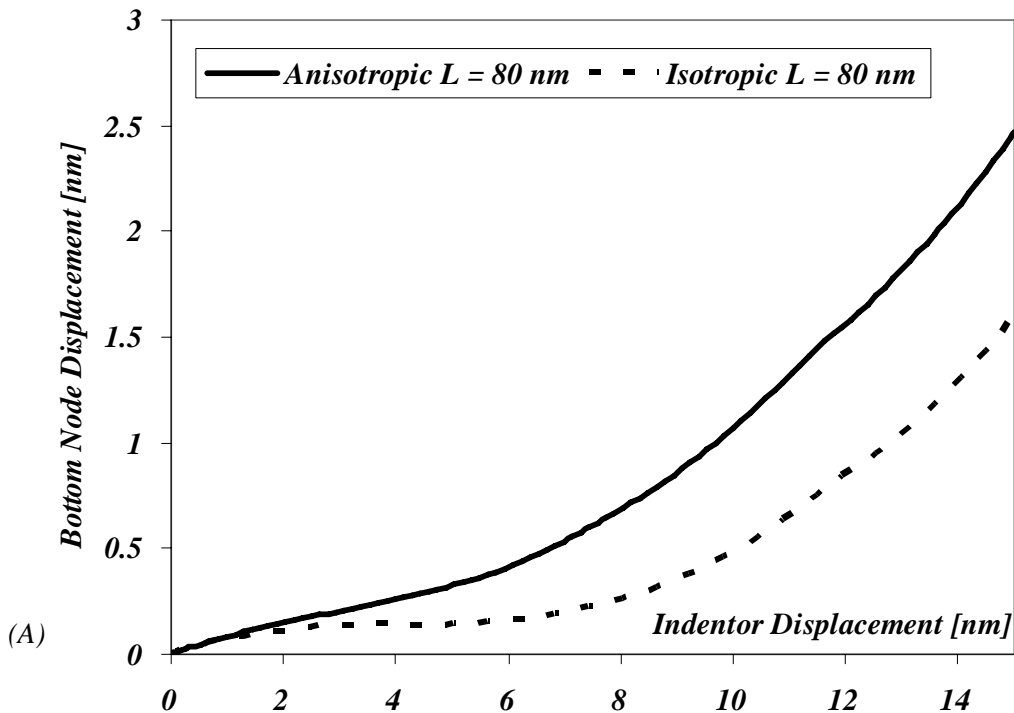
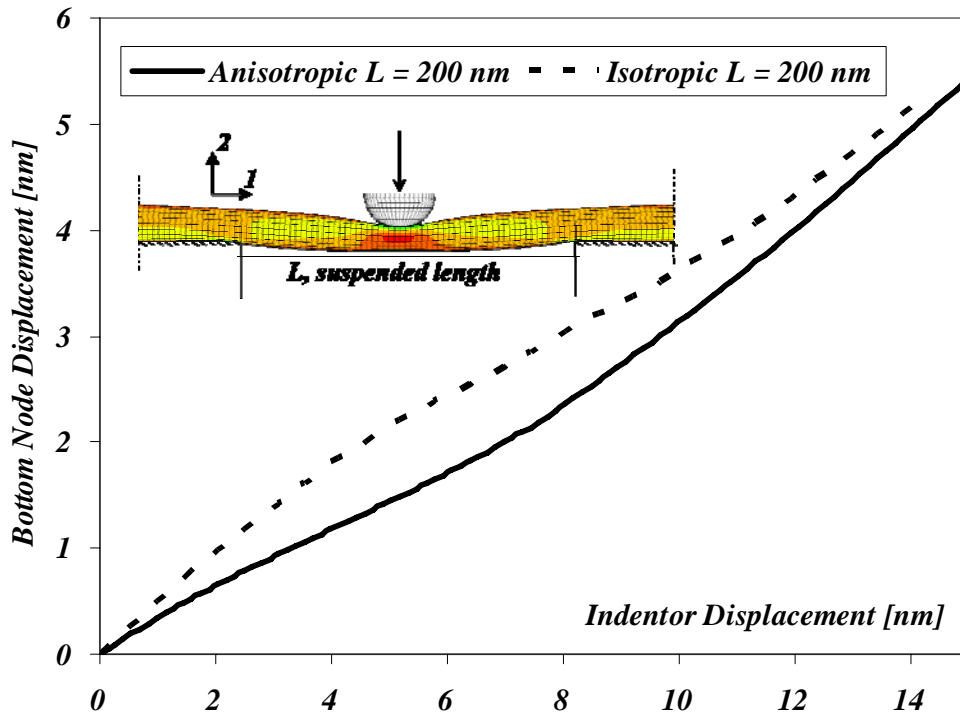


Figure 3-9 Contour plots showing the shear strain distribution (LE_{12}) for the three-point bending of (A) Anisotropic tube and (B) Isotropic tube with a suspension length of $L = 80\text{ nm}$.

In order to investigate this further for the 80 nm suspension case, we can plot the displacement of the bottom node of the tube which is located on the opposite direction to the indenter (Figure 3-8) with respect to the indenter vertical displacement. Figure 3-10 shows that although the indenter is given a vertical displacement of 15 nm , the bottom node of the tube is only displacing 1.5 nm for the isotropic tube and 2.5 nm for the anisotropic tube. The nonlinearity in these two plots (Figure 3-10) show that until about 10 nm indenter vertical displacement what was observed in the force versus indenter displacement plots (Figure 3-7) has been the tube wall deformation/ovalization beneath the indenter. For this reason for the anisotropic tube or the isotropic tube, equation (54) cannot be expected to give the tube bending modulus for the “tube bending”.

A comparison of the 80 nm suspension length and 200 nm suspension length cases is given in Figure 3-10. Here we can observe that for a suspension length of 200 nm (the longest suspension length Kis et al. (2002; 2003) used), the vertical displacement of the bottom node ($\sim 6\text{ nm}$) is still much less than the vertical displacement of the indenter (15 nm) for both the isotropic and anisotropic cases. There is still a strong contribution of tube wall bending and shearing to the indenter displacement.

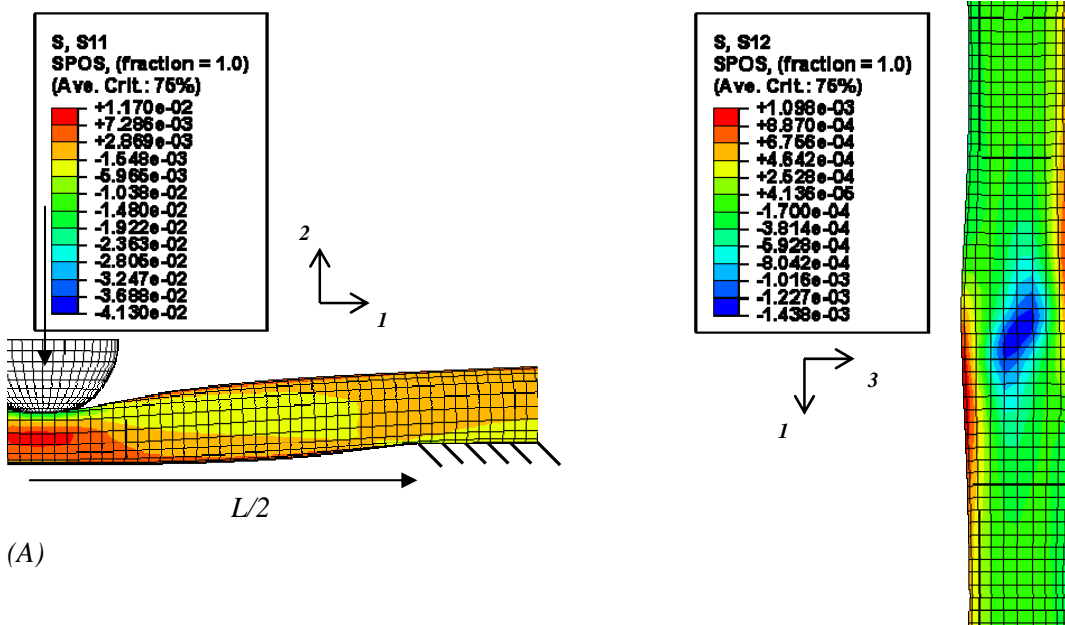




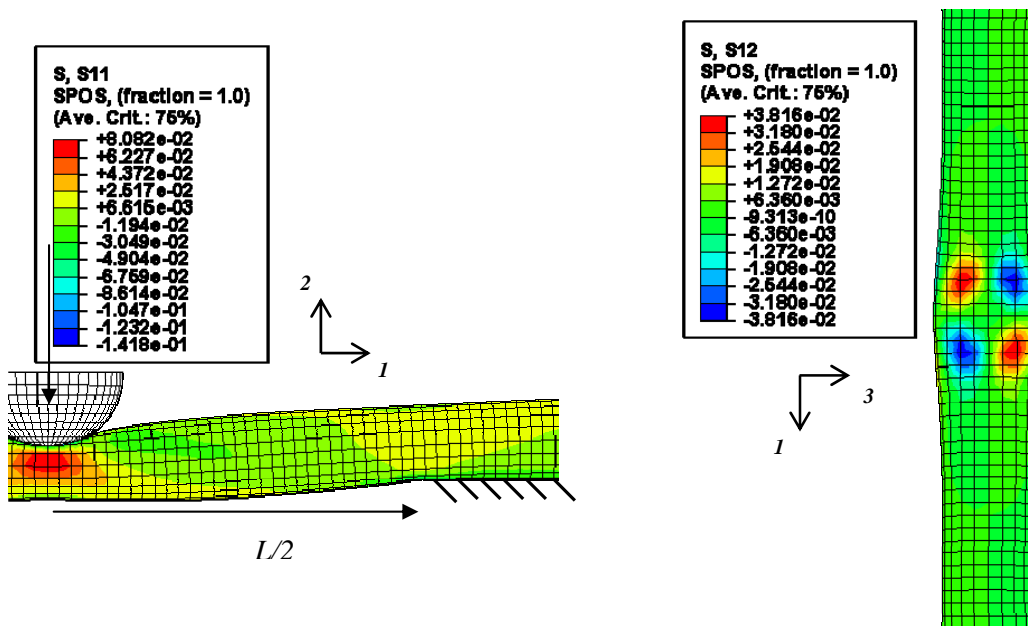
(B)

Figure 3-10 The plot shows the vertical displacement of the bottom node opposite to the top surface of the tube which is in contact with the indenter for a suspension length of (A) 80 nm and (B) 200 nm.

Figure 3-11 shows the contour profiles for a suspension length of 200 nm for the anisotropic and the isotropic tubes. Ovalization of the tube is still observed for the suspension length of $L = 200$ nm.

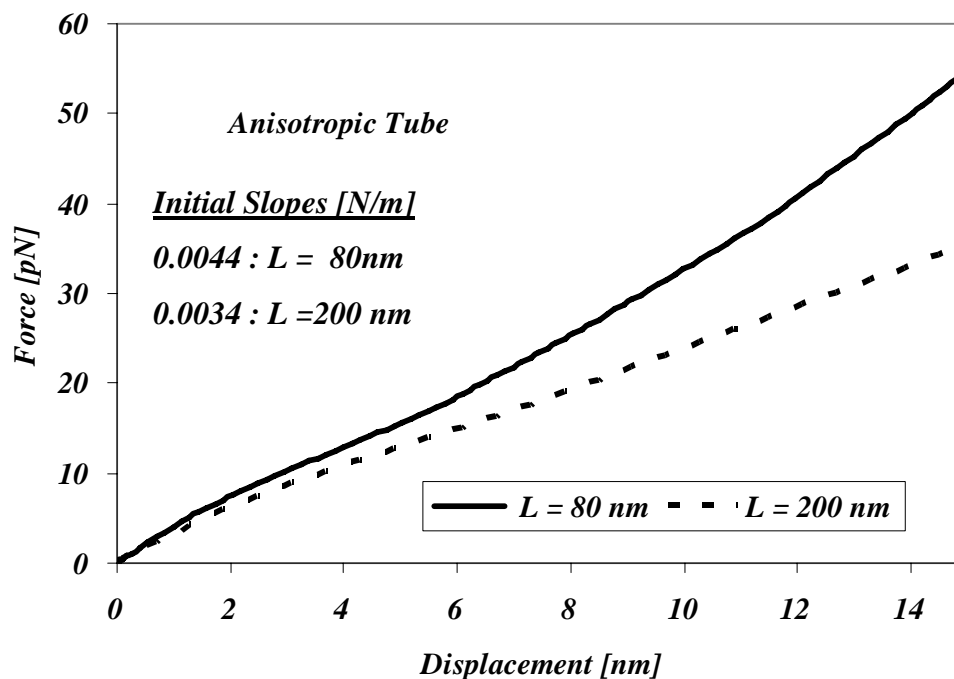


(A)

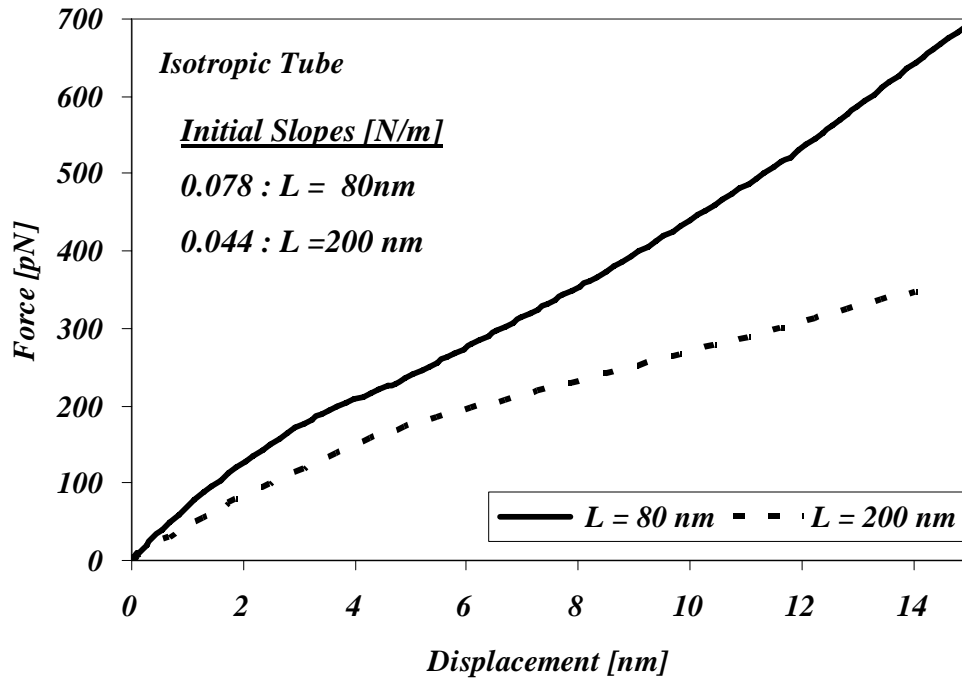


(B)

Figure 3-11 Contour plots showing the longitudinal stress distribution (S_{11}) for the three-point bending of (A) Anisotropic tube and (B) Isotropic tube with a suspension length of $L = 200$ nm. On the right is the top view of the experiments depicting the shear stress distribution (S_{12}) profiles for each case.



(A)



(B)

Figure 3-12 Force vs. displacement curves for the three-point bending simulation comparing the anisotropic responses (A) and the isotropic responses (B) for an effective modulus and thickness pair of $E_{11}^* = 2.4\text{GPa}$ and $t^* = 1\text{nm}$ with suspension lengths; $L = 80$ and $L = 200$ nm.

In this section through our analyses, even though we have found that bending equations are an inappropriate method for reducing the data, we will still use the bending equation (equation (54)) for the purpose of comparison of our results to the Kis et al. (2002; 2003) results. We will also be investigating longer suspension lengths (200, 500 nm, 1000 nm) in order to see if the effect of tube wall flattening/ovalization and shearing become negligible at longer suspension lengths.

Figure 3-12 shows the force versus indenter displacement curves for the anisotropic and isotropic tube responses for suspension lengths of 80 nm and 200 nm. After a vertical displacement equal to the tube thickness (1 nm), there is the flattening of the shell tube causing nonlinearity and a decrease in the slope for all of the cases. A vertical indenter displacement of 15 nm results in forces up to 55 pN for the 80 nm suspension length case, while this force is around 35 pN for 200 nm suspension length. The reduced slope for the

200 nm case compared to the 80 nm case does reflect the increasing contribution of tube bending as the length is increased.

Using equation (54), the bending stiffness, K_B , comes out to be: $K_{B80nm} = 1.1 \times 10^{-26} Nm^2$ and $K_{B200nm} = 1.4 \times 10^{-25} Nm^2$ for 80 nm and 200 nm tube suspension lengths respectively. Calculating the second moment of area I (equation (58)) for the tube with an average radius of 11.14 nm and an effective modulus and thickness pair of $E_{11}^* = 2.4 GPa$ and $t^* = 1 nm$, the bending moduli are calculated as: $E_{Bending 80nm} = 2.5 MPa$ and $E_{Bending 200nm} = 33 MPa$, respectively using equation (55). From Figure 3-6 we can observe that Kis et al. (2002; 2003) observed values of approximately 3 MPa and 40 MPa for each of these cases which are comparable to our anisotropic thin shell tube model results.

For the same set of suspension lengths, Figure 3-12 also shows the force vs. displacement responses using an isotropic material approximation with properties: $E_{11}^* = 2.4 GPa$ and $\nu_{12} = 0.34$. Using equation (54), the bending stiffness, K_B for the isotropic tube comes out to be: $K_{B80nm} = 2.1 \times 10^{-25} Nm^2$ and $K_{B200nm} = 1.8 \times 10^{-24} Nm^2$ for 80 nm and 200 nm tube suspension lengths, respectively. The bending moduli are calculated as: $E_{Bending 80nm} = 48 MPa$ and $E_{Bending 200nm} = 420 MPa$, respectively. The bending stiffness values for the isotropic tube come out to be much higher than for the anisotropic tube.

In summary, our numerical simulations using an anisotropic thin shell cylinder to capture the microtubule behaviour are in agreement with the Kis et al. data for three-point bending with suspension lengths of 80 – 200 nm. At the same time, our results also reveal that the dominating deformation mechanism in the Kis et al. experiments is not tube bending or not only tube shear effects during bending, but also is tube wall bending and shear beneath the indenter as evidenced by ovalization and flattening.

In order to reduce the tube ovalization and flattening effects during three-point bending, the suspension length of the microtubules should be increased. As the suspension length

increases, the effective bending modulus will more adequately reflect tube bending. As tube length increases, the influence of local wall bending and wall shearing beneath the indenter on indenter displacement will diminish. However, the presence of the shear force on three-point bending is an additional contaminating influence on the displacement especially for the anisotropic case which has a low shear modulus. The influence of the shear force will decrease with increase in suspension length since the ratio of bending moment to shear force increases with increasing length.

Kis et al. could not use longer microtubule suspension lengths as this would require recording much lower forces with even higher sensitivity than their instrumentation could measure (Kis et al., 2003). The advantage of the finite element simulations is that it lets us model longer tubes. We carried the three-point bending simulations for suspension lengths of: 500 nm with clamped-end condition and $1\mu\text{m}$ with pinned-end condition for anisotropic and isotropic tubes.

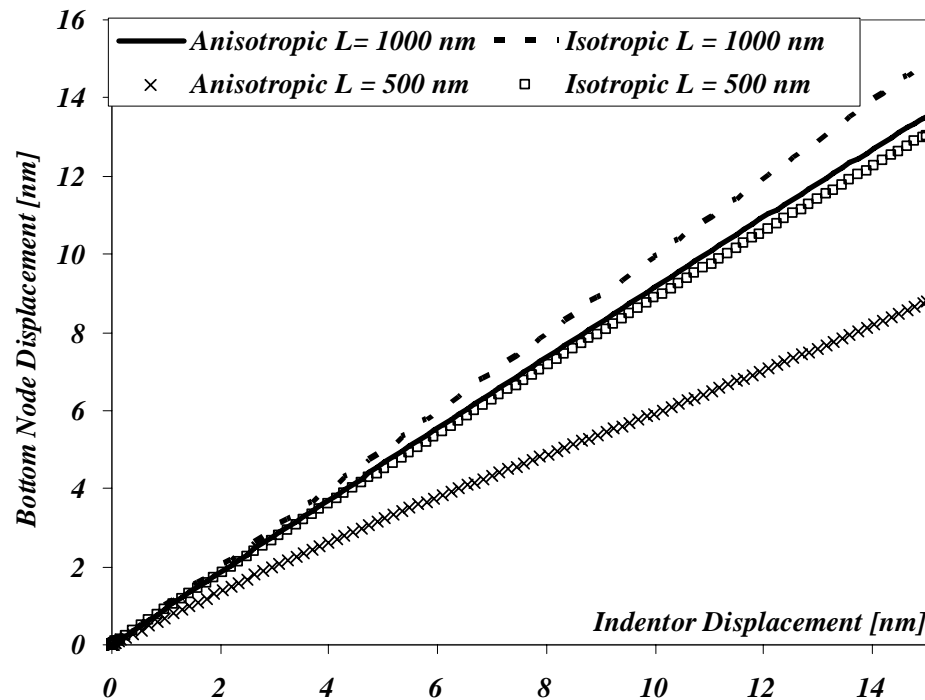
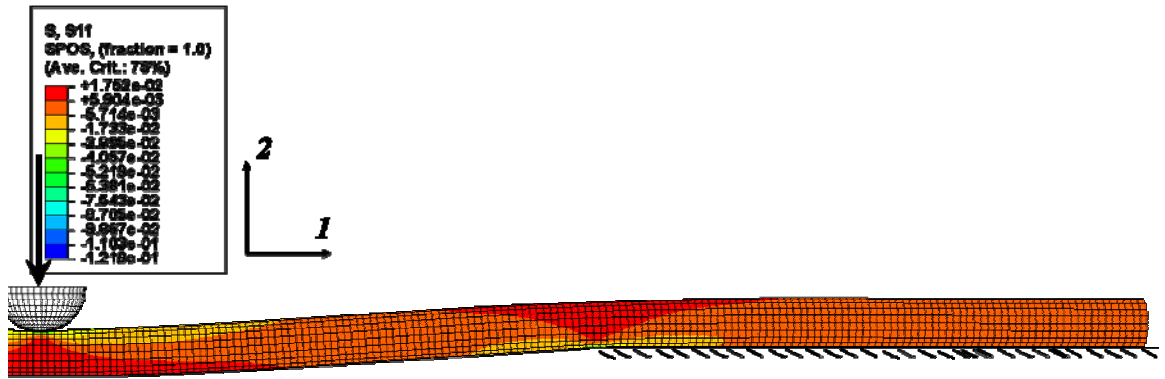
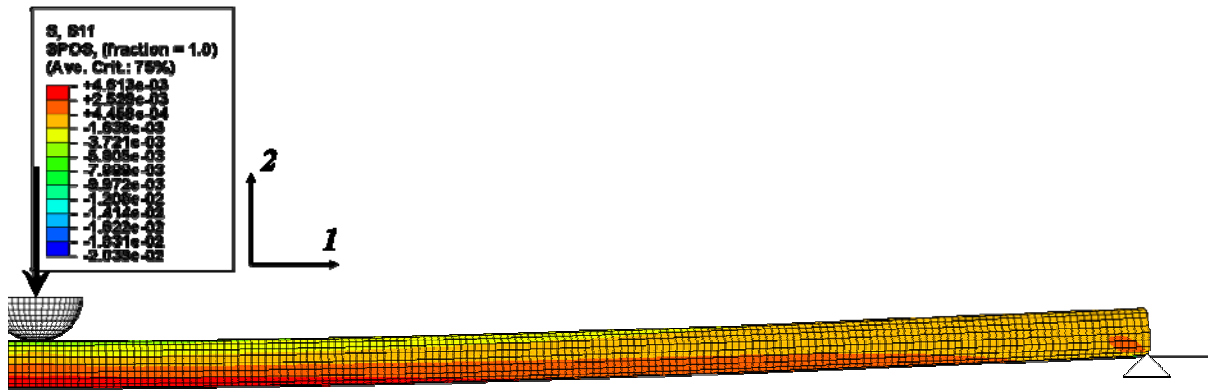


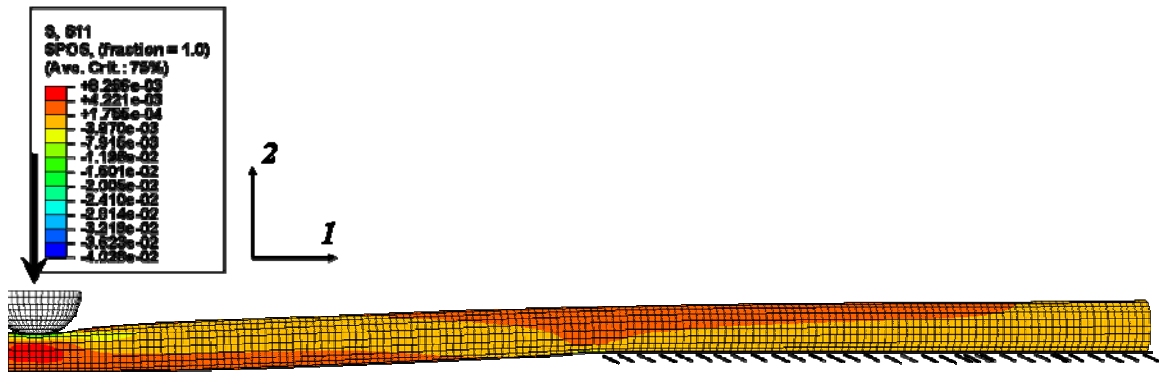
Figure 3-13 The plot shows the vertical displacement of the bottom node opposite to the top surface of the tube which is in contact with the indenter for an effective modulus and thickness pair of $E_{11}^* = 2.4\text{GPa}$ and $t^* = 1\text{nm}$ for an isotropic and an anisotropic tube. The suspension length (L) of the microtubule is $L = 500\text{ nm}$ and $L = 1000\text{ nm}$.



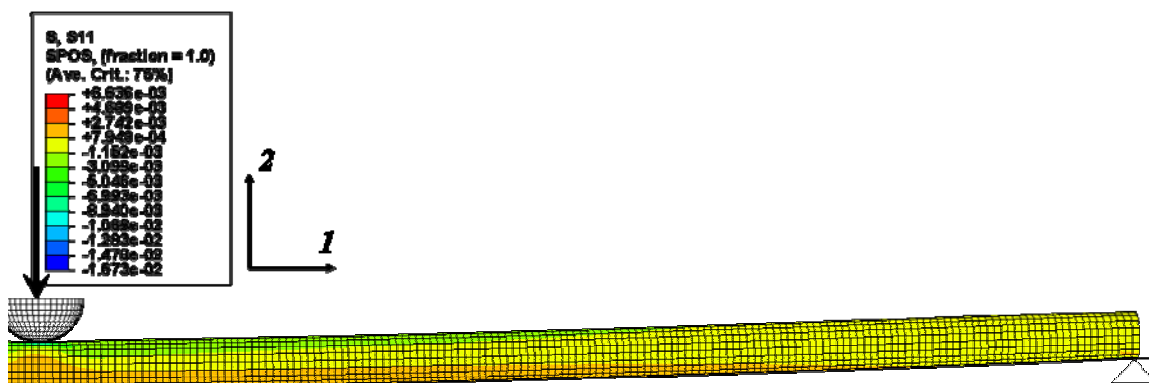
(A)



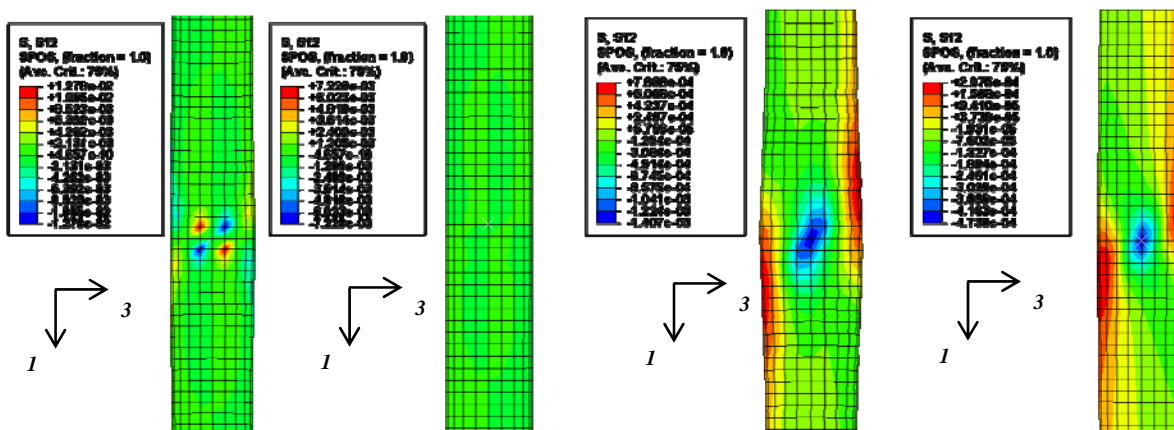
(B)



(C)



(D)



(E)

(F)

(G)

(H)

Figure 3-14 Contour plots showing the longitudinal stress distribution (S_{11}) and the shear stress distribution (S_{12}) for (A,E) Isotropic Tube with a suspension length of 500 nm, (B, F) Isotropic Tube with a suspension length of 1000 nm, (C, G) Anisotropic Tube with a suspension length of 500 nm and (D, H) Anisotropic Tube with a suspension length of 1000 nm.

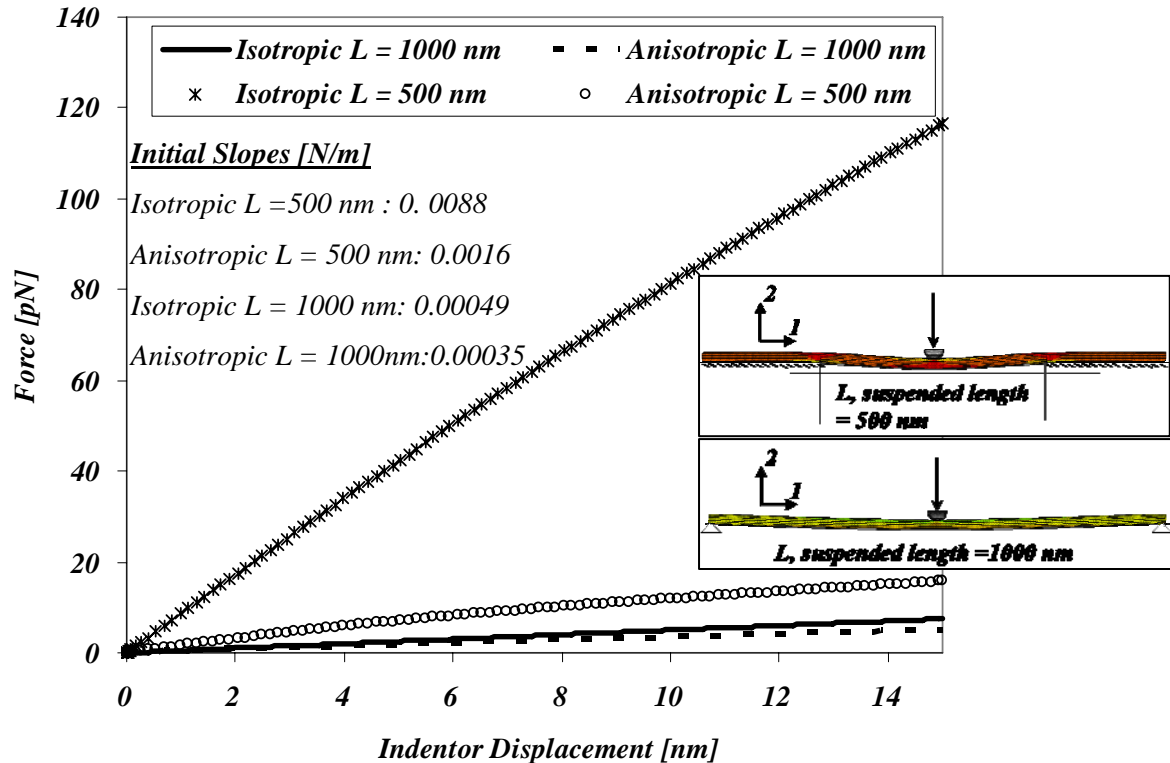


Figure 3-15 Force vs. displacement curves for the three-point bending simulation comparing the anisotropic responses and the isotropic responses for an effective modulus and thickness pair of $E_{11}^* = 2.4 \text{ GPa}$ and $t^* = 1 \text{ nm}$ with suspension lengths; $L = 500 \text{ nm}$ and $L = 1000 \text{ nm}$.

Figure 3-13 shows the displacement of the bottom node with respect to the applied indenter displacement. For the isotropic tube with a suspension length of 1000 nm , the bottom node displacement is exactly equal to the indenter displacement (15 nm). For the 500 nm suspension length for the isotropic tube, it is again almost 15 nm . This would imply that the tube ovalization effect is negligible for both of these cases. For the anisotropic tube, the longer suspension length, 1000 nm , gives a bottom node displacement of about 12 nm as well while the 500 nm suspension length still suffers from the flattening of the tube under the indenter and gives a vertical displacement of about 8 nm .

Figure 3-14 shows the contours of shear stress for the isotropic tube (A, B, E, F) and for the anisotropic tube (C, D, G, H). We can observe from the longitudinal stress contours

(S_{11}) in (B) and (D) that for a suspension length of 1000 nm , the stress profile is that of a tube bending event. This shows the transition from tube shear and ovalization to tube bending. Less tube shearing and higher longitudinal stresses are observed for the isotropic tube.

For the isotropic tube with a suspension length of 500 nm (E) there is a symmetric shear stress and ovalization at the indenter contact area while this effect vanishes for the 1000nm case (F). For the anisotropic tube; at a suspension length of 1000 nm there is almost no ovalization but highly directional shear stress on the surface area while we can observe more ovalization/tube flattening for the 500 nm suspension length (G). These results agree with the bottom node displacement conclusions (Figure 3-13). The presence of this ovalization/flattening in the anisotropic case and not in the isotropic case also reflects a strong wall shearing contribution to the flattening.

Figure 3-15 shows the force vs. indenter displacement curves for each of these cases. Force vs. indenter displacement results are very close to each other for a suspension length of 1000 nm for the isotropic and the anisotropic tubes as the long suspension length the deformation is driven by the longitudinal stiffness ($E_{11}^* = 2.4\text{GPa}$). On the other hand, for a suspension length of 500 nm , if we assumed that the ovalization is small enough to be neglected, then we can conclude that for the low shear stiffness ($G_{12}^* = 0.012\text{GPa}$); i.e. the sliding between the protofilaments contributes to both the wall flattening and to the shear effect in the beam bending, as opposed to being governed by the longitudinal stiffness ($E_{11}^* = 2.4\text{GPa}$), whereas for the 1000 nm suspension length case, the deformation is completely driven by the bending moment and the effect of the shear forces diminish.

The forces experienced for the long suspension lengths (i.e. 1000 nm) decrease (down to about $7\text{-}8\text{ pN}$ for the suspension length of 1000 nm). These forces haven't been able to be measured by experiments using three-point bending experiments (Kis et al., 2002; 2003) as they are very small forces.

Next, we will compare the responses for the suspension lengths we have shown for isotropic and anisotropic cases. Table 3-1 and Table 3-2 show the bending modulus, $E_{bending}$, for anisotropic and isotropic cases, respectively.

Table 3-1 The bending modulus and flexural rigidity values for different boundary conditions for the thin-shell discrete formulation of an individual microtubule of length $1\mu\text{m}$ for an effective modulus and thickness pair of $E_{11}^* = 2.4\text{GPa}$ and $t^* = 1\text{nm}$.

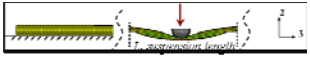
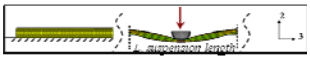
ANISOTROPIC THIN SHELL TUBE MODEL ($E^* = 2.4\text{GPa}$, $t^* = 1\text{nm}$)		
Suspension Length 	K_B ($E_{bending} I_{t=1\text{nm}}$) (Equation 54)	$E_{bending}$ $I = \frac{\pi}{4} \left[\left(R_{avg} + \frac{1}{2}t^* \right)^4 - \left(R_{avg} - \frac{1}{2}t^* \right)^4 \right]$
80 nm	$1.1 \times 10^{-26} \text{Nm}^2$	2.5 MPa
200 nm	$1.4 \times 10^{-25} \text{Nm}^2$	33 MPa
500 nm	$1 \times 10^{-24} \text{Nm}^2$	242 MPa
$1 \mu\text{m}^2$	$9.4 \times 10^{-24} \text{Nm}^2$	2.2 GPa

Table 3-2 The bending modulus and flexural rigidity values for different boundary conditions for the thin-shell discrete formulation of an individual microtubule of length $1\mu\text{m}$ for an effective modulus and thickness pair of $E_{11}^* = 2.4\text{GPa}$ and $t^* = 1\text{nm}$.

ISOTROPIC THIN SHELL TUBE MODEL ($E^* = 2.4\text{GPa}$, $t^* = 1\text{nm}$)		
Suspension Length 	K_B ($E_{bending} I_{t=1\text{nm}}$) (Equation 54)	$E_{bending}$ $I = \frac{\pi}{4} \left[\left(R_{avg} + \frac{1}{2}t^* \right)^4 - \left(R_{avg} - \frac{1}{2}t^* \right)^4 \right]$
80 nm	$2.1 \times 10^{-25} \text{Nm}^2$	48 MPa
200 nm	$1.8 \times 10^{-24} \text{Nm}^2$	420 MPa
500 nm	$5.7 \times 10^{-24} \text{Nm}^2$	1.3 GPa
$1 \mu\text{m}$	$10.5 \times 10^{-24} \text{Nm}^2$	2.4 GPa

² For the $1 \mu\text{m}$ suspension length, “pinned-pinned” boundary conditions are used utilizing the formula

$$\delta = \frac{PL^3}{48K_B} \text{ for the displacement of the indenter.}$$

The conflict in the bending modulus results reported in the literature is due to the length dependent behaviour of the microtubules during “bending” tests; where our simulation results find that some of the tests are not probing bending of the tube. The model proposed here shows that the bending modulus measured is dependent on the tube length: for longer microtubules, the bending modulus corresponds to the longitudinal elastic modulus as seen in the 1000 nm suspension length case ($E_{bending} = E_{11}^*$). For shorter deformation lengths, the mechanical response depends on the local tube wall bending/giving ovalization and flattening and also on tube shear contributions to displacement during bending.

The flexural rigidity, K_B , values are given in Table 3-1. For long microtubules ($1\mu\text{m}$), the flexural rigidity values are comparable to the ones that are found by Gittes et al. (1993) and Venier et al. (1994) by thermal fluctuation analysis and hydrodynamic flow respectively ($2.2 \times 10^{-23}\text{ Nm}^2$ and $1 \times 10^{-23}\text{ Nm}^2$, respectively).

Monoclinic Effect

Here, in this section we will investigate if there is an effect of the tension-shear coupling on the overall force versus displacement behaviour for the three-point bending.

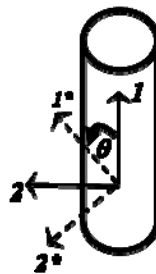


Figure 3-16 The sketch of the principal 1- and 2- direction of the microtubule and the transferred coordinate system as shown in Chapter 2.

In order to see any potential effect of the tension-shear coupling on the three-point bending in the axis system used, we will compare the effect of equating the tension-shear coupling components of this axis system (ν_{16} and ν_{26}) to zero. The axis system used (1-2) is shown again on Figure 3-16 where the transformation angle $\theta = 0^\circ$ (In Chapter 2 it was derived that the B lattice type microtubules were almost orthotropic

(with $\nu_{16} = \nu_{26} = 0.05$) at $\theta = 40^\circ$; interestingly, at $\theta = 40^\circ$, the shear modulus is the highest and at $\theta = 0^\circ$, the shear modulus is the lowest). The orthotropic material properties in the current axis system (1-2) are taken as: $E_{11}^* = 2.4GPa$, $E_{22}^* = 0.1GPa$, $G_{12}^* = 0.012GPa$, $\nu_{12} = 0.34$ for an effective thickness of $t^* = 1nm$.

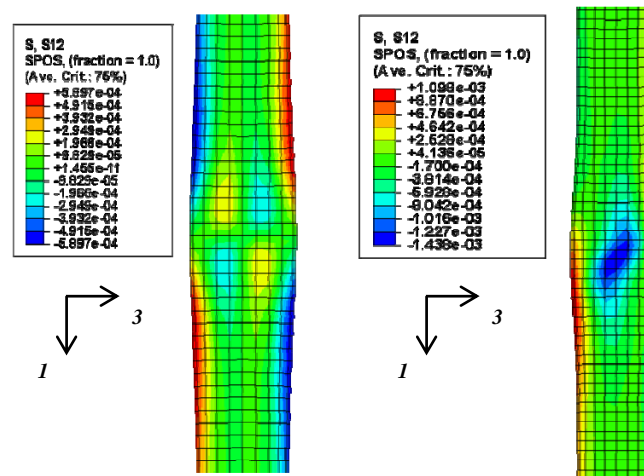
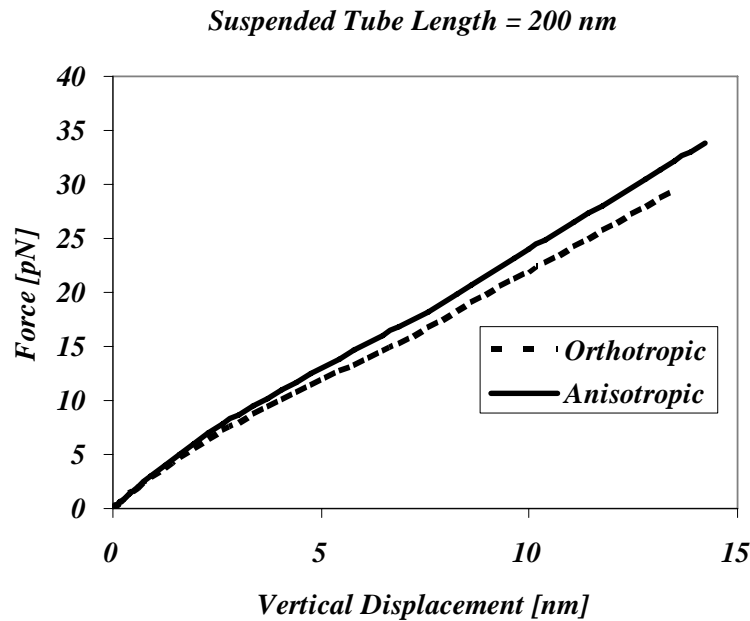


Figure 3-17 Force vs. displacement curve for the three-point bending results comparing an anisotropic and an orthotropic response for a microtubule suspension length of 200nm and an effective modulus and thickness pair of $E_{11}^* = 2.4GPa$ and $t^* = 1nm$.

Figure 3-17 shows force versus displacement behaviour for a suspension length of 200 nm for an orthotropic and a monoclinic material behaviour with an effective modulus and thickness pair of $E_{11}^* = 2.4GPa$ and $t^* = 1nm$. For the orthotropic material, ν_{16} and ν_{26} components are set to zero and the rest of the elastic properties are the same as in the monoclinic case ($E_{11}^* = 2.4GPa$, $E_{22}^* = 0.1GPa$, $G_{12}^* = 0.012GPa$, $\nu_{12} = 0.34$).

Recall that the 200 nm case is strongly influenced by ovalization and shear. The similarity in the orthotropic and actual anisotropic cases indicate that the shear effect of the anisotropic case is dominated by the low shear modulus, G_{12}^* , and not by the normal-shear coupling behaviour (ν_{16} and ν_{26}). The contour profiles of S_{12} show same similarities and same differences where the monoclinic anisotropic tube show a directional shear at the contact point with the indenter while the shear stress is symmetrical for the orthotropic tube.

Influence of Modulus, thickness pairing on Simulation Results

Here we will show the comparison of the response for different effective modulus and thickness pairs. These two different pairs we simulated are an effective modulus and thickness pair of $E_{11}^* = 1.2GPa$ and $t^* = 2nm$ and also an effective modulus and thickness pair of $E_{11}^* = 0.96GPa$ and $t^* = 2.5 nm$. The longitudinal modulus is derived by taking the tensile stiffness, K_A , to be constant and using: $E_{11}^* = K_A/t^*$. The lateral modulus is derived from the lateral stiffness K_L : $E_{22}^* = K_L/t^*$. The shear modulus is derived from the shear stiffness K_S : $G_{12}^* = K_S/t^*$. K_A , K_L and K_S were calculated in Chapter 2 to be 2.4, 0.1 and 0.012 N/m respectively. The effective material properties used are shown in Table 3-3.

Table 3-3 The effective microtubule properties for different mechanical thicknesses

	$t^* = 1nm$	$t^* = 2.0nm$	$t^* = 2.5nm$
E_{11}^* [GPa]	2.40	1.20	0.96
E_{22}^* [GPa]	0.10	0.05	0.04
G_{12}^* [GPa]	0.012	0.006	0.0048

We start our analysis by firstly checking the bottom node displacement (Figure 3-18) in order to detect the extent to which the tube flattens under the applied indenter displacement for a suspension length of 80 nm and 200 nm for different “ E^* , t^* ” pairs. Figure 3-18 displays that for thicker shells, the amount of tube flattening is much less (eg. for a suspension length of 200 nm, and a thickness of 2.5 nm, the bottom node displaces 9 nm with an indenter displacement of 15nm; while this displacement is about 5 nm for a thickness of 1nm). The reduced flattening with increased t^* is a direct result of the increased wall bending stiffness (where wall bending stiffness increases with t^{*3}).

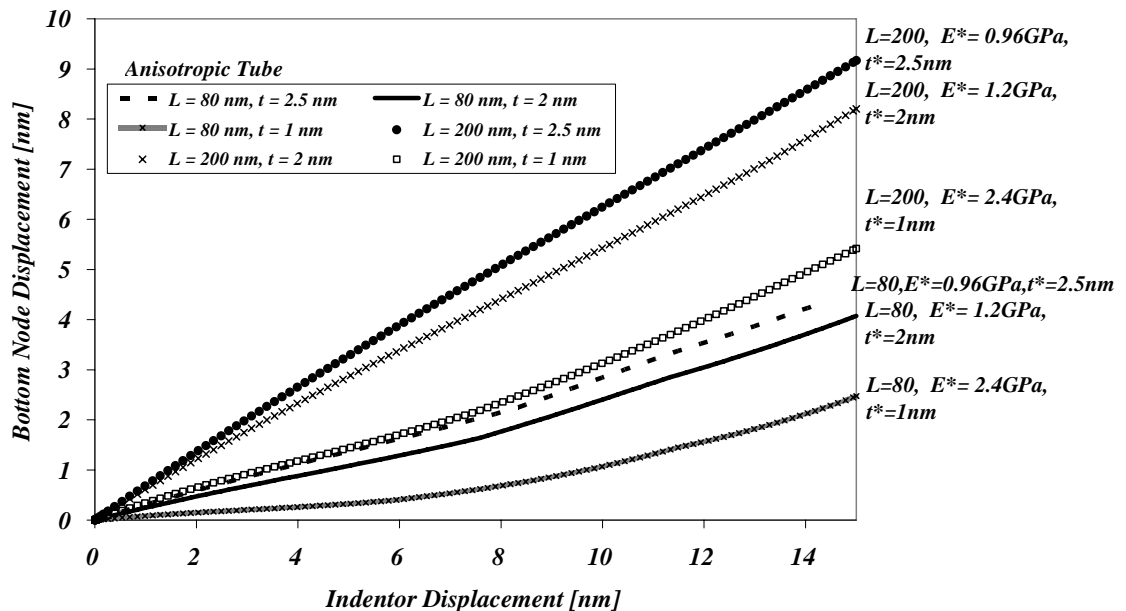


Figure 3-18 Force vs. displacement curve for an effective modulus and thickness pair of $E_{11}^* = 2.4GPa$ and $t^* = 1 nm$, an effective modulus and thickness pair of $E_{11}^* = 1.2GPa$ and $t^* = 2nm$ also an effective modulus and thickness pair of $E_{11}^* = 0.96GPa$ and $t^* = 2.5 nm$. The simulations given are for suspension lengths of 80 nm and 200 nm.

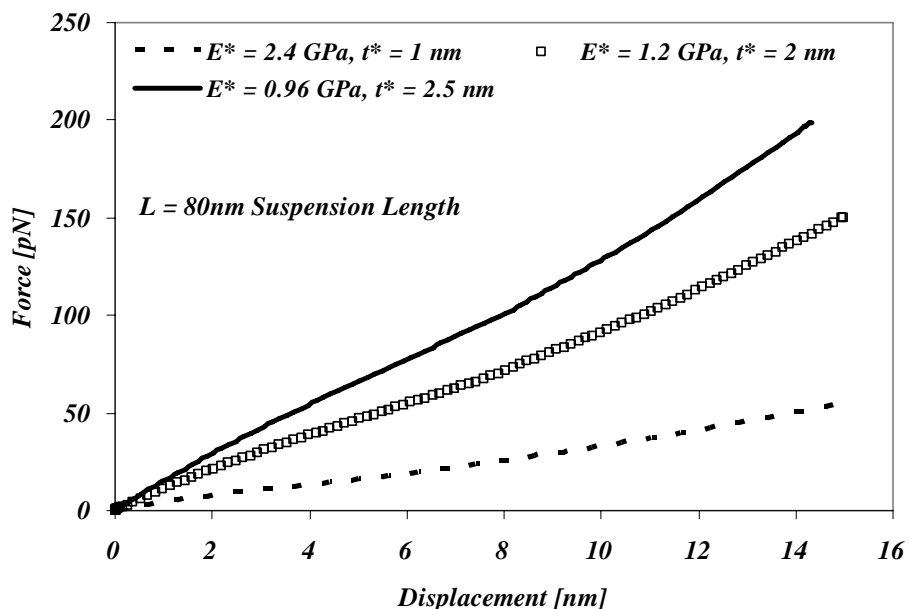


Figure 3-19 Force vs. displacement curves for an effective modulus and thickness pair of $E_{11}^* = 2.4\text{GPa}$ and $t^* = 1\text{ nm}$, an effective modulus and thickness pair of $E_{11}^* = 1.2\text{GPa}$ and $t^* = 2\text{nm}$ also an effective modulus and thickness pair of $E_{11}^* = 0.96\text{GPa}$ and $t^* = 2.5\text{ nm}$. The simulations given are for a suspension length of 80 nm.

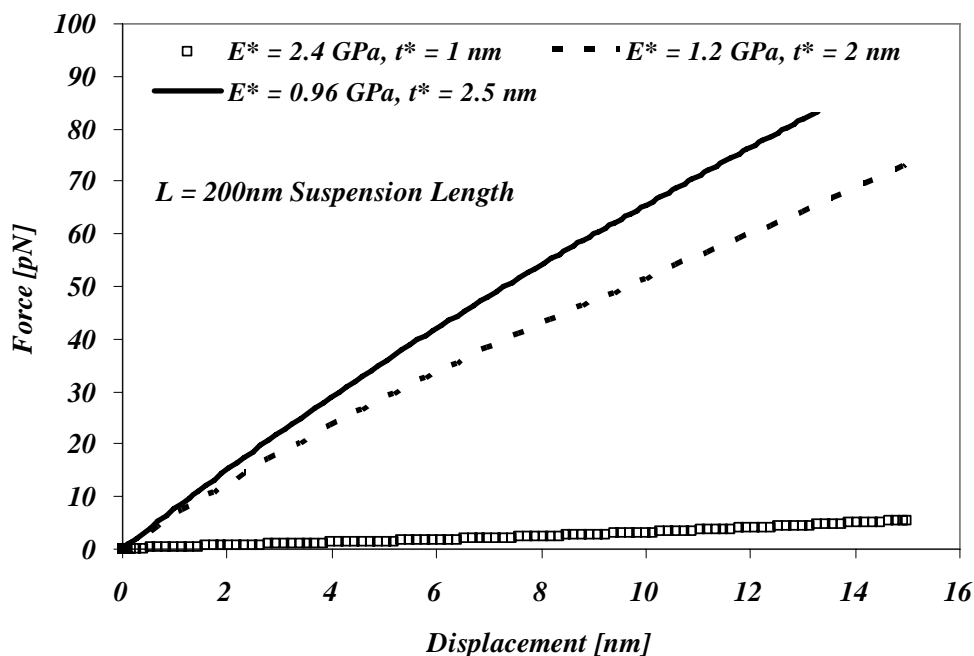


Figure 3-20 Force vs. displacement curves for the three-point simulations for an effective modulus and thickness pair of $E_{11}^* = 2.4\text{GPa}$ and $t^* = 1\text{ nm}$, an effective modulus and thickness pair of $E_{11}^* = 1.2\text{GPa}$ and $t^* = 2\text{nm}$ also an effective modulus and thickness pair of $E_{11}^* = 0.96\text{GPa}$ and $t^* = 2.5\text{ nm}$. The simulations given are for a suspension length of 200 nm.

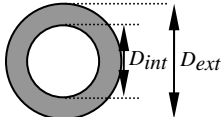
Figure 3-19 and Figure 3-20 show the force versus indenter displacement results for different “ E^* , t^* ” pairs for a suspension length of $L = 80 \text{ nm}$ and $L = 200 \text{ nm}$, respectively.

Here we have shown that for different E^* , t^* pairs for the anisotropic wall, the bottom node displacement is still different than the indenter displacement even when the thickness is increased and, indeed, the different thickness cases are similar to one another. This suggests that the wall flattening and tube ovalization for the anisotropic case is more dominated by wall shear in the wall locally beneath and near the indenter rather than wall bending. The tube flattening/tube wall shear and tube shear are the dominant contributions to the indenter displacement for the short anisotropic tubes and it is a result of the low shear modulus giving wall shear in the indent region and in the complete tube.

Comparison with the Experimental Results

In this section, we will further compare our results with the experimental results given in the literature.

Table 3-4 The bending modulus and flexural rigidity values obtained by Kis et al. (2002; 2003) using AFM three-point bending experiments.

AFM Three Point Bending Results			
Kis et al. (2002; 2003)			
Suspension Length	$K_B(E_{bending} I)$	$I = \frac{\pi}{64} [D_{ext}^4 - D_{int}^4]$	$E_{bending}$
80 nm	$5.0 \times 10^{-26} \text{ Nm}^2$	$1.67 \times 10^{-32} \text{ m}^4$	3 MPa
200 nm	$6.7 \times 10^{-25} \text{ Nm}^2$	$1.67 \times 10^{-32} \text{ m}^4$	40 MPa

As shown earlier, in the Kis et al., (2002; 2003) work, microtubules were deposited on APTES-functionalized alumina membranes, they were strongly crosslinked with 0.5 % of glutaraldehyde and imaged under varying suspension lengths. The researchers, using equation (54), calculated the flexural rigidity of the microtubules with different suspension lengths. For the geometry of the microtubules, they assumed a hollow cylinder with an external diameter of 25 nm and an internal diameter of 15 nm as mentioned before. Some of the results of Kis et al.'s work are given in Table 3-4.

For a suspension length about 80 nm, they reported a flexural rigidity of $K_{B80nm} = 5 \times 10^{-26} \text{ Nm}^2$ and for a suspension length of 200 nm, they reported a flexural rigidity $K_{B200nm} = 6.7 \times 10^{-25} \text{ Nm}^2$. The equation: $K_B = E_{bending} I$ and the second moment of area for a hollow cylinder revealed bending moduli of 3 MPa and 40 MPa for respective cases (Figure 3-6).

We have shown earlier that our simulation results are in good agreement (2.5 MPa and 33 MPa) when we reduce our results in the same way as they reduced their results, although we concluded earlier that equation (54) does not provide an accurate estimate for the three-point bending of microtubules. Table 3-5 shows a comparison between the flexural

rigidity values obtained from the experimental work and the model proposed for different thickness values for suspension lengths of 80 nm and 200 nm.

Table 3-5 The bending modulus and flexural rigidity values obtained by Kis et al. (2002; 2003) compared to the simulations carried out for different microtubule thickness values.

Comparison			
Three Point Bending,		Suspension Length = 80 nm (grey cells)and 200nm	
	$K_B(E_{bending} I)$	$I = \frac{\pi}{4} \left[\left(R_{avg} + \frac{1}{2} t^* \right)^4 - \left(R_{avg} - \frac{1}{2} t^* \right)^4 \right]$	$E_{bending}$
Experimental Kis et al. (2002; 2003) $R_{avg} = 10nm$, $t^* = 5nm$	$5 \times 10^{-26} \text{ Nm}^2$	$1.67 \times 10^{-32} \text{ m}^4$	3 MPa
	$6.7 \times 10^{-25} \text{ Nm}^2$	$1.67 \times 10^{-32} \text{ m}^4$	40 MPa
Simulation $R_{avg} = 11.14nm$ $t^* = 1nm$	$1.1 \times 10^{-26} \text{ Nm}^2$	$0.44 \times 10^{-32} \text{ m}^4$	2.5 MPa
	$1.4 \times 10^{-25} \text{ Nm}^2$	$0.44 \times 10^{-32} \text{ m}^4$	32 MPa
Simulation $R_{avg} = 11.14nm$ $t^* = 2nm$	$3 \times 10^{-26} \text{ Nm}^2$	$0.88 \times 10^{-32} \text{ m}^4$	3.4 MPa
	$2.6 \times 10^{-25} \text{ Nm}^2$	$0.88 \times 10^{-32} \text{ m}^4$	30 MPa
Simulation $R_{avg} = 11.14nm$ $t^* = 2.5nm$	$4.1 \times 10^{-26} \text{ Nm}^2$	$1.1 \times 10^{-32} \text{ m}^4$	3.7 MPa
	$3.1 \times 10^{-25} \text{ Nm}^2$	$1.1 \times 10^{-32} \text{ m}^4$	28 MPa

The experimental bending modulus values to be directly comparable to the simulation results, have to imply an assumption of an equivalent geometry. Kis et al. did not directly measure the diameter and the thickness of the microtubules they have worked with although the geometry of the microtubules alters the results significantly. Kis et al., as mentioned before, assumed a geometry of a hollow cylinder with an external diameter of 25 nm and an internal diameter of 15 nm as opposed to an average radius of 11.14nm

(derived from a circumferential separation of protofilaments of 5nm as explained earlier) with a thin bridge thickness varying from 1nm to 2.5nm (Chretien and Wade, 1991). It would be significant to take the assumed geometry of Kis et al. and back out the actual experimental results (force vs. indenter displacement) they obtained and to compare them with our results for different E^* , t^* pairs.

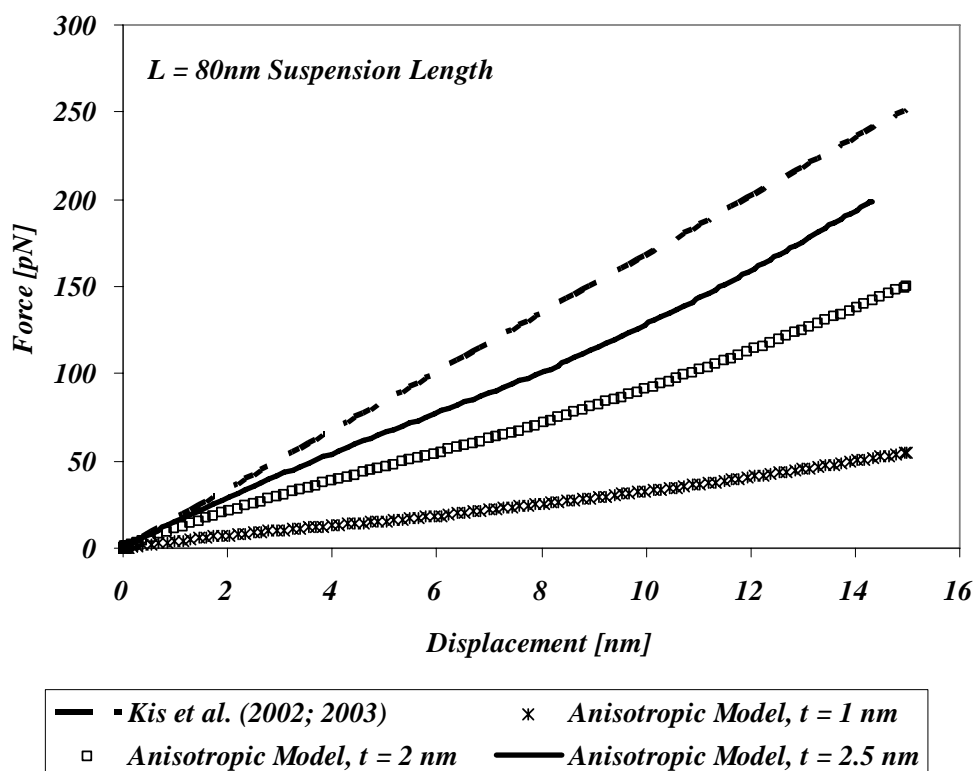


Figure 3-21 Force vs. displacement curve for the three point simulations for an effective modulus and thickness pair of and $t^*= 1\text{ nm}$, an effective modulus and thickness pair of and $t^*=2\text{nm}$ also an effective modulus and thickness pair of and $t^*=2.5\text{ nm}$. The simulations given are for a suspension length of 80 nm .

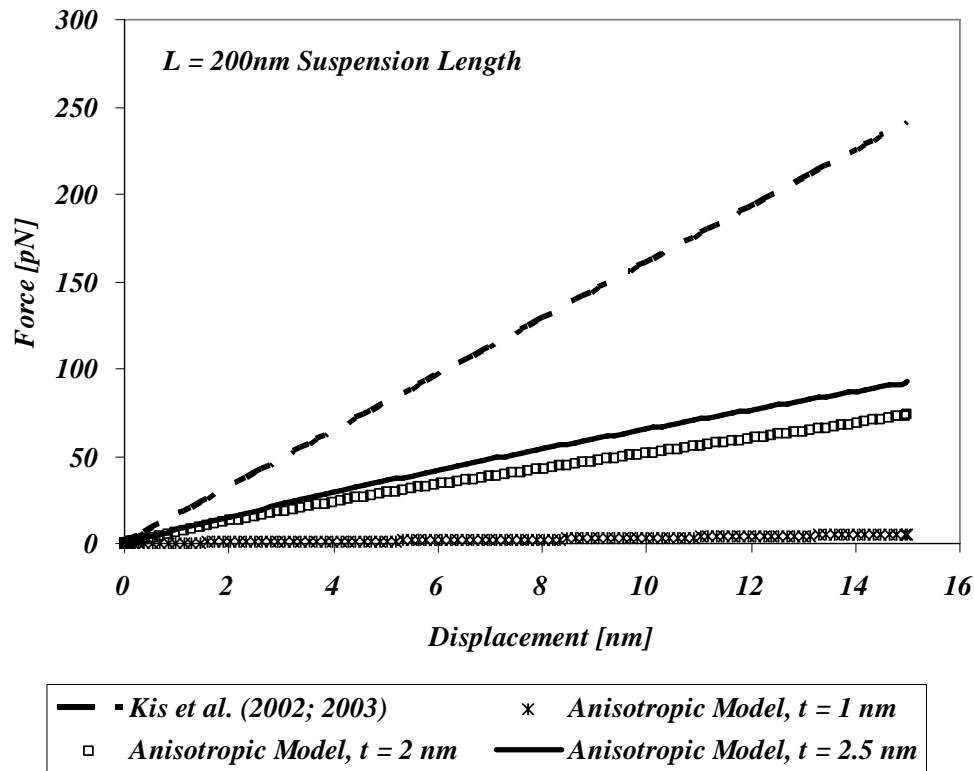


Figure 3-22 Force vs. displacement curve for the three point simulations for an effective modulus and thickness pair of $E_{11}^* = 2.4\text{GPa}$ and $t^* = 1\text{ nm}$, an effective modulus and thickness pair of $E_{11}^* = 1.2\text{GPa}$ and $t^* = 2\text{nm}$ also an effective modulus and thickness pair of $E_{11}^* = 0.96\text{GPa}$ and $t^* = 2.5\text{ nm}$. The simulations given are for a suspension length of 200 nm.

Figure 3-21 shows the force vs. indenter displacement results different “ E^* , t^* ” pairs and a linear Kis et al. (2002; 2003) data for a suspension length of $L = 80\text{ nm}$. For an effective modulus and thickness pair of $E_{11}^* = 0.96\text{GPa}$ and $t^* = 2.5\text{ nm}$ and an effective modulus and thickness pair of $E_{11}^* = 1.2\text{GPa}$ and $t^* = 2\text{nm}$ we get the same initial linear slope for the force displacement results as Kis et al. However, for a suspension length of $L = 200\text{ nm}$, our force vs. displacement slopes (Figure 3-22) are lower than Kis et al. data.

The discrepancy between the simulation results and the experimental results could be due to several reasons. Firstly, Kis et al. assumed thicker tubes (with a thickness of 5 nm) which is not a reasonable assumption. Secondly, as mentioned before, the discrepancy between the simulation results and Kis et al. results could be due to the effect of the stabilizing agent altering the mechanical response observed in the experiments. The result for a “pure microtubule” would be different. The chemical crosslinking has been reported to be necessary for stabilizing the microtubules for the contact operation mode of AFM (Vinckier et al., 1996) as the microtubules are too fragile; i.e. they collapse under high loads. However, we have to note here that the cross-linking process would result in different material properties for the microtubules as their geometry and the bond strengths will be altered. In fact, from Vinckier et al. (1996) results, Kis (2003) predicted a factor of “2” for the stiffening of the microtubules with glutaraldehyde. Here the comparison of the indentation work with the low suspension lengths of Kis et al. is a valid comparison as the Kis et al. experiments almost resemble indentation experiments with significant tube flattening/ovalization.

Vinckier et al. (1996) is reported to be the only systematic study of glutaraldehyde on the mechanical properties of microtubules and will be referred to later in the next section where radial indentation will be studied. Here since we are modeling the pure microtubule, it would be reasonable to observe a discrepancy between Kis et al. (2002) force-displacement results and ours (ours will give a more compliant response).

Figure 3-23 shows the force versus displacement data plotted again taking into account the stiffening factor due to the stabilizing agent ($\times 2$). Table 3-6 shows the modified Kis et al. results. The modified results, as expected, give a closer match to our simulation results (Table 3-5 and Table 3-6), especially for the effective pair of $E^* = 1.2\text{ GPa}$ and $t^* = 2\text{ nm}$.

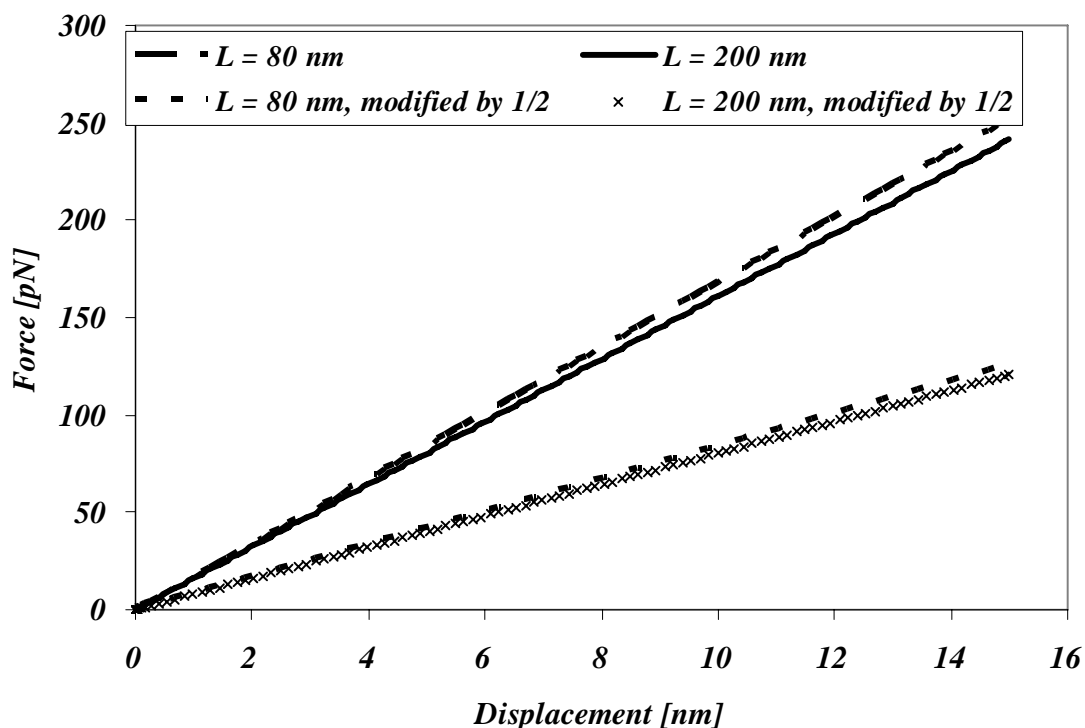


Figure 3-23 Force vs. displacement curves reduced from the results of the three-point bending experiments of Kis et al. (2002; 2003) for suspension lengths of 83 nm and 200 nm including the results modified by a factor of “1/2”.

Table 3-6 The bending modulus and flexural rigidity values of Kis et al. (2002; 2003) modified by a factor of “1/2” to mimic the effect of a pure microtubule.

AFM Three Point Bending Results		Kis et al. (2002; 2003)
Suspension Length		$K_B(E_{bending} I)$
80 nm		$2.5 \times 10^{-26} \text{ Nm}^2$
200 nm		$3.4 \times 10^{-25} \text{ Nm}^2$

There is an ongoing debate over the thickness of microtubules. Microtubules have two physical thicknesses, one corresponds to the thickness of a monomer ($\sim 5 \text{ nm}$) and the other is the bridge thickness or the thickness of the lateral contacts (Figure 3-24), which is a source of debate in the field. If we observe the current work of Chretien (Figure 3-24), the bridge thickness is observed to be 2- 2.5 nm. Furthermore, there are different interactions which govern mechanical behaviours of stretching and bending which give

an effective mechanical thickness, t^* , which is not necessarily equal to any physical thickness measurement. This raises another question. If one takes a physical measure of thickness as the mechanical thickness of the microtubules, then the energy for bending a single dimer into a curved configuration (as discussed earlier in the beginning of this chapter) would have to be higher than $2.5 k_B \theta$ (the VanBuren (2002) data from where we calculated our initial effective properties) in order to meet the Kis et al. (2002; 2003) bending data.

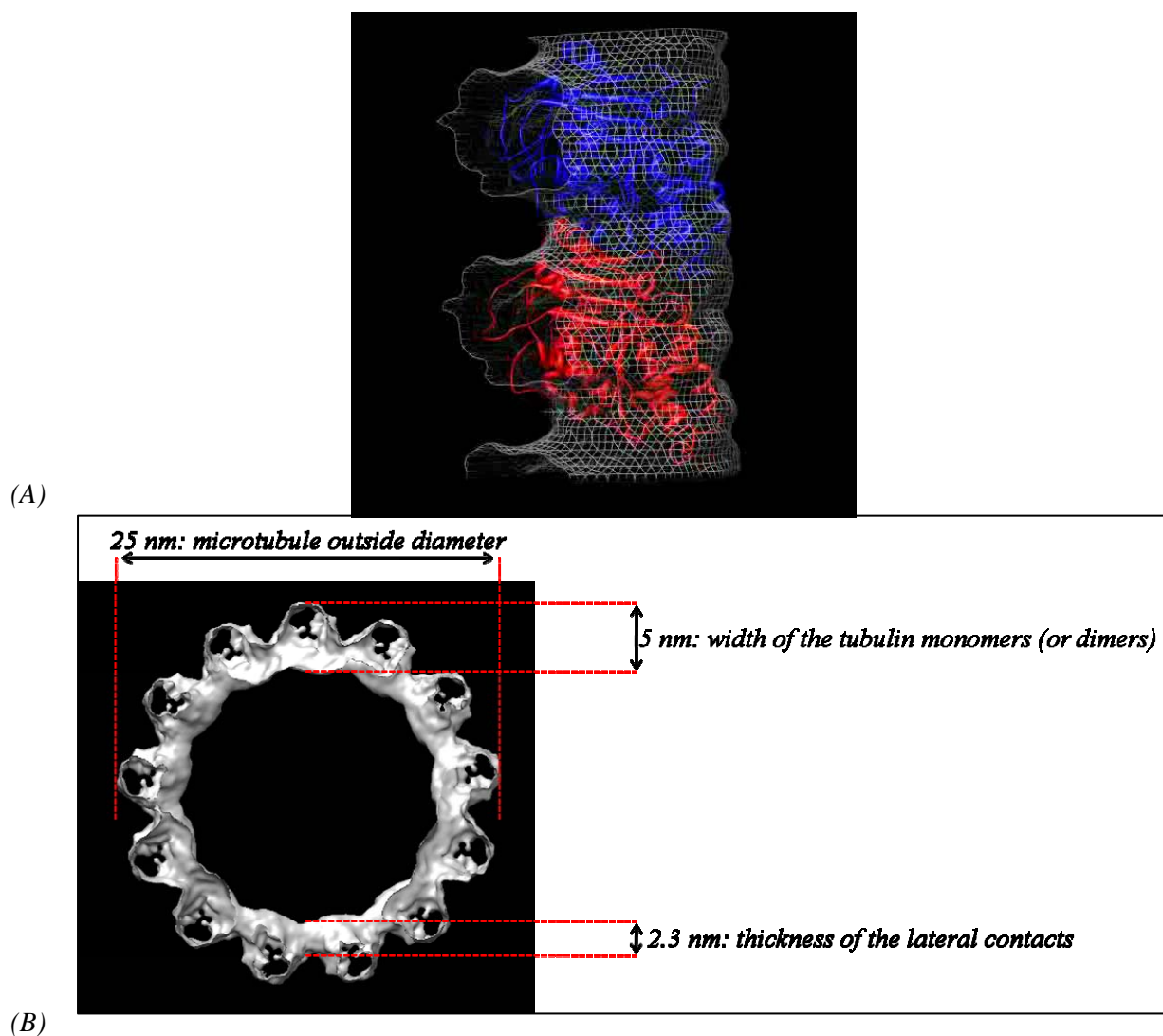


Figure 3-24 (A) Side view of a dimer and a (B) top view of a 13 protofilament created using cryo electron microscope images (courtesy of Dr. Denis Chretien) showing the thickness and the external diameter of the microtubule

3.3.2. Radial Indentation

The first measurements of microtubule stiffness using atomic force microscopy were made by Vinckier et al. (1995). In order to study the elasticity of microtubules, the researchers indented microtubules in the radial direction using the contact mode of AFM (in liquid).

Microtubules are too fragile to withstand the interaction with the AFM tip during a contact type radial indentation experiment, thus they had to be strongly crosslinked with glutaraldehyde. The glutaraldehyde concentration was altered in each set of experiments to measure the effect of the agent in the force-displacement curves (Figure 3-25) giving parabolic curves which depicted an indentation limit for each sample as well as a glutaraldehyde dependence on the initial slope. From the results of altering the glutaraldehyde concentration, the researchers predicted the response of the pure microtubules.

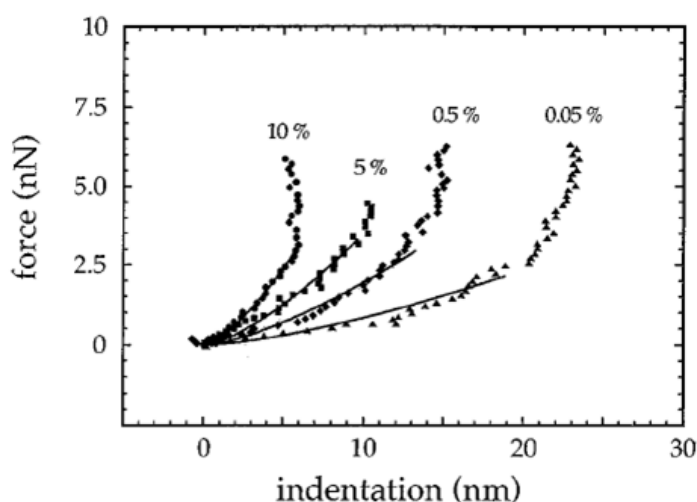


Figure 3-25 Experimental force versus vertical displacement (indentation depth) curves obtained by Vinckier et al. (1996), nonlinear curves depicting Hertz approximations.

Vinckier et al. fitted the curves with the Hertz formula for indentation into an elastic solid;

$$F = \frac{4\sqrt{RE}}{3(1-\nu^2)} d^{1.5} \quad (59)$$

Here, E is the elastic modulus, ν is the Poisson ratio and R is the indenter radius ($R = 50 \pm 20nm$), and d is the indentation depth. Extrapolating from the curves created from the indentation experiments, the researchers approximated a pure tubulin case to derive the microtubule elastic properties. They obtained an elastic modulus ranging from *1 MPa to 12 MPa*.

It should be noted here, that the Hertz model approximates the sample as linear elastic isotropic solid occupying an infinitely extending half space. If these conditions are met, then the elastic modulus of the sample can be fitted or calculated using the Hertz model. However, the tubes are not solid but instead are essentially hollow cylindrical structures where the indentation results in wall bending, buckling and shearing (much like what we found for the case of three-point “bending” of the 80 nm suspension length). Therefore, the Hertz model does not provide a good approximation for fitting the indentation curves for the microtubule indentation experiments.

Later work by de Pablo et al. (2003) have also employed atomic force microscopy to measure the radial indentation deformation of microtubules, and found the radial indentation force response of the microtubules to be linearly proportional to the applied displacement (Figure 3-26, A). In the de Pablo et al. work, the taxol stabilized microtubules were deposited on a glass surface that was coated with aminopropyltriethoxysilane to promote their adhesion and they were imaged using AFM operated in “jumping mode”. Jumping mode was introduced as a new scanning probe microscopy mode (de Pablo et al., 1998) which allowed the simultaneous measurement of topography and physical properties. An important feature of this mode (Moreno et al., 2000) is that the sample is moved laterally with respect to the tip while the tip (with a radius $20nm$) and sample are out of contact, minimizing the shear forces. As the shear forces are believed to be the main cause of damage in indentation experiments, this operating mode helps avoid any potential damage.

The force-distance curves measured were recorded in the linear or elastic mode before the microtubules locally collapsed. The authors reported that the microtubules behaved linearly up to an indentation of 4 nm. To explain the nano indentation behaviour of microtubules, the microtubules were then considered thin walled pipes under a diametrical point load. According to thin shell theory (Niordson, *Shell Theory*, 1985), the vertical displacement is given as:

$$k^* = \frac{P}{\delta} = C \frac{E_{indent} t^{5/2}}{R^{3/2}} \quad (60)$$

Here, E_{indent} is the elastic modulus, k^* is the tube effective spring stiffness and C is a prefactor. The researchers (de Pablo et al., 2003) used a prefactor of 1.18 to fit their experimental results. The researchers (de Pablo et al., 2003; Schaap et al., 2006) described the elastic response by using isotropic cylindrical shells with diameters of 20 nm, a Young's modulus of 0.8 GPa and an "effective thickness" of 1.6 nm.

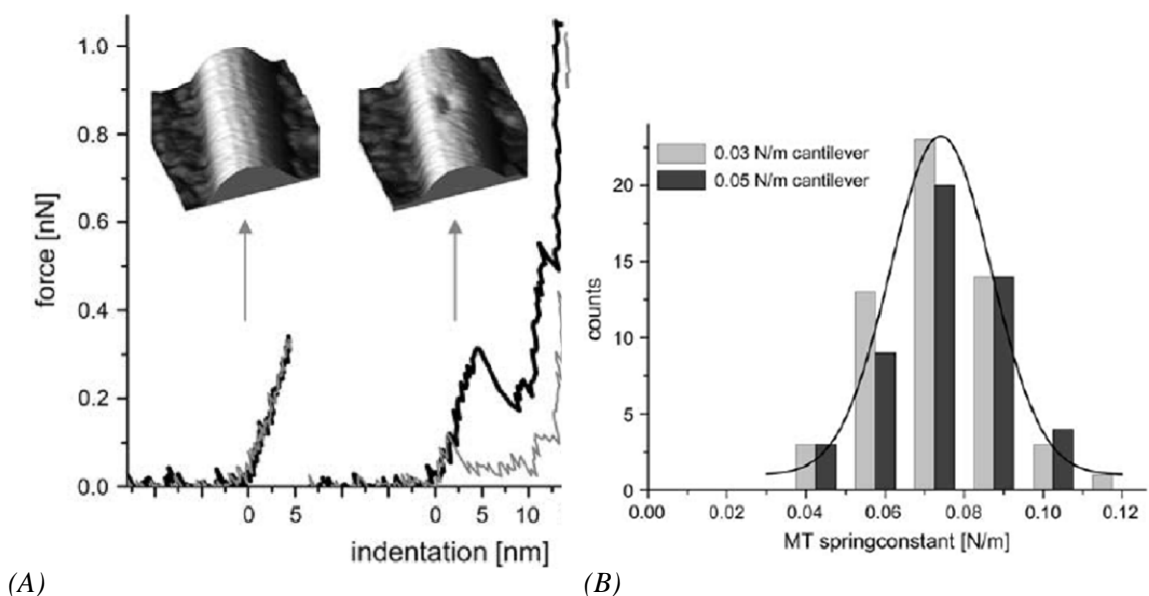


Figure 3-26 (A) de Pablo et al. (2003) experiments show that microtubule indentation is linear and reversible for forces up to 300 pN. (B) Schaap et al. (2006) show that for 2 different types of cantilever stiffnesses the microtubule stiffness averages to give a mean of 0.074 N/m.

We note that the de Pablo et al. modulus, thickness pair of 0.8 GPa and 1.6 nm giving an axial stiffness of $K_A = Et = 1.28 \text{ N/m}$ does not result in the reported axial stiffness of 2.4 N/m that we have used in determining our effective properties; also, this pair produces an effective bending stiffness $E^* t^{*3}$ of 3.28 nN.nm compared to our 2.4 nN.nm . Also note that the researchers assumed isotropy of the wall and we have found the compliant shear behaviour of anisotropic tube to be important.

The aim of the next section is to simulate the radial indentation experiments using finite element analysis and the material properties derived in Chapter 2 also accounting for the effective thickness.

3.3.2.1. FEM: Loading and Boundary Conditions

In the anisotropic tube simulation, a spherical indenter of 20 nm radius is used to indent B Lattice type (14_4) microtubules.

- The material properties for the anisotropic material and effective thickness of the “thin shell analysis” are chosen to be $\sim 1.0, 1.5, 2.0$ and 2.5 nm with corresponding effective longitudinal moduli: $2.4, 1.6, 1.2$ and 0.96 GPa , respectively. The corresponding effective shear moduli are: $0.012, 0.008, 0.006, 0.0048 \text{ GPa}$, respectively.
- The average radius of the B Lattice microtubules is 11.14 nm .
- The microtubule is placed on a rigid plate.
- The indenter is given a vertical displacement of 4 nm .

Finite element analysis is performed using the software ABAQUS. The model consists of 6420 nodes and 6400 shell elements (S4R).

3.3.2.2. Results

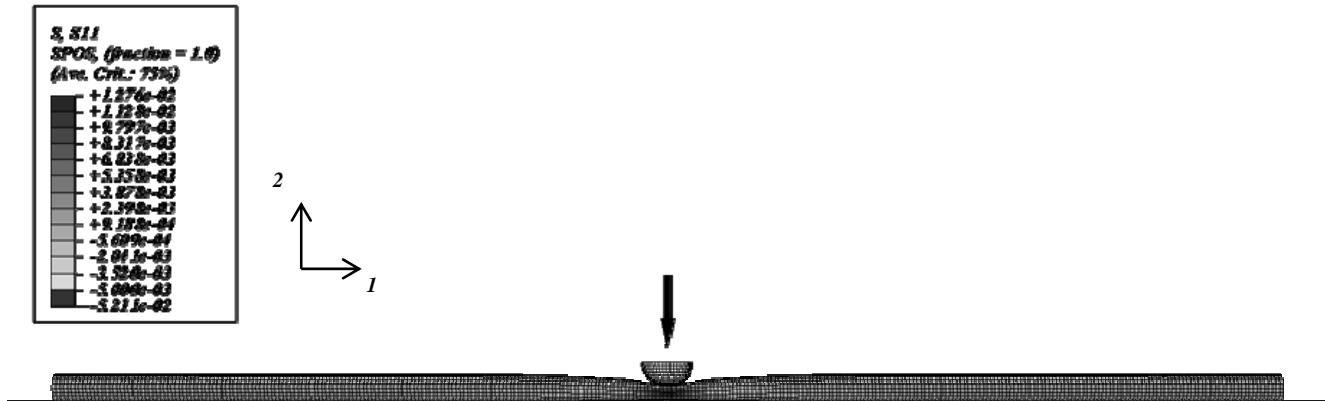


Figure 3-27 The indentation experiment is simulated in the finite element medium. The example shown is the indentation of a 11.14 nm radius tube with anisotropic properties and for effective modulus and thickness pair of $E_{11}^* = 2.4 \text{ GPa}$ and $t^* = 1.0 \text{ nm}$.

In order to compare and investigate the validity of equation (60), we will investigate both isotropic and anisotropic tubes. For two different effective modulus-thickness pair (2.4 GPa and 1 nm and also 1.6 GPa and 1.5 nm) the force vs. displacement curves are plotted as shown in Figure 3-28 up to an indentation depth of 4 nm.

For an effective thickness of 1 nm, the effective longitudinal modulus is

$$E_{11}^* = \frac{K_A}{t^*} = 2.4 \text{ N/m}$$

and for an effective thickness of 1.5 nm, the effective longitudinal modulus is $E_{11}^* = \frac{K_A}{t^*} = 1.6 \text{ GPa}$, noting that the tensile stiffness of microtubules was

calculated to be $K_A = 2.4 \text{ N/m}$ in Chapter 2.

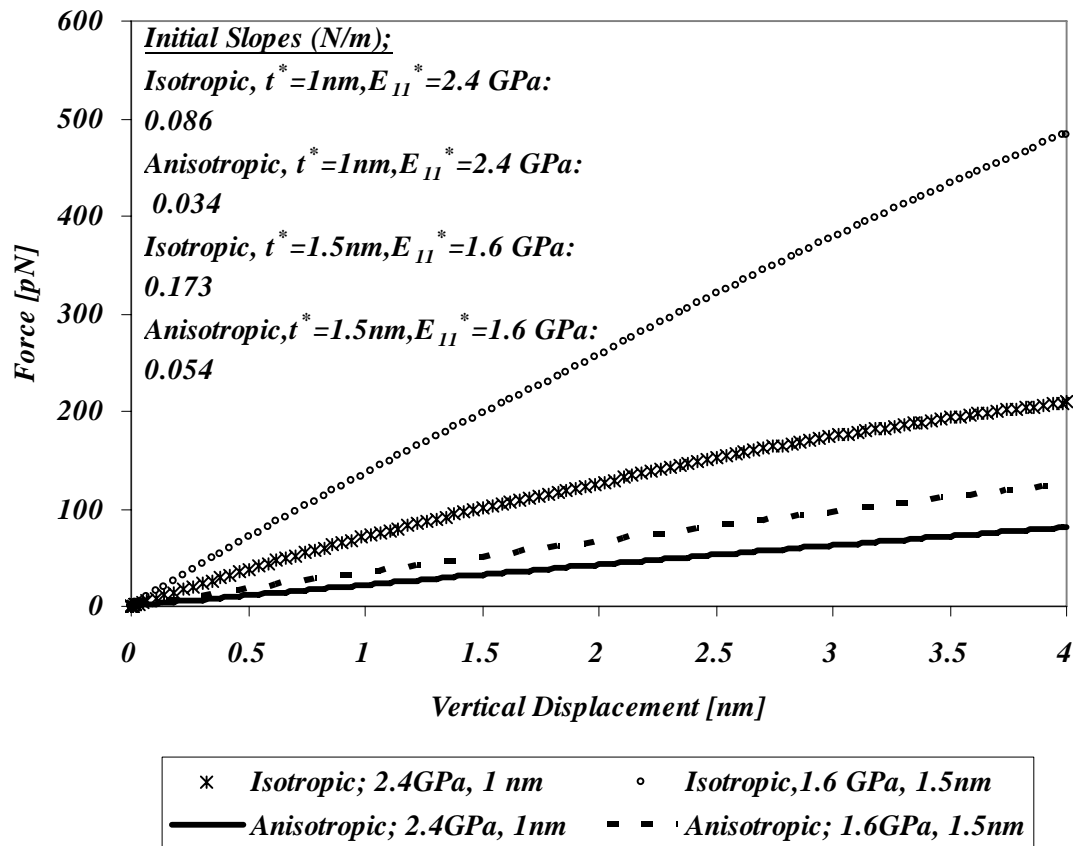


Figure 3-28 Force versus displacement for the radial indentation for an isotropic and an anisotropic tube for two different effective pairs: for an effective modulus and thickness pair of $E_{11}^* = 2.4\text{GPa}$ and $t^* = 1.0\text{ nm}$, also an effective modulus and thickness pair of $E_{11}^* = 1.6\text{GPa}$ and $t^* = 1.5\text{ nm}$.

It is observed from Figure 3-28 that as the mechanical thickness of the tube is increased, the stiffer the indentation response (P/δ ratio) becomes as expected since the tube wall bending stiffness increases with t^3 and with E ; the cubic dependence on thickness therefore overwhelms the linear dependence on E . For isotropic tubes, for the same effective thickness and vertical displacement, the force response is higher. This is due to the compliant shear in the anisotropic tube strongly contributing to the displacement and thus giving a much more compliant indentation behaviour.

In order to examine the validity of equation (60), the modulus corresponding to indentation is calculated for each case:

$$E_{indent} = \left(\frac{P}{\delta} \right)_{slope} \frac{R^{3/2}}{Ct^{5/2}} \quad (61)$$

For an isotropic tube with a radius of $R = 11.14 \text{ nm}$ and an effective stiffness of $E_{11}^* = 2.4 \text{ GPa}$ and an effective thickness of 1 nm using the slope (P/δ) of 0.086 N/m (Figure 3-28) and a prefactor of $C = 1.33$, the indentation modulus, E_{indent} is calculated to be 2.4 GPa . For the second case of the isotropic tube with an effective stiffness of $E_{11}^* = 1.6 \text{ GPa}$ and an effective thickness of 1.5 nm , using equation (61) and the same prefactor, the indentation modulus comes out to be equal to the longitudinal modulus ($E_{indent} = E_{11}^* = 1.6 \text{ GPa}$). It is demonstrated here that for isotropic tubes, the indentation modulus is shown to be equal to the longitudinal modulus as expected. This shows the validity of equation (60) for the isotropic tube.

Next, we will demonstrate the responses for anisotropic tubes with different effective properties and we will calculate the indentation modulus for each case using equation (61) even though we do not expect equation (61) to be valid for the anisotropic cases due to the compliant shear response.

Figure 3-29 shows the anisotropic tube force vs. displacement curves for different effective modulus, thickness pairs. It is observed from here that as the mechanical thickness of the tube is increased, the stiffer the indentation response (P/δ ratio) becomes due to the scaling of the tube wall bending contribution via t^3 . The responses obtained from the experiments had given a range of $0.03 \text{ N/m} < P/\delta < 0.12 \text{ N/m}$ (Figure 3-26, B) which is what we have obtained in the simulations for the different effective E_{11}^* , t^* pairs; $0.034 < P/\delta < 0.094 \text{ N/m}$ (where $E_{11}^* = 2.4 \text{ GPa}$, $t^* = 1 \text{ nm}$ gives 0.034) for the effective properties assigned in this section (Table 3-7).

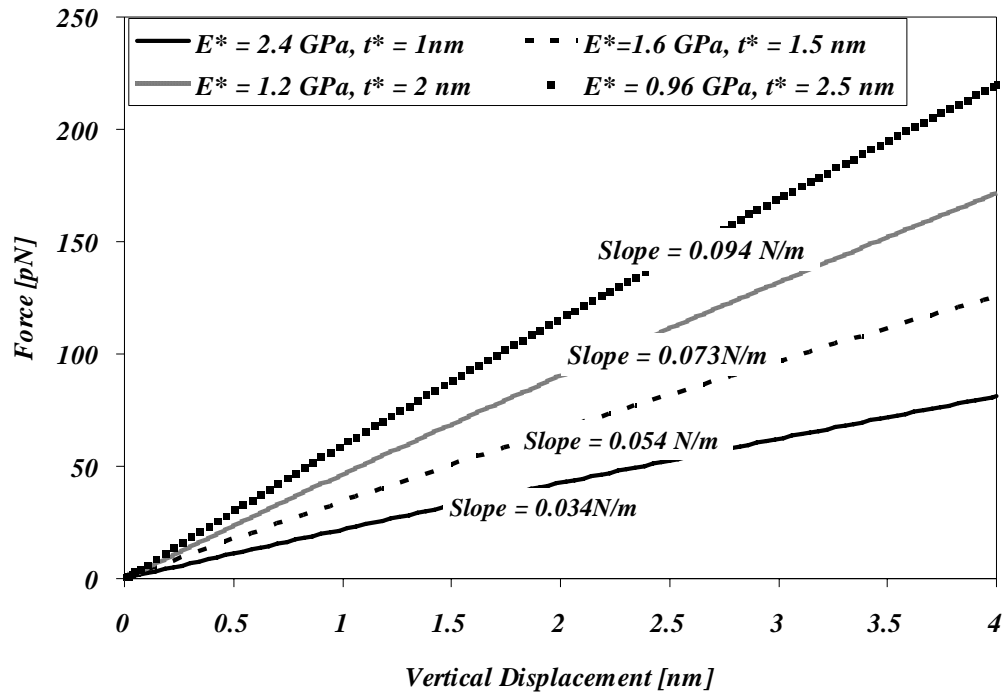
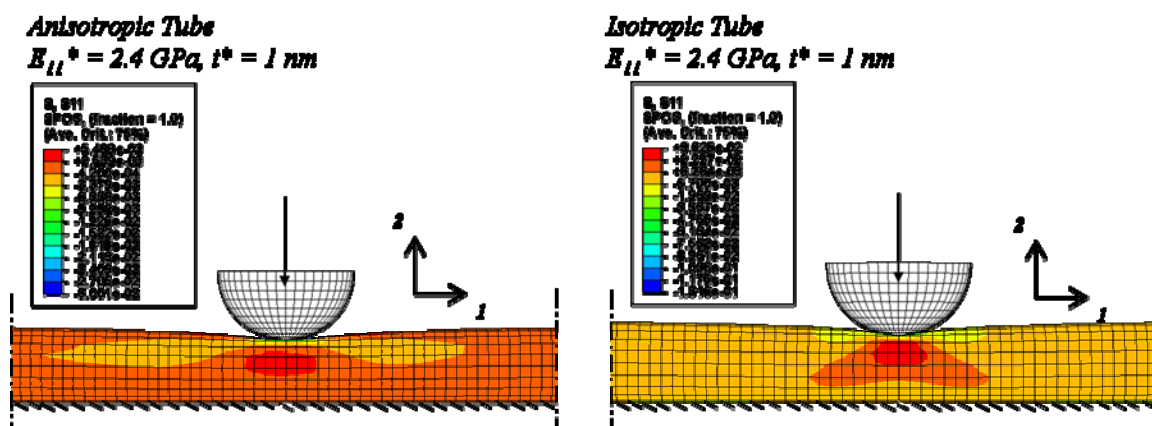


Figure 3-29 Force versus displacement plots for the radial indentation of anisotropic tubes with different set of effective properties. Here E^* is the effective longitudinal modulus and t^* is the effective mechanical thickness.

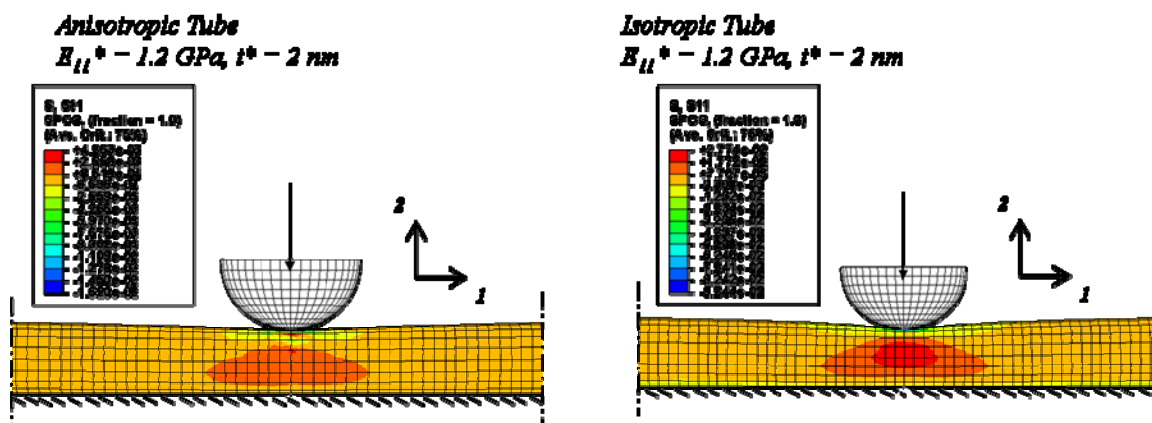
Table 3-7 The effective microtubule properties for different effective “E, t” pairs.

Anisotropic Tube	$t^* = 1\text{nm}$	$t^* = 1.5\text{nm}$	$t^* = 2.0\text{nm}$	$t^* = 2.5\text{nm}$
$K_A = E_{11}^* t^* \left[\frac{\text{N}}{\text{m}} \right]$	2.4	2.4	2.4	2.4
$E_{11}^* \text{ [GPa]}$	2.4	1.6	1.2	0.96
$E_{11}^* t^{*2.5} \left[\text{nN}\sqrt{\text{nm}} \right]$	2.4	6.6	13.6	23.7
$E_{\text{indent}} = \left(\frac{P}{\delta} \right)_{\text{slope}} \frac{R^{3/2}}{Ct^{5/2}} \text{ [GPa]}$	0.95	0.55	0.36	0.27
$E_{\text{indent}} t^{*2.5} \left[\text{nN}\sqrt{\text{nm}} \right]$	0.96	1.5	2.0	2.60

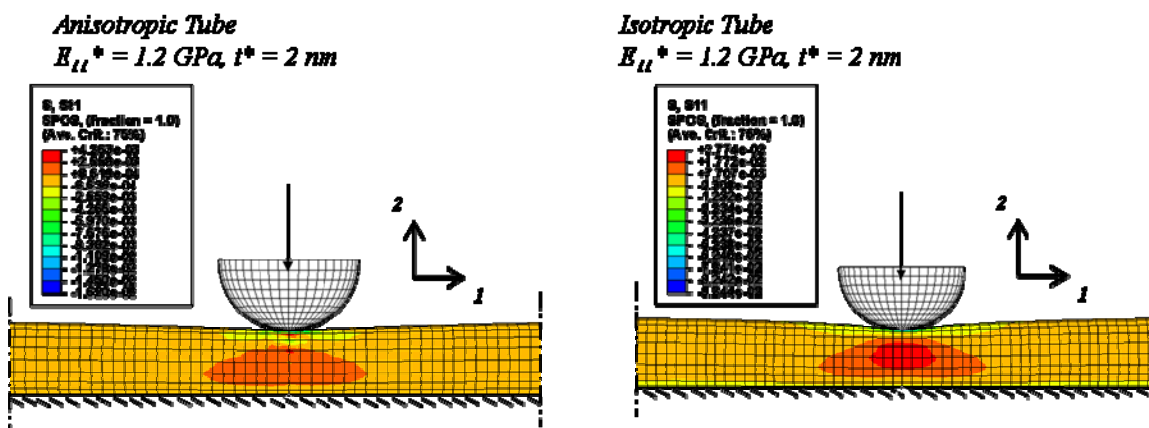
Table 3-7 shows the effective longitudinal modulus, E_{11} , and the indentation modulus E_{indent} for each effective thickness calculated using equation (61). The indentation modulus is shown to be smaller than the longitudinal modulus for each case. This is due to the highly compliant shear behaviour (low G_{12}^*) of the anisotropic tube. Figure 3-30 shows the contour profiles for different effective properties.



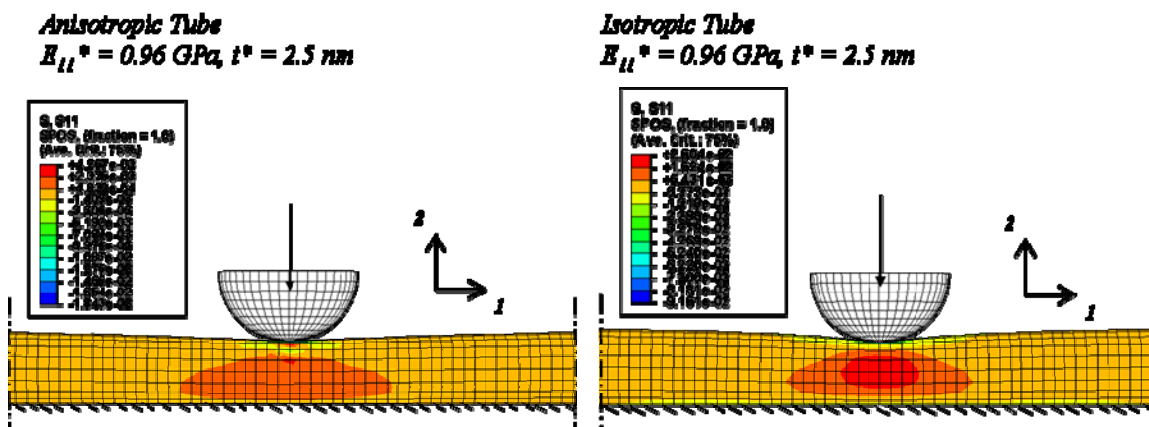
(A)



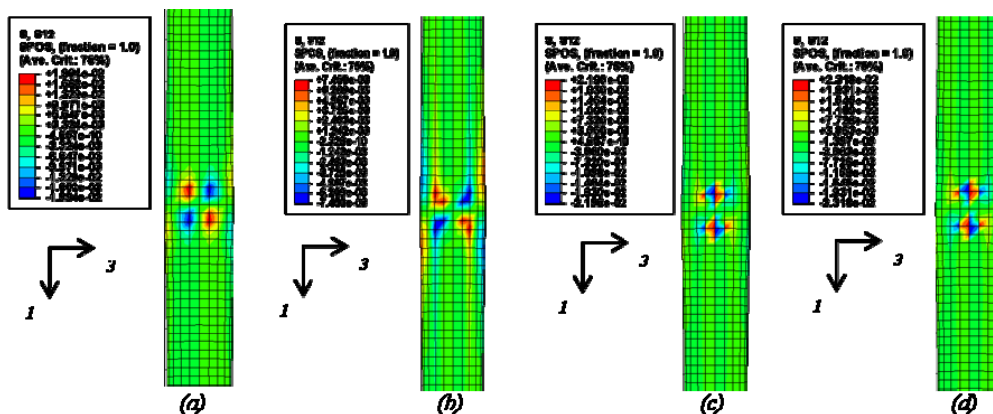
(B)



(C)



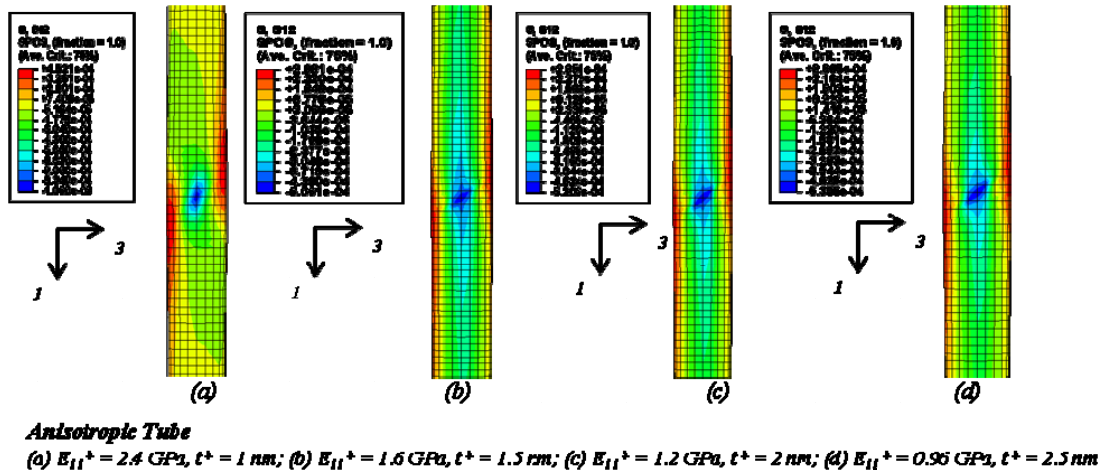
(D)



Isotropic Tube

(a) $E_{11}^* = 2.4 \text{ GPa}, t^* = 1 \text{ nm}$; (b) $E_{11}^* = 1.6 \text{ GPa}, t^* = 1.5 \text{ nm}$; (c) $E_{11}^* = 1.2 \text{ GPa}, t^* = 2 \text{ nm}$; (d) $E_{11}^* = 0.56 \text{ GPa}, t^* = 2.5 \text{ nm}$

(E)



(F)

Figure 3-30 The stress contours indicating the longitudinal stress (S_{11}) distribution [A-D] and the shear stress (S_{12}) distribution [E-F] at the indenter contact area for different E^* , t^* pairs and comparing isotropic and anisotropic tubes.

Figure 3-30 shows the contour plots of the longitudinal stress distribution, S_{11} , (A-D) and the shear stress distribution, S_{12} , (E-F) for isotropic and anisotropic tubes for different effective E^* , t^* pairs. We can observe higher stresses (S_{11} and S_{12}) associated with the isotropic tubes for each of the cases. Note that the shear strain contours for each of these cases are given in Appendix 3-3.

The longitudinal stress distributions, the shear stress distributions and the related ovalization resemble the short suspension length tube "bending" cases (80 nm , 200 nm) described in the previous section (although we are simulating a smaller indenter displacement here: 4 nm). There is significant stress differences for the different thickness cases as expected (associated with the t^3 factor for the wall bending). For the anisotropic tube cases, we can observe a directional shear stress distribution and low shear stresses associated with the low shear modulus.

Next, we will compare the anisotropic tube simulation results with the experiments.

Comparison with the Experimental Results

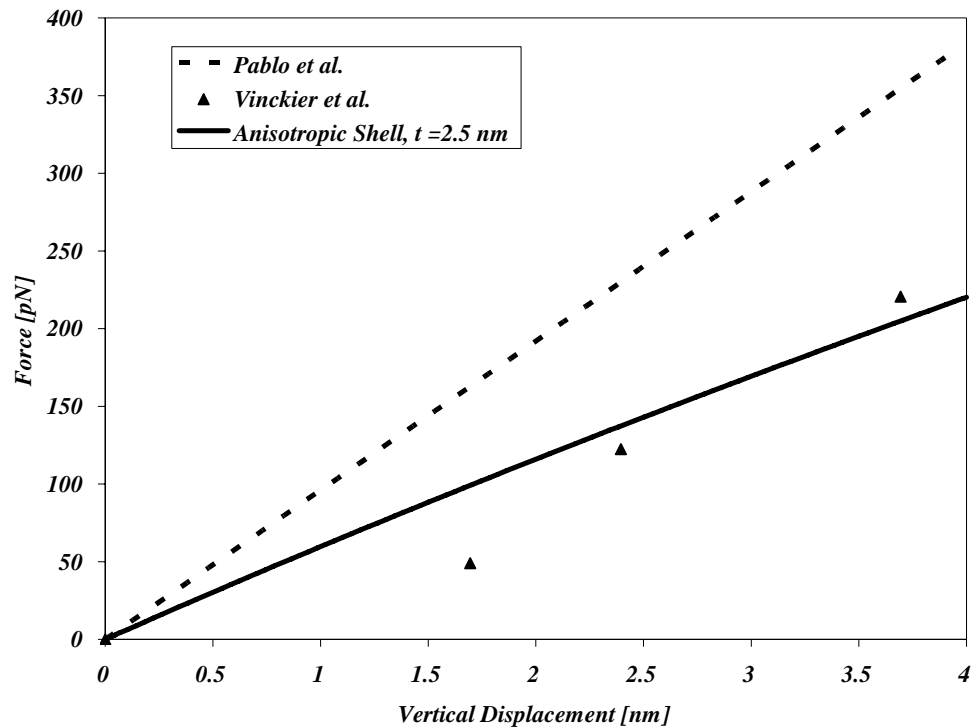


Figure 3-31 Force versus displacement for the radial indentation simulation giving a comparison with the experimental results.

Figure 3-31 compares the anisotropic material response to the two experimental results by Vinckier et al. (1996) and de Pablo et al. (2003) together with an isotropic shell response comparison. Here, the experimental data shown has been recreated from the Vinckier et al. (1996) and de Pablo et al. (2003) publications.

It is observed from this figure that the anisotropic shell response using an effective modulus and thickness pair of $E_{11}^* = 0.96 \text{ GPa}$ and $t^* = 2.5 \text{ nm}$, gives a close approximation to the Vinckier et al. result in addition to providing close results to those given by de Pablo et al. as well.

3.4. Discussion and Concluding Remarks

Here, a methodology for building continuum shell theory finite element models for microtubules has been established. The different estimates for the combination of effective elastic properties and effective mechanical thickness values help predict the deformation of the microtubules.

In this chapter, using the protofilament bending energy data and the molecular level modeling, the effective elastic properties and the effective thickness for the microtubules were derived. Following the derivation of effective elastic properties, two types of experiments were simulated: three-point bending and radial indentation. A thin shell analysis was performed for different sets of effective material properties. *The results were presented for the B Lattice (14_4) microtubules as it has been predominantly found in the in vitro samples and is predicted to be the lattice structure of the samples used in the experiments which are compared to the finite element simulations presented.*

In order to examine and compare the flexural rigidity results obtained by the three-point bending experiments by *Kis et al. (2002; 2003)*, similar suspension lengths (80nm, 200 nm) were simulated using the effective anisotropic model. *Kis et al.* results were here modified for a “pure microtubule” (in line with the *Vinckier et al. (1996)* microtubule indentation work). The flexural rigidity results are in excellent agreement with *Kis et al.* results, especially for an effective longitudinal modulus, thickness pair of $E^* = 1.2 \text{ GPa}$ and $t^* = 2 \text{ nm}$. This *mechanical* thickness lies in the *physical* bridge thickness range suggested by biologists (*Chretien, Li*) and the longitudinal modulus is in agreement with the moduli reported in the literature (*Gittes et al., 1993; Venier et al....*).

Kis et al., in order to find a longitudinal modulus and a shear modulus, reduced their force versus displacement data using the *Timoshenko beam bending equation*. The researchers obtained a longitudinal modulus of 100 MPa and a shear modulus of 1.5MPa. (as opposed to the results reported in this thesis work: $E^* = 1.2 \text{ GPa}$ and $G^* = 6 \text{ MPa}$,

respectively for $t^* = 2 \text{ nm}$). The set of elastic properties derived by *Kis et al.* being low compared to the present work (*and what has been reported in the literature*) shows that the *beam bending equation* does not provide an accurate estimate for the three-point bending of microtubules due to their thin-walled anisotropic microstructure.

Here in this thesis work, the dominating deformation mechanism for short suspension lengths that *Kis et al.* used (80 nm , 200 nm) was found to be tube wall bending similar to the wall bending in a typical indentation experiment. The flattening/ovalization as the driving mechanism of three-point bending for short suspension lengths, alters the stress distributions and force-displacement data significantly. The three-point bending analysis should account for this factor.

In order to reduce the flattening/ovalization effect, longer suspension lengths (*which have not been able to be shown in the literature because of experimental restrictions*) were considered in this thesis work. For a tube suspension length of 500 nm , here it was shown that the tube flattening/ovalization effect is not completely eliminated and the total displacement of the indenter is due to the combination of flattening/ovalization, shearing and tube bending. The flattening/ovalization factor was shown to be completely eliminated for suspension lengths of 1000 nm , where the force versus displacement is governed by longitudinal modulus but is also affected slightly by the very low shear modulus ($E_{\text{bending}} = 2.2 \text{ GPa}$ for an effective modulus, thickness pair of: $E_{11}^* = 2.4 \text{ GPa}$ and $t^* = 1 \text{ nm}$).

In the second part of this chapter, radial indentation (*with a spherical indenter of 20 nm radius*) results were presented for a thin shell tube with the same effective material properties.

In the radial indentation experiments, researchers (*de Pablo et al., 2003 and Schaap et al., 2006*) observed that microtubules exhibit a linear indentation force versus indenter displacement behaviour up to indentation depths of 4 nm .

In the simulations presented here, comparable indentation slopes were obtained for the same indenter diameter for the linear region of indentation simulated. It was also shown here that the radial indentation response for the anisotropic tubes is not solely governed by their longitudinal modulus; the low shear modulus lowers the overall indentation modulus.

As a summary, in this work, by examining both the three-point-bending and indentation experiments through finite element simulations suggest that the three-point bending analysis should actually have an additional term for the displacement equation; the displacement should account for the tube flattening for short suspension lengths as well as tube shearing and overall tube bending. This is shown by the following equation:

$$\delta_{Total} = \delta_{indentation} + \delta_{bending} + \delta_{shearing} \quad (62)$$

Here, the displacement due to indentation, $\delta_{indentation}$, governs the wall bending observed in short suspension lengths. The displacement due to shear, $\delta_{shearing}$, is the anisotropic shearing effect that is governed by the low shear modulus of the tube and $\delta_{bending}$ is the factor that is governed by the longitudinal modulus of the tube. This equation can also be written in terms of the effective properties of the microtubules (*using the equations (6) and (11) from this chapter*):

$$\delta_{Total} = \frac{PR^{1.5}}{CE^*t^{*2.5}} + \frac{PL^3}{192E^*I} + \frac{fPL}{G^*A} \quad (63)$$

Here, P is the force, R is the average tube radius, L is the suspended tube length, C is a prefactor ($C \approx 1$), f is a constant ($f = 1.38$ for hollow cylinders), I is the second moment of tube's area A . The effective elastic properties are the longitudinal modulus, E^* ; the shear modulus G^* and the thickness is t^* .

This equation is a modified form of the *Timoshenko beam bending equation* and governs three-point bending. As the effective shear modulus G^* is very low for microtubules, the effect of the shearing deformation will be significant even at long suspension lengths but the dominance of this factor will be accompanied by the tube wall flattening/ ovalization for short suspension lengths. Also, one must notice here that equation (63) is not the exact expression for anisotropic tubes as the contribution of the indentation displacement (i.e. the first term) is not solely a function of the longitudinal modulus but rather a lower modulus which reflects the wall shear (as it was shown in this chapter for a case of the anisotropic tube $E_{indent} < E$).

In order to quantify this analysis the ratios of each displacement contribution in equation (63) can be expressed in terms of L , R , t and the axial stiffness ($K_A = E^* t^*$) and the shear stiffness ($K_s = G^* t^*$); where L is the suspension length ($80 < L < 1000$), R is the average radius of the tube ($R = 11.14 \text{ nm}$) and t^* is the mechanical thickness derived according to the related E^*, t^* pair in question ($2.4 \text{ GPa and } 1 \text{ nm}$; $1.2 \text{ GPa and } 2 \text{ nm}$; $0.96 \text{ GPa and } 2.5 \text{ nm}$).

The following ratios are obtained:

$$\frac{\delta_{shear}}{\delta_{bend}} = f 96\pi \left(\frac{R}{L} \right)^2 \frac{K_A}{K_s}. \quad (64)$$

Here f is 1.38 for a hollow cylinder.

$$\frac{\delta_{indent}}{\delta_{bend}} = \frac{192\pi}{C} \left(\frac{R^{4.5}}{L^3 t^{1.5}} \right). \quad (65)$$

Here: $0 < C < 2$

$$\frac{\delta_{indent}}{\delta_{shear}} = \frac{2\pi}{fC} \left(\frac{R^{2.5}}{Lt^{1.5}} \right) \left(\frac{K_s}{K_A} \right). \quad (66)$$

Here, one must observe that the indentation contributions differ with the mechanical thickness used, thus the indentation ratios to either bending or shearing is a function of the thickness.

For the isotropic tube with a poisson ratio of $\nu = 0.35$, $\left(\frac{K_s}{K_A} \right)$ ratio is $\frac{1}{2(1+\nu)} = 0.37$;

while this ratio is $\left(\frac{K_s}{K_A} \right) = \left(\frac{0.012}{2.4} \right) = 0.005$ for the anisotropic tube. This will impact the effect of contribution of each displacement on the overall displacement of the indenter.

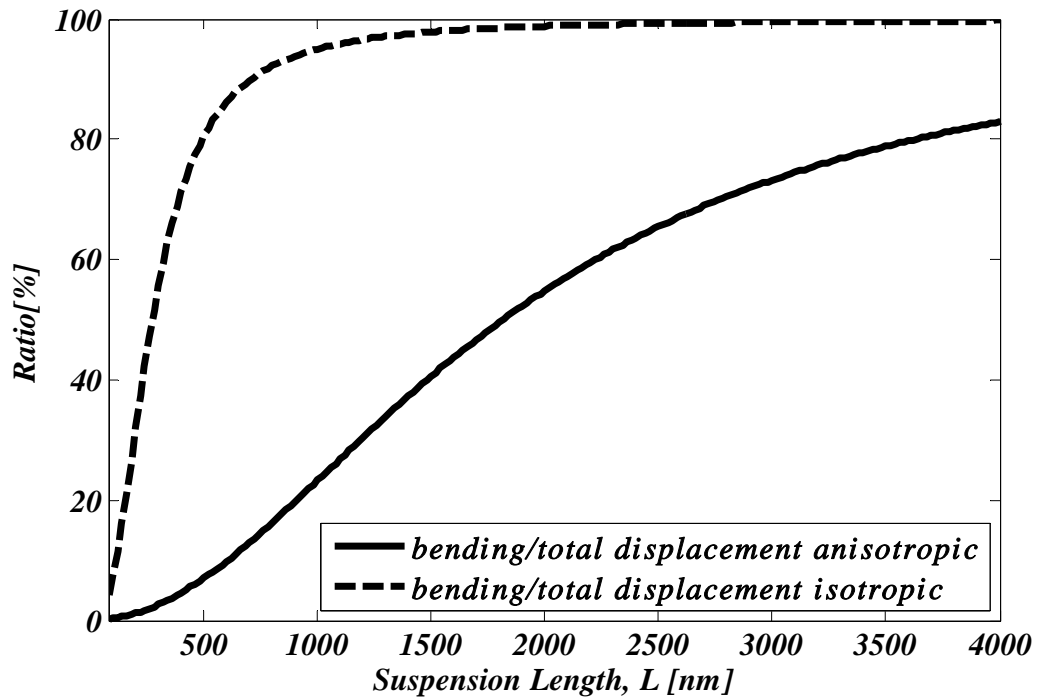


Figure 3-32 The relative contributions of the tube bending deformation on the total displacement of the indenter in three-point bending for an isotropic and anisotropic tube.

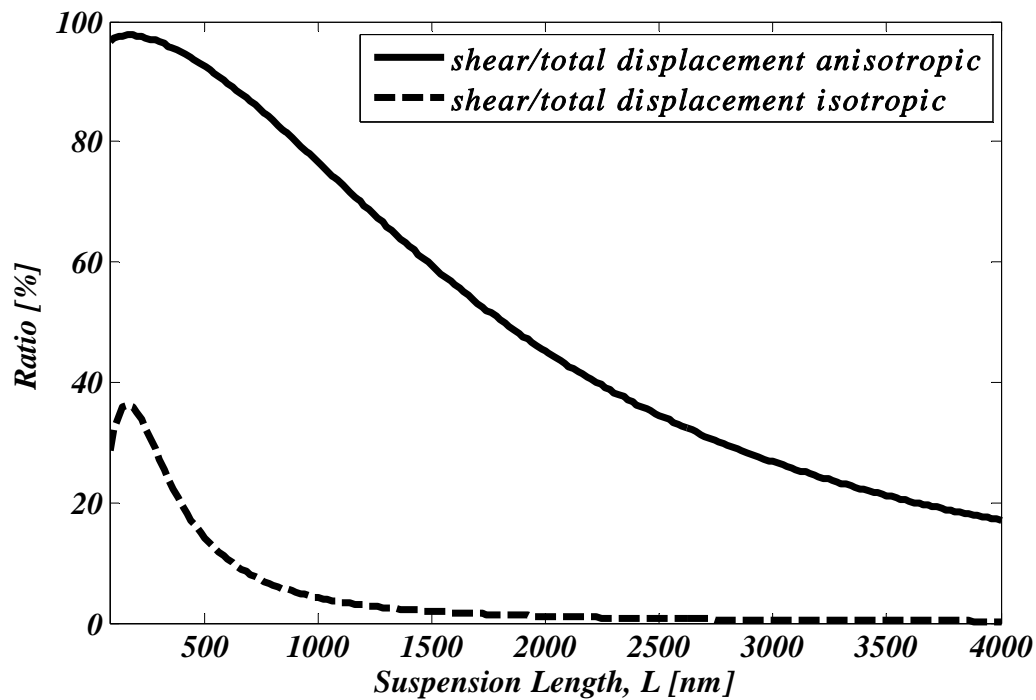


Figure 3-33 The relative contributions of the shearing deformation on the total displacement of the indenter in three-point bending for an isotropic and anisotropic tube.

Figure 3-32 shows the relative contribution of the tube bending $\left[\frac{\delta_{bend}}{\delta_{Total}} \right]$ (governed by the second term in equation (63) for suspension lengths of $80nm < L < 4000nm$. Note that, here, the maximum suspension length for the figures is $4000 nm$, as the “pinned-pinned” case used for the suspension of a $1000 nm$ tube would bring “x4” factor in the force-displacement relationships as mentioned before.

From Figure 3-32, for a suspension length of $L \geq 1000nm$, the indenter displacement is completely governed by the tube bending for the isotropic tube. On the other hand, for the anisotropic tube the indenter displacement, even for long suspension lengths is not completely governed by the tube bending.

Figure 3-33 shows the relative contribution of the tube shearing on the overall indenter displacement; $\left[\frac{\delta_{shear}}{\delta_{Total}} \right]$ (i.e. the third term in equation (63)). Here one can observe that for the anisotropic tube initially most of the deformation is governed by the shearing deformation while this effect gets reduced at long suspension lengths. The shear effect is completely eliminated at long suspension lengths for isotropic tubes. Here, note that the shearing and tube bending contributions on the indenter displacement are independent of the mechanical thickness.

Figure 3-34 shows the tube wall bending/ovalization effect on the overall displacement of the indenter. This effect is governed by the first term in equation (63) and is plotted as: $\left[\frac{\delta_{indent}}{\delta_{Total}} \right]$ as it is an indentation type deformation for the three-point bending of thin-walled tubes.

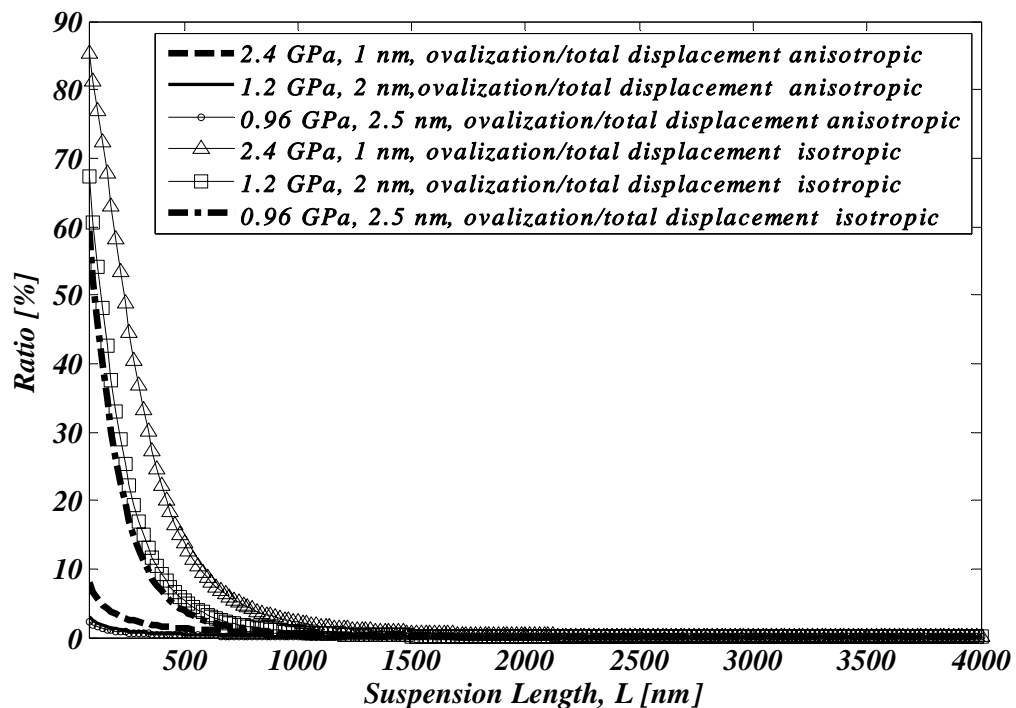


Figure 3-34 The relative contributions of tube wall bending/ ovalization deformation on the total displacement of the indenter in three-point bending for an isotropic and anisotropic tube for different E^* , t^* pairs.

One can observe from Figure 3-34 that for short suspension length, for isotropic tubes, the indenter displacement/ the total displacement is governed by the tube wall bending/ovalization. This effect is 0-10 % for the anisotropic tubes for different effective E^* , t^* pairs. The ovalization effect diminished for both isotropic and anisotropic tubes for long suspension lengths as expected. The ovalization effect is dependent on the effective E^* , t^* pair used and here it is shown that the lower the mechanical thickness is, the higher is the contribution of ovalization in the overall indenter displacement.

Résumé

Ici, une méthode permettant de construire un modèle éléments finis (avec éléments coque) a été développée. Les estimations obtenues des propriétés élastiques et épaisseur effectives ont permis de prédire la déformation des microtubules.

Au cours de ce chapitre, aidé des données d'énergie de flexion du protofilament et des simulations à l'échelle moléculaire, les propriétés élastiques et épaisseur effectives des microtubules sont déduites. A partir de la détermination des propriétés élastiques effectives, 2 types d'expériences sont ensuite simulées. Flexion 3-point et indentation radiale. Une analyse coque mince est conduite pour différents jeux de paramètres matériaux « effectifs ». *Les résultats sont présentés dans le seul cas de la configuration B (14_4) dans la mesure où cette organisation a été identifiée comme majoritaire dans les échantillons in vitro. De plus, cet arrangement correspond à la structure des échantillons utilisés au cours des expériences qui sont comparés aux simulations par éléments finis conduites.*

En vue d'examiner et de comparer quantitativement les valeurs de rigidité de flexion obtenues par Kis et al. (2002; 2003) dans des tests de flexion 3 points, des longueurs utiles (distance suspendue) similaires (80 et 200nm) sont utilisées dans le modèle continu anisotrope développé. Les résultats de Kis et al. ont été modifiés de manière à reproduire un "microtubule naturelle" (en accord avec les tests d'indentation menés par Vinckier et

al. (1996)). La rigidité de flexion calculée est en excellent accord avec les données présentées par Kis, plus particulièrement pour des valeurs du module longitudinal et de l'épaisseur effectifs de 1.2GPa et 2mm respectivement. Cette épaisseur "mécanique" est de l'ordre de grandeur de l'épaisseur physique suggérée par des biologistes et le module longitudinal est en accord avec le valeurs reportées dans la littérature (Gittes et al., 1993; Venier et al....).

Pour calculer les modules longitudinal et de cisaillement, Kis et al ont réduit leur mesure de force et déplacement suivant la théorie des poutres en flexion proposée par Timoshenko. Ils ont alors obtenu un module longitudinal et de cisaillement de 100MPa et 1,5 MPa respectivement (dans ce travail de thèse : $E^* = 1.2 \text{ GPa}$ et $G^* = 6 \text{ MPa}$, pour $t^* = 2 \text{ nm}$). Les propriétés élastiques calculées par Kis sont inférieures aux valeurs ici reportées (et reportées plus généralement dans la littérature). Cette différence notable montre que la « théorie des poutres en flexion » ne permet pas d'estimer précisément la réponse mécanique de microtubules soumises à un essai de flexion 3 points, cette erreur provenant de la forte anisotropie de leurs fines parois.

Dans le présent travail de thèse, le mécanisme de déformation identifié dominer la réponse des microtubules pour les faibles longueurs utiles (de l'ordre des longueurs utilisées par Kis et al.) est la flexion des parois du tube, similaire à la flexion des parois lors de tests conventionnels d'indentation. L'aplatissement/ l'ovalisation étant le mécanisme moteur, l'état de contrainte et les valeurs de force-déplacement sont fortement perturbés. L'analyse de ces essais doit prendre en considération ce facteur.

Afin de réduire les effets d'aplatissement/ovalisation, des calculs impliquant de plus grandes longueurs de suspension ont été conduits (les restrictions expérimentales ne permettent pas de retrouver ces résultats dans la littérature). Pour des longueurs de suspension aussi importantes que 500nm, il est ici montré que les phénomènes d'aplatissement/ovalisation ne sont pas entièrement éliminés et de fait le déplacement complet de l'indenteur provient des effets combinés d'aplatissement/ovalisation, de

cisaillement, et de flexion du tube. L'effet d'aplatissement/ovalisation disparaît pour des longueurs de suspension de 1000nm, où le profil de force-déplacement est gouverné par le module longitudinal mais est aussi légèrement perturbé par le faible module de cisaillement ($E_{flexion} = 2.2GPa$ pour les module et épaisseur effectifs suivant: $E_{11}^* = 2.4GPa$ et $t^* = 1nm$).

Dans une seconde partie de ce chapitre, des tests d'indentation radiale sont simulés sur un tube mince présentant les propriétés effectives détaillées ci-dessus (*indenteur sphérique de 20nm de rayon*) Au cours de tests d'indentation radiale menés sur des microtubules, différents groupes de chercheurs ont observé une réponse force/déplacement linéaire pour des profondeurs d'indentation allant jusqu'à 4nm.

Ici, des profils linéaires similaires sont obtenus pour un indenteur de diamètre identique. Il est également montré que la réponse radiale de tubes anisotropes n'est pas uniquement gouvernée par leur module longitudinal : le faible module de cisaillement diminue en effet le module global d'indentation.

En résumé, en examinant à la fois la réponse en flexion 3 points et par indentation via des simulations par éléments finis, ce travail nous amène aux conclusions suivantes: Les tests de flexion 3 points devraient incorporer un terme supplémentaire à l'expression de la déformée totale: le déplacement doit en effet intégrer l'aplatissement du tube observé aux faibles longueurs de suspension au même titre que le cisaillement et la flexion du tube. L'équation qui suit est alors proposée:

équation (62)

Ici, le déplacement attribué au chargement de type indentation gouverne la flexion des parois observées aux petites longueurs de suspension. Le déplacement associé au cisaillement provient des effets de cisaillement anisotrope résultant du faible module de cisaillement du tube. Enfin, $\delta_{bending}$ est le facteur gouverné par le module longitudinal du tube. L'équation précédente peut également être présentée en fonction des propriétés

effectives du microtubule (module longitudinal, module de cisaillement et épaisseur) (cette expression est obtenue par substitution des équations 6 et 11 de ce même chapitre.)

équation (63)

avec P la force, R le rayon moyen du tube, L la longueur suspendue du tube, C un préfacteur ($C \approx 1$), f une constante ($f=1.38$ pour un cylindre débouchant), I le second moment du tube de section A . Comme précisé plus haut, les propriétés élastiques effectives sont le module axial E^* , le module de cisaillement G^* et l'épaisseur effective t^* .

Cette expression correspond à une forme modifiée de l'équation de flexion des poutres proposée par Timoshenko et gouverne la réponse en flexion 3 points. De part le faible module de cisaillement effectif, la déformation par cisaillement sera significative et ce, même pour des longueurs de suspension élevées. Cependant, l'importance relative de ce facteur sera contestée par l'aplatissement/ovalisation des parois des tubes aux faibles longueurs de suspension. Aussi, il est à noter que l'équation (63) ne correspond pas à la formulation exacte reproduisant le comportement d'un tube mince et anisotrope. En effet, la contribution à la déformation totale associée au chargement par indentation (*i.e* le 1er terme de l'expression) ne peut être uniquement reliée à la contribution du module longitudinal mais plutôt à une valeur inférieure qui refléterait le cisaillement des parois (comme il a été démontré dans ce chapitre dans le cas du tube anisotrope $E_{indent} < E$)

Afin de quantifier cette analyse, les ratios des différentes contributions au déplacement total peuvent être présentés en fonction de L , R , t et des rigidités axiale ($K_A = E^* t^*$) et par cisaillement ($K_s = G^* t^*$); L est la longueur de suspension ($80 < L < 1000 \text{ nm}$), R le rayon moyen du tube ($R = 11.14 \text{ nm}$) et t^* l'épaisseur mécanique identifiée selon la valeur du module longitudinal effectif E^* ; les couples E^*, t^* utilisés sont: 2.4 GPa et 1 nm; 1.2 GPa et 2 nm ; 0.96 GPa et 2.5 nm.

Les rapports suivant sont étudiés:

équation (64)

Ici f vaut 1.38 dans le cas d'un tube débouchant.

équation (65)

Avec, $0 < C < 2$

équation (65)

Il est à noter que la contribution par indentation varie selon l'épaisseur mécanique utilisée. De fait, les ratios des effets d'indentation relatifs à la flexion ou au cisaillement dépendent également de l'épaisseur.

Dans le cas d'un tube isotrope avec un coefficient de poisson $\nu = 0.35$, le rapport $\left(\frac{K_s}{K_A}\right)$ vaut $\frac{1}{2(1+\nu)} = 0.37$; ce même rapport devient $\left(\frac{K_s}{K_A}\right) = \left(\frac{0.012}{2.4}\right) = 0.005$ dans le cas du tube anisotrope. Cette particularité a une incidence sur l'amplitude des différentes composantes au déplacement total de l'indenteur.

La Figure 3-32 présente la contribution relative à la déformation totale des effets de flexion du tube (gouvernés par le second terme de l'équation 63) sur une échelle des longueurs de suspension s'étalant de 80 à 4000nm. Il est important de noter que la longueur de suspension maximale est de 4000nm, dans la mesure où un essai "encastrement-encastrement" d'un tube ayant une longueur de suspension de 1000nm induirait un facteur multiplicatif "4" dans les relations force-déplacement présentées précédemment.

Au regard de la Figure 3-32, l'étude du tube isotrope montre que le déplacement de l'indenteur est entièrement gouverné par la flexion du tube pour des longueurs de suspension $L \geq 1000nm$. En revanche, les simulations conduites sur le tube anisotrope

montrent que déplacement de l'indenteur ne se réduit en aucun cas au seul fléchissement du tube, et ce même pour les grandes longueurs de suspension étudiées.

La Figure 3-33 présente la contribution relative à la déformation totale des effets de cisaillement du tube $\left[\frac{\delta_{shear}}{\delta_{Total}} \right]$ (troisième terme de l'équation). Dans le cas du tube anisotrope, la majeure partie de la déformation totale aux petites longueurs de suspension peut être associée aux effets de cisaillement. L'importance relative diminue avec l'augmentation de la longueur de suspension. La contribution par cisaillement est entièrement éliminée aux grandes longueurs de suspension dans le cas d'un tube isotrope. Il est important de noter ici que les contributions par cisaillement et flexion sont indépendantes de l'épaisseur mécanique.

La Figure 3-34 illustre l'importance du fléchissement/ovalisation des parois sur le déplacement complet de l'indenteur. Cette contribution correspond au 1er terme de l'équation (63) et est figuré ici par le terme: $\left[\frac{\delta_{indent}}{\delta_{Total}} \right]$ dans la mesure où cet effet correspond à une déformation de type indentation lors d'un test conventionnel de flexion 3 points mené sur un tube à parois minces.

A la lecture de la Figure 3-34, il est à noter qu'aux courtes longueurs de suspension, le déplacement de l'indenteur (le déplacement total) est contrôlé par le fléchissement/ovalisation des parois du tube isotrope. Cet effet est réduit à 0-10% dans le cas du tube anisotrope pour différents jeux de paramètres E^* , t^* . Les effets d'ovalisation diminuent avec l'augmentation des longueurs de suspensions quelle que soit la description adoptée pour le tube (isotrope ou anisotrope). Enfin. L'ovalisation dépend des paramètres effectifs utilisés et il est démontré ici que la diminution de l'épaisseur mécanique conduit à amplifier l'importance de l'ovalisation sur le déplacement total de l'indenteur.

4. CHAPTER 4: MICROTUBULE DYNAMICS

4.1. Introduction

One of the unique properties of the microtubules is that they can polymerize, depolymerise or disassemble without any additional external work. Microtubules accomplish this by changing chemical energy into disassembly energy to decompose their strongly bound structure. This is done by a self-organizational process.

The wall of the microtubule can be thought of as an elastic sheet material with an intrinsic curvature which is observed in the disassembly of the microtubule wall into curved protofilaments.

In this chapter, we will demonstrate the applicability of the intrinsic curvature energy related instability to the tube model proposed in the previous chapters. This will allow us to present the capabilities of the model to capture microtubule dynamics by incorporating the effects of the desired intrinsic curvature of the protofilaments.

The methodology will start by defining a disassembly energy allowing us to derive an initial stress state in the microtubule lattice. This initial stress state will be imposed in the thin shell tube model and the cylindrical tube will be allowed to release this energy. In order to add the lateral interaction complexities in the discrete model, a “connector model”, a cylindrical tube made up of 14 thin shell strands (the protofilaments) connected to one another will be presented. In order to facilitate the incorporation of the breaking of the lateral bonds during disassembly, the lateral dimer-dimer interactions will be approximated by a typical protein-protein interaction potential function. Allowing the thin strands to change conformation under their own forces, a tapered configuration for the microtubule will be obtained resembling the microtubule images obtained with cryo-electron microscope (Mandelkow et al., 1991; Chretien et al., 1995; Muller-Reichert et al., 1998...)

4.2. Intrinsic Curvature and Energy Exchange

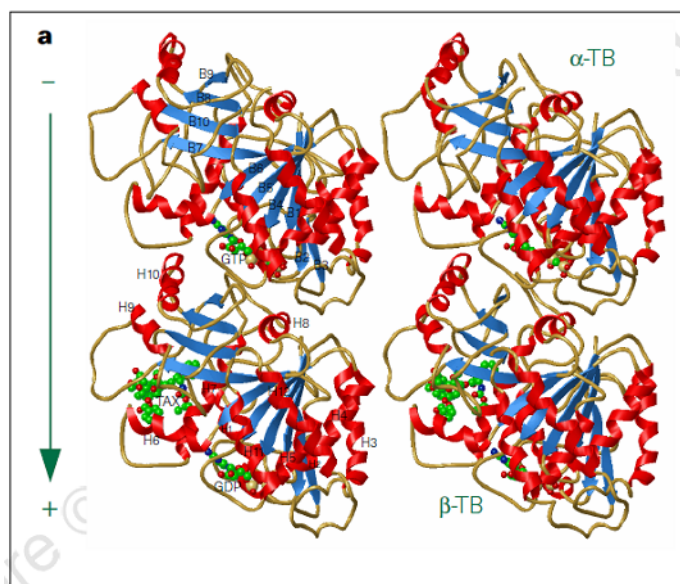


Figure 4-1 Ribbon diagram of the tubulin dimer showing α -tubulin with bound GTP (top), and β -tubulin containing GDP (bottom). The arrow indicates the direction of the protofilament and microtubule axis (Nogales, 1998).

Each tubulin heterodimer (α -tubulin and β -tubulin) binds 2 GTP (Guanosine-5'-triphosphate) molecules (Figure 4-1). The polymerization and depolymerization of microtubules is unusual compared to those of most polymers in nature. They are created through the loss and gain of a short region known as the “GTP cap” (Kirschner, 1978). Tubulin-bound GTP is hydrolyzed to tubulin-GDP and Pi (inorganic phosphate) at the time that tubulin-GTP adds to the microtubule ends or shortly thereafter. Ultimately the cap disassociates from the microtubule, leaving the microtubule core consisting of GDP (Guanosine-5'-diphosphate) bound to beta-tubulin. The tubulin GDP remains non-dissociable and non-exchangeable until the tubulin subunit disassociates from the microtubule. In other words, the dynamic behaviour of the microtubules is based on the binding and hydrolysis of GTP by tubulin subunits. GTP is necessary for stabilization as GDP has weaker bonds with tubulin. The straightening of protofilaments occurs by the “zipping” of adjacent protofilaments via lateral contacts and the effect of GTP hydrolysis could be explained as “unzipping” by the weakened lateral contacts (Figure 4-2).

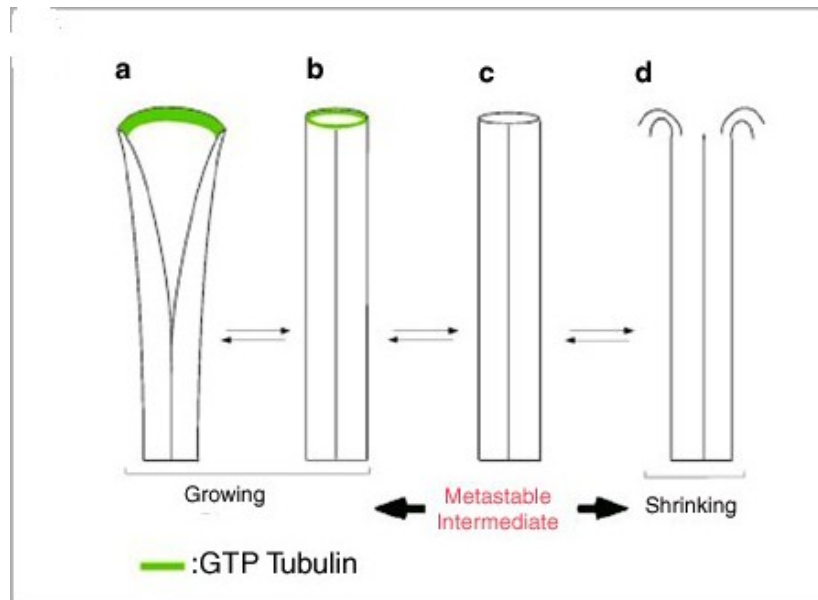


Figure 4-2 Structural model showing the microtubule instability. (a) Microtubules grow as 2D-sheets, (b) GTP hydrolyzed resulting in “blunt-ended” microtubules, (c) Microtubules lateral bonds are in a strained state about to break, (d) The unstable blunt-ended microtubule results in the loss of the GTP region (Arnal et al., 2000). During assembly, microtubules are observed to have “blunt ends”, while during disassembly they are observed to have “tapered” or “coiled” ends.

GTP polymerizes forming protofilaments that have a straight conformation, but following GTP hydrolysis, the tubulin conformation changes to a curved form forming GDP that is connected to the microtubule leaving the core of the microtubule in a strained conformation. The bent form of GDP bound tubulin is constrained by the microtubule lattice. On the other hand, when the GTP or GDP-Pi cap is present, the end of the microtubule is stabilized and the microtubule can grow. When the cap is lost, the relatively unstable core of the microtubule is exposed and the end shortens rapidly (Figure 4-2).

Microtubule dynamics have been observed and imaged using cryo-electron microscopy (Mandelkow et al., 1991; Chretien et al., 1995; Muller-Reichert et al., 1998, Arnal et al., 2000...) (Figure 4-3).

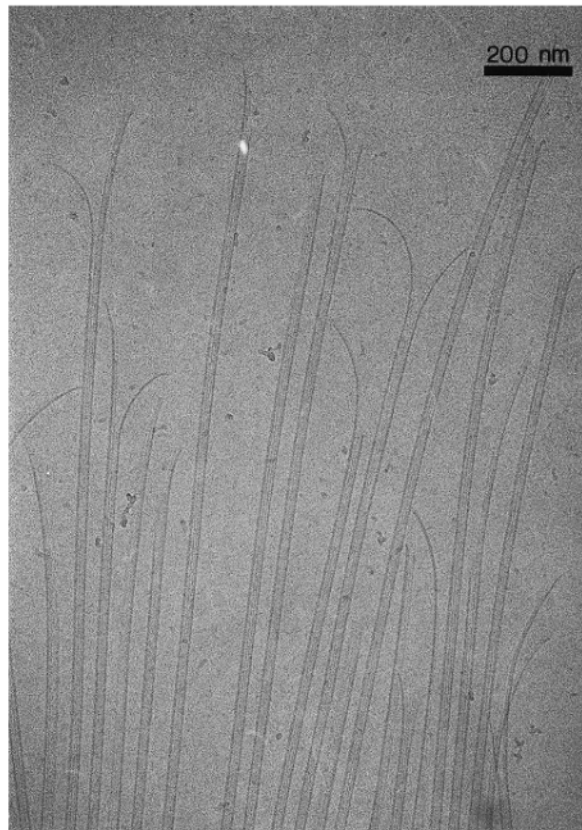


Figure 4-3 The micrographs show that growing ends of microtubules often taper to long, narrow tips that curve away from the microtubule (Chretien et al., 1995).

4.3.Previous Models

Microtubules undergo large conformational changes during microtubule assembly and disassembly. The change in the curvature during the assembly process induces an accumulation of elastic energy in the microtubule wall. Near the end of the microtubule wall, this accumulated energy is relieved through slight protofilament bending which might result in disassembly and even catastrophes. This is a consequence of the fact that the microtubule wall material is elastic and it yields to the force that is created by its own in-built energy.

Prior to introducing our approach, we will give a summary of the previous models.

A filament model was proposed by Janosi et al. (2002) considering a semi-infinite microtubule with 13 laterally bound protofilaments running parallel to the microtubule axis (Figure 4-4, A). The researchers investigated the filament conformation and the energy associated with it. Adding the bending and stretching energies of a filament, the researchers derived the energy of a single filament in terms of the length of the microtubule (z) as:

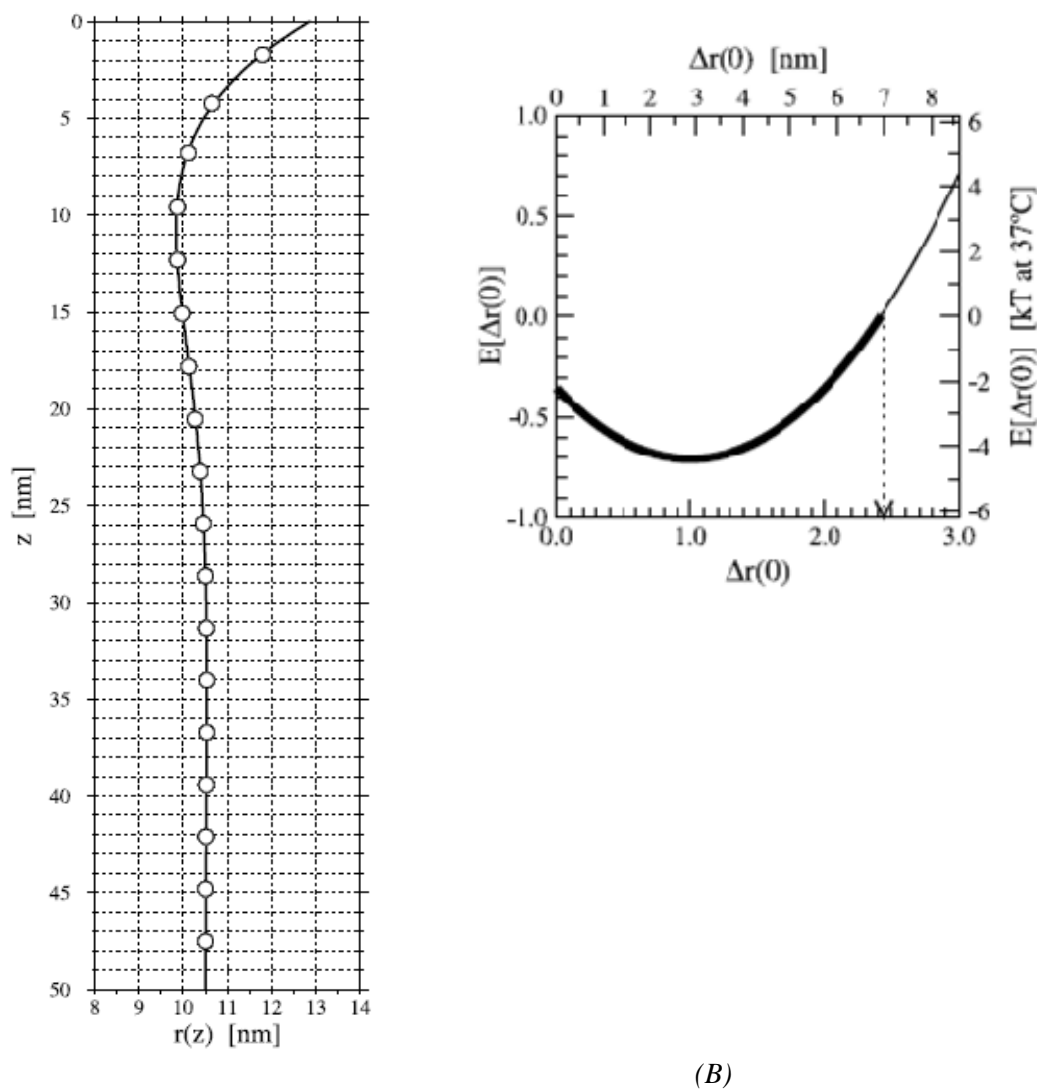
$$E(z) = \int_0^{\infty} (E_c(z) + E_s(z)) \quad (67)$$

Here $E_c(z)$ is the bending energy density and $E_s(z)$ is stretching per unit length. In terms of the curvature; $c(z)$ and the radius $r(z)$, it was rewritten as:

$$E(z) = \int_0^{\infty} \frac{1}{2} \{ a(c(z) - c_o)^2 + k(r(z) - r_o)^2 \} \quad (68)$$

Here r_o is the equilibrium radius and c_o is the equilibrium curvature, a is the bending stiffness, and k is the axial stretching stiffness of the protofilament.

The minimal total energy was shown in terms of the end deflection (Figure 4-4, B). The arrow in the figure depicts the point where the desired intrinsic curvature (c_o) is realized. The curve is later discussed in the paper to show the possible lateral bond breakage under the lateral stresses created by the conformation change. The energy level associated with the stretching and the bending of the protofilaments decreases initially as the intrinsic curvature is being approached but during this energy relief, the lateral stress in the structure builds up as the conformation of the protofilaments change.



(A) (B)

Figure 4-4 (A) A fit of the derived $r(z)$ is shown here. (B) Energy is in the units of $\frac{ac_o^2 z_o}{\sqrt{2}}$ (a is a material parameter) on the left axis and $k_B\theta$ on the right axis. The end deflection is in the units of r_o in the bottom axis and nanometers in the top axis. The dotted limit shows a hypothetical value beyond which the lateral bonds break (Janosi et al., 2002). Note that the parameters are not given in the article.

Another mechanochemical model was proposed by VanBuren et al. (2002). A stochastic model that estimates the tubulin-tubulin bond energies was developed. The researchers used Monte Carlo simulations to estimate bond energies. Using the published shrinking ($k_{(-)}$) and growth ($k_{(+)}$) rates of microtubules in vitro (Koren and Hammes, 1976; Hill, 1985; Erickson, 1989; Bayley et al., 1989; Northrup and Erickson, 1992 and Martin et al.;

1993), they estimated the lateral and longitudinal bond strengths using the free energy change (Hill, 1985):

$$\Delta G = -k_B \theta \ln \left(\frac{k_{(+)}}{k_{(-)}} \right) \quad (69)$$

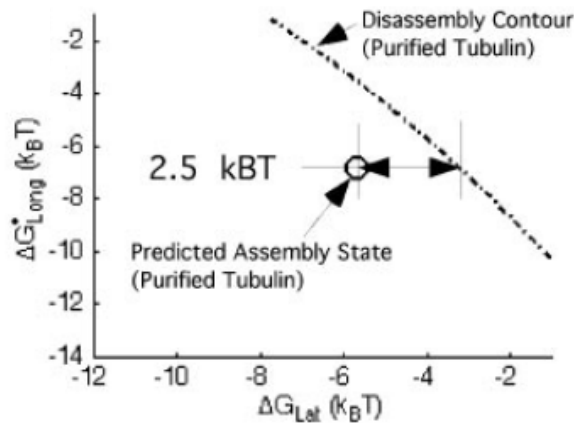


Figure 4-5 Estimation of $\Delta G_{longitudinal}$ versus $\Delta G_{lateral}$ is shown. The researchers (VanBuren et al., 2002) predicted the energy of “curling out” as $2.5k_B\theta$ from the lateral energy change for a disassembly of $-30\mu\text{m}/\text{min}$.

$\Delta G_{lateral}$ was predicted to be in the range of $3.2k_B\theta$ to $5.7k_B\theta$ and $\Delta G_{longitudinal}$ was predicted to be $6.8k_B\theta$ to $9.4k_B\theta$. Besides these findings they also showed that the energy required to straighten a tubulin GDP or equivalently curl out a tubulin-GTP to be $2.5k_B\theta$ (Figure 4-5). This result was mentioned in Chapter 3 and used in our determination of the effective mechanical thickness and will be referred to later for comparison.

Another parametric model was derived by Molodtsov et al. (2005). The researchers assumed a microtubule to be made up of 13 rods connected and held together by lateral bonds. They derived the energy of the microtubule as the sum of the longitudinal and lateral interaction energies for the 13 protofilaments as:

$$U^{(i)} = \sum_{i=1}^{13} U^{(i)} \quad (70)$$

The intra-protofilament energy of the i^{th} protofilament was thought of as the addition of the energy of the k^{th} dimer to $(k-1)^{\text{th}}$ dimer interaction:

$$g_{(k)}^{(i)} = \frac{1}{2} B(\theta_{(k)}^{(i)} - \theta_{(k-1)}^{(i)}) \quad (71)$$

Here B is a bending energy parameter and $(\theta_{(k)}^{(i)} - \theta_{(k-1)}^{(i)})$ represents the change of the angles in an intra-protofilament interaction between two dimers.

The inter-protofilament energies were defined using:

$$U^* = k \left(\frac{(r - r_o)}{r_o} \right)^2 \exp \left(- \frac{(r - r_o)}{r_o} \right) \quad (72)$$

Here r_o is the distance in which the bonds exert the maximum attractive force, $(r - r_o)$ characterizes the dimers' deviation from the equilibrium configuration and k is an inter-protofilament stiffness parameter. This function is a typical protein-protein interaction (Jiang et al., 2002) derived upon high-resolution protein-protein complex structures in the Protein Data Bank (PDB). The total potential energy of the microtubule was defined as the addition of the inter- and intra-protofilament energies:

$$U^{(i)} = \sum_k g_{(k)}^{(i)}(X_{(k)}^{(i)}) + \sum_j \mathcal{U}_{(j)}(r_{(j)}^{(i)}) \quad (73)$$

Molodtsov et al. (2005) estimated k to be 4.4 kcal/mol using the average activation energy barrier between the disassembly rates of two dimers:

$$E_a = \ln \left(\frac{k_{(-)(k)}}{k_{(-)(k-1)}} \right) \quad (74)$$

The disassembly rates were obtained from the literature (Koren and Hammes, 1976; Hill, 1985; Erickson, 1989; Bayley et al., 1989; Northrup and Erickson, 1992; Martin et al.; 1993). r_o was chosen as 0.12 nm representing a typical distance for protein-protein interactions.

The model provided an explanation of the stability and the shape of microtubules and the catastrophic peeling-off effect giving the formation of “ram’s horns” (Figure 4-6).

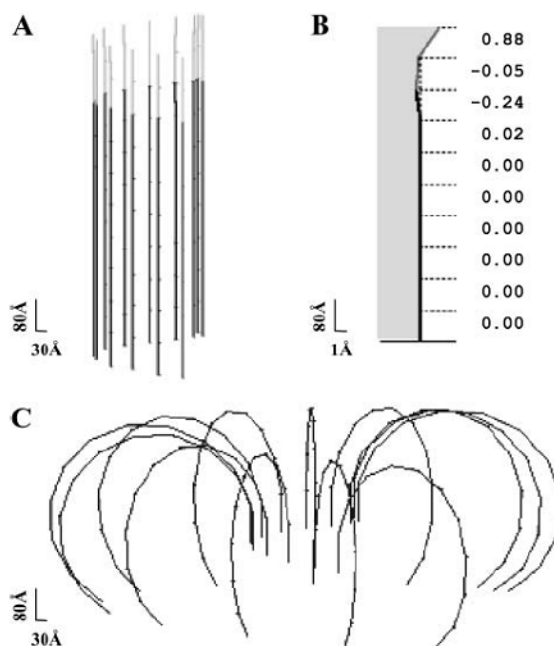


Figure 4-6 (A) Initial microtubule configuration, (B) Side view of the protofilaments in the initial state, (C) The equilibrium configuration of the microtubule forming “ram’s horns” (Molodtsov et al., 2005).

Each of these previous models provides a sound basis for further investigation and offers parameters that will be useful in the present work. The models described do not give an

exact definition of the complete mechanical properties of a microtubule lattice whilst accounting for the dynamic instabilities.

In the following sections, our aim is to incorporate the dynamic behaviour of the microtubules in mechanical terms into our discrete model (Chapter 3) and to develop a complete description that accounts for the material properties of the microtubule as well as capturing the dynamic effect that has been observed *in vitro* since the early 1990s.

4.4.Prestress

In this section, a prestress that accounts for the intrinsic curvature of the microtubules will be derived defining a “disassembly energy function” that can be used to formulate an initial stress state expression. The continuum model that has been developed in the previous chapters will be used, this time including the effect of the initial stress state.

The disassembly energy can be described as

$$U_D = \frac{K_B}{2\rho^2} = \frac{1}{2} E_{11}^* I \frac{1}{\rho^2} \quad (75)$$

This energy explains the amount of the energy to bend a lattice structure with a longitudinal modulus of E_{11}^* into a curvature of ρ . Here K_B is the bending stiffness of the microtubule (as defined in Chapter 2 and 3) and E_{11}^* is the effective longitudinal modulus, I is the second moment of area of the microtubule wall and ρ is the radius of curvature that the microtubule wall curls out to and is calculated from the electron micrographs to have an average value of $\rho = 19$ nm (Muller-Reichert et al., 1998).

The initial internal stress state is added to the continuum model. The initial stress state is quantified with the following related expression:

$$\sigma_{11,i} = E_{11}^* \frac{1}{\rho} (r - R_{avg}) \quad (76)$$

Here, R_{avg} is the average radius of the shell tube and r is the radial location of a point on the tube. The initial stress state will be incorporated into the continuum model and first demonstrated with a “whole tube stress relief analysis” in the next section.

4.5. Finite Element Methods for Analyzing Microtubule Dynamics

4.5.1. Whole Tube Stress Relief Analysis

Here, finite element analysis of the “prestress relief” will be presented on B Lattice type (14_4) microtubules. The effective material properties used are: $E_{11}^* = 2.4GPa$, $E_{22}^* = 0.1GPa$, $G_{12}^* = 0.012GPa$, $\nu_{12} = 0.34$, $\nu_{16} = -1.2$, $\nu_{26} = 1.2$ (the latter two representing the monoclinic/shear-tension coupling effect) with an effective thickness of $t^* = 1nm$ (the derivation of these are given in Chapter 2 and 3).

The stated assumptions and steps for the finite element analysis of the microtubule are:

- The material is linear anisotropic elastic.
- The length of the microtubule is chosen to be $160 nm$. It is believed that the chosen length captures the necessary mechanical behaviour to be portrayed.
- The average radius of the microtubule is $R_o = 11.14 nm$ for the B Lattice.
- The microtubule is fixed at one end mimicking the end that is the inert end; while the other end is set free. The “curling out” is realized at the “top end” in the cell, not the “bottom end” which is close to the microtubule organizing center. This implies that the instability will be highest at the ends of the microtubule and results in the shape observed in the micrographs of the dynamically unstable microtubules.
- A prestress as defined by equation (76) is applied to the whole structure.

- Finite element analysis is performed using the software ABAQUS. The model consists of 10400 nodes and 10335 shell elements (S4R).
- A multi-step analysis is followed; i.e. the relief of the prestress history is divided into "steps" solely on the basis of convenience. Each step is typically one stage in the overall loading history. The initial condition for each step is the state of the model at the end of the previous step.

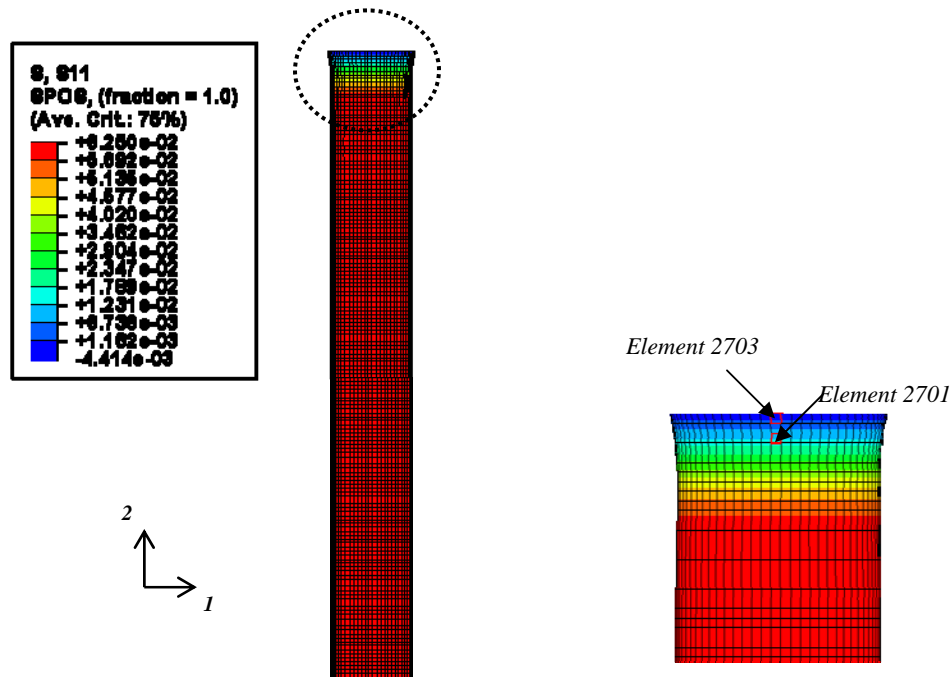


Figure 4-7 The plot shows the relief of the prestress at the tip of the tube, two different shell elements are marked (2701 and 2703) for future reference.

Here, an initial axial stress dependent on radial position through the shell thickness is applied to the whole tube shell structure following equation (76). The initial stress for an effective thickness of $t^* = 1nm$ is given as:

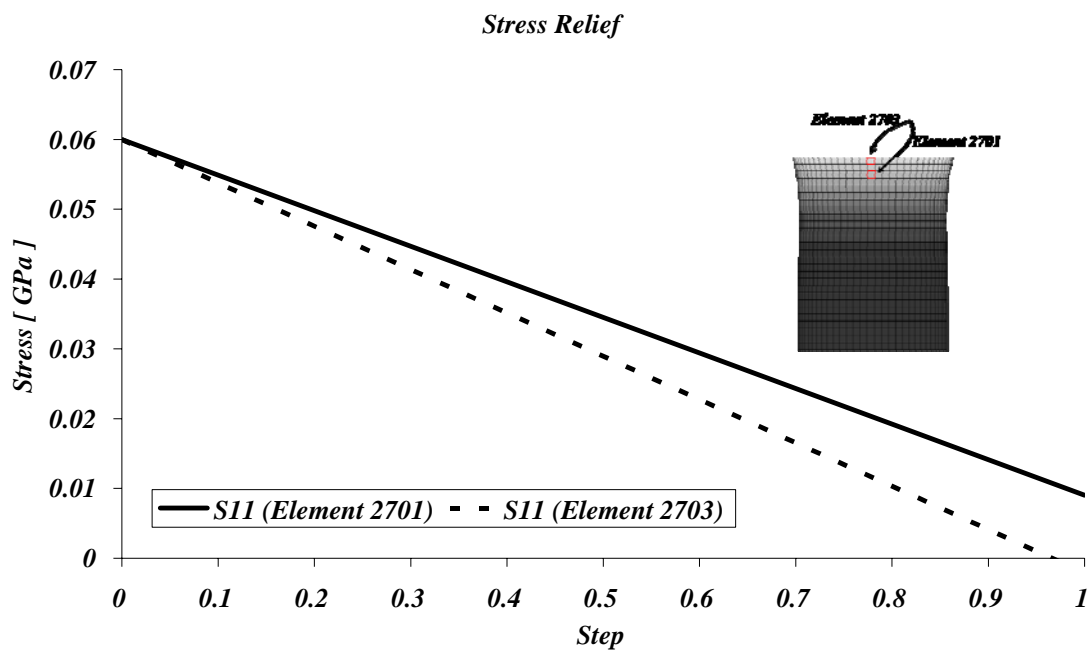
$$\sigma_{11,i} = E_{11}^* \frac{1}{\rho} (r - R_{avg}) = 2.4GPa \frac{1}{19nm} (r - 11.14nm). \quad (77)$$

Here r is the radial location of a point on the tube. For the external wall of the thin shell tube, $\left\{ R_o + \frac{t}{2} = 11.64nm \right\}$, the initial axial stress is calculated to be $0.06GPa$.

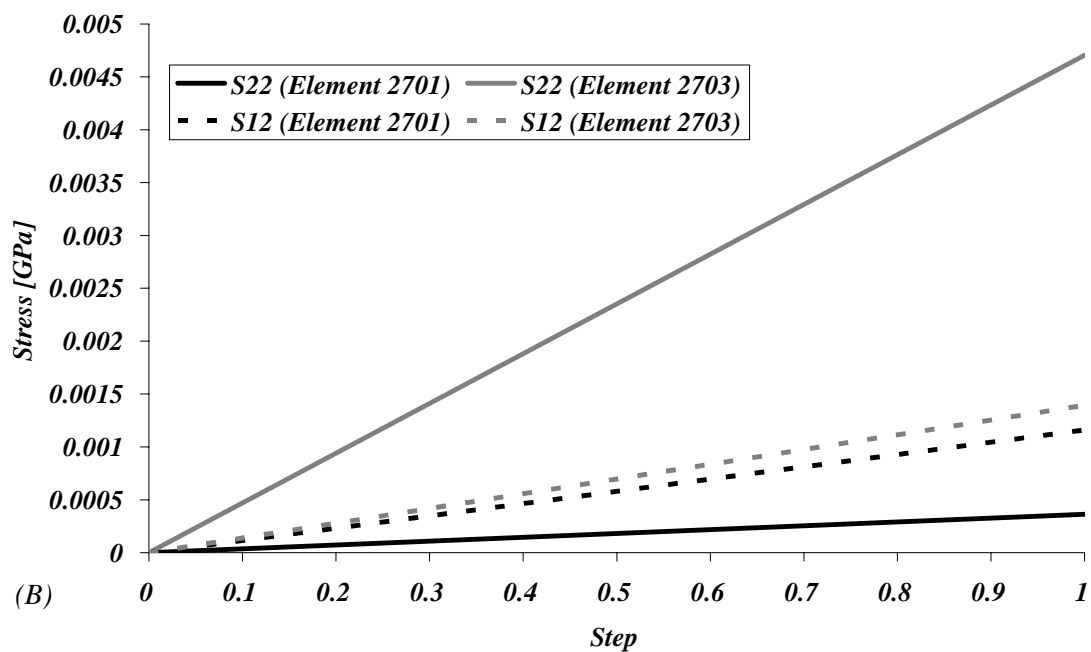
Figure 4-7 shows the deformed tip and the tube axial stress distribution upon letting the tube acknowledge the stress free tip boundary conditions. As the initially contained stress is relieved at the tip of the tube, the tip attempts to achieve the stress free curved conformation. In microtubules, since the dimers are all bound in a closed tube, the curving out cannot be realized. Instead, the energy released by GTP hydrolysis is stored as stress within the microtubule wall.

Figure 4-8, A shows that near the end of the microtubule, some relief of the built-in stress is exhibited. The release of the axial stress, results in a built-up of lateral stress in the microtubule. This can be explained in microtubules by the fact that the desired configuration is a cylindrical configuration for the dimers and any “peeling-off/curling-out” effect would result in the building up of stress in the lateral direction. In other words, in microtubules, depolymerisation does not require extra energy, the energy that is in the microtubule wall converts into the energy that is used to change the conformation of the microtubule, thus resulting in a lateral stress in the wall and eventually in the lateral bond breakage and depolymerisation.

Figure 4-8, B shows the tensile stress built-up in the lateral direction, S_{22} , and the shear stress built up, S_{12} . In the microtubule wall this corresponds to the intra-protofilament interactions. As mentioned earlier, the intra-protofilament interactions are much weaker than the inter-protofilament interactions in the microtubule wall. Therefore, it is expected that in the course of depolymerisation-disassembly, the lateral bonds will break much sooner than the longitudinal bonds. This effect is also referred as the “unzipping” effect where the lateral stress built-up in the microtubule wall eventually results in the bond breakage in the lateral direction. The lateral stress build-up is shown with the contour plots in Figure 4-9.



(A)



(B)

Figure 4-8 (A) The tensile stress relief in the 1-direction (tube axis direction, S_{11}) is shown (B) which results in the accumulation of lateral tensile stress (S_{22}) and shear stress (S_{12}).

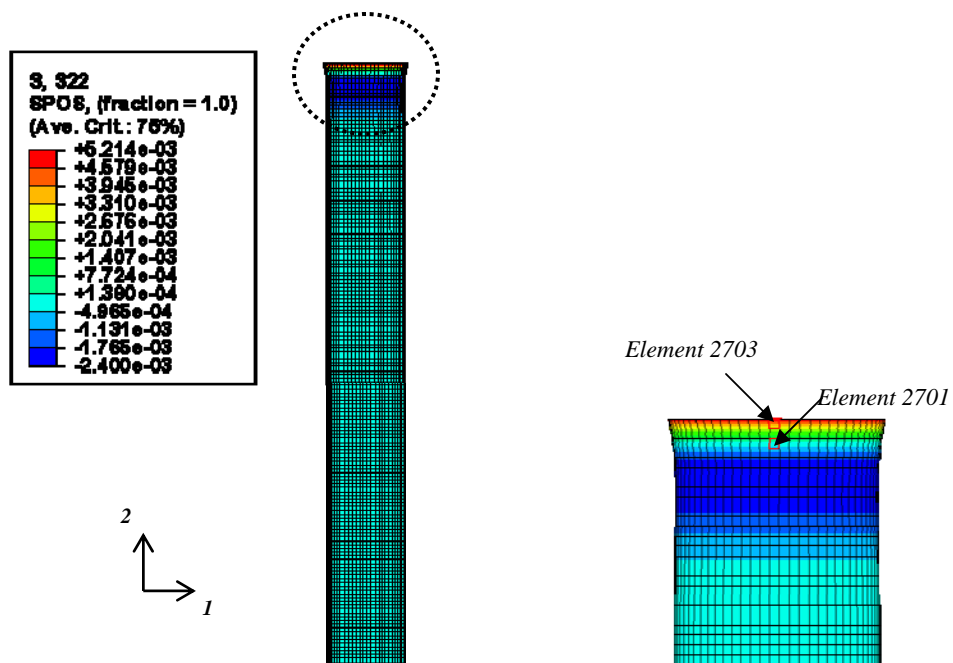


Figure 4-9 The plot shows the built-up of the lateral stress at the tip of the tube, two different shell elements are marked (2701 and 2703) for reference.

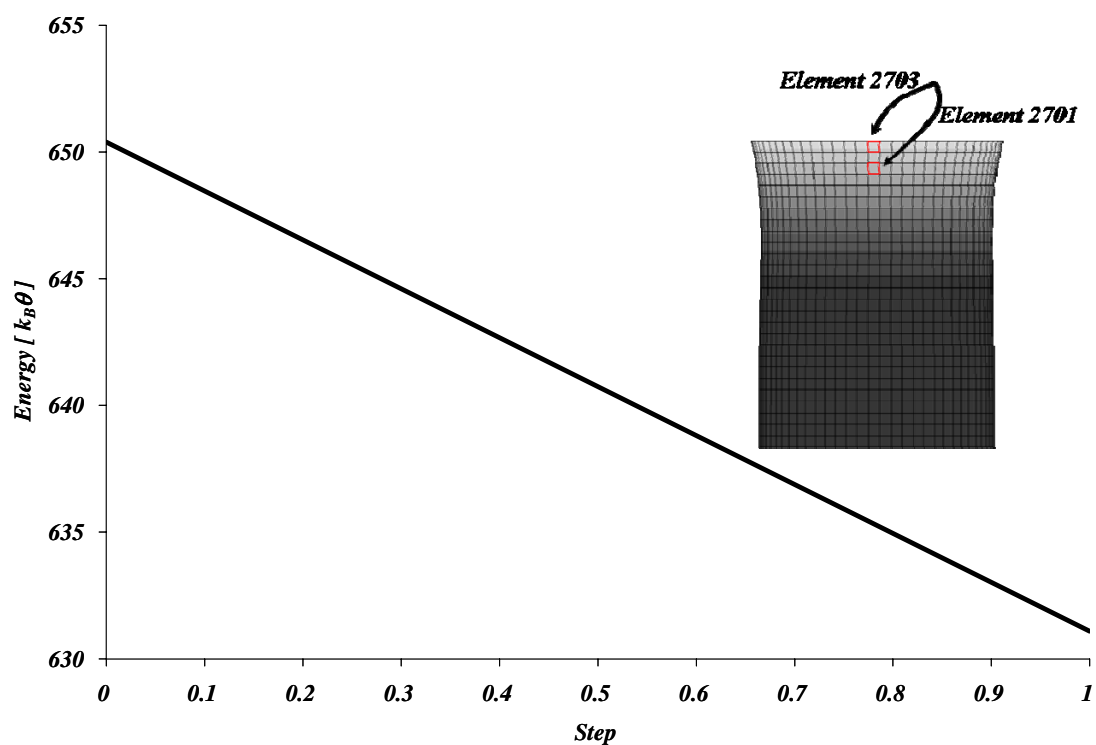


Figure 4-10 The plots shows the strain energy relief of the whole tube shell model; θ is chosen as 280 K.

Figure 4-10 shows the energy relief in the microtubule in a step-type incremented solution process. Microtubules are believed to have excess energy from their “assembly” process and this assembly energy can be thought of as the addition of the individual “curling out” energies of the constituent protofilaments. As mentioned in the beginning of the chapter, in the stochastic model of VanBuren et al. (2002), the estimated energy per 8 nm long dimer for this conformation change is $2.5 k_B\theta$. For a 160 nm tube, as shown here, this energy would amount to $20 \text{ dimers} \times 14 \text{ protofilaments} \times 2.5 k_B\theta = 700k_B\theta$.

With the prestress definition, this energy amounts to $650k_B\theta$ initially (shown in Figure 4-9) which is quite a close result (θ is chosen as 280 K; *depolymerization happens at low temperatures*). Following the stress relief, this energy drops to $\sim 630k_B\theta$. The initial energy in the tube here cannot be completely released. In order to model the release of more energy; i.e. unzipping of the microtubule wall, a “connector model” will be introduced. In this model, protofilament bending and breaking of the lateral bonds will be captured by using a typical protein-protein interaction function which was introduced in Chapter 1 (equation (2)) and in the beginning of this chapter (equation (72)).

Before we introduce the “connector model”, we will present a single strand analysis where the single strand will be assigned a monoclinic material behaviour and will mimic a portion of the microtubule wall that undergoes stress relief.

4.5.2. Single Strand Analysis

Microtubules grow by elongation of tubulin sheets that later close to form the cylindrical wall, whereas they depolymerise through the coiling of the protofilaments (in the presence of calcium or magnesium – which tend to accelerate the depolymerization process) and the eventual release of curled oligomers as we can see from the cryo-electron image by Muller-Reichert et al. (1998) given in Figure 4-11, A. The oligomer radii are roughly $\rho = 20\text{-}30 \text{ nm}$ (Mandelkow et al., 1991). GTP hydrolysis by increasing

the curvature of protofilaments forces them to peel off the microtubule wall. The coiling starts at the weakest points of the microtubule, the ends, thereby releasing the energy stored within the microtubule lattice. The effect of calcium and magnesium is likely linked to them weakening the lateral bonding in the microtubules.

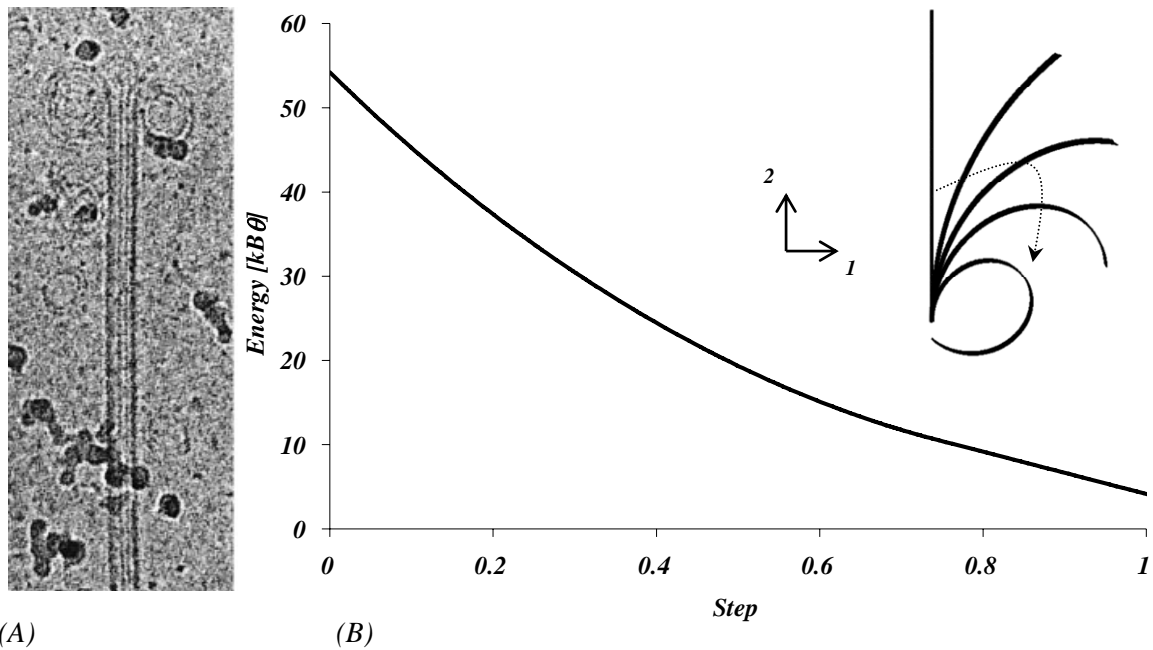


Figure 4-11 (A) Depolymerization at the tip of the microtubules in the presence of calcium Muller-Reichert *et al.* (1998), (B) The single strand finite element analysis showing the strain energy release from a single strand with the inset depicting the evolution of the conformation change in the strand with the stress release.

In Figure 4-11, a simulation which mimics the peeling off effect of the protofilaments of the microtubule wall is presented. In this finite element analysis:

➤ The material is linear elastic with properties as previously described:

$$E_{zz}^* = 2.4GPa, E_{\theta\theta}^* = 0.1GPa, G_{z\theta}^* = 0.012GPa, \nu_{z\theta} = 0.34, \nu_{16} = -1.2, \nu_{26} = 1.2.$$

➤ The length of the strand is 160 nm.

➤ The width of the strand is 5nm.

- The radius of curvature with respect to the tube axis of the strand is $R_o = 11.14 \text{ nm}$ (which would imply that 14 of these strands would form a whole cylindrical tube).
- A thin shell thickness of $t^* = 1 \text{ nm}$ is used.
- The strand is fixed at one end while the other end is set free.
- A prestress as defined by equation (76) is applied to the strand.
- Finite element analysis is performed using the software ABAQUS. The model consists of 3840 nodes and 3509 shell elements (S4R).

The strand is allowed to relieve the prestress which gives the curling into the intrinsic curvature (Figure 4-11, *B-inset*). Here the length of the strand is 160 nm which would correspond to about 20 dimers which would go into the desired configuration of about $\rho \sim 20 \text{ nm}$ radius of curvature to reduce the excess energy of $2.5 \times 20 = 50 k_B\theta$. The energy is completely released upon the formation of the oligomeric ring (Figure 4-11, B).

In living cells, microtubules help produce movement without additional chemical energy. In other words, they convert the strain energy into mechanical work. One example is the chromosome movement during mitosis as shown in Chapter 1. This is made possible by depolymerizing the microtubule lattice into strands made up of 1 or more protofilaments as shown here. This could be a very interesting application of the presented “single strand” model.

In the next section a new approach to the whole tube analysis will be presented. The release of the intrinsic energy upon depolymerisation will be shown incorporating the single strand behaviour presented here.

4.5.3. Connector Analysis

Energy related to hydrolysis allows the changing of the conformation of microtubules. This energy associated with the intrinsic curvature of the microtubule is completely

released during the catastrophic disassembly of the tube ends. The “whole tube model” introduced doesn’t capture the breaking of the lateral bonds of microtubules leading to disassembly. Therefore, in this section, a “connector model” will be introduced.

In order to enable an analysis of protofilament bending and the eventual breaking of lateral bonds between the protofilaments, the lateral protein-protein interactions are explained by the function introduced in the beginning of this chapter:

$$U^* = k \left(\frac{(r - r_o)}{r_o} \right)^2 \exp \left(- \frac{(r - r_o)}{r_o} \right) \text{ with equation (72). Here } r_o \text{ is the distance in which}$$

the bonds exert the maximum attractive force, $(r - r_o)$ characterizes the dimers’ deviation from the equilibrium configuration and k is a stiffness parameter. Molodtsov et al. (2005) estimated k to be 4.4 kcal/mol using the average activation energy barrier between the disassembly rates of two dimers (equation (74)). The potential function is recreated and shown with the corresponding force and stiffness of the bonds curve in Figure 4-12.

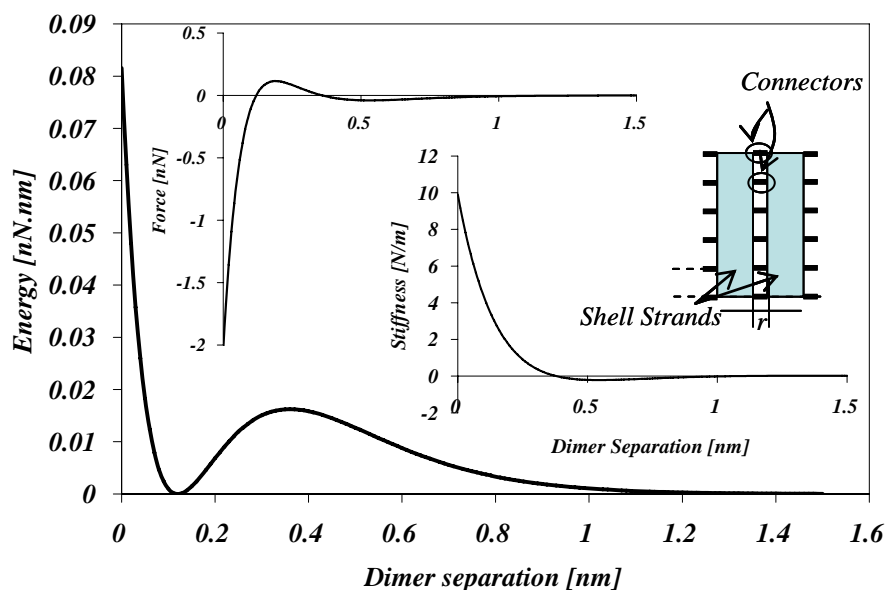


Figure 4-12 The potential function used for the lateral connectors depicting the corresponding force versus extension (dimer separation) and the related stiffness in the inset are created using equation (72) and taking the necessary derivatives with respect to the dimer separation.

The related force-extension behaviour is given as:

$$P_{connector} = \frac{k(r-r_o)}{r_o^2} \left(\frac{(r-r_o)}{r_o} - 2 \right) \exp\left(-\frac{(r-r_o)}{r_o} \right) \quad (78)$$

With a stiffness that varies with the applied extension:

$$\hat{k} = \frac{k}{r_o^2} \left(-\left(\frac{(r-r_o)}{r_o} \right)^2 + \frac{4(r-r_o)}{r_o} - 2 \right) \exp\left(-\frac{(r-r_o)}{r_o} \right) \quad (79)$$

The force versus dimer separation and the nonlinear stiffness is shown in Figure 4-12, inset. Note that the stiffness of the connectors is a highly nonlinear function which vanishes over a dimer separation of about “ $2r_o$ ”.

In this finite element analysis:

➤ The material is linear elastic with properties as previously described:

$$E_{11}^* = 2.4GPa, E_{22}^* = 0.1GPa, G_{12}^* = 0.012GPa, \nu_{12} = 0.34, \nu_{16} = -1.2, \nu_{26} = 1.2.$$

➤ A thin shell thickness of $t^* = 1nm$ is used.

➤ The length of the cylindrical tube is $160 nm$.

➤ The radius is $R_o = 11.14 nm$.

➤ 14 thin shells (single strands as shown in the previous section), with a characteristic separation of $0.12 nm$, are placed in a tube form and are connected by lateral elements whose behaviour is imposed by the given function in equation (6) by using “user defined element behaviour” in ABAQUS.

➤ The tube is fixed at one end while the other end is set free.

➤ A prestress as defined by equation (76) is applied to 14 thin shell strands.

➤ The model consists of 3159 nodes and 2080 shell elements (S4R). There are 21 connector springs in each of the thin strands, $21 \times 14 = 294$ in total separated by $8 nm$ (the dimer to dimer distance) along the microtubule’s body.

The initial undeformed conformation of the microtubule is given in Figure 4-13 showing the initial axial stress distribution.

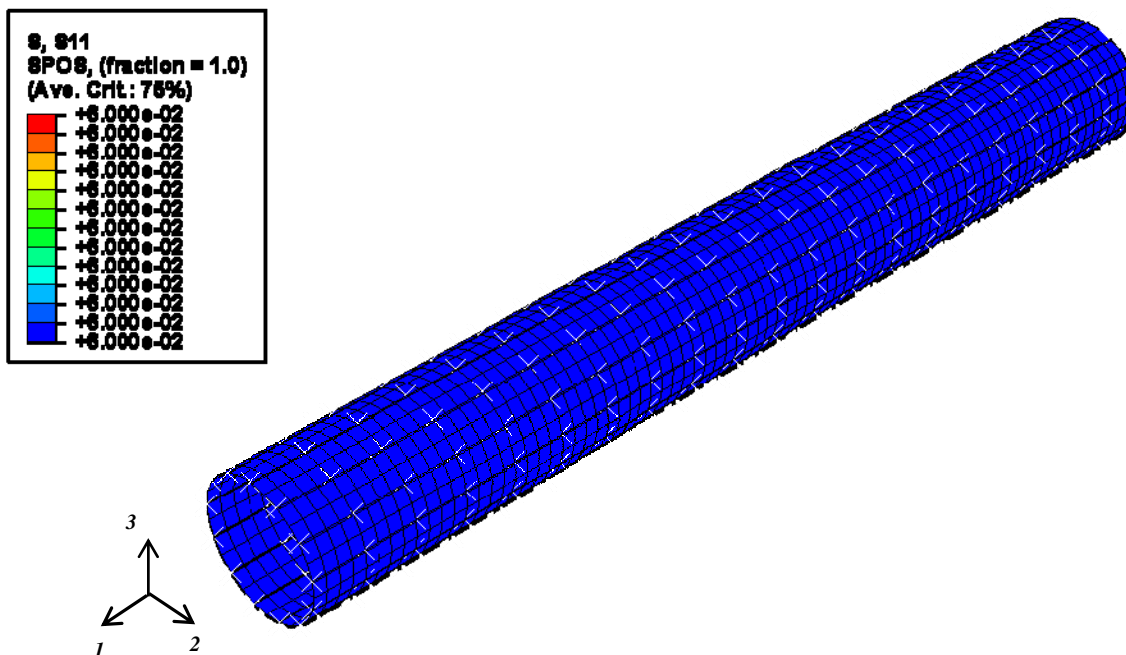


Figure 4-13 The undeformed configuration of the cylindrical tube with an axial prestress of 0.06 GPa at the most outer radial position.

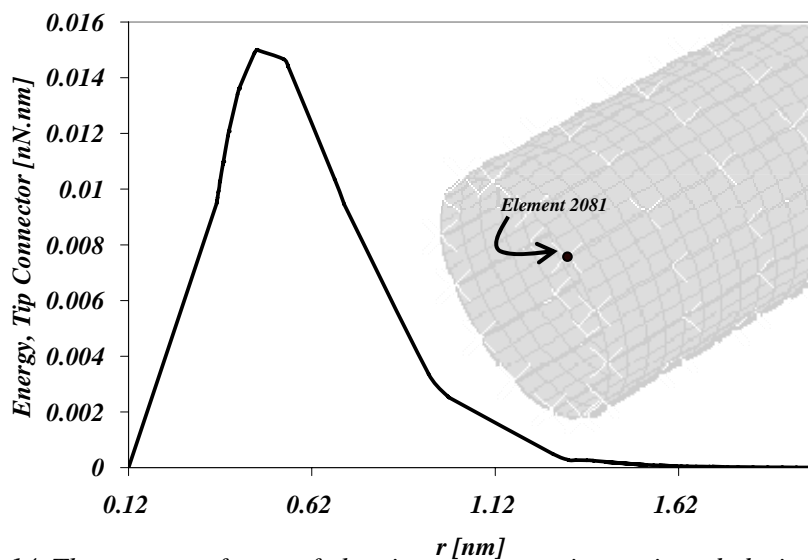


Figure 4-14 The energy of one of the tip connectors is monitored during the finite element analysis with respect to the tip radius change of the tube giving a profile showing the energy profile suggested by equation (72). The inset shows the tip of the tube with the related connector element.

In order to observe microtubule instability and the energy levels associated with it, the cylindrical tube is allowed to release the applied initial axial stress by a step-type static analysis. The excess axial bending stress distribution in the microtubule body causes an unfavourable condition laterally in the microtubule. Although it is favourable for the microtubules to curl out at the ends, they also desire to stay in the cylindrical shape. The longitudinal initial stress caused by the unstable GDP results in high lateral stresses which cause an energy shift in the microtubule. The longitudinal stress is converted into the conformation change of the microtubule and even to catastrophe eventually in some cases.

Figure 4-14 shows the energy state of the connector element 2081; from the initial set of connectors; the tip connectors. Characteristically, at an initial distance of $r = 0.12 \text{ nm}$ (Molodtsov et al., 2005), the connectors exert the maximum attractive force corresponding to the zero-energy level. With the effect of the initial stress imposed, the connectors stretch leading to an increase in their energy. The element follows the protein-protein interaction characteristic behaviour with a characteristic peak in the potential level which drops to zero when the bond breaks at about a stretch of $r - r_o = 1.5 \text{ nm}$.

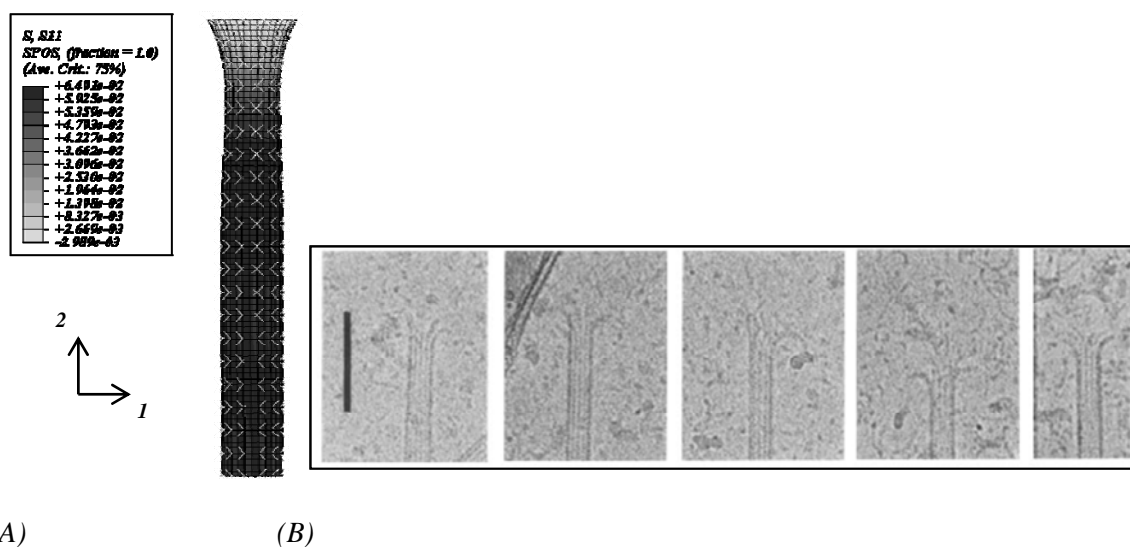


Figure 4-15 (A) The pictures shows the deformed contours of the cylindrical tube after the prestress is allowed to release, the tip elements are stress-free, (B) Similar conformations have been observed in the literature by researchers (Mandelkow et al., 1991).

Figure 4-15, *A* shows the final configuration of the strands constituting the cylindrical tube after the analysis is completed. The initial average tip radial coordinate of 11.14 nm expands to a radius of 14.0 nm owing to the breakage of the first set of lateral connectors (Figure 4-16). This conformation is also known as “tapered end” conformation. Figure 4-15, *B* shows the shrinking of microtubules observed by Mandelkow et al. (1991) resembling the conformation observed from the simulation.

The probability of a given microtubule switching into a more or less stable state is related to the energy stored in the lattice. Next we will investigate whether the excess energy stored in the 14-protofilament lattice due to the intrinsic curvature of the microtubules would be sufficient to destabilize the capping region and induce the catastrophe of the microtubule; i.e. would all the connectors break resulting in the disassembly of the microtubule strands?

As shown in Figure 4-16, the tip of the microtubule expands out to a radius of $\sim 14.0 \text{ nm}$ under its own forces. This would amount to a radial expansion of 3 nm , which would impose a “curling out angle” of about 21° for a dimer of length 8 nm [the distance between 2 connectors; i.e. the dimer-dimer distance]. Here we can observe that the 22° “curling out angle” measured by Muller-Reichert et al. (2002) using cryo-electron microscopic images has been realized when the analysis is completed.

The stress accumulation in the microtubule tube lattice is referred to as the “unfavorable conditions” by Hunyadi et al. (2005). The researchers suggested that 2D microtubule sheets may act as capping structures allowing the incorporation of unfavorable configurations. The stress accumulation (shear stress and tangential stress; i.e. S_{12} and S_{22}) in our model is shown in Figure 4-17, *A*.

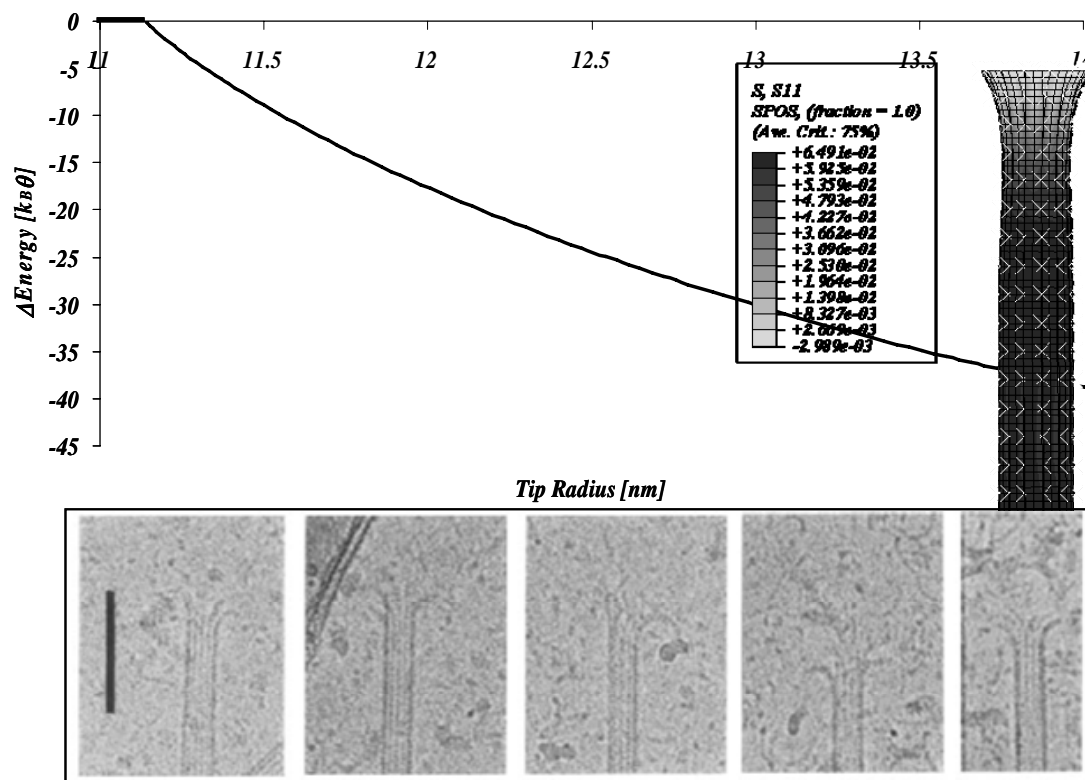


Figure 4-16 The plot shows the “energy change” associated with the prestress release for the model. A comparison of the contour plot and cryo-electron microscope images (Mandelkow et al., 1991) are shown.

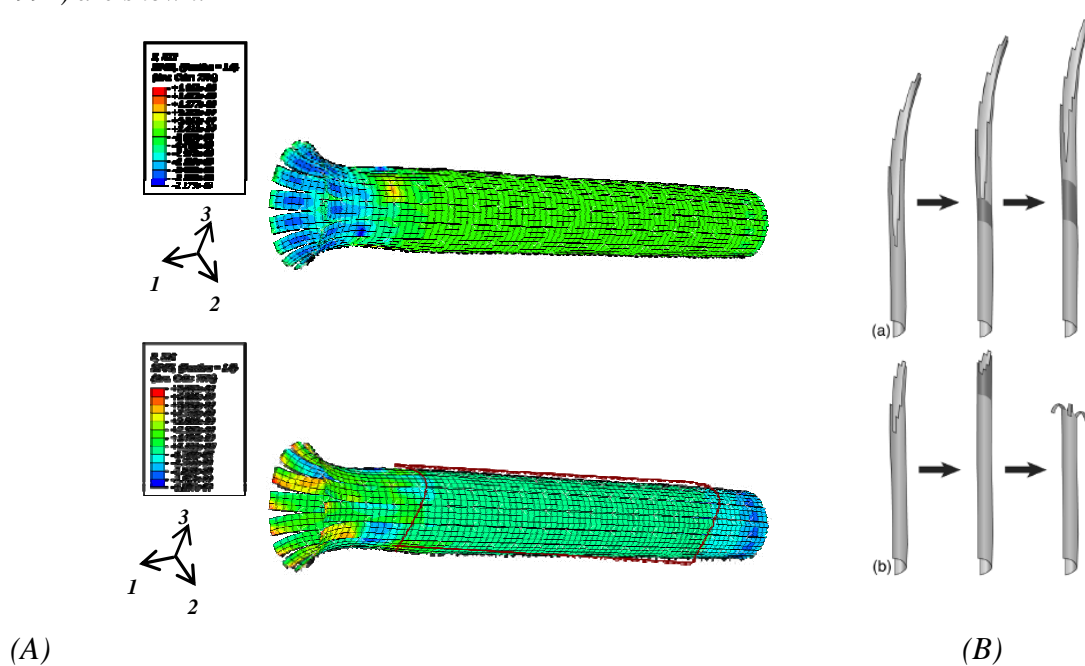
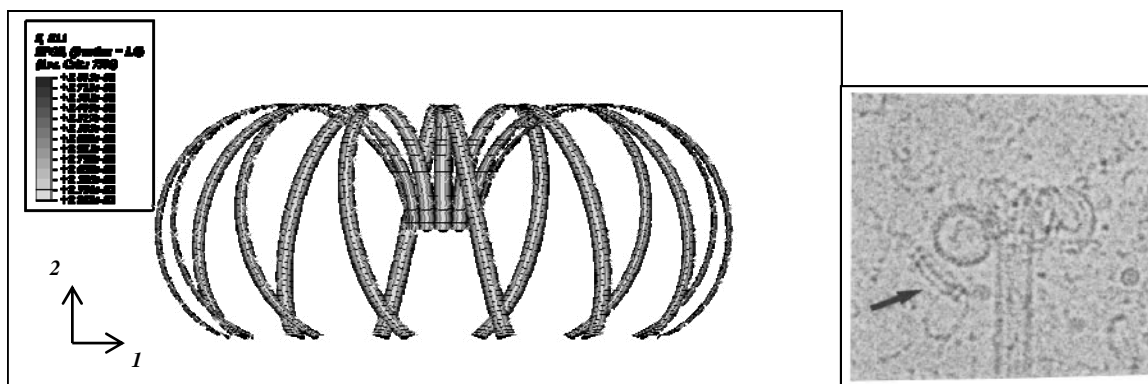


Figure 4-17 (A) The contours for the cylindrical tube showing the accumulated lateral stress and the shear stress causing an unfavourable condition for the tube, (B) This unfavourable condition was discussed earlier with this sketch by Hunyadi et al. (2005).

The release of the energy from the tip of the microtubule (i.e. the breaking of one set of connectors and the stretching of the second set of connectors) results in the conformation change in the microtubule. As the microtubule realizes the “tapered” configuration some the relative energy potential of the microtubule drops; however the total energy doesn’t drop to zero owing to the lateral stresses stored in the microtubule wall (Figure 4-16) to be released upon being exposed to different environmental conditions (calcium or magnesium ion concentration, concentration of monomers, temperature, surrounding pressure, etc...).

In experimental studies (Mandelkow et al., 1991; Muller-Reichert et al., 2002), the length of the curling out protofilaments/flaring out 2D microtubule sheets were observed to depend on the buffer condition but in any case to acquire a radius of curvature similar to that of the oligomeric rings (as seen in the “Single Strand Analysis”). Mandelkow et al. (1991) referred to the “tapering” response as “moderate peeling” where the curled out ends are shorter than the oligomeric ring circumferences. The researchers later realized the “coiling” effect (Figure 4-18, B) by inducing Mg^{2+} to the buffer. Oligomers are then observed.



(A)

(B)

Figure 4-18 (A) The simulation result having changed the connector stiffness down to about 0.001 N/m resulting in breaking of them under the induced prestress showing the “catastrophe” form. (B) The cryo-electron microscopic image shows the depolymerization and “coiling out” of microtubules in the presence of calcium (Muller-Reichert et al., 1998).

In order to demonstrate that the proposed model is able to capture the complete depolymerization; i.e. the stress release effect being sustained moving down the tube; we altered the properties of the connectors. With an initial connector stiffness of $\sim 0.001 \text{ N/m}$ (Figure 4-12), one can realize a coiled microtubule configuration from a “tapered-ended” tube by the change of all the chemical energy in the tube to mechanical energy. This is also referred to as “catastrophe” and could be caused by many factors such as addition of agents in the microtubule buffer, as mentioned earlier, which would lower the lateral bond strength of the microtubules or microtubule’s interaction with microtubule associated proteins.

Our results, thus, support the idea that some of the chemical energy from GTP hydrolysis is stored in the lattice as mechanical stress, ready to be released when depolymerisation is triggered by different means.

The net effect of the catastrophe is that the straight part of the tube is shortened and this shortened length is then turned into rolled up protofilaments forming the so-called “Rams’ horns” (Figure 4-18).

It should be noted here that owing to the monoclinic structure of the constituent strands of the tube, the “coiling out” of the strands is in an angular way (Figure 4-18, A). This is due to the helical structure of the microtubules and could be further analyzed in future work. This is also known as the “conformation cap” destabilization. This is realized in the microtubules in cryo-electron microscope images but only from a limited end length of a microtubule.

Microtubules in reality are found in different protofilament numbers and different helix start numbers. Chretien and Fuller discussed in one of their articles (2000) that the microtubule lattice is believed to accommodate these different configurations by skewing the protofilaments so that the lateral interactions between tubulin subunits are maintained. They also believe that microtubules switch occasionally into unfavourable configurations as a direct consequence of their two-dimensional assembly process.

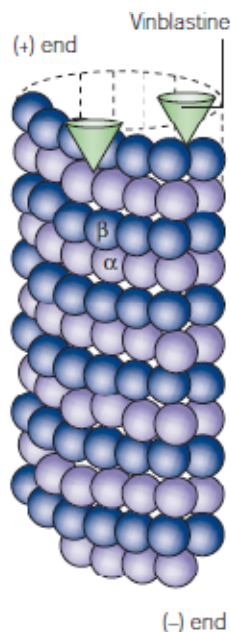


Figure 4-19 A few molecules of Vinblastine bound to the microtubule end to suppress microtubule dynamics (Jordan and Wilson, 2004).

The addition of agents can alter the mechanical behavior of the microtubules in a grand aspect. For instance a microtubule-targeted cancer drug Vinblastine as shown in Figure 4-19, connects to the microtubule lattice. Vinblastine binds to the lattice structure of the microtubules altering the microtubule dynamics to avoid the cell division to inhibit cancer cell multiplication. The agents interact laterally with the dimers, changing the bonding features of the microtubule resulting in an alteration of the microtubule elastic properties and ultimately the microtubule dynamic behavior.

We can view this as one of the applications of the proposed model. By altering the connector nature and the properties, one can observe the effects adding different agents to the microtubule lattice as their binding characteristics are geometry related.

Another application of the proposed model is the force production mechanisms of the depolymerizing microtubules. There is ongoing research (Molodtsov et al. 2005; Grischuck et al., 2005 and Laan et al., 2008) on measuring the force production of microtubules over characteristic distances. This model would help monitor the force production mechanisms to be able to discuss the nature of the deformations involved and the possible nonlinear forces produced, as well as the effect of the force production on the rest of the microtubule.

4.6. Discussion and Concluding Remarks

In this chapter, we extended the effective continuum model for the microtubules to include the effects of polymerizing-depolymerizing dynamics. The model proposed here provides a new link between the biophysical characteristics of microtubules and their physiological behaviour.

Following GTP hydrolysis, tubulin conformation changes from a straight to a curved form leaving the core of the microtubule in a strained condition. In some microtubules, GTP hydrolysis can be observed in extended flat sheets. The sheets relax some of their elastic stresses by adopting a curved configuration, bending out longitudinally. This type of a tapered-end is observed to be much more stable than a closed tube.

Here, introducing an initial stress-state function, a discrete model made up of 14 thin shell strands mimicking a microtubule is presented. In order to incorporate the breaking of the lateral bonds, the lateral dimer-dimer interactions are approximated by a typical protein-protein interaction potential function. Allowing the strands to change conformation under their own forces, a tapered configuration for the microtubule is obtained. The advantage of the proposed model is that the protofilament bending is not restricted to one plane as given in some of the previous work (Janosi et al., 2002 and Molodtsov et al., 2005) but has a more complex formation of two-dimensional sheet bending. This provides a more realistic approach for future applications. A change in the strength of the lateral bonds between protofilaments is sufficient to cause the disassembly of the microtubule to form the coiled out configuration (“ram’s horns”).

In this work, cryo-electron microscopy images of microtubules “in vitro” have been utilized for comparison. It was shown in the literature (Pierson et al., 1978; Langford 1980 and Chretien et al., 1992) that microtubules assembled in vitro are usually of 14 protofilaments. The two-dimensional “tapered-out sheets” have been observed both in

vivo and in vitro. Thus, the proposed model is believed to shed light on the microtubule dynamics both in vivo and in vitro.

The addition of the seam (see: Chapter 1) would bring a new dimension to this study. Dimer attachment to a non-helical microtubule; i.e. a bond formation between an α and β monomer laterally, would result in an instability laterally. This mismatch could explain the preferred opening up of the two-dimensional sheets. It would require a higher lateral force to disassociate the mismatch as the α and β monomer interactions are reported to be stronger than the conventional α and α monomer and β and β monomer interactions.

Résumé

Dans ce chapitre, le modèle continu de comportement mécanique des microtubules est complété de manière à considérer les phénomènes dynamiques de polymérisation-dépolymérisation. Le modèle proposé ici permet de relier les caractéristiques biophysiques des microtubules et leur comportement physiologique.

Suite à l'hydrolyse du GTP, la conformation des tubulines, auparavant droite, présente, une courbure vers l'extérieur. Dans certains microtubules, l'hydrolyse du GTP peut être observée pour des plans plats étirés. Une partie de leur contrainte élastique est relaxée aboutissant à la courbure radiale vers l'extérieur. Cette configuration est avérée plus stable qu'un tube ferme.

Dans ce chapitre, en considérant un état de contrainte initial, un modèle discret composé de 14 filaments d'éléments coques est utilisé pour représenter le microtubule. De plus, en vue d'intégrer la rupture des liaisons, les interactions latérales entre dimères sont approchées par une fonction potentielle d'interaction protéine-protéine. En permettant aux bandes de changer de conformation sous l'effet de leur propre force, une nouvelle configuration du microtubule est obtenue. L'avantage du modèle proposé repose sur le fait que la flexion du protofilament n'est pas réduite à un plan unique comme simulé dans

de précédents travaux (Janosi et al., 2002 and Molodtsov et al., 2005) mais conduit à la flexion d'un plan plus complexe aboutissant à une approche plus réaliste en vue d'applications futures. La modification de la résistance des liaisons latérales entre protofilaments suffit à provoquer le démantèlement du microtubule pour former la configuration présentée plus haut et identifiée à des « cornes de bélier » dans la littérature (Mandelkow et al., 1991).

De plus, des images de microscopie électronique à balayage cryogénisé de microtubules “in vitro” ont été utilisées pour comparaison. Il a été montré dans la littérature (Pierson et al., 1978; Langford 1980 and Chrétien et al., 1992) que les microtubules assemblées in vitro sont pour la plupart formées de 14 protofilaments. Des observations in vivo et in vitro ont montré que le plan obtenu est légèrement incurvé à ses extrémités. Aussi, le modèle proposé semble rendre compte du comportement dynamique des microtubules à la fois in vivo et in vitro.

Compléter le présent travail de recherche en associant les discontinuités hélicoïdales (voir chapitre 1) permettrait une étude plus aboutie. L'attache des dimères à un microtubule non-hélicoïdal (i.e. la formation d'une liaison latérale entre les monomères α et β , conduirait à une instabilité latérale. Cette discontinuité pourrait expliquer la préférence des microtubules à s'écarter à leur extrémité. Un tel phénomène nécessiterait des forces latérales plus importantes pour pouvoir dissocier l'imperfection vu que les interactions α - β , sont reportées plus fortes que les interactions α - α et β - β .

APPENDICES

Appendix 2-1

Formulation of the Constitutive Relationships

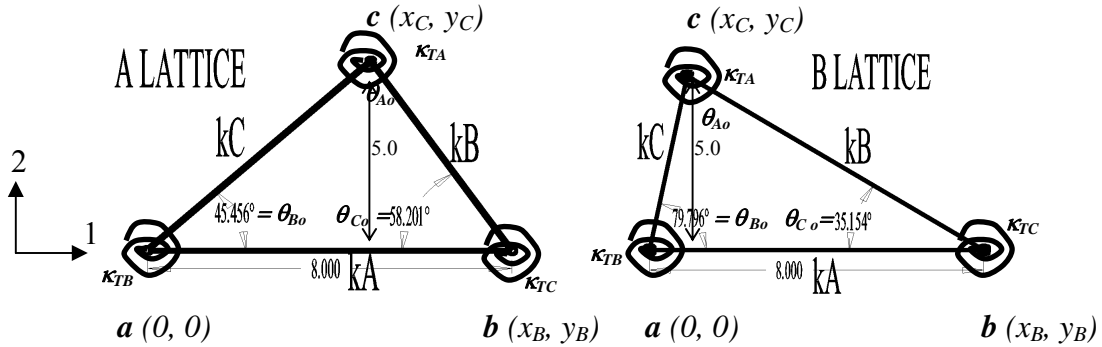


Figure A1.1 The undeformed configurations of the seamless lattice structures of A and B for 13 protofilament- and 14 protofilament-microtubules respectively.

In the undeformed configuration, the lengths of the bonds are calculated as follows;

$$L_{Ao} = \sqrt{x_{Bo}^2 + y_{Bo}^2} = 8 \quad (A1.1)$$

$$L_{Bo} = \sqrt{(x_{Co} - x_{Bo})^2 + (y_{Co} - y_{Bo})^2} = \left(\frac{5}{\sin(\theta_{Co})} \right), \quad (A1.2)$$

$$L_{Co} = \sqrt{x_{Co}^2 + y_{Co}^2} = \left(\frac{5}{\sin(\theta_{Bo})} \right). \quad (A1.3)$$

At any instant these lengths are given in terms of the displacements of the junctions and the initial coordinates of them as;

$$L_A = \sqrt{(x_{Bo} + u_{b1})^2 + (y_{Bo} + u_{b2})^2}, \quad (A1.4)$$

$$L_B = \sqrt{\{(x_{Co} + u_{c1}) - (x_{Bo} + u_{b1})\}^2 + \{(y_{Co} + u_{c2}) - (y_{Bo} + u_{b2})\}^2}, \quad (A1.5)$$

$$L_C = \sqrt{(x_{Co} + u_{c1})^2 + (y_{Co} + u_{c2})^2}. \quad (\text{A1.6})$$

This helps calculate the stretches for each bond;

$$\lambda_A = \frac{L_A}{L_{Ao}}, \lambda_B = \frac{L_B}{L_{Bo}}, \lambda_C = \frac{L_C}{L_{Co}}. \quad (\text{A1.7})$$

For an arbitrary planar deformation gradient, $\mathbf{F} = \begin{bmatrix} F_{11} & F_{12} \\ F_{21} & F_{22} \end{bmatrix}$, the displacement for each junction (dimer center) is calculated using:

$$\mathbf{u}_i - \mathbf{u}_j = (\mathbf{F} - \mathbf{I})(\mathbf{X}_i - \mathbf{X}_j). \quad (\text{A1.8})$$

Here \mathbf{u}_i is the displacement of the junction point i and \mathbf{X}_i is the initial coordinates of the given junction.

Working through this equation, the displacements of the junctions are given as:

$$\mathbf{u}_{a1} = 0, \mathbf{u}_{a2} = 0, \quad (\text{A1.9})$$

$$\mathbf{u}_{b1} = 8(F_{11} - 1), \mathbf{u}_{b2} = 8F_{21}, \quad (\text{A1.10})$$

$$\mathbf{u}_{c1} = \frac{5}{\tan(\theta_{Bo})} F_{12} + \frac{5}{\tan(\theta_{Bo})} (F_{11} - 1), \mathbf{u}_{c2} = \frac{5}{\tan(\theta_{Bo})} (F_{22} - 1) + \frac{5}{\tan(\theta_{Bo})} F_{21}. \quad (\text{A1.11})$$

Here 1 and 2 denote the material coordinate points which would transform as the longitudinal and the lateral directions for the microtubule respectively.

Appendix 2-2

Formulation of the Torsional Potential

In the present work, we ignored any torsional potential at the junction points (as marked in Figure A1.1) due to the lack of information on the exact bond energies.

The angles of the constituent bonds could be calculated as follows;

$$\theta_A = \cos^{-1} \left(\frac{L_A^2 - L_B^2 - L_C^2}{2L_B L_C} \right), \quad (\text{A2.1})$$

$$\theta_B = \cos^{-1} \left(\frac{L_B^2 - L_A^2 - L_C^2}{2L_A L_C} \right), \quad (\text{A2.2})$$

$$\theta_C = \cos^{-1} \left(\frac{L_C^2 - L_A^2 - L_B^2}{2L_A L_B} \right). \quad (\text{A2.3})$$

The angles can be rewritten in terms of the applied deformation gradient using the expressions (A1.4-6) and (A1.9-11).

This would allow define the density of the potential for the torsional stiffnesses which would be expressed in terms of the contribution from each bond angle's torsional potential as:

$$\mathcal{U}_T^* = \frac{1}{2\mathcal{A}_{triangle}} (\mathcal{U}_{T\theta_A} + \mathcal{U}_{T\theta_B} + \mathcal{U}_{T\theta_C}). \quad (\text{A2.4})$$

The torsional potential of each angle ($i = A, B, C$) is expressed as;

$$\mathcal{U}_{T\theta_i} = \frac{1}{2} k_{Ti} (\theta_i - \theta_{i0})^2 \quad (\text{no sum on } i). \quad (\text{A2.5})$$

The contribution to the Cauchy Stress expression (equation (20) in Chapter 2) would be expressed as follows;

$$\mathbf{T}_T = \frac{1}{J} \left(\frac{\partial \mathcal{U}_T^*}{\partial \mathbf{F}} \right) \mathbf{F}^T \quad (\text{A2.6})$$

which can also be written as;

$$\mathbf{T}_T = \left[\frac{\partial(\mathcal{U}_{T\theta A}^*)}{\partial(\theta_A)} \frac{\partial(\theta_A)}{\partial(\mathbf{F})} + \frac{\partial(\mathcal{U}_{T\theta B}^*)}{\partial(\theta_B)} \frac{\partial(\theta_B)}{\partial(\mathbf{F})} + \frac{\partial(\mathcal{U}_{T\theta C}^*)}{\partial(\theta_C)} \frac{\partial(\theta_C)}{\partial(\mathbf{F})} \right] \mathbf{F}^T. \quad (\text{A2.7})$$

The total Cauchy Stress would be addition of the stretching and the torsional components;

$$\mathbf{T} = \mathbf{T}_S + \mathbf{T}_T = \frac{1}{J} \left\{ \left(\frac{\partial \mathcal{U}_T^*}{\partial \mathbf{F}} \right) \mathbf{F}^T + \left(\frac{\partial \mathcal{U}_S^*}{\partial \mathbf{F}} \right) \mathbf{F}^T \right\}, \quad (\text{A2.8})$$

where the stretching component was given in the text (equation (21)) as;

$$\mathbf{T}_S = \frac{1}{J} \left[\frac{\partial(\mathcal{U}_A^*)}{\partial(\lambda_A)} \frac{\partial(\lambda_A)}{\partial(\mathbf{F})} + \frac{\partial(\mathcal{U}_B^*)}{\partial(\lambda_B)} \frac{\partial(\lambda_B)}{\partial(\mathbf{F})} + \frac{\partial(\mathcal{U}_C^*)}{\partial(\lambda_C)} \frac{\partial(\lambda_C)}{\partial(\mathbf{F})} \right] \mathbf{F}^T. \quad (\text{A2.9})$$

Solving for the constitutive relationship in the case where the torsional potential is included would require the estimation of the torsional stiffnesses: $k_{T\theta A}$, $k_{T\theta B}$, $k_{T\theta C}$ as well as the bond stretching coefficients: k_A , k_B , k_C . Because of the lack of experimental data, this thesis work ignored the torsional potentials at the junction points.

Appendix 2-3

Material Stiffness Matrix Derivations

Engineering matrix mapping of stress T into e strain tensors written as “vectors”:

$$\begin{bmatrix} T_{11} \\ T_{22} \\ T_{33} \\ T_{23} \\ T_{13} \\ T_{12} \end{bmatrix} = \begin{bmatrix} C_{1111} & C_{1122} & C_{1133} & C_{1123} & C_{1112} & C_{1113} \\ & C_{2222} & C_{2233} & C_{2223} & C_{2213} & C_{2212} \\ & & C_{3333} & C_{3323} & C_{3313} & C_{3312} \\ sym & & & C_{2323} & C_{2313} & C_{2312} \\ & & & & C_{1313} & C_{1312} \\ & & & & & C_{1212} \end{bmatrix} \begin{bmatrix} e_{11} \\ e_{22} \\ e_{33} \\ \gamma_{23} \\ \gamma_{13} \\ \gamma_{12} \end{bmatrix} \quad (\text{A3.1})$$

This equation can also be written as:

$$\begin{bmatrix} T_{11} \\ T_{22} \\ T_{33} \\ T_{23} \\ T_{13} \\ T_{12} \end{bmatrix} = \begin{bmatrix} C_{11} & C_{12} & C_{13} & C_{14} & C_{15} & C_{16} \\ & C_{22} & C_{23} & C_{24} & C_{25} & C_{26} \\ & & C_{33} & C_{34} & C_{35} & C_{36} \\ sym & & & C_{44} & C_{45} & C_{46} \\ & & & & C_{55} & C_{56} \\ & & & & & C_{66} \end{bmatrix} \begin{bmatrix} e_{11} \\ e_{22} \\ e_{33} \\ \gamma_{23} \\ \gamma_{13} \\ \gamma_{12} \end{bmatrix} \quad (\text{A3.2})$$

A similar relation employing compliance matrix is represented as:

$$e_{ij} = \sum_{k=1}^3 \sum_{l=1}^3 S_{ijkl} T_{kl} \quad (\text{A3.3})$$

with the matrix form as:

$$\begin{bmatrix} e_{11} \\ e_{22} \\ e_{33} \\ \gamma_{23} \\ \gamma_{13} \\ \gamma_{12} \end{bmatrix} = \begin{bmatrix} S_{11} & S_{12} & S_{13} & S_{14} & S_{15} & S_{16} \\ & S_{22} & S_{23} & S_{24} & S_{25} & S_{26} \\ & & S_{33} & S_{34} & S_{35} & S_{36} \\ sym & & & S_{44} & S_{45} & S_{46} \\ & & & & S_{55} & S_{56} \\ & & & & & S_{66} \end{bmatrix} \begin{bmatrix} T_{11} \\ T_{22} \\ T_{33} \\ T_{23} \\ T_{13} \\ T_{12} \end{bmatrix} \quad (\text{A3.4})$$

The advantage of using compliance matrix rather than the stiffness matrix is the ease of expressing the compliance matrix elements by engineering constants.

By expressing relation (A3.4) using Hooke's terms of engineering constants; the S matrix can be rewritten as:

$$\begin{bmatrix} e_{11} \\ e_{22} \\ e_{33} \\ \gamma_{23} \\ \gamma_{13} \\ \gamma_{12} \end{bmatrix} = \begin{bmatrix} \frac{1}{E_{11}} & \frac{-\nu_{12}}{E_{11}} & \frac{-\nu_{13}}{E_{11}} & \frac{-\nu_{14}}{E_{11}} & \frac{-\nu_{15}}{E_{11}} & \frac{-\nu_{16}}{E_{11}} \\ & \frac{1}{E_{22}} & \frac{-\nu_{23}}{E_{22}} & \frac{-\nu_{24}}{E_{22}} & \frac{-\nu_{25}}{E_{22}} & \frac{-\nu_{26}}{E_{22}} \\ & & \frac{1}{E_{33}} & \frac{-\nu_{34}}{E_{33}} & \frac{-\nu_{35}}{E_{33}} & \frac{-\nu_{36}}{E_{33}} \\ & sym & & \frac{1}{G_{23}} & \frac{-\nu_{45}}{G_{23}} & \frac{-\nu_{46}}{G_{23}} \\ & & & & \frac{1}{G_{13}} & \frac{-\nu_{56}}{G_{13}} \\ & & & & & \frac{1}{G_{12}} \end{bmatrix} \begin{bmatrix} T_{11} \\ T_{22} \\ T_{33} \\ T_{23} \\ T_{13} \\ T_{12} \end{bmatrix} \quad (A3.5)$$

Or equivalently, using simple symmetry arguments; the e matrix is given as:

$$\begin{bmatrix} e_{11} \\ e_{22} \\ e_{33} \\ \gamma_{23} \\ \gamma_{13} \\ \gamma_{12} \end{bmatrix} = \begin{bmatrix} \frac{1}{E_{11}} & \frac{-\nu_{21}}{E_{22}} & \frac{-\nu_{31}}{E_{33}} & \frac{-\nu_{41}}{G_{23}} & \frac{-\nu_{51}}{G_{13}} & \frac{-\nu_{61}}{G_{12}} \\ & \frac{1}{E_{22}} & \frac{-\nu_{32}}{E_{33}} & \frac{-\nu_{42}}{G_{23}} & \frac{-\nu_{52}}{G_{13}} & \frac{-\nu_{62}}{G_{12}} \\ & & \frac{1}{E_{33}} & \frac{-\nu_{43}}{G_{23}} & \frac{-\nu_{53}}{G_{13}} & \frac{-\nu_{63}}{G_{12}} \\ & sym & & \frac{1}{G_{23}} & \frac{-\nu_{54}}{G_{13}} & \frac{-\nu_{64}}{G_{12}} \\ & & & & \frac{1}{G_{13}} & \frac{-\nu_{65}}{G_{12}} \\ & & & & & \frac{1}{G_{12}} \end{bmatrix} \begin{bmatrix} T_{11} \\ T_{22} \\ T_{33} \\ T_{23} \\ T_{13} \\ T_{12} \end{bmatrix} \quad (A3.6)$$

It's important to note that $z=0$ is the symmetry plane for the 3-dimensional behaviour of the microtubules. Such material behaviour is called 'monoclinic material behaviour'. Crystals whose crystalline structure is monoclinic are examples of materials possessing a

single plane of elastic symmetry (Solecki and Conant, 2003). For such materials, the elastic coefficients in the stress-strain law must remain unchanged when subjected to a transformation that represents a reflection in the symmetry plane. If $z=0$ is the symmetry plane, such a transformation is represented by;

$$x' = x, y' = y, z' = -z \quad (\text{A3.7})$$

The number of independent elastic constants for monoclinic materials is 13. In contrast to isotropic materials, each normal stress depends on the shear strain e_{12} and the shear stress T_{12} depends on all of the three normal strains. Only the shear stresses T_{23} and T_{13} are independent of the normal strains. However all of these strains depend on both shear strains e_{23} and e_{13} . In other words; the stiffness matrix reduces to:

$$C = \begin{bmatrix} C_{11} & C_{12} & C_{13} & 0 & 0 & C_{16} \\ & C_{22} & C_{23} & 0 & 0 & C_{26} \\ & & C_{33} & 0 & 0 & C_{36} \\ & \text{sym} & & C_{44} & C_{45} & 0 \\ & & & & C_{55} & 0 \\ & & & & & C_{66} \end{bmatrix} \quad (\text{A3.8})$$

Appendix 3-1

Three Point Bending

In order to figure out the tube flattening, shearing and tube bending contributions in three-point bending analysis, the ratios are derived as follows.

The total displacement, as mentioned in Chapter 3 is given as:

$$\delta_{Total} = \delta_{indent} + \delta_{bend} + \delta_{shear} \quad (A4.1)$$

Here, the displacement due to indentation, $\delta_{indentation}$, governs the wall bending observed in short suspension lengths. The displacement due to shear, $\delta_{shearing}$, is the anisotropic shearing effect that is governed by the low shear modulus of the tube and $\delta_{bending}$ is the factor that is governed by the longitudinal modulus of the tube.

$$\delta_{Total} = \frac{PR^{1.5}}{CEt^{2.5}} + \frac{PL^3}{192EI} + \frac{fPL}{GA} \quad (A4.2)$$

Here, P is the force, R is the average tube radius, L is the suspended tube length, C is a prefactor ($C \approx 1$), f is a constant ($f = 1.38$ for hollow cylinders), I is the second moment of tube's area A . The effective elastic properties are the longitudinal modulus, E^* ; the shear modulus G^* and the thickness is t^* .

Note that:

The cross sectional area for the thin-walled cylinder: $A = 2\pi Rt$

The second moment of the area: $I = \frac{\pi}{4} \left\{ (R + 0.5t)^4 - (R - 0.5t)^4 \right\} \approx \pi R^3 t$

Recall Chapter 2:

The axial stiffness: $K_A = E^* t^*$

The shear stiffness: $K_s = G^* t^*$

For the anisotropic tube: $\frac{K_A}{K_s} = \frac{2.4}{0.012} = 200$;

For the isotropic tube: $\frac{K_A}{K_s} = 2(1 + \nu) = 2.7$; where $\nu = 0.35$ is the poisson ratio.

From here, further reductions would yield:

$$\frac{\delta_{indent}}{P} = \frac{R^{1.5}}{CEt^{2.5}} = \frac{R^{1.5}}{C \frac{K_A}{t} t^{2.5}} = \frac{R^{1.5}}{CK_A t^{1.5}} = \frac{1}{C} \left(\frac{R}{t} \right)^{1.5} \frac{1}{K_A} \quad (A4.3)$$

$$\frac{\delta_{bend}}{P} = \frac{L^3}{192EI} = \frac{L^3}{192 \frac{K_A}{t} \pi R^3 t} = \frac{L^3}{192\pi K_A R^3} = \frac{1}{192\pi} \left(\frac{L}{R} \right)^3 \frac{1}{K_A} \quad (A4.4)$$

$$\frac{\delta_{shear}}{P} = \frac{fL}{GA} = \frac{fL}{\frac{K_s}{t} 2\pi R t} = \frac{fL}{2\pi K_s R} = \frac{f}{2\pi} \left(\frac{L}{R} \right) \frac{1}{K_s} \quad (A4.5)$$

The ratios of each term would be calculated as:

$$\frac{\frac{\delta_{shear}}{P}}{\frac{\delta_{bend}}{P}} = \frac{\delta_{shear}}{\delta_{bend}} = \frac{\frac{f}{2\pi} \left(\frac{L}{R} \right) \frac{1}{K_s}}{\frac{1}{192\pi} \left(\frac{L}{R} \right)^3 \frac{1}{K_A}} = f 96\pi \left(\frac{R}{L} \right)^2 \frac{K_A}{K_s} \quad (A4.6)$$

Here f is 1.38 for a hollow cylinder.

$$\frac{\frac{\delta_{indent}}{P}}{\frac{\delta_{bend}}{P}} = \frac{\delta_{indent}}{\delta_{bend}} = \frac{\frac{1}{C} \left(\frac{R}{t}\right)^{1.5} \frac{1}{K_A}}{\frac{1}{192\pi} \left(\frac{L}{R}\right)^3 \frac{1}{K_A}} = \frac{192\pi}{C} \left(\frac{R^{4.5}}{L^3 t^{1.5}}\right) \quad (\text{A4.7})$$

Here: $0 < C < 2$

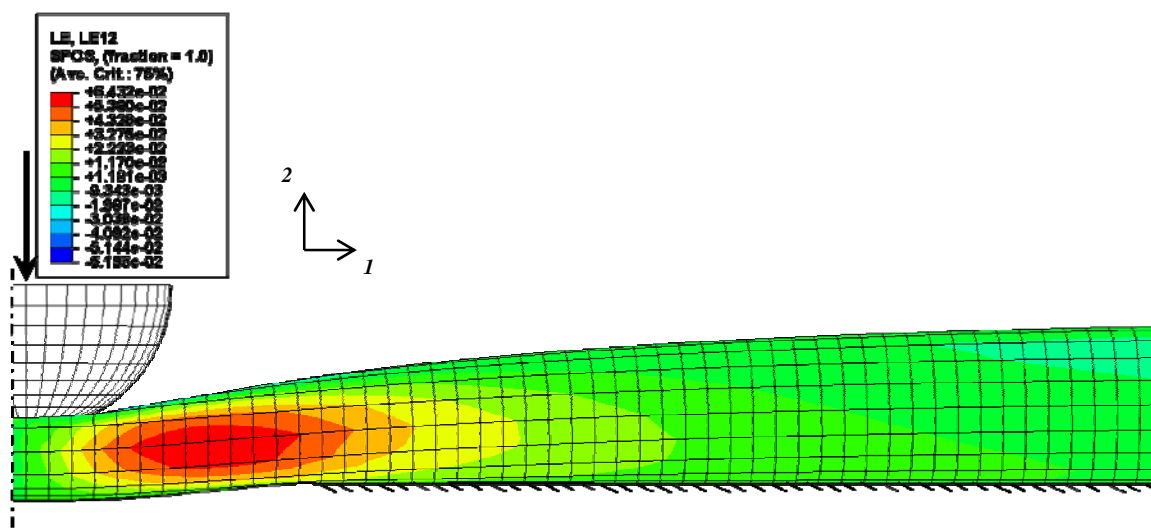
And finally:

$$\frac{\frac{\delta_{indent}}{P}}{\frac{\delta_{shear}}{P}} = \frac{\delta_{indent}}{\delta_{shear}} = \frac{\frac{1}{C} \left(\frac{R}{t}\right)^{1.5} \frac{1}{K_A}}{\frac{f}{2\pi} \left(\frac{L}{R}\right) \frac{1}{K_s}} = \frac{2\pi}{fC} \left(\frac{R^{2.5}}{Lt^{1.5}}\right) \left(\frac{K_s}{K_A}\right) \quad (\text{A4.8})$$

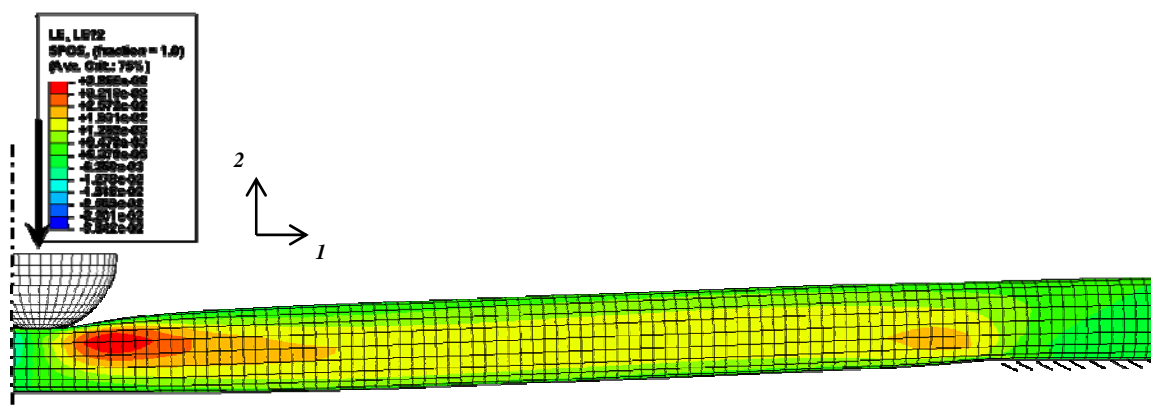
Appendix 3-2

THREE-POINT BENDING, Shear Strain Contours ANISOTROPIC TUBE

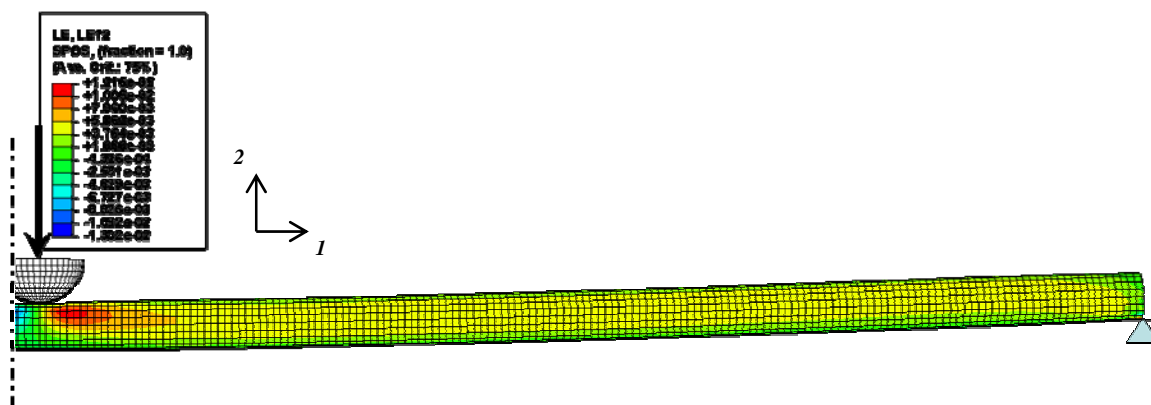
80 nm suspension length

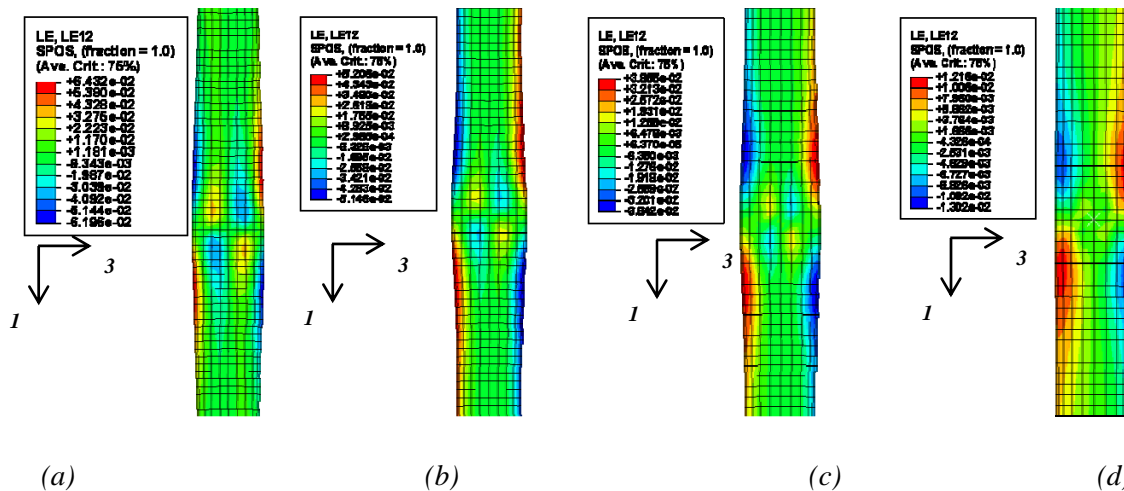


500 nm suspension length



1000 nm suspension length

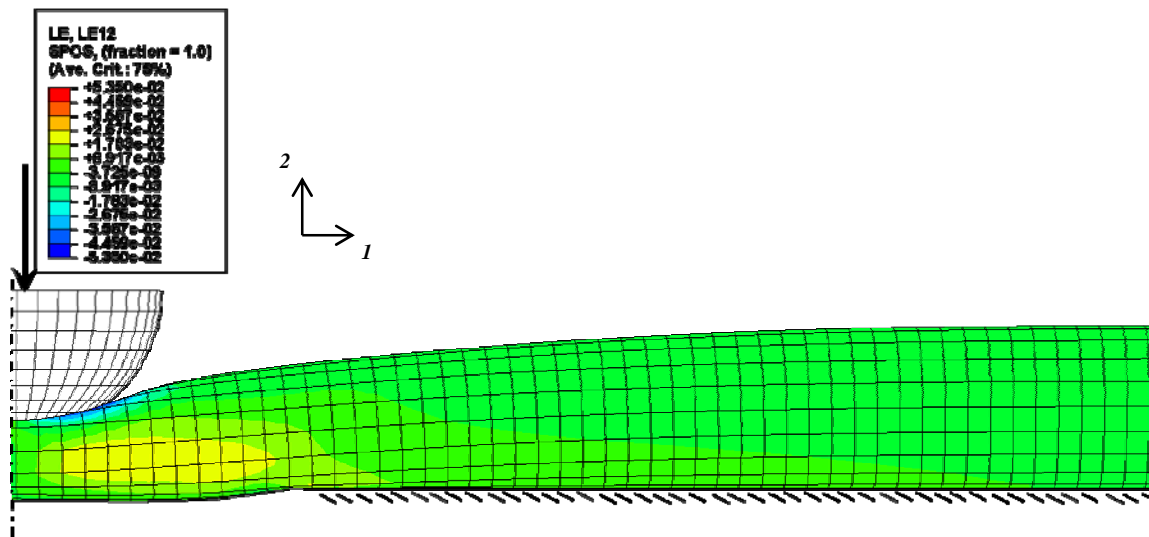




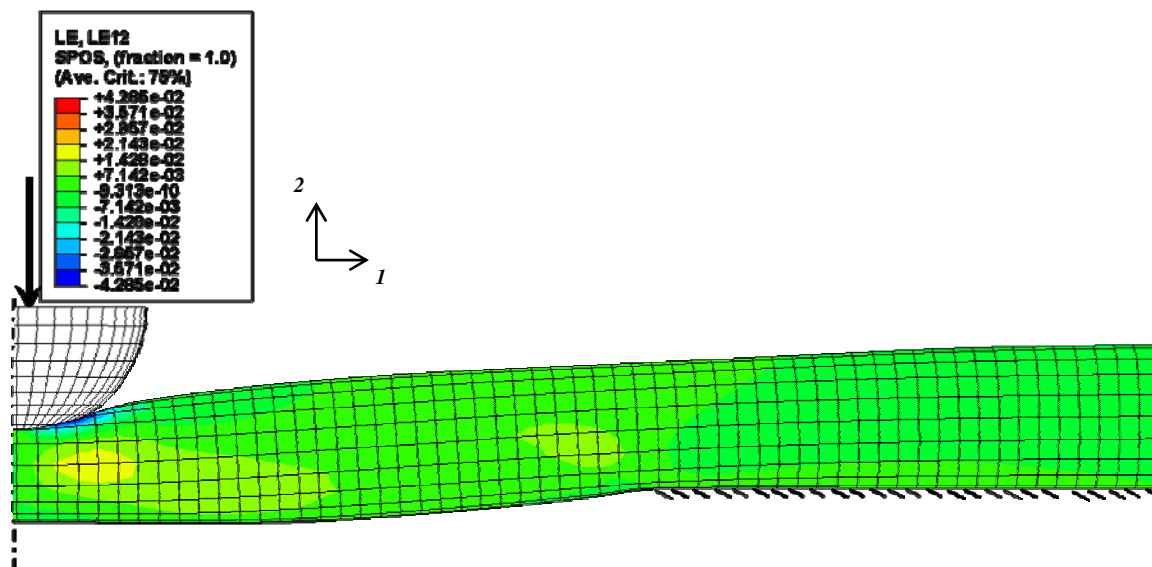
- (a) 80 nm suspension length
- (b) 200 nm suspension length
- (c) 500 nm suspension length
- (d) 1000 nm suspension length

THREE POINT BENDING, Shear Strain Contours ISOTROPIC TUBE

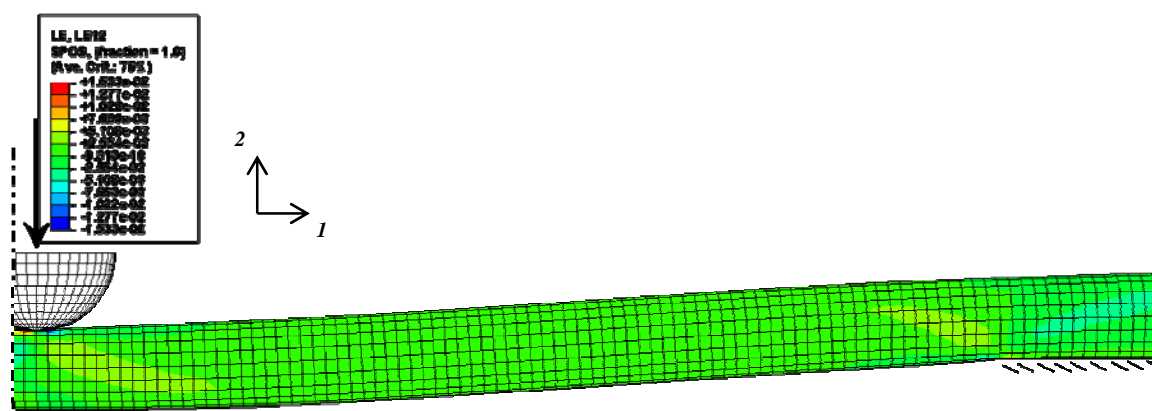
80 nm suspension length



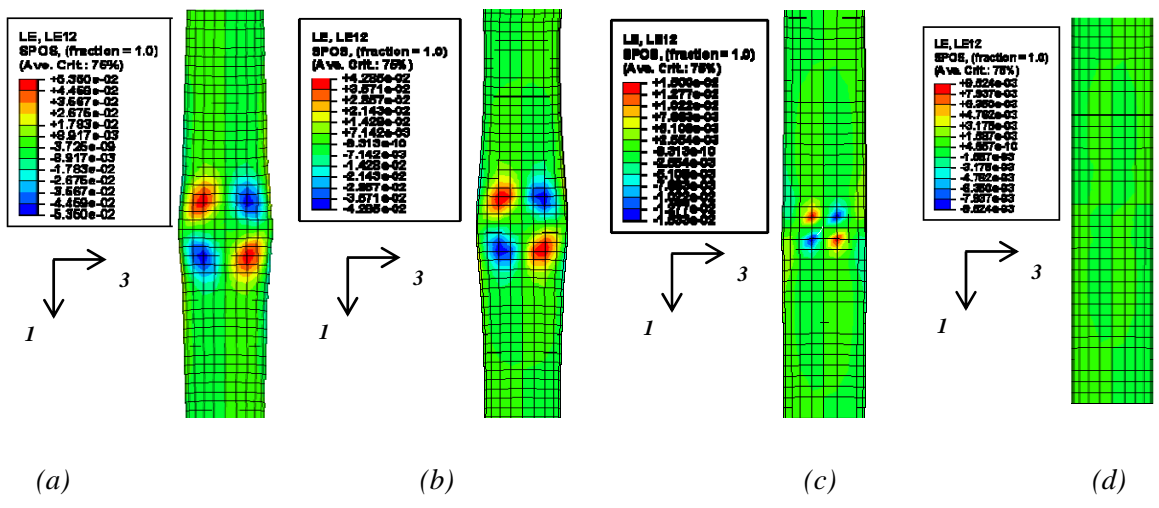
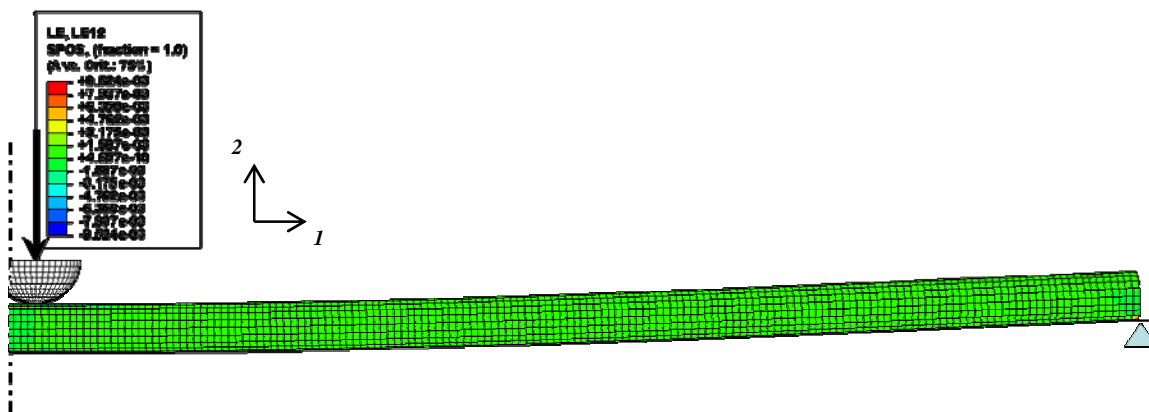
200 nm suspension length



500 nm suspension length



1000 nm suspension length



(a) 80 nm suspension length

(b) 200 nm suspension length

(c) 500 nm suspension length

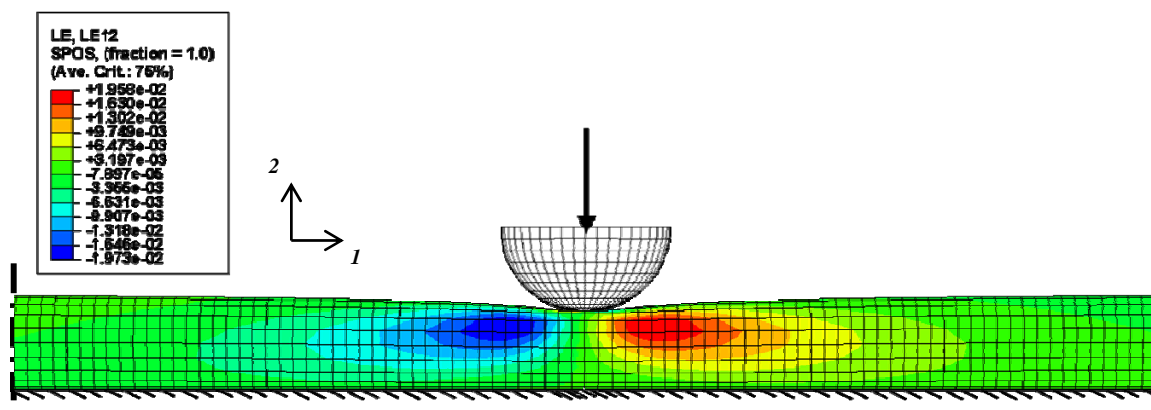
(d) 1000 nm suspension length

Appendix 3-3

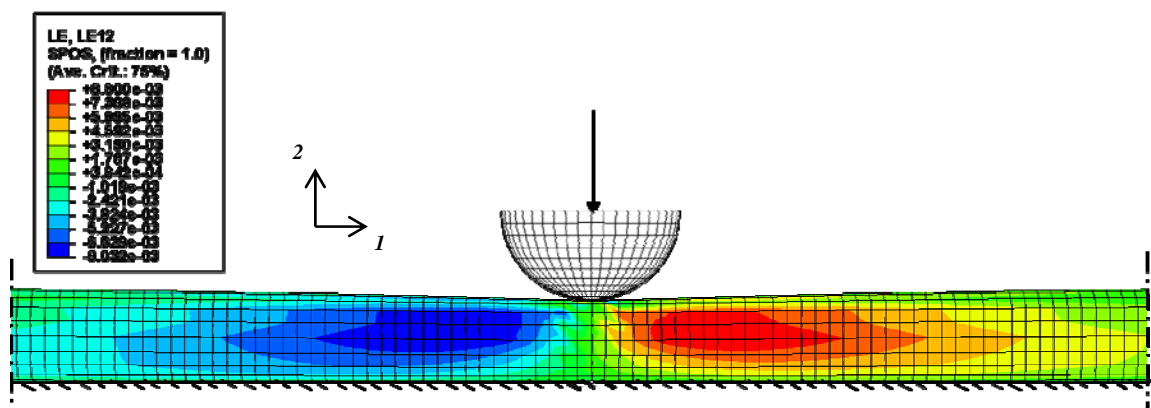
RADIAL INDENTATION, Shear Strain Contours

ANISOTROPIC TUBE

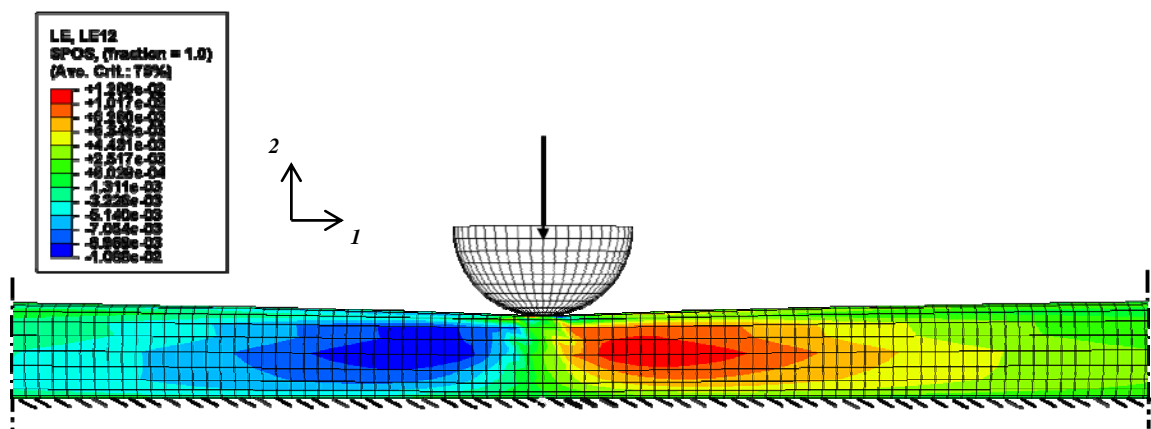
$$E^* = 2.4 \text{ GPa}, t^* = 1 \text{ nm}$$



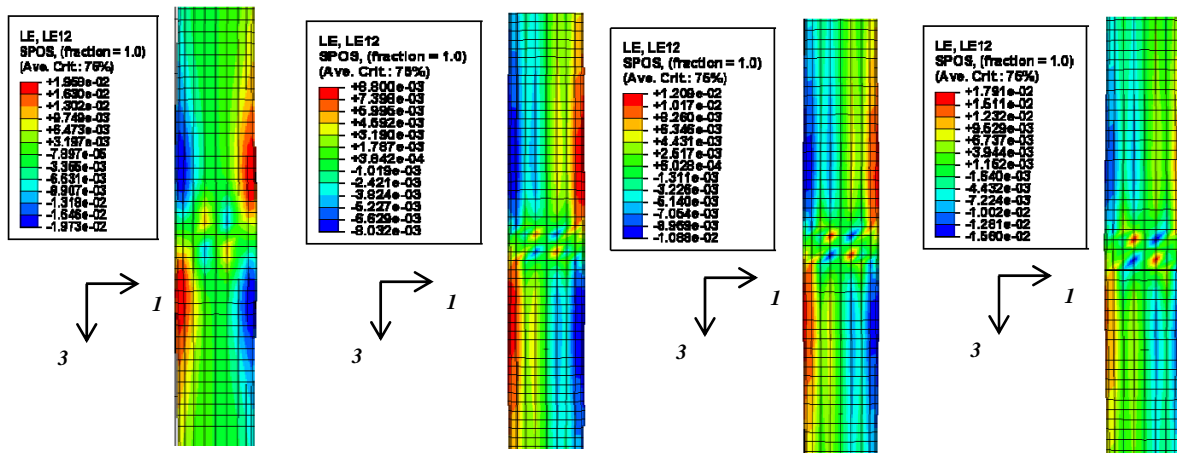
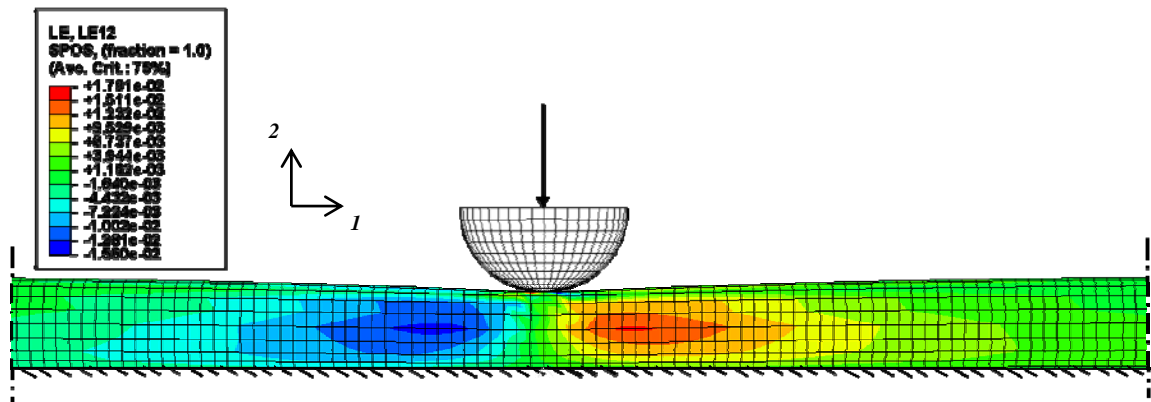
$$E^* = 1.6 \text{ GPa}, t^* = 1.5 \text{ nm}$$



$$E^* = 1.2 \text{ GPa}, t^* = 2 \text{ nm}$$



$E^*=0.96GPa, t^*=2.5nm$



(a) (b) (c) (d)

(a) $E^*=2.4 GPa, t^*=1nm$

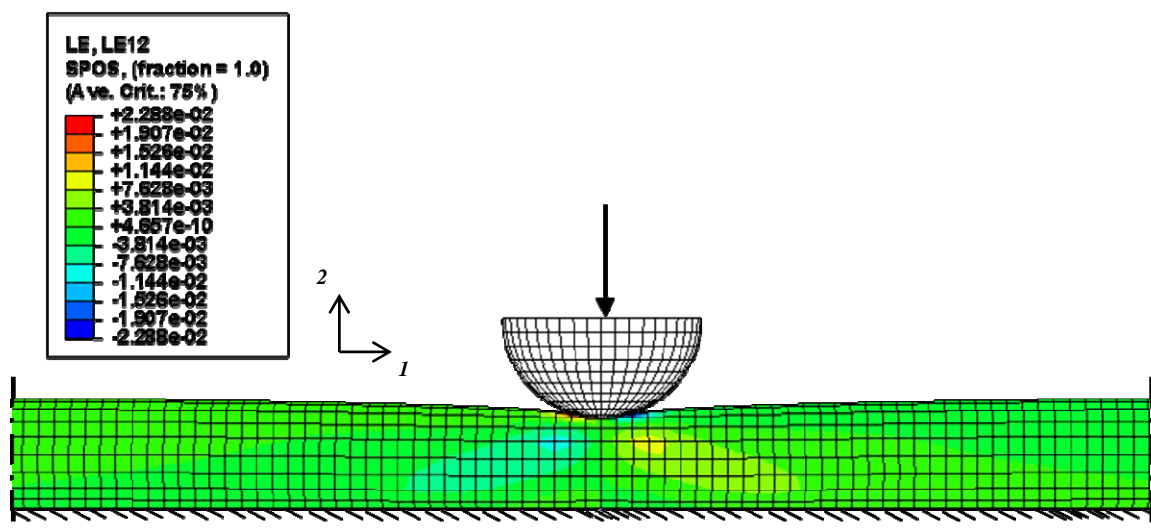
(b) $E^*=1.6 GPa, t^*=1.5nm$

(c) $E^*=1.2 GPa, t^*= 2 nm$

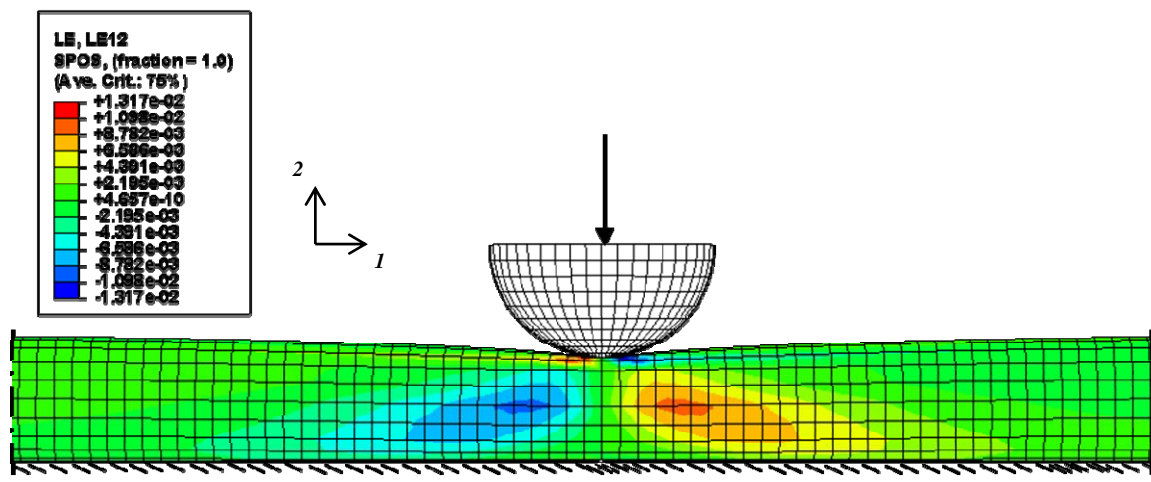
(d) $E^*=0.96 GPa, t^*= 2.5 nm$

RADIAL INDENTATION, Shear Strain Contours ISOTROPIC TUBE

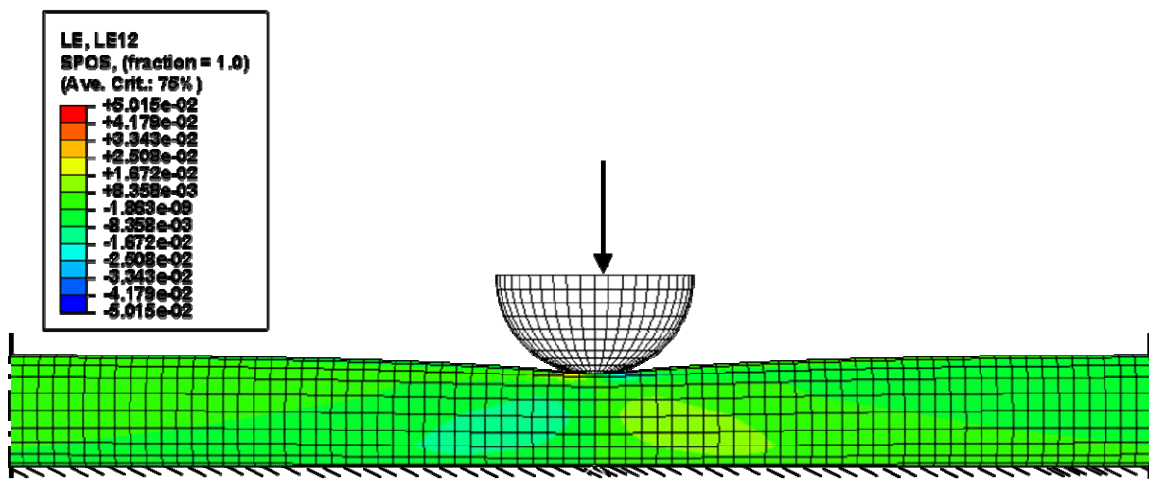
$$E^* = 2.4 \text{ GPa}, t^* = 1 \text{ nm}$$



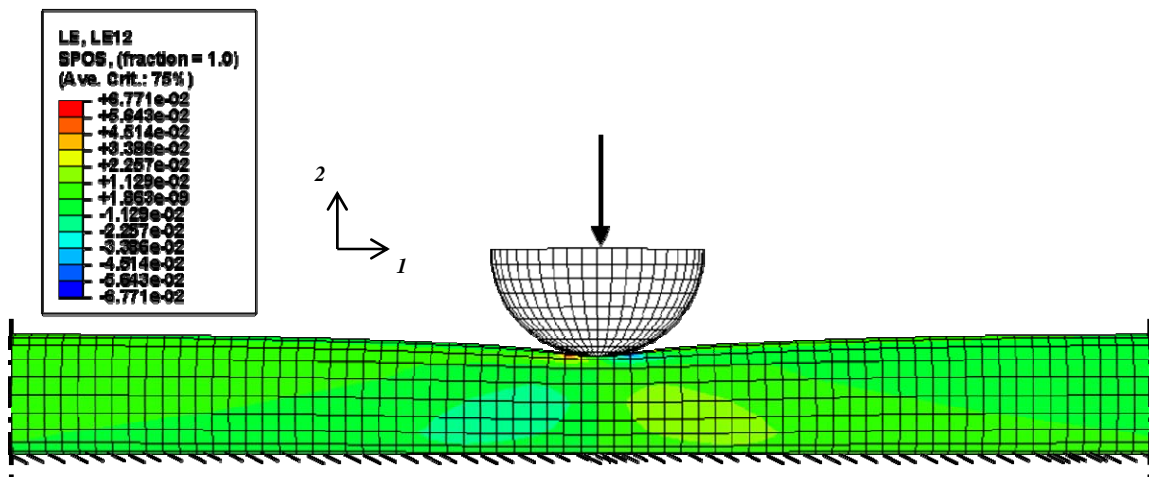
$$E^* = 1.6 \text{ GPa}, t^* = 1.5 \text{ nm}$$

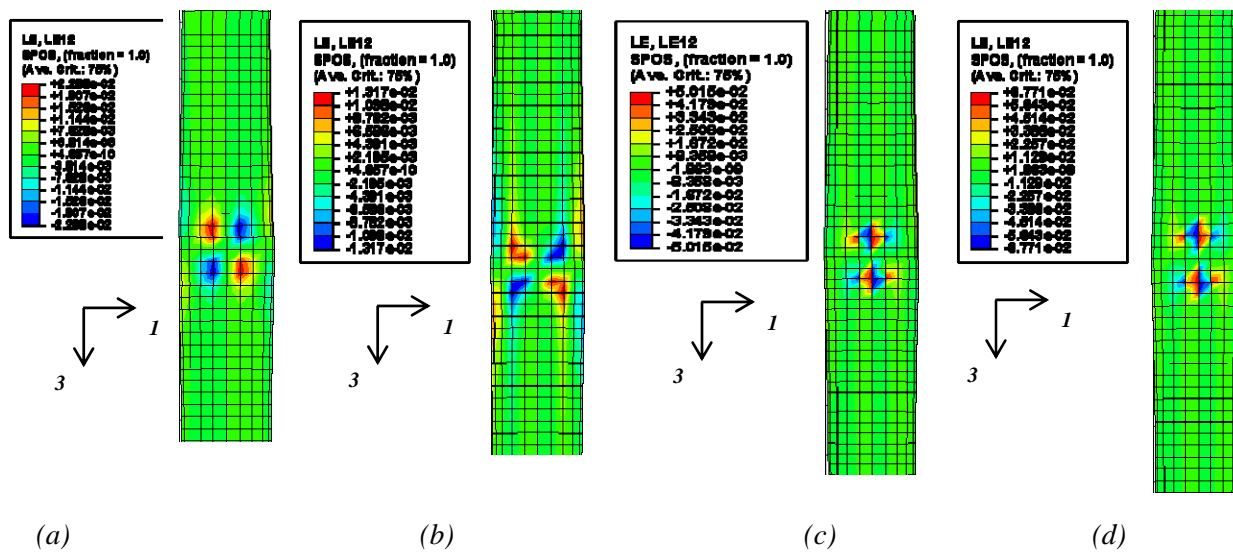


$$E^* = 1.2 \text{ GPa}, t^* = 2 \text{ nm}$$



$$E^* = 0.96 \text{ GPa}, t^* = 2.5 \text{ nm}$$





(a) $E^*=2.4 \text{ GPa}$, $t^*=1 \text{ nm}$

(b) $E^*=1.6 \text{ GPa}$, $t^*=1.5 \text{ nm}$

(c) $E^*=1.2 \text{ GPa}$, $t^*=2 \text{ nm}$

(d) $E^*=0.96 \text{ GPa}$, $t^*=2.5 \text{ nm}$

REFERENCES

- Amos, L. A. and A. Klug. 1974. Arrangement of Subunits in Flagellar Microtubules. *Jnl. Cell Sci.* 14: 523–549.
- Amos, L. A. and T. S. Baker. 1979. The three-dimensional structure of tubulin protofilaments. *Nature.* 279: 607–612.
- Amos, L. A., and J. Lowe. 1999. How Taxol stabilises microtubule structure. *Chem. Biol.* 6:R65–R69.
- Arnal, I., E. Karsenti, and A. A. Hyman. 2000. Structural transitions at microtubule ends correlate with their dynamic properties in *Xenopus* egg extracts. *Jnl. Cell Biol.* 149:767–774.
- Arslan, M. and M. C. Boyce. 2006. Constitutive Modeling of the Finite Deformation Behavior of Membranes Possessing a Triangulated Network Microstructure. *Jnl Appl. Mech.* 73: 536–543.
- Baker, N., Sept, D., Joseph, S., Holst, M., and J.A. McCammon. 2001. Electrostatics of nanosystems. Application to microtubules and the ribosome. *Proc. Natl. Acad. Sci.* 98: 10037–10041.
- Bayley P., Schilstra M. and S. Martin. 1989. A lateral cap model of microtubule dynamic instability. *FEBS Lett.* 259. 1:181–184.
- Becker, W. M., Kleinsmith L. J., Hardin, J., and G. P. Bertoni. 2008. *World of the Cell.* 7th edn. Benjamin Cummings.
- Binnig, G., Quate C. F., and C. Gerber. 1986. Atomic Force Microscope, *Phys. Rev. Lett.* 56, 930–934.
- Boal, D. 2002. *Mechanics of the cell.* Cambridge University Press. London
- Bolterauer, H., Limbach, H.-J. and J.A. Tuszynski. 1999. Microtubules: Strange Polymers inside the Cell. *Bioelectrochem. and Bioener.* 48: 285–295.
- Brangwynne, C.P., MacKintosh, F.C., Kumar, S., Geisse, N.A., Talbot, J., Mahadevan, L., Parker, K. K., Ingber, D. E., and D.A. Weitz. 2006. Microtubules can bear enhanced compressive loads in living cells because of lateral reinforcement. *Jnl. Cell Biol.* 173:733–741.

Caplow, M., R. L. Ruhlen, and J. Shanks. 1994. The free energy for hydrolysis of a microtubule-bound nucleotide triphosphate is near zero: all of the free energy for hydrolysis is stored in the microtubule lattice. *Jnl. Cell Biol.* 127:779–788.

Caplow, M., and J. Shanks. 1996. Evidence that a single monolayer tubulin-GTP cap is both necessary and sufficient to stabilize microtubules. *Mol. Biol. Cell.* 7:663–675.

Cassimeris, L., and C. Spittle. 2001. Regulation of microtubule associated proteins. *Int. Rev. Cytol.* 210:163–226.

Chrétien D. and R. H. Wade. 1991. New data on the microtubule surface lattice. *Biol. Cell.* 71: 161–174.

Chretien, D., F. Metz, F. Verde, E. Karsenti, and R. H. Wade. 1992. Lattice defects in microtubules: protofilament numbers vary within individual microtubules. *Jnl. Cell Biol.* 117:1031–1040.

Chretien, D., S. D. Fuller, and E. Karsenti. 1995. Structure of growing microtubule ends: two-dimensional sheets close into tubes at variable rates. *Jnl. Cell Biol.* 129:1311–1328.

Chretien, D., H. Flyvbjerg, and S. D. Fuller. 1998. Limited flexibility of the interprotofilament bonds in microtubules assembled from pure tubulin. *Eur. Biophys. Jnl.* 27:490–500.

Chretien, D., and S. D. Fuller. 2000. Microtubules switch occasionally into unfavorable configurations during elongation. *Jnl. Mol. Biol.* 298:663–676.

Cook, R. D. 1981. *Concepts and Application of Finite Element Analysis*. John Wiley & Sons.

de Pablo, P. J., J. Colchero, J. Gomez-Herrero, and A. M. Baro. 1998. Jumping mode scanning force microscopy. *Appl. Phys. Lett.* 73:3300–3302.

de Pablo, P. J., I. A. T. Schaap, F. C. MacKintosh, and C. F. Schmidt. 2003. Deformation and collapse of microtubules on the nanometer scale. *Phys. Rev. Lett.* 91:098101.

Deriu, M. A., Enemark, S., Soncini, M., Montevecchi, F. M., and A. Redaelli. 2007. Tubulin: from atomistic structure to supramolecular mechanical properties. *Jnl. Mat. Sci.* 42: 8864–8872.

Downing, K. H., and E. Nogales. 1998. Tubulin and microtubule structure. *Curr. Opin. Cell. Biol.* 10:16–22.

Elbaum, M., Fygenson, D. K., and A. Libchaber. 1996. Buckling Microtubules in Vesicles. *Phys. Rev. Lett.*, 76: 4078–4081.

- Enemark, S., Deriu, M. A., Soncini, M. and A. Redaelli. 2008. Mechanical Model of the Tubulin Dimer Based on Molecular Dynamics Simulations. *Jnl. Biomech. Eng.* 130: 041008.
- Erickson, H.P. 1989. Co-operativity in protein-protein association. The structure and stability of the actin filament. *Jnl. Mol. Biol.* 206: 465–474.
- Felgner, H., R. Frank, and M. Schliwa. 1996. Flexural rigidity of microtubules measured with the use of optical tweezers. *Jnl. Cell Sci.* 109:509–516.
- Felgner, H., Frank, R., Biernat, J., Mandelkow, E. M., Mandelkow, E., Ludin, B., Matus, A., and M. Schliwa. 1997. Domains of neuronal microtubule-associated proteins and flexural rigidity of microtubules. *Jnl. Cell Biol.*, 138: 1067–1075.
- Fuchs, E and D. W. Cleveland. 1998. A structural scaffolding of intermediate filaments in health and disease. *Science.* 27: 514–519.
- Gates, T.S., Odegard, G. M., Frankland, S. J. V., and T. C. Clancy. 2005. Computational Materials: Multi-Scale Modeling and Simulation of Nanostructured Materials. *Comp. Sci. and Tech.* 65: 2416–2434.
- Gibson, L. J., and M. F. Ashby. 1988. *Cellular solids : structure & properties*. Pergamon Press. Oxford. New York.
- Grimstone, A. V., and A. Klug. 1966. Observations in the substructure of flagellar fibres. *Jnl. Cell Sci.* I: 351–362.
- Gittes, F., B. Mickey, J. Nettleton, and J. Howard. 1993. Flexural rigidity of microtubules and actin filaments measured from thermal fluctuations in shape. *Jnl. Cell Biol.* 120:923–934.
- Gittes, F., E. Meyhofer, S. Baek, and J. Howard. 1996. Directional loading of the kinesin motor molecule as it buckles a microtubule. *Biophys. Jnl.* 70:418–429.
- Grishchuk, E.L., Molodtsov, M.I., McIntosh, J.R., and F. I. Ataullakhanov. 2005. Force production by disassembling microtubules. *Nature.* 438: 384–388.
- Hartwig, J. H. 1992. Mechanisms of actin rearrangements mediating platelet activation. *Jnl. Cell Biol.* 118. 6: 1421–1442.
- Horio, T., and H. Hotani. 1986. Visualization of the dynamic instability of individual microtubules by dark-field microscopy. *Nature.* 321:605–607.

- Howard, J. 2001. *Mechanics of Motor Proteins and the Cytoskeleton*. Sinauer Assoc., Sunderland, MA.
- Hunyadi, V., Chretien, D., and I.M. Janosi. 2005. Mechanical stress induced mechanism of microtubule catastrophes. *Jnl. Mol. Biol.* 348:927–938.
- Ingber, D.E. 1998. The architecture of life. *Scientific American*. 48–57.
- Janmey, P.A., Euteneuer, U., Traub, P., and M. Schliwa. 1991. Viscoelastic properties of vimentin compared with other filamentous biopolymer networks. *Jnl. Cell Biol.* 113:155–60.
- Janosi, I. M., D. Chretien, and H. Flyvbjerg. 1998. Modeling elastic properties of microtubule tips and walls. *Eur. Biophys. J.* 27:501–513.
- Janosi, I. M., D. Chretien, and H. Flyvbjerg. 2002. Structural microtubule cap: stability, catastrophe, rescue, and third state. *Biophys. Jnl.* 83:1317–1330.
- Jiang, L., Y. Gao, F. Mao, Z. Liu, and L. Lai. 2002. Potential of mean force for protein-protein interaction studies. *Proteins*. 46:190–196.
- Jordan, M. A., and L. Wilson. 2004. Microtubules as a target for anticancer drugs. *Nature Rev. Cancer*. 4: 253–265.
- Kirschner, M. W. 1978. Microtubule assembly and nucleation. *Int. Rev. Cytol.* 54:1–71.
- Kirschner M. and T. Mitchison. 1986. Beyond self-assembly: from microtubules to morphogenesis. *Cell*. 45. 3:329–42.
- Kirschner, M. and T. Mitchison. 2004. *Dynamic Instabilities of Microtubules*. Virtual Text/www.ergito.com.
- Kis, A., Kasas, S., Babic, B., Kulik, A. J., Benoît, W., Briggs, G. A. D., Schönenberger, C., Catsicas, S. and L. Forró. 2002. Nanomechanics of Microtubules. *Phys. Rev. Lett.* 89: 248101.
- Kis A. 2003. Mechanical properties of mesoscopic objects. Thèse EPFL, no 2876. Dir.: László Forró.
- Koren R. and G. G. Hammes. 1976. A kinetic study of protein-protein interactions. *Biochem.* 15. 5:1165–1171.
- Kurachi, M., Hoshi, M., and H. Tashiro. 1995. Buckling of a Single Microtubule by Optical Trapping Forces: Direct Measurement of Microtubule Rigidity. *Cell Motil. Cytoskeleton*. 30:221–228.

- Kurz, J. C., and R.C. Williams. 1995. Microtubule-associated proteins and the flexibility of microtubules. *Biochemistry*. 34: 13374–13380.
- Landau, L. D., and E. M. Lifshitz. 1986. *Theory of Elasticity*. Pergamon Press, New York.
- Langford G. M. 1980. Arrangement of subunits in microtubules with 14 protofilaments. *Jnl Cell Biol.* 87: 521–526.
- Ledbetter, M. C. and K. R. Porter. 1963. A “microtubule” in plant cell fine structure. *Jnl. Cell Biol.* 19: 239–250.
- Li, H., D. J. DeRosier, W. V. Nicholson, E. Nogales, and K. H. Downing. 2002. Microtubule structure at 8Å resolution. *Structure*. 10:1317–1328.
- Liedewij L., Husson, J., Munteanu, E. L., Kerssemakers, J. W. J. and D. Marileen. 2008. Force-generation and dynamic instability of microtubule bundles. *Proc. Natl. Acad. Sci. USA*. 105. 26: 8920–8925.
- Lodish, H., Matsudaira, P., Berk, A., Ploegh, H., and M. P. Scott. 2007. *Molecular Cell Biology*. 6th edn. W. H. Freeman Company.
- Ma, L., Xu, J., Coulombe, P. A., and D. Wirtz. 1999. Keratin filament suspensions show unique micromechanical properties. *Jnl. Biol. Chem.* 274: 19145–19151.
- Mandelkow, E. M., and E. Mandelkow. 1985. Unstained microtubules studied by cryo-electron microscopy. Substructure, supertwist and disassembly. *Jnl. Mol. Biol.* 181:123–135.
- Mandelkow, E. M., Schultheiss, R., Rapp, R., Müller, M. and E. Mandelkow. 1986. On the surface lattice of microtubules : helix starts, protofilament number, seam, and handedness . *Jnl. Cell Biol.* 102 :1067-1073 .
- Mandelkow, E. M., E. Mandelkow, and R. A. Milligan. 1991. Microtubule dynamics and microtubule caps: a time-resolved cryo-electron microscopy study. *Jnl. Cell Biol.* 114:977–991.
- Martin, S. R., Schlistra, M. J. and P. M. Bayley. 1993. Dynamic instability of microtubules: Monte Carlo simulation and application to different types of microtubule lattice *Biophys. Jnl.* 65: 578–596.
- Metoz, F., and R. H. Wade. 1997. Diffraction by Helical Structures with Seams: Microtubules. *Jnl. Struc. Biol.* 118:128–139.

- Meurer-Grob, P., J. Kasparian, and R. H. Wade. 2001. Microtubule structure at improved resolution. *Biochemistry*. 40:8000–8008.
- Mickey, B., and J. Howard. 1995. Rigidity of microtubules is increased by stabilizing agents. *Jnl. Cell Biol.* 130:909–917.
- Mitchison, T., and M. Kirschner. 1984. Dynamic instability of microtubule growth. *Nature*. 312:237–242.
- Molodtsov M. I., Ermakova E. A., Shnol E. E., Grishchuk E. L., McIntosh J. R., and F. I. Ataullakhanov. 2005. A molecular-mechanical model of the microtubule. *Biophys. Jnl.* 88. 5:3167–79.
- Molodtsov M. I., Grishchuk E. L., Efremov A. K., McIntosh J. R., and F. I. Ataullakhanov. 2005. Force production by depolymerizing microtubules: a theoretical study. *Proc. Natl. Acad. Sci. USA*. 102. 12:4353–8.
- Moreno-Herrero, F., de Pablo, P. J., Fernandez-Sanchez, R., Colchero, J., Gómez -Herrero, J. and A.M. Baro. 2002. Scanning Force Microscopy Jumping and Tapping modes in liquids. *Appl. Phys. Lett.* 81: 2620–2622.
- Muller-Reichert, T., D. Chretien, F. Severin, and A. A. Hyman. 1998. Structural changes at microtubule ends accompanying GTP hydrolysis: information from a slowly hydrolyzable analogue of GTP, guanylyl (alpha,beta)methylenediphosphonate. *Proc. Natl. Acad. Sci. USA*. 95:3661–3666.
- Needleman, D. J., M. A. Ojeda-Lopez, U. Raviv, K. Ewert, J. B. Jones, H. P. Miller, L. Wilson, and C. R. Safinya. 2004. Synchrotron x-ray diffraction study of microtubules buckling and bundling under osmotic stress: a probe of interprotofilament interactions. *Phys. Rev. Lett.* 93:198104.
- Needleman, D. J., Ojeda-Lopez, M. A., Raviv, U., Ewert, K., Miller, H. P., Wilson, L., and C. R. Safinya. 2005. Radial compression of microtubules and the mechanism of action of taxol and associated proteins. *Biophys. Jnl.* 89:3410–3423.
- Nicholson, W. V., M. Lee, K. H. Downing, and E. Nogales. 1999. Cryoelectron microscopy of GDP-tubulin rings. *Cell Biochem. Biophys.* 31:175–183.
- Niordson, F. 1985. *Shell Theory*. North-Holland, New York.
- Nogales, E., S. G. Wolf, and K. H. Downing. 1998. Structure of the $\alpha\beta$ tubulin dimer by electron crystallography. *Nature*. 391:199–203.
- Nogales, E., M. Whittaker, R. A. Milligan, and K. H. Downing. 1999. High-resolution model of the microtubule. *Cell*. 96:79–88.

- Nogales, E. 2001. Structural insights into microtubule function. *Annu. Rev. Biophys. Biomol. Struct.* 30:397–420.
- Nogales, E., H. W. Wang, and H. Niederstrasser. 2003. Tubulin rings: which way do they curve? *Curr. Opin. Struct. Biol.* 13:256–261.
- Northrup, S. H. and H. P. Erickson. 1992. Kinetics of protein-protein association explained by Brownian dynamics computer simulation. *Proc. Natl. Acad. Sci. USA* 89: 3338–3342.
- Odde, D. J., L. Cassimeris, and H. M. Buettner. 1995. Kinetics of microtubule catastrophe assessed by probabilistic analysis. *Biophys. Jnl.* 69:796–802.
- Pantano, A., Parks, D.M., and M.C., Boyce. 2003. Nonlinear structural mechanics based modeling of carbon nanotube deformation. *Phys. Rev. Lett.* 91. 14: 145504.
- Pantano, A., Boyce, M. C., and D. M., Parks. 2004-a. Mechanics of Axial Compression of Single and Multi-Wall Carbon Nanotubes. *Jnl. Eng. Mat. Tech.* 126: 279–284.
- Pantano, A., Parks, D. M., and M. C. Boyce. 2004-b. Mechanics of deformation of single- and multi-wall carbon nanotubes. *Jnl. Mech. Phys. Solids.* 52: 789–821.
- Pampaloni F., Lattanzi G., Jonás A., Surrey T., Frey E., and E. L. Florin. 2006. Thermal fluctuations of grafted microtubules provide evidence of a length-dependent persistence length. *Proc. Natl. Acad. Sci. USA.* 103. 27:10248–53.
- Pampaloni F. and E. L. Florin. 2008. Microtubule architecture: inspiration for novel carbon nanotube-based biomimetic materials. *Trends in biotech.* 26. 6:302–10.
- Portet, S., Tuszynski, J. A., Hogue, C. M. and J.M. Dixon. 2005. Elastic vibrations in seamless microtubules. *Eur. Biophys. Jnl.* 34: 912–920.
- Raven, P., Johnson, G., Singer, S. and J. Losos. 2004. *Biology*. McGraw-Hill Co. New York.
- Reif, F. 1965. *Fundamentals of Statistical and Thermal Physics*. McGraw-Hill, New York.
- Salvetat, J.-P., Bonard, J. M., Thomson, N. H., Kulik, A. J., Forró, L., Benoit W., and L. Zuppiroli. 1999. Mechanical Properties of Carbon Nanotubes, *Applied Phys. A* 69:255–260.
- Sataric, M. V., and J.A. Tuszynski. 2003. Relationship Between the Nonlinear Ferroelectric and Liquid Crystal Models for Microtubules. *Phys. Rev. E* 67: 011901-1-11.

- Schaap, I. A. T., P. J. de Pablo, and C. F. Schmidt. 2006. Resolving the molecular structure of microtubules under physiological conditions with scanning force microscopy. *Eur. Biophys. Jnl.* 33:462–467.
- Sept, D., N. A. Baker, and J. A. McCammon. 2003. The physical basis of microtubule structure and stability. *Protein Sci.* 12:2257–2261.
- Sirenko, Y. M., Stroschio, M.A., and K. W., Kim. 1996a. *Phys. Rev. E* 54:1816.
- Sirenko, Y. M., Stroschio, M. A., and K. W., Kim. 1996b. *Phys. Rev. E* 53:1003.
- Sneddon, I. N. 1965. The relation between load and penetration in the axisymmetric Boussinesq problem for a punch of arbitrary profile. *Int. Jnl. Eng. Sci.* 3:47–57.
- Song Y. H. and E. Mandelkow. 1993. Recombinant Kinesin Motor Domain Binds to Beta-Tubulin and Decorates Microtubules with a B-Surface Lattice. *Proc. Natl. Acad. Sci. USA.* 90: 1671–1675.
- Takasone, T., Juodkazis, S., Kawagishi, Y., Yamaguchi, A., Matsuo, S., Sakakibara, H., Nakayama, H., and H. Misawa. 2002. Flexural Rigidity of a Single Microtubule. *Jap. Jnl. Appl. Phys. Part 1.* 41: 3015–3019.
- Timoshenko, S. 1970. *Theory of Elasticity*. McGraw-Hill, New York.
- Tuszynski, J.A., Brown, J. A., Crawford, E., Carpenter, E. J., Nip, M. L. A., Dixon, J. M., and M.V. Sataric. 2005. Molecular Dynamics Simulations of Tubulin Structure and Calculations of Electrostatic Properties of Microtubules. *Math. and Comp. Model.* 41:1055-1070.
- VanBuren, V., D. J. Odde, and L. Cassimeris. 2002. Estimates of lateral and longitudinal bond energies within the microtubule lattice. *Proc. Natl. Acad. Sci. USA.* 99:6035–6040.
- Vanburen, V., L. Cassimeris, and D. J. Odde. 2005. A mechanochemical model of microtubule structure and self-assembly kinetics. *Biophys. Jnl.* 89:2911–2926.
- Venier, P., A. C. Maggs, M. F. Carlier, and D. Pantaloni. 1994. Analysis of microtubule rigidity using hydrodynamic flow and thermal fluctuations. *Jnl. Biol. Chem.* 269:13353–13360.
- Vinckier, A., C. Dumortier, Y. Engelborghs, and L. Hellemans. 1996. Dynamical and mechanical study of immobilized microtubules with atomic force microscopy. *Jnl. Vac. Sci. Technol. B.* 14:1427–1431.

Wang, H. W., and E. Nogales. 2005. Nucleotide-dependent bending flexibility of tubulin regulates microtubule assembly. *Nature*. 435:911–915.

Title : Micromechanical Modeling of Microtubules

ABSTRACT :

Microtubules serve as one of the structural components of the cell and take place in some of the important cellular functions such as mitosis and vesicular transport. Microtubules comprise of tubulin subunits tubulin dimers arranged in a cylindrical beta and formed by alpha hollow tube structure with a diameter of 20nm. They are typically comprised of 13 or 14 protofilaments arranged in spiral configurations. The longitudinal bonds between the tubulin dimers are much stiffer and stronger than the lateral bonds. This implies the anisotropic structure and properties of the microtubule. In this work, the aim is to define a complete set of elastic properties that capture the atomistic behavior and track the deformation of the microtubules under different loading conditions. A seamless microtubule wall is represented as a two dimensional triangulated lattice of dimers from which a representative volume element can be defined. A harmonic potential is adapted for the dimer–dimer interactions. Estimating the lattice elastic constants and following the methodology from the analysis of the mechanical behavior of triangulated spectrin network of the red blood cell membrane (Arslan and Boyce, 2006); a general continuum level constitutive model of the mechanical behavior of the microtubule lattice wall is developed. The model together with the experimental data given in the literature provides an insight to defining the parameters required for the discrete numerical model created in finite element analysis medium. The three point bending simulations for a microtubule modeled using shell elements, give tube bending stiffness values that are in accordance with the experimental bending stiffness values. The micrographs also show that shrinking ends of microtubules (due to microtubule instabilities) curl out. This implies the existence of prestress. A “connector model” is proposed to include the effect of the prestress and to capture the dynamic instabilities of microtubules.

Keywords : constitutive modeling,protein,microtubule,flexural rigidity,shear stiffness

